Structural and energetic properties of pentacene derivatives and heterostructures

DISSERTATION

zur Erlangung des akademischen Grades
doctor rerum naturalium
(Dr. rer. nat.)
im Fach Physik

eingereicht an der
Mathematisch-Naturwissenschaftlichen Fakultät I
Humboldt-Universität zu Berlin

von
Herrn Dipl.-Ing. Ingo Salzmann
geboren am 10.07.1974 in Linz, Österreich

Präsident der Humboldt-Universität zu Berlin:
Prof. Dr. C. Markschies

Dekan der Mathematisch-Naturwissenschaftlichen Fakultät I:
Prof. Dr. L. H. Schön

Gutachter:

1. Dr. Norbert Koch
2. Prof. Dr. Wolfgang Neumann
3. Prof. Dr. Roland Resel

eingereicht am: 03.12.2008
Tag der mündlichen Prüfung: 19.12.2008

Abstract

The scope of this work is the combination of the organic semiconductor pentacene (PEN) with different conjugated organic molecules to form application relevant heterostructures in vacuum sublimed films. Following a multi-technique approach – comprising x-ray diffraction, vibrational spectroscopy, atomic force microscopy and photoelectron spectroscopy – PEN heterostructures with (i) fullerene (C60), (ii) perfluoropentacene (PFP) and (iii) 6,13-pentacenequinone (PQ) were thoroughly characterized to judge on the respective application potential for organic electronic devices. (i) PEN heterostructures with C60 were investigated regarding the correlation of energetic, structural and morphological properties with the performance of organic photovoltaic cells (OPVCs) for both layered and mixed structures. Morphological rather than energetic or structural issues were identified to account for performance differences of bulk-heterojunction OPVCs compared to layered devices. (ii) Structural investigations were carried out on pure PFP films as well as on layered and mixed heterostructures with PEN. The thin film polymorph of PFP was solved and it is evidenced that blended films form a mixed crystal structure. This result led to the finding of both fundamental and application-related relevance that the ionization energy of organic films composed of molecules with intramolecular polar bonds (like C-H and C-F for PEN and PFP, respectively), can be tuned through the mixing ratio of the compounds. (iii) For pure PQ films a so far unknown thin film polymorph on silicon-oxide substrates was solved using x-ray diffraction reciprocal space mapping evidencing a loss of the herringbone arrangement known from the PQ bulk structure. For PEN heterostructures with PQ a highly molecular-orientation dependent ionization energy and energy level offsets interesting for the use in OPVCs were found. Mixed films of PEN and PQ exhibit phase separation and no intercalation was found even at PQ concentrations as low as 2%. Finally, the possible oxidation of PEN to PQ under oxygen exposure was investigated via the defined exposure of PEN films and single crystals to O_2 and/or water and to reactive oxygen species. It is demonstrated that O_2 and water do not react noticeably with PEN, whereas singlet oxygen and ozone readily oxidize the PEN film, however, producing highly volatile reaction products instead of PQ.

Keywords:
organic semiconductors, x-ray diffraction, photoelectron spectroscopy,
organic photovoltaic cells

Zusammenfassung

Das Ziel dieser Arbeit ist die Herstellung und die eingehende Charakterisierung von Heterostrukturen des organischen Halbleiters Pentazen (PEN) mit verschiedenen konjugierten organischen Materialien im Hinblick auf das Anwendungspotenzial im Bereich der organischen Elektronik. Für die Untersuchung von PEN-Heterostrukturen mit (i) Fulleren (C60), (ii) Perfluoropentazen (PFP) und (iii) 6,13-Pentazenchinon (PQ) wurden mehrere komplementäre experimentelle Techniken angewendet: Röntgenbeugung, Schwingungsspektroskopie, Rasterkraftmikroskopie und Photoelektronenspektroskopie. (i) Für PEN - Heterostrukturen mit C60 wurden die elektronischen, strukturellen und morphologischen Eigenschaften mit der Leistung von organischen Solarzellen (OSCs) für geschichtete und gemischte Systeme korreliert. Dabei wurde gezeigt, dass morphologische anstatt struktureller oder energetischer Ursachen die Leistungsunterschiede der beiden untersuchten Zelltypen erklären. (ii) Strukturuntersuchungen an reinen PFP-Filmen sowie an geschichteten und gemischten Heterostrukturen mit PEN wurden durchgeführt. Dabei wurde die Struktur der PFP-Dünnfilmphase gelöst und das Wachstum von PEN+PFP Mischkristallen gezeigt. Diese Mischung auf molekularer Ebene wurde erfolgreich angewandt, um die Ionisationsenergie (IE) des Films mit dem Mischungsverhältnis durchzustimmen, was durch die Existenz von innermolekularen polaren Bindungen (C-H und C-F für PEN und PFP) erklärt wurde. (iii) Für reine PQ Filme wurde die Struktur der PQ-Dünnfilmphase gelöst, dabei ist im Gegensatz zur Einkristallstruktur nur ein Molekül pro Einheitszelle vorhanden. Es wurde eine stark orientierungsabhängige IE von PQ und PEN gefunden und gezeigt, dass die relative Lage der Energieniveaus für die Anwendung als OSC geeignet ist. Die Untersuchung von Mischsystemen zeigte phasenseparierten Wachstum ohne Hinweise auf Interkalation selbst bei PQ Konzentrationen von nur 2%. Des Weiteren wurde eine mögliche Oxidation von PEN in dünnen Filmen und Einkristallen zu PQ mittels definierter Einwirkung von molekularem Sauerstoff und/oder Wasser sowie reaktiven Sauerstoffspezies untersucht, wobei O_2 und Wasser keine nachhaltigen Auswirkungen zeigten. Singlett-Sauerstoff und Ozon hingegen greifen PEN-Filme an und liefern flüchtige Reaktionsprodukte.

Schlagwörter:
organischer Halbleiter, Röntgenbeugung, Photoelektronenspektroskopie, organische Solarzellen

Contents

Chapter 1

Introduction

Since the early eighties of the last century enormous research efforts have been directed towards the exploration of organic semiconductors focussing on both the fundamental physical properties and the use as active material in the field of organic electronics. This high interest can be explained by the applicability of molecular thin films formed by conjugated organic compounds for novel electronic devices including organic field-effect transistors (OFETs), organic light-emitting diodes (OLEDs) or organic photovoltaic cells (OPVCs) [1–14]. Most notably, the possibility to alter both the electronic and the structural properties of molecular compounds through chemical substitution is regarded as *the* key advantage of organic compounds over inorganic semiconductors [15]. At the current stage of development and research organic electronic devices are already entering the market. In particular, OLED based displays allow for ultra-thin and mechanically flexible device architectures as well as low energy consumption. Obviously, the possibility to chemically *design* materials with specific desired properties demands a comprehensive understanding of the underlying physical phenomena in order to further the ongoing technological research.

The leitmotif of this work is the combination of pentacene (PEN) – without doubt one of the most prominent organic semiconductors [14–17] – with three different organic compounds to form application-relevant heterostructures in vacuum sublimed films: fullerene (C60), perfluoropentacene (PFP) and pentacenequinone (PQ). The objective is to provide understanding of the structural, energetic and morphological properties allowing for a well-founded judgement on the respective application potential in organic electronics. Throughout this work a multi-technique approach is followed comprising x-ray diffraction, vibrational spectroscopy, atomic force microscopy and photoelectron spectroscopy to access complementary information on the structural and energetic properties of PEN-based heterostructures.

This work is structured in the following way: First, in Chap. 2 the fundamental properties of organic semiconductors are outlined and structural, morphological and energetic basic principles are introduced (Sec. 2.1). Exemplarily for the broad field of organic electronics the basic operation principles of organic photovoltaic cells (OPVCs) are described. In the following (Sec. 2.2), the principles of crystallography and x-ray diffraction (XRD) are outlined to the extent necessary for the discussion of the x-ray diffraction methods in Chap. 3. Moreover, this section covers the principles of the other experimental methods applied in this work: ultraviolet photoelectron spectroscopy (UPS), Fourier transform infrared spectroscopy (FT-IR) and atomic force microscopy (AFM). In Chap. 4 details on the materials used within this work are given and the experimental setups and parameters are described in-depth.

The results of the experimental studies carried out in this work represent the central part of this thesis (Chap. 5). The first PEN heterostructure presented is the highly application-relevant combination of PEN with C60 (Sec.5.1), which was investigated regarding the correlation of energetic, structural and morphological properties with the performance of OPVCs for both layered and blended structures. In contrast to OPVCs based on layered C60/PEN structures, which are already well documented in literature to exhibit notable device performance results [18–22], OPVCs based on *blends* of this material pair acting as donor/acceptor bulk-heterojunction have not yet been reported. Devices of this type are characterized and the underlying blended C60/PEN heterostructures are investigated in detail by UPS, XRD and AFM and compared to layered structures. The experimental results confirm that only a comprehensive multi-technique view on the physical properties allows a correct interpretation of OPVC characteristics.

A second heterostructure of PEN that is presented in the following sections is the combination with PFP, which was reported to exhibit outstanding application relevance, in particular as active material in OFETs [23–25]. In Sec. 5.2 it is demonstrated that PFP exhibits polymorphism in thin films and the corresponding structure of this up to now unknown thin film phase, solved using various XRD techniques including reciprocal space mapping, is presented. Structural investigations were carried out on layered PFP/PEN and co-deposited PEN:PFP films, which were both reported to exhibit ambipolar behaviour in OFETs [23]. It is found that PFP forms a crystalline thin film nicely wetting PEN underlayers, which is of importance for organic electronic devices like OFETs relying on the existence of thin continuous films. Furthermore, it is shown that PFP forms a mixed crystal structure with PEN in blended films achieved via co-deposition. This experimental result led to a finding of both fundamental and application-related relevance, which

is presented in Sec. 5.3: The ionization energy of organic films composed of molecules with intramolecular polar bonds (like C-H and C-F for PEN and PFP, respectively), which mix on a molecular scale, can be tuned through the mixing ratio of the compounds. This is experimentally evidenced by UPS investigations, which are accompanied by XRD and FT-IR measurements to demonstrate the mixing, by AFM investigations to investigate morphology and by electrostatic modelling to theoretically substantiate the findings.

The third PEN heterostructure covered in this work is the combination with PQ. First, the results of UPS investigations on PEN/PQ and PQ/PEN layered films are presented (Sec. 5.4), where a highly molecular-orientation dependent ionization energy was found. This is explained by the different surface termination of films comprising lying molecules (π-system surface termination) and standing molecules (C-H bond surface termination), once more confirming the necessity for the detailed knowledge on the structural arrangement in thin organic films used for applications in organic electronics. The energy level offset determined by UPS seems applicable for the use as heterojunction for charge separation (exciton dissociation) in OPVCs. Bulk-heterojunction based OPVCs are however based on mixed structures exhibiting phase separation, desirably at the length scale of the exciton diffusion length. Therefore, pure, layered and 1:1 co-deposited films of PEN and PQ were extensively characterized regarding the structural arrangement and morphological properties using XRD, FT-IR and AFM (Sec. 5.5). It is found that PEN and PQ exhibit pronounced phase separation in the case of co-deposition and that (textured) growth of PQ in its bulk phase polymorph is suppressed in this case. Moreover, the length scale of phase separation revealed to be changeable by the deposition rate. It is evidenced that PQ exhibits polymorphic growth comprising a thin film polymorph on silicon-oxide substrates, which was solved using x-ray diffraction reciprocal space mapping (Sec. 5.6). Surprisingly, the molecular arrangement is markedly different from the bulk structure, as the unit cell comprises only one molecule, which leads to a loss of the herringbone arrangement known from the PQ bulk. Apart from forming an interesting functional heterojunction with PEN, the energy level offset between PEN and PQ deduced from UPS shows that PQ can form deep traps for electrons if present in PEN films. Since PQ is a common chemical impurity found in commercially available PEN source material, even low PQ concentrations may strongly impact the corresponding device performance. This issue is addressed by controlled co-evaporated of PEN with different (low) PQ concentrations (Sec. 5.7). Via structural investigations it is demonstrated that PQ does not significantly intercalate with PEN but rather forms either phase-separated patches or accumulates at PEN grain boundaries. Finally, a further possible path to PQ presence in PEN

films may be the oxidation of PEN to PQ under oxygen exposure, which is highly relevant issue for applications. This matter is investigated via defined exposure of PEN thin films and single crystals to O_2 and/or water as well as to reactive oxygen species (ozone and singlet oxygen).

Finally, in the last chapter of this work, the experimental results are summarized and an outlook on further work based on the current outcomes is given. Certainly, a work of this extent can only provide an insight into limited aspects of this intriguing field of research following the aim of depth instead of breadth.

Chapter 2

Fundamentals

This chapter introduces the physical fundamentals necessary for the discussion of the experimental techniques (Chap. 3) and results (Chap. 5). Furthermore, the basic principles of organic semiconductor (OSC) physics and of their application to organic photovoltaic devices are presented in the following. This outline is restricted to the introduction of the terms and basics necessary for the comprehension of the experimental results obtained with the applied techniques.

2.1 Organic molecular solids

Molecules consisting primarily of carbon (and usually hydrogen) are referred to as *organic molecules* for historical reasons [26], since they are the basis of all life processes. Their outstanding importance is based on the electron configuration of atomic carbon in the ground state ($1s^2 2s^2 2p^2$), which leads to the degeneration of one s- and two p-orbitals to three hybrid orbitals oriented in a plane (sp^2-hybridization). The hybrid orbitals can form σ-bonds with other atoms, while the third p-orbital remains oriented perpendicular to the sp^2-hybrid plane. This leads to the possibility of forming π-bonds in molecules resulting in a delocalized electron density above and below the molecular plane and therefore allows the formation of double bonds via σ- *and* π-bonds. *Conjugated organic molecules* (COMs) exhibit alternating single and double bonds with delocalized electrons along the molecule. The most important group of COMs are *aromatic molecules* containing cyclicly arranged conjugated constituents like six conjugated carbon atoms in case of benzene. In the solid state, these COMs form molecular crystals exhibiting relatively low intermolecular bond strengths dominantly of *Van der Waals* (VdW) type, which is caused by dipole-dipole interactions of neutral molecules. Compared

to covalent or ionic bonding, this type of force is weak and short ranged (declines with the 7^{th} power of the distance), which explains the low melting points of organic molecular crystals and the fact that the physical properties of molecular solids can often be well deduced from the properties of individual molecules [13, 27]. All molecules investigated in this work are aromatic molecules in the solid state.

2.1.1 Molecular packing in organic molecular crystals

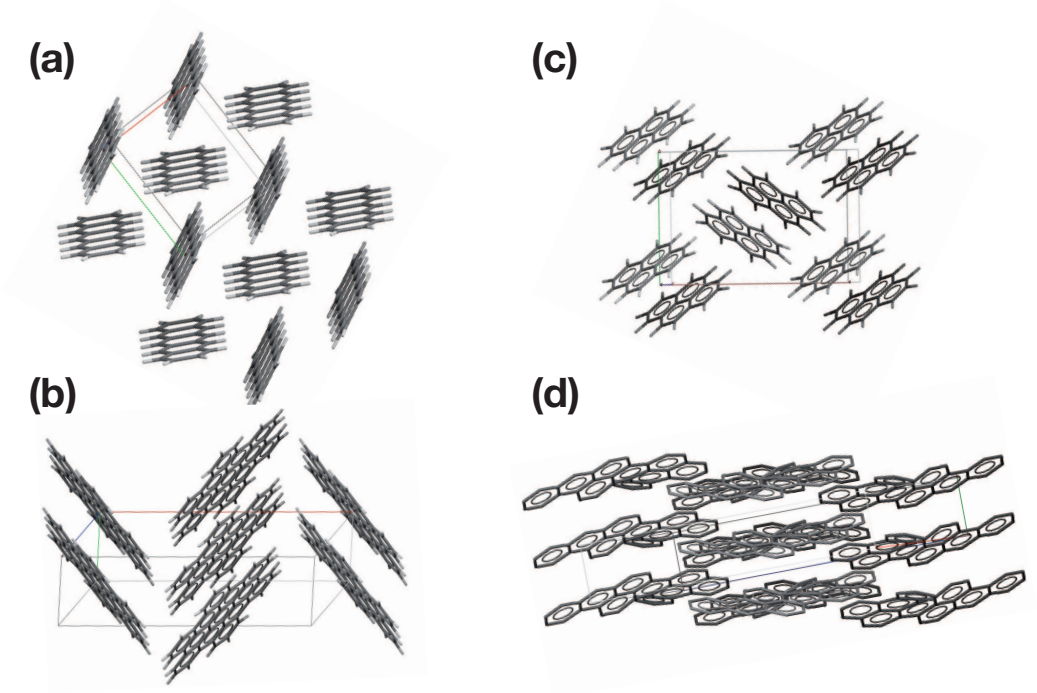

Figure 2.1: The four fundamental types of crystal packing found for aromatic hydrocarbons with the compound names and reference codes from the Cambridge Structural database in brackets: (a) Herringbone structure (pentacene, PENCEN), (b) γ-structure (hexabenzocoronene, HBZCOR), (c) sandwich herringbone (pyrene, PYRENE) and (d) β-structure (violanthrene, CORXAI10).

The molecular interaction in organic molecular solids is most often dominated by weak VdW interactions. Moreover, organic molecules are often anisotropically shaped, directly influencing their packing in molecular crystals. In the considerations of close packing of molecules the concept of the *Van der Waals volume* [28, 29], which is defined as the volume occupied by a

molecule impenetrable by other neighbouring molecules, showed to be highly important. For the atoms forming a molecule, *Van der Waals radii* are introduced, and in the *rigid-atom model* [29] the distance between peripheral atoms in neighbouring molecules, which are in contact without overlap, is the sum of the respective Van der Waals radii of the constituting atoms. For the atomic compounds that form the molecules investigated in this work, *i.e.*, for hydrogen, carbon, oxygen and fluorine, values of 1.1 Å, 1.7 Å, 1.5 Åand 1.5 Å, respectively, have been determined [29]. Note, that within the force field simulations presented in this work the molecules were treated as rigid bodies with an extension of the Van der Waals volume.

Already from the molecular structure valuable assumptions about the crystal packing can be made. This approach was pioneered by A. Gavezotti and G. R. Desiraju for aromatic hydrocarbons [30, 31]. They categorized the structures into four different structure types that are adopted due to the relative importance of C-C, C-H and H-H interactions, and therefore the stoichiometric C/H ratio in the molecule. The four types are illustrated in Fig. 2.1: (a) the herringbone structure, (b) the γ-structure (flattened-out herringbone), (c) the sandwich herringbone structure and (d) the layered β-structure made up of 'graphitic' planes. While the C-C interactions are best optimized between molecules of *high C/H ratio* oriented parallel with respect to their molecular plane (π-π stacking [32]) (Fig. 2.1d), the C-H interactions are most effective between inclined molecules with *low C/H ratio* comprising electrostatic interactions between positive H(δ^+) and negative C(δ^-) partial charges (Fig. 2.1a). The structure types in Figs. 2.1b and 2.1c are intermediate cases. However, anticipative considerations on crystal structures based on the molecular shape and compounds can only give a first guess on the real structural order in molecular crystals. Organic molecular crystals composed of *one* molecular compound can exhibit numerous polymorphs, which can even adopt a highly different molecular arrangement, as will be demonstrated in Sec. 5.6. Despite recent progresses [33, 34], crystal structures of organic molecular compounds are far from being predictable and structural investigations are therefore indispensable.

2.1.2 Thin film growth

Thin organic films are often produced under vacuum conditions by molecular beam deposition. This implies that molecules are deposited with a certain rate of arrival R ($\mathrm{m^{-2}s^{-1}}$) onto a given substrate surface. The growth process of a thin organic film is a non-equilibrium process and dynamic rather than equilibrium thermodynamic considerations have to be applied to describe the various growth behaviours. Although the process of thin film growth is far

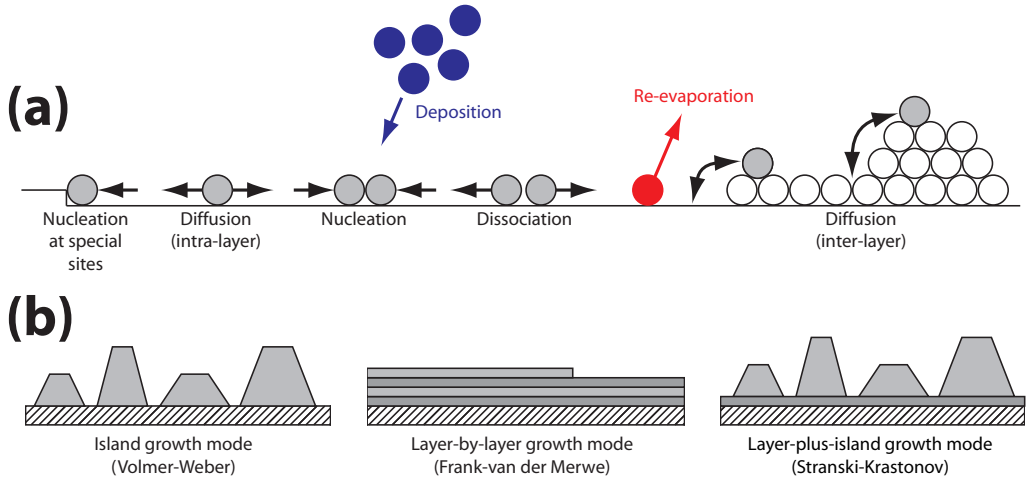

Figure 2.2: (a) Schematic diagram of processes on a molecular scale in nucleation and film growth on surfaces. (b) Schematic representation of the three crystal growth modes.

from being completely understood there exist several models that have been applied for various OSCs [17, 35, 36]. Upon deposition the following dynamic processes occur on a molecular scale (see Fig. 2.2a): Intra-layer diffusion of the molecule on the layer of arrival, inter-layer diffusion overcoming steps between layers of the film, formation of molecular assemblies (*i.e.*, nucleation as basis of film growth), dissociation of previously formed nuclei smaller or equal to the critical cluster size[1], nucleation at special sites of the substrate (*e.g.*, structural defects, chemical impurities etc.) or re-evaporation into vacuum [37, 40, 41]. The resulting film morphology essentially depends on the interaction between the substrate and the adsorbate and the growth of thin films can be divided qualitatively into three different modes (see Fig. 2.2b). If the interaction between the adsorbate molecules is stronger than the interaction with the substrate, small clusters are nucleated directly at the substrate and grow into 3D islands (*Volmer-Weber mode*). In the opposite extreme case of the adsorbate-substrate interaction strength exceeding the intermolecular interaction strength a closed layer is formed on the substrate followed by closed top layers (*Frank- van der Merwe mode*). The intermediate case of

[1]The critical cluster size (i) is the most unstable size, *i.e.*, only clusters composed of $> i$ molecules tend to grow rather than decay (whereas for $< i$ decay is more probable and local equilibrium tends to hold) [37]. The value of i can be experimentally determined using a scaling law formalism, which takes into account the deposition rate, nucleation density and the island size distribution at a specific sub-monolayer coverage [38]. For example, $i = 4$ was determined for PEN using this model [39].

islands nucleating on a (few) closed monolayer(s) is often found in organic thin film growth (*Stranski-Krastanov mode*), where subsequent layer growth becomes unfavorable at a certain film thickness. This mode is observed for PEN and PFP on SiO_x in this work (see Sec. 5.2 and 5.5) [37].

In general, organic molecules (*e.g.*, rod-like molecules like PEN) have an anisotropic shape. This implies that the kinetic processes illustrated in Fig. 2.2a have to take into account the molecular flexibility and the molecular orientation on the substrate. The intuitive assumption that single molecules arriving at the substrate adopt a lying orientation was experimentally confirmed [17]. However, when several molecules meeting in the diffusion process have finally formed a stable agglomerate they can tilt out of the substrate plane and adopt a certain intrinsic crystal structure, which is often found to be specific for thin film growth and usually denoted as *thin film phase* [17]. Models often applied to describe the growth of thin films are *diffusion-limited aggregation* (DLA) with the diffusing particles simply sticking to the growing aggregate leading to fractal island shapes [42], a *generalized formulation of DLA* including a curvature dependent sticking probability as well as diffusion along the fractal branches of an initial island in order to maximize the number of nearest neighbours leading to more regular structures [43], and growth models based on the *Ehrlich-Schwoebel effect* [44, 45] comprising an energy barrier for downward interlayer mass transport that leads to the nucleation of mounds in the form of terraces with monomolecular steps [17, 35, 36]. Attempts to model experimentally found morphologies must be based on a combination of the above models.

2.1.3 Electronic structure

Fundamental terms and definitions

Pentacene (PEN) (see Sec. 4.1) is a *polycyclic aromatic hydrocarbon* and is likely one of the most thoroughly investigated organic molecular compounds due to its applicability as an OSC in the field of organic electronics. PEN and the shorter molecules in the series of the polyacenes, *i.e.*, tetracene, anthracene, naphthalene and benzene, exhibit optical absorption wavelengths of their fundamental absorption directly proportional to the molecular length. In more detail, the optical gap depends on extension of the π-electron system present in COMs [13, 46]. The fundamental optical absorptions are due to excitations of the π-electron system and exhibit excitation energies of some eV thus commonly absorbing in the range of visible light. For instance, the fundamental transition of PEN in thin solid films is found around 670 nm (1.85 eV), which is in the red range of the visible spectrum. In terms of

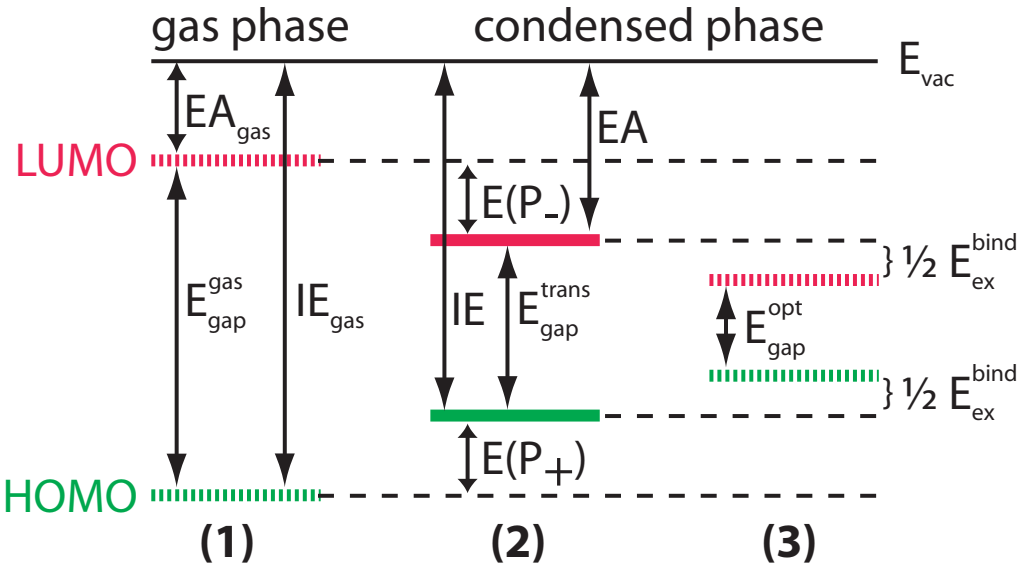

Figure 2.3: Energy levels in organic molecules and molecular crystals. This figure illustrates the energy level difference between an organic molecule (1) in the gas phase and (2 - 3) in its condensed phase, where the energy levels of the separated electron-hole pair (2) is compared to the energy levels of a Frenkel-exciton (3) of energy E_{gap}^{opt} with binding energy E_{ex}^{bind} generated by optical excitation. E_{vac} denotes the vacuum level; IE and IE_{gas} the ionization energies; EA and EA_{gas} the electron affinities; E_{gap}^{trans} and E_{gap}^{gas} the HOMO-LUMO gaps of the molecule in condensed and gas phase, respectively. $E(P_+)$ and $E(P_-)$ denote the positive and negative polarization energies.

molecular physics this molecular excitation is explained as π-electron transition from the *highest occupied molecular orbital* (HOMO) energy level to the *lowest unoccupied molecular orbital* (LUMO) energy level. The energy value of the fundamental optical transition onset therefore is the *optical gap* (E_{gap}^{opt}) of the COM. However, optical excitations usually do not lead to the generation of uncorrelated electron/hole pairs. Bound states of electrons and holes termed *excitons* are generated in OSCs upon optical excitation. Usually, these excitons consist of an electron-hole pair on the *same* molecule (Frenkel-excitons) exhibiting an energy lower than the energy difference between the respective separated electron-hole pair at infinite distance (the *transport gap* E_{gap}^{trans}) by the *exciton binding energy* (E_{ex}^{bind} =E_{gap}^{trans}-E_{gap}^{opt}) [47–49]. The energy levels of an organic molecular solid are illustrated in Fig. 2.3 in comparison to the energy levels of the free molecule in gas phase; E_{vac} denotes the *vacuum level* (VL) (for a detailed discussion see Sec. 3.2), *i.e.*, the

energy of an electron at infinite distance from the surface as energy reference level, IE denotes the *ionization energy* and EA the *electron affinity*[2]. The IEs [EAs] of the free molecule and molecule in the condensed state differ by the positive [negative] polarization energy $E(P_+) = IE_{gas}$ - IE [$E(P_-) =$ EA - EA_{gas}], which is caused by the polarizability of the surrounding molecules in the molecular crystal. The values of IE and IE_{gas} and therefore $E(P_+)$ are experimentally accessible by means of ultraviolet photoelectron spectroscopy (UPS) (see Sec. 3.2 and Fig. 3.5) and $E(P_+)$ was found to be in the order of 1.6 eV for the series of the polyacenes [13, 46].

Interfaces of organic molecules with metal substrates

Interfaces of semiconducting COMs with electrodes are common to all devices in the field of organic electronics. Besides electrodes based on intrinsically conducting polymers (ICPs) that permit production of all-organic devices [51], electrodes made of metals are of outermost importance. Hence, the energy level alignment at interfaces of COMs with metals is of high research interest, since it strongly impacts the charge injection processes into the electrode. In particular, a parameter of highest importance is *the hole injection barrier* (Δ_h), which is defined as the difference in energy between the *electrode Fermi level* (E_F) and the organic transport level at the interface, which can be experimentally assessed by photoelectron spectroscopy; the fundamental energetics at COM/metal interfaces are illustrated in Fig. 2.4.

First and foremost, the nature of interaction between the COM and the substrate is decisive for interface energetics, where the extreme cases of chemical interaction (*chemisorption*) are differentiated from weak adsorption purely based on the VdW interaction (*physisorption*) in literature [52]. Chemisorbed COMs exhibit covalent or ionic bonds to the substrate, which significantly alters the electronic structure of the COM, as often found for strong electron accepting molecules on metal substrates [53]. In contrast, the electronic structure of purely physisorbed COMs remains in principal undisturbed upon adsorption and the potential between COM and substrate can be well described with the Lennard-Jones-potential, [52]:

$$V = 4V_0 \left[\left(\frac{\sigma}{r} \right)^{12} - \left(\frac{\sigma}{r} \right)^{6} \right], \tag{2.1}$$

[2]The IE is defined as the energy necessary to promote an electron from the HOMO-level to the vacuum level and the EA as energy necessary to remove an electron from the LUMO to E_{vac}. Note, that molecules are n-electron systems of rather low order being significantly disturbed by addition or removal of an electron. Therefore, the (more common) definition of EA as energy gained by an originally neutral atom upon formation of a negative ion has to be treated with caution [50].

where V_0 denotes the minimal potential energy, σ the effective molecular diameter and r the surface-molecular distance. The repulsive term proportional to r^{-12} is due to Coulomb and Pauli repulsion; the attractive term $\propto r^{-6}$ describes the VdW interaction being proportional to the square of the molecular polarizability. Therefore it becomes clear that the VdW interaction is strong for highly polarizable compounds like COMs (with their delocalized π-orbitals) adsorbed on metals, which preferentially leads to lying adsorption geometries of rod-like or disk-shaped COMs on metallic substrates [13].

Energy level alignment at interfaces

The simplest model for discussing interfacial energetics is that of *vacuum level alignment*, also known as the *Schottky-Mott limit*; this case is illustrated in Fig. 2.4a. Herein, Δ_h and the corresponding value for electron injection, the *electron injection barrier*[3] (Δ_e), are simply derived from the IE and the EA of the COM and the *work function* of the metal substrate (ϕ) via $\Delta_h = \mathrm{IE} - \phi$ and $\Delta_e = \phi - \mathrm{EA}$. However, this case is more the exception than the rule for interfaces of COMs with electrodes, since the adsorption of COMs on metal substrates prevalently leads to more complicated interfacial energetics comprising changes in the vacuum level due to *interface dipoles* (IDs): The work function of a metal is the sum of bulk and surface contributions, *i.e.*, the bulk chemical potential of the metal and surface dipoles mostly due to electrons spilling out from the metal surface into the vacuum. Upon adsorption of COMs the repulsion between the COM electrons and the metal electron tail into the vacuum compresses the tail and decreases the intrinsic surface dipole present at the bare metal. This leads to an abrupt *downward shift of the vacuum level* (Δ_{vac}) due to the so-called *push-back effect*, which can exceed 1 eV [54–56]. Compared to the situation of the Schottky-Mott limit, this also leads to an increase in Δ_h by Δ_{vac}, which hence leads to the unfortunate consequence of a reduction of the hole injection performance [50, 54, 57, 58]; this situation is illustrated in Fig. 2.4b. Further mechanisms that cause Δ_{vac} include chemical interactions of COMs with the substrate involving charge transfer across the interface or effects of intrinsic permanent dipoles of the COMs [57]. Using ICPs like poly(3,4-ethylenedioxythiophene):poly(styrenesulfonate) (PEDOT:PSS) as substrates

[3]Since it is difficult to experimentally access the value of EA, which has been done via inverse photoelectron spectroscopy for few materials only [54] and since these experiments have not been performed within this work, the discussion is restricted to Δ_h in the following.

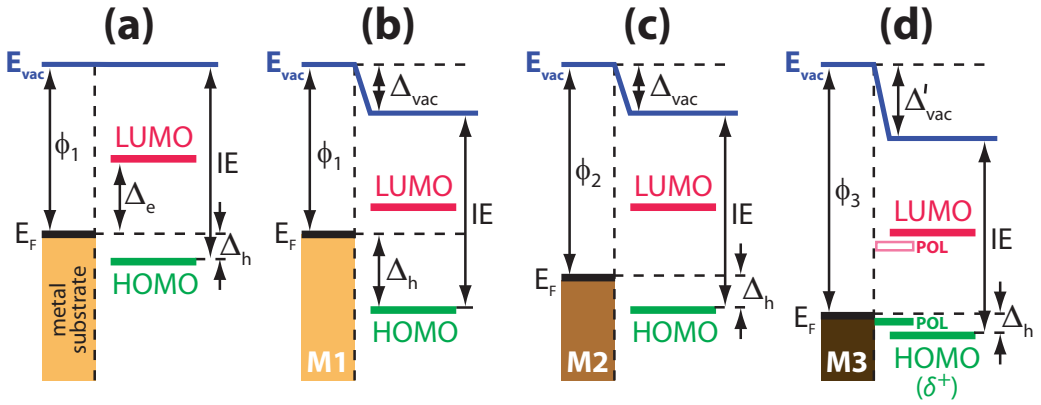

Figure 2.4: Schematic energy level diagrams for interfaces between metal substrates of different work functions ϕ_1, ϕ_2, ϕ_3 with an organic adsorbate of ionization energy IE (a) in the Schottky-Mott limit (vacuum level alignment), (b) with an ID present leading to a downward shift of E_{vac} by Δ_{vac} for a substrate of work function ϕ_1, (c) same as (b) but with a higher work function ϕ_2, and (d) in the case of Fermi-level pinning for a substrate with ϕ_3 leading to a higher VL-shift (Δ'_{vac}). E_F denotes the Fermi energy of the metal substrate; E_{vac} the vacuum level; Δ_h (Δ_e) the hole (electron) injection barrier; *POL* the energetic position of the positive (negative) polaron level colored green (red) and δ^+ symbolizes the HOMO level being slightly positively charged.

(see Sec. 4.1), which exhibit a work function[4] comparable to high-ϕ metals like gold, leads to a significantly *lower* Δ_h compared to metal substrates. This is due to the closed-shell character of the polymer, which has much fewer free electrons than metals and therefore does not exhibit a significant electron-tail and the corresponding push-back effect [58].

In both cases, the Schottky-Mott limit and in the presence of an ID, Δ_h depends on ϕ. As long as ϕ is small compared to the IE of the COM (or $\mathrm{IE} + \Delta_{vac}$ if IDs are present), using substrates with higher ϕ will lead to a decrease in Δ_h (Fig. 2.4c). However, if ϕ is in the range of the IE (or respectively $\mathrm{IE} + \Delta_{vac}$) the situation becomes more complicated, since a further increase in ϕ leads to charge transfer from the COM to the substrate to establish thermodynamic equilibrium. In general, the electronic structure of charged molecules is significantly different from the neutral case: The absent (additional) charge in the HOMO (LUMO) level leads to changes

[4]The work function range found for different PEDOT:PSS formulations in thin films is $\phi = 4.3 - 5.2\,\mathrm{eV}$ depending on the PEDOT to PSS ratio as well as on the morphology of the films, since local dipoles are present [59].

in the molecular conformation and the geometry of the molecule, *positive (negative) polarons* are formed. The corresponding energy level, the *positive (negative) polaron level* is different from the neutral HOMO (LUMO) state by the *positive (negative) polaron relaxation energy* of the positive (negative) polaron, which can be several hundred meV [60, 61]. For the case of organic molecules adsorbed on high-ϕ substrates this can lead to the following scenario: if ϕ (minus possible contributions from surface dipoles) exceeds the IE minus the positive polaron relaxation energy, spontaneous charge-transfer occurs across the organic/metal interface consequently forming an (additional) interface dipole (further) shifting the vacuum level downwards. Hence, Δ_h becomes independent of ϕ. A further increase in ϕ solely increases Δ_{vac}, a situation referred to as *Fermi-level pinning* in literature [60–63] (see Fig. 2.4d). Since Δ_{vac} due to IDs (*e.g.*, caused by the push-back effect) can exceed 1 eV on metal substrates, Fermi-level pinning of COMs like PEN on metal substrates has not yet been observed[5]. In contrast, on ICPs like PEDOT:PSS Fermi-level pinning is the dominant mechanism of energy level alignment for PEN. It was found that Δ_h for PEN on PEDOT:PSS is almost constant at 0.35 ± 0.05 eV for different substrate-ϕ values (see also Sec. 5.1), which can be varied by almost 1 eV through changing the PEDOT to PSS ratio, *i.e.*, this value of Δ_h should correspond to the positive polaron relaxation energy of PEN on PEDOT:PSS. The effect of Fermi-level pinning was explained by electron transfer from PEN to PEDOT at the interface inducing an ID of up to almost 1 eV for increasing values of ϕ [59].

Molecular orientation dependence of the ionization energy

Orientation dependent IEs have been observed for numerous systems including PEN on highly oriented graphite [65] or α,ω-dihexylsexithiophene on Ag(111) [66]. This observation has often been attributed to an orientation dependent *intermolecular screening of the photo-hole* generated by the experimental photoemission process in the measurement of the IE (see Sec. 3.2), which was expressed in terms of the *polarization energy* P [67, 68] depending on the local state of aggregation and the crystal structure [69]. However, it was shown in a recent study that the upper limit for the difference in photo-hole screening by differently orientated neighboring molecules

[5]PEN deposited on metal substrates of increasing ϕ exhibits a linear decrease of Δ_h together with a linear increase of the IDs shifting Δ_{vac} to lower energies [59]. Metals pre-covered with strong electron acceptors like 2,3,5,6-tetrafluoro- 7,7,8,8-tetracyanoquinodimethane (F4-TCNQ) that undergo a charge-transfer reaction with the metal substrate were reported to exhibit Fermi-level pinning due to the corresponding increase of the substrate work-function [64].

of α-sexithiophene (6T) is 0.15 eV, although an IE difference between lying and standing molecules of 0.6 eV was experimentally observed in this case[6]. Therefore the experimentally observed orientation dependence of the IE cannot be explained in terms of photo-hole screening effects (alone) [70].

It was demonstrated in the cited study that the IE of OSCs is a parameter that *intrinsically* depends on the molecular orientation. In this context it must be emphasized that *one* isolated *individual* molecule clearly exhibits only *one* value of IE but that *multiple* values are found for molecules in ordered assemblies. Using density functional theory based calculations and electrostatic modelling it was shown that the IE of oriented molecular assemblies depends on the surface termination of the layer, *i.e.*, on the surface dipole *built into* the molecular layers. In case of PEN, the IE depends on whether the conjugated π-system with its negative charge density (lying molecules) or the hydrogen-terminated molecular ends carrying a slightly positive partial charge (standing molecules) form the film surface, since this yields a differently oriented surface dipole. Taking into account these considerations, the difference in IE for lying and standing PEN was calculated to 0.6 eV [70], which is in very good agreement with the difference in the observed IE values deduced from UPS in the present work (see Sec. 5.4). As a consequence of this effect, surface dipoles of organic assemblies caused by polar end-groups can presumably be used to predictably tune the IE of thin films, which was carried out by mixing PEN with perfluoropentacene (see Fig. 4.1) in the study presented in Sec. 5.3.

Charge injection and transport

Applications in the field of organic electronics invariably employ (mostly metal-) contacts for charge injection/extraction and the efficiency of these processes is a crucial parameter for device performance. Since the transport gap of typical undoped COMs like PEN ($E_{gap}^{trans} = 2.2$ eV [54]) is by far larger than the thermal energy at room temperature ($k_B T \approx 25$ meV) the number of free charge carriers is usually low [13, 46]. Assuming *ohmic contacts*, *i.e.*, contacts that do not limit the current flow, the current at low external

[6] In the cited study [70], the difference in polarization energy was estimated for a 6T film on Ag(111) by the investigation of a sulfur core-level shift in x-ray photoelectron spectroscopy: The observed shift between the pure film on Ag(111) and the film covered with a closed layer of an amorphous, conjugated organic material (not containing sulfur itself) was much lower (0.14 eV) than the IE difference between lying and standing 6T (0.6 eV). Therefore it was concluded that the *presence* or *absence* of neighboring molecules in the upper half-space must clearly have a stronger effect on the polarization energy and therefore on the measured IE than differences in the *orientation* of the neighboring molecules.

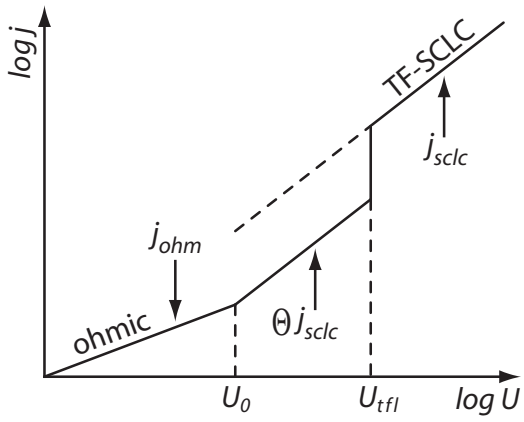

Figure 2.5: The current density versus voltage characteristics through an OSC with ohmic contacts exhibiting ohmic and space charge limited current. U_0 denotes the threshold voltage between ohmic and SCLC behaviour, U_{tfl} the critical voltage of trap filling and Θ is a parameter accounting for the density and depth of the traps.

voltages is determined by the motion of the intrinsically present free electrons and holes with a current density j_{ohm} scaling linearly with the externally applied voltage U (see Fig. 2.5), which is given by Ohm's law [71]:

$$j_{ohm} = en_0\mu\frac{U}{d}, \tag{2.2}$$

where e is the elementary charge, n_0 the density of intrinsically present free charge carriers, μ the charge carrier mobility and d the length of the sample[7]. The charge carrier mobility[8] is the fundamental charge transport quantity specific for a certain OSC and is a tensor of second rank with six independent components accounting for the anisotropy of charge transport in ordered (crystalline) OSCs [72, 73].

If the contact between OSC and metal electrodes is different from ohmic there are two dominating processes of charge injection to overcome energetic interfacial barriers: (i) Tunneling at the Fermi energy of the metal through the barrier (*Fowler-Nordheim tunneling* dominant for large barriers and/or low temperatures [74]) and (ii) thermally-activated *thermionic injection* both allowing for the Schottky-effect, *i.e.*, the mirror charge of the injected electron lowering the barrier height. The current density of a realistic Schottky-barrier

[7]Note that the relations presented in this chapter hold analogously for holes.

[8]There are various methods to experimentally determine μ, the most important are time-of-flight measurements [72], the space charge limited current method in diode configuration from j_{sclc} (see text) and the extraction of μ from the electrical characteristics of field-effect transistors in the saturation regime via $\mu = \frac{2LI_{sd}}{WC(V_g-V_t)^2}$, where I_{sd} is the current between source and drain, V_g the gate voltage, V_t the threshold voltage at which the current starts to rise, L and W are the length and width of of the conducting channel and C is the capacitance on the gate dielectric [3]. In these devices the charge transport takes place in a very narrow channel at the interface and therefore μ is highly sensitive to structural defects at the organic/dielectric interface.

is approximately given by the *Shockley-formula* [75]:

$$j = AT^2 \exp\left(-\frac{\Delta_e'}{k_B T}\right) \exp\left(\frac{eU}{\xi k_B T} - 1\right), \tag{2.3}$$

where A denotes the Richardson constant, T the absolute temperature, Δ_e' the *effective* electron-injection barrier, k_B Boltzmann's constant, U the externally applied voltage and ξ accounts for the ideality of the Schottky-diode. This equation holds in full analogy for the injection of holes. Note that Δ_e' is lower than Δ_e by $\sqrt{e^3 F/4\pi\varepsilon_0\varepsilon}$ due to the Schottky-effect, with F being the external electric field, ε the relative permittivity and ε_0 the permittivity of free space [13]. The exponential dependence of j on Δ_e (and Δ_h, respectively) demonstrates the importance of low injection barriers in organic electronics.

At higher external voltages the electrons injected from the electrodes outnumber the intrinsically present carriers of the OSC, *i.e.*, the density of the injected excess-electrons becomes larger than n_0. The OSC hence exhibits a space charge density that significantly determines the internal electric field and the current [13]. In the absence of traps, *i.e.*, accessible energetic states in the energy gap due to chemical impurities or structural defects, the current is denoted as *trap-free space charge limited current* (TF-SCLC) scaling quadratically with the externally applied voltage (see Fig. 2.5), which can be described by the Mott-Gurney equation (Child's law):

$$j_{sclc} = \frac{9}{8}\varepsilon\varepsilon_0\mu\frac{U^2}{d^3}, \tag{2.4}$$

where μ is assumed to be independent of the external field. In the more realistic case of traps present in the OSC, which suppress current flow by localizing charge carriers [76], the equation has to be modified by $\mu \rightarrow \mu_{eff} = \Theta\mu$, where Θ is a parameter that accounts for the density and the depth of the traps and can be $\ll 1$ [13]. This modified equation can be used to approximate the region between the ohmic and the TF-SCLC region (see Fig. 2.5). At a certain critical voltage, U_{tfl}, the charge injected through the contacts is sufficient to fill all the deep traps and an abrupt increase of the current density occurs. The current-voltage characteristics can be used to determine the mobility values in OSCs [76].

The mechanism of charge transport at the nanoscale is strongly dependent on the structural order in the molecular assembly. In ultra-pure organic single crystals (*e.g.*, of PEN) *band transport* has been observed exhibiting a temperature dependent mobility $\mu(T) \propto T^n$ with n around $-\frac{3}{2}$ for polyacenes [72, 76–78]. In the case of band-like transport, μ for electrons is often almost equal to that of holes and the increase in mobility at decreasing temperature

indicates phonon scattering as dominant limitating process. For instance, the hole mobility in PEN single crystals was reported to increase from 35 to 58 cm^2/Vs by cooling from room temperature to 225 K [77]. Moreover, band dispersion has also been observed for well-ordered thin organic films [79–82].

In contrast to the case of single crystals, the opposite extreme example, *i.e.*, amorphous OSCs, exhibits mobilities lower by several orders of magnitude and μ rising with temperature. This points to a fundamentally different transport mechanism, which is modelled in the framework of the *Bässler model* as thermally assisted *hopping transport* between neighbouring molecules comprising an energetically inhomogeneous Gaussian distribution of the localized transport states [83]. The hopping rate between neighbouring sites depends on the wave function overlap, which is itself the subject of a Gaussian distribution, since in disordered media the inter-site distance is locally variable and the coupling among the (generally non-spherical) molecules is dependent on the mutual orientation. Hopping processes to energetically lower sites do not need activation, whereas hopping to energetically higher sites requires an activation energy of the difference between the neighbouring transport levels, which is itself dependent on the external field strength [13, 83]. This model predicts a temperature dependence of $\mu \propto \exp(-T^{-2})$, which allows fitting experimental data reasonably well [73].

2.1.4 Organic photovoltaic cells

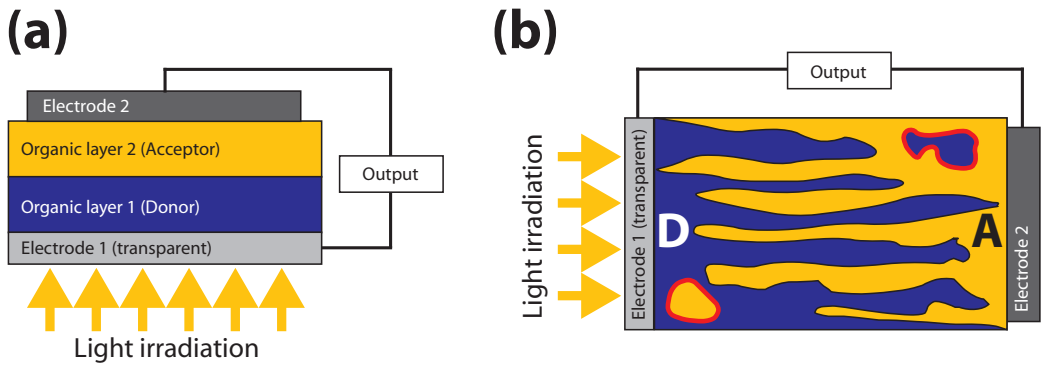

Figure 2.6: (a) Schematic representation of a layered organic solar cell, where layers of donor and acceptor materials are sandwiched between two electrodes in comparison to an idealized bulk-heterojunction organic photovoltaic device (b), where the organic materials are blended together. Isolated domains of the respective materials that are parasitic to the solar cell performance are drawn with a red border.

Although photoconductivity in anthracene was already discovered about one century ago [84, 85], it took until 1986 for organic photovoltaic cells (OPVCs) to attract significant interest, as C. W. Tang introduced a two layer OPVC with a power conversion efficiency of almost 1% [8]. This device introduced the concept of an *organic heterojunction* (OH) into the field of organic photovoltaics, which uses two materials of different values of IE and EA as strategy to enable efficient dissociation of photo-generated excitons. In 1991 M. Hiramoto et al. introduced a further development of OHs by sandwiching a co-deposited layer of the two materials between the pure layers significantly enhancing the performance of the OPVC [86]. Devices based on this concept are denoted as *organic bulk-heterojunction (or: dispersed)* photovoltaic cells and are nowadays often based on blends of COMs with polymers [9, 87–89]. A schematic illustration of layered and bulk-heterojunction OPVCs is given in Fig. 2.6.

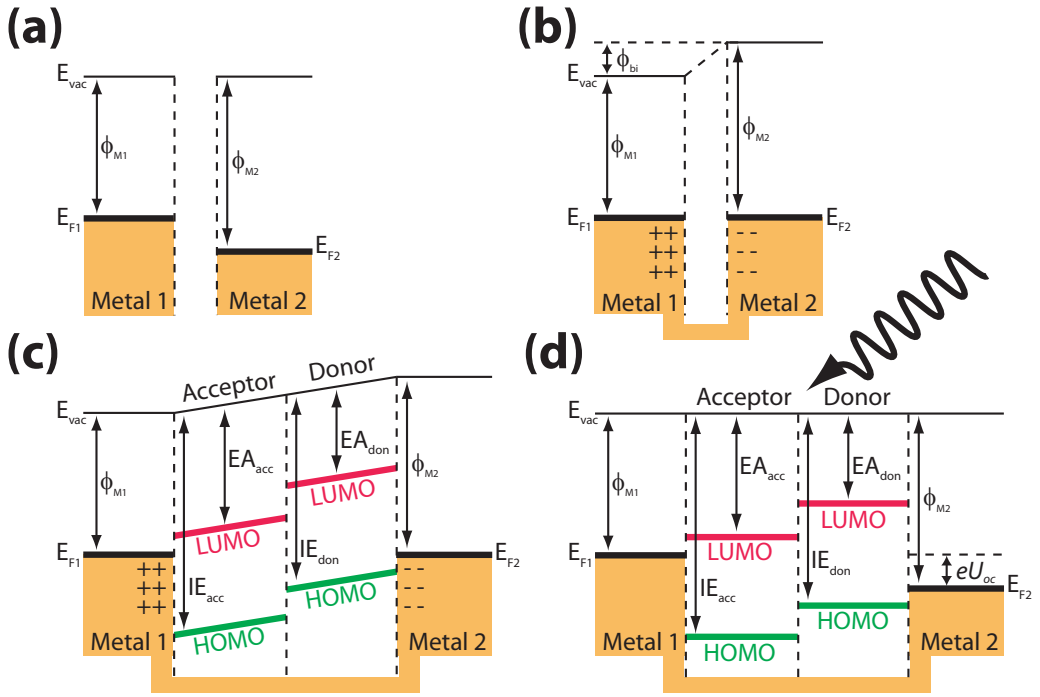

Figure 2.7: Schematic Energy level diagrams of two metals (a) being not in contact and (b) after contact and of two different organic semiconducting layers sandwiched between the metals (c) under short-circuit conditions and (d) flat-band conditions under illumination. For simplification, interface dipoles occurring at the metal/COM interfaces (see Sec. 2.1.3) are neglected in this schematic.

All OPVCs comprise contacts of the organic materials with conducting electrodes (*e.g.*, metals) and in general, electrodes with different ϕ are being used; the corresponding schematic energy diagram is shown in Fig. 2.7a. If the metals are brought into contact, a current between the metals flows until the Fermi levels E_{F1} and E_{F2} are aligned, with metal 1 (2) being positively (negatively) charged at the interface. This gives rise to a *built-in voltage* (U_{bi}), which depends on the *difference of the respective work functions* (ϕ_{bi}) of the metals with ϕ_{M1} and ϕ_{M2}: $U_{bi} = \phi_{bi}/e = (\phi_{M2} - \phi_{M1})/e$ (see Fig. 2.7b) [13]. In a layered OH based OPVC two layers of OSCs are sandwiched between such metal electrodes of different ϕ, this case is schematically illustrated in Fig. 2.7c, where the low IE material is denoted as *donor* and the high EA material as *acceptor*, since in the process of charge separation an electron from the donor is transferred into the acceptor material. In the general case, the electrodes are externally short-circuited, since the purpose of the device is to drive an external consumer load. Hence, in analogy to the case shown in Fig. 2.7b, the Fermi levels of the electrodes are aligned and U_{bi} leads to an electric field in the heterostructure with a profile changing linearly through the layers in the absence of space charges, as do the respective HOMO and LUMO levels. This situation is generally denoted as *short-circuit condition*. If the OPVC is operated, *i.e.*, the device is illuminated and excitons are successfully dissociated, electrons (holes) flow through the acceptor (donor) material to the low-ϕ (high-ϕ) electrode driven by U_{bi} and at a certain point these carriers induce an electric field that cancels the built-in field leading to *flat-band conditions* (Fig. 2.7c). If the circuit is open, *i.e.*, if the OPVC is illuminated but no load is connected, the voltage between the electrodes is denoted as the *open circuit voltage* (U_{oc}); if the device is short circuited, the *short circuit current density* J_{sc} flows (see Fig. 2.8). In this simplified picture it is evident that the maximum photovoltage that can be achieved equals the built-in voltage[9].

The *power conversion efficiency* η_p of a OPVC under a given incident *optical power density* (P_{inc}) depends on the following parameters that can be deduced from the current density versus voltage characteristics (J-V curve) (see Fig. 2.8): (i) U_{oc}, (ii) the current density under zero bias, J_{sc}, and (iii) the *fill factor* (FF) characterizing the shape of the J-V curve in the power-generating forth quadrant, which is defined as $FF = \max(JV)/J_{sc}U_{oc}$, where $\max(JV)$ defines the maximum power point (MPP) of the device:

$$\eta_p = J_{sc}U_{oc}FF/P_{inc}. \tag{2.5}$$

[9]This assumption is denoted as *metal-insulator-metal picture* and its validity is still under debate since an additional influence of the energy level offset of the organic compounds was observed [90].

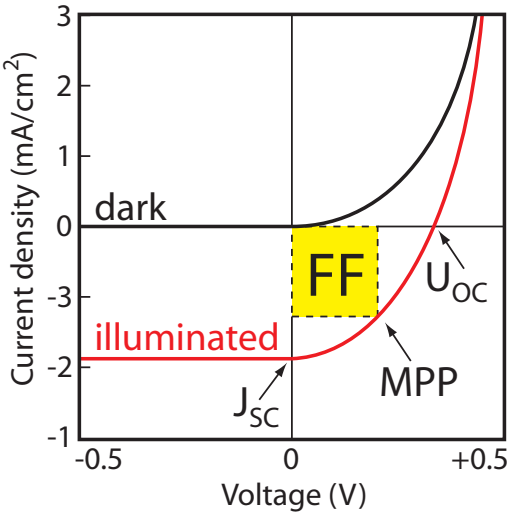

Figure 2.8: Schematic current density versus voltage characteristics of an organic solar cell in dark (black) and under illumination (red). J_{sc} denotes the short circuit current density, U_{oc} the open circuit voltage, FF the fill factor and MPP the maximum power point. From these parameters the power conversion efficiency of the device can be derived.

The central process in an OPVC is the process of charge separation, which is illustrated in Fig. 2.9 in detail. Under illumination with light of sufficient energy, Frenkel excitons (see Sec. 2.1.3) are generated in the OSC with an *absorption efficiency* η_A, which can reach 100% for sufficiently thick organic films (step (1) in Fig. 2.9a). The excitons with a binding energy E_{ex}^{bind} exhibit an undirected diffusion independent of the external electric field, since they do not carry a net charge (step (2) in Fig. 2.9b)[10]. This step is quantified by the *exciton diffusion efficiency* η_{ed}, which is the ratio of excitons reaching a heterojunction via diffusion to the excitons that prematurely recombine. Highly efficient exciton dissociation occurs at donor/acceptor material heterojunctions if the mutual energy level alignment is appropriate: If the exciton energy E_{ex} is larger than the energetic offset of the HOMO of the donor and the LUMO of the acceptor, exciton dissociation at the heterojunction is energetically favourable and will occur with an efficiency η_{ct} of almost 100%, since it occurs at a much faster timescale (< 100 fs) compared to the competing processes of radiative (ns-scale) and non-radiative recombination (sub-ns scale) [13] (step (3) in Fig. 2.9c). In contrast to η_A and η_{ct}, the exciton diffusion efficiency η_{ed} is generally a significant limiting factor. It strongly depends on the distance between the location of exciton generation and the heterojunction, which therefore should be at the length scale of the *exciton diffusion length* L_D (in the range of tens of nanometers) [9, 10]. After the dissociation process the built-in field transports the separated electron and hole to the respective electrodes where the charge carriers are collected. In

[10]The built-in field can- to a certain extent- lead to the dissociation of the excitons [91], which is the photocurrent generating process in a single layer OPVC, however, at low efficiency, since the field strength is low.

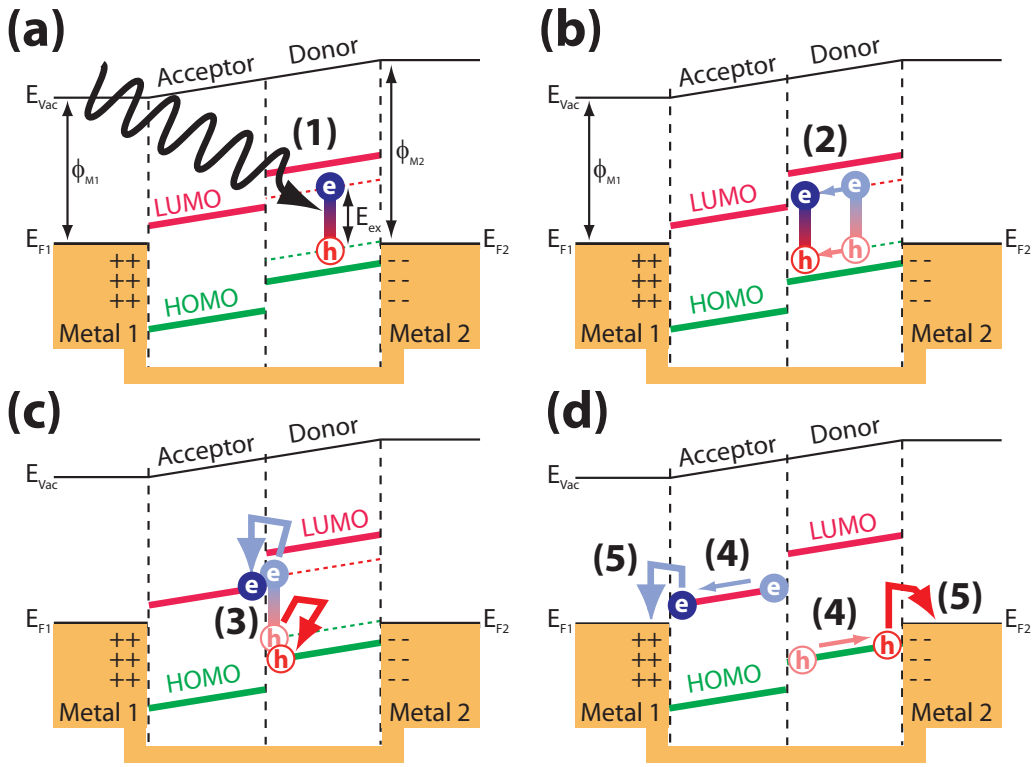

Figure 2.9: The process of charge separation in an OPVC illustrated for absorption in the donor material. (a) Excitation with light leads to the formation of excitons with an efficiency η_A (step 1). (b) The excitons exhibit anisotropic diffusion and meet a donor/acceptor heterojunction with efficiency η_{ed} (step 2). (c) At the heterojunction exciton dissociation occurs with an efficiency η_{ct} transferring the electron in the acceptor material and leaving the hole in the donor in the respective transport levels (step 3). (d) The built-in field transports the charge carriers to the respective electrodes (step 4) where they are collected with an efficiency η_{cc} (step 5).

the aspired but often unrealistic case of homogenous layers of high structural order and therefore high charge carrier mobilities this process can exhibit a *charge collection efficiency* η_{cc} of almost ∼100% [92]. The complete *external quantum efficiency* η_{eqe}, *i.e.*, the total number of electrons flowing into the external circuit per incident photon, finally is the product of the efficiencies of the individual consecutive steps:

$$\eta_{eqe} = \eta_A \eta_{iqe} = \eta_A \eta_{ed} \eta_{ct} \eta_{cc}, \tag{2.6}$$

where η_{iqe} denotes the *internal quantum efficiency*, which is the ratio of the number of carriers collected at an electrode to the number of photons

absorbed [49]. This relation clearly demonstrates *the* central advantage of bulk-heterojunction based OPVCs as schematically illustrated in Fig. 2.6: Compared to the case of the layered OPVC, where only those excitons generated in a capture zone of extension L_D contribute to the photocurrent, excitons generated in the interpenetrating network of donor and acceptor material reach the interface with high probability if the length scale of phase separation is in the range of L_D. It is evident that the existence of continuous paths to the electrodes formed by the donor and acceptor materials is mandatory, since isolated domains trap charges and lead to recombination (areas marked with red borders in Fig. 2.6b). However, the value of η_{cc}, which can be almost 100% leading to $\eta_{eqe} \approx \eta_A \eta_{ed}$ in layered OPVCs of high structural order, can be significantly reduced in bulk heterojunction based devices due to poor charge transport and increased trapping and recombination processes [92]. This particularly demonstrates the importance of control over structural properties at the nanoscale to achieve highest order in thin films of phase separated donor/acceptor blends.

2.2 Crystallography and x-ray diffraction

The thorough structural characterization of OSCs and their mutual heterojunctions represents a central point of this work. In the following section, basic ideas of crystallography and x-ray diffraction are outlined to the extent needed for the description of the applied experimental techniques.

2.2.1 Fundamentals of crystallography

A *crystal* is a three-dimensional repetition of a given motif (atoms or molecules) by translation within a lattice, called the *direct lattice*. This lattice is defined by *base vectors* $\vec{a}$, $\vec{b}$, $\vec{c}$ of length a, b, c and angles α between b and c, β between a and c and γ between a and b, where this whole set of parameters represents the *unit cell parameters* of the crystal structure. Calculations of lengths of vectors in the lattice, of mutual angles and of distances between planes can easily be performed using the *metric tensor of the direct lattice* (direct metric) G_{ik}, which is advantageous in computerized methods:

$$G_{ik} = \begin{pmatrix} \vec{a}\cdot\vec{a} & \vec{a}\cdot\vec{b} & \vec{a}\cdot\vec{c} \\ \vec{b}\cdot\vec{a} & \vec{b}\cdot\vec{b} & \vec{b}\cdot\vec{c} \\ \vec{c}\cdot\vec{a} & \vec{c}\cdot\vec{b} & \vec{c}\cdot\vec{c} \end{pmatrix} = \begin{pmatrix} a^2 & ab\cos\gamma & ac\cos\beta \\ ba\cos\gamma & b^2 & bc\cos\alpha \\ ca\cos\beta & cb\cos\alpha & c^2 \end{pmatrix} . \quad (2.7)$$

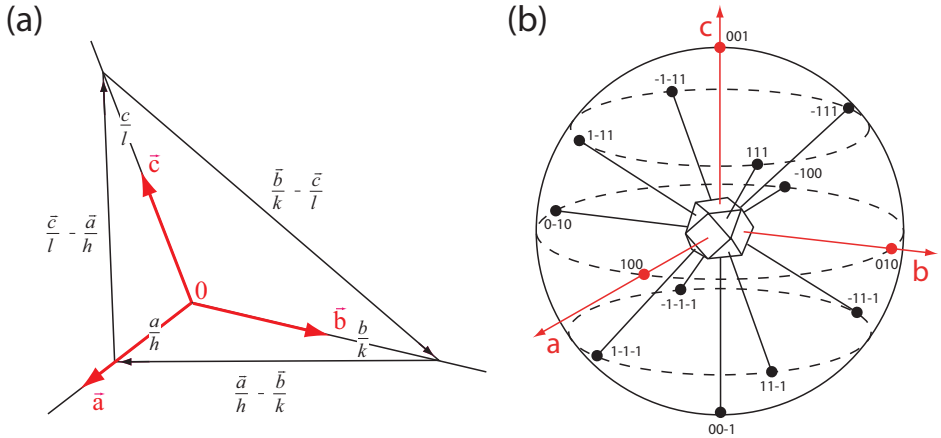

Figure 2.10: (a) The definition of the Miller indices h, k, l, of a net plane (hkl). (b) The spherical projection of a (cubic) crystal structure. The intersection of the normal vectors on planes (*poles*) of a cubic crystal structure with the unit sphere yields a unique representation of the crystal system. The respective Miller indices of the planes are given at the points of intersection.

The most important property of G_{ik} is that it relates the components of direct lattice vectors $e_k = G_{ik}e^i$ to the respective components in reciprocal space e^i, using the Einstein summation convention and the tensor algebra formalism of covariant (direct) and contravariant (reciprocal) vectors [93]. The inverse of the direct metric is the *metric tensor of the reciprocal lattice* (reciprocal metric) $G^{ij} = (G_{ij})^{-1}$, which then performs the inverse operation $e^j = G^{ij}e_j$. It is analogously defined as the direct metric with the corresponding *reciprocal unit cell parameters* a^*, b^*, c^*, α^*, β^*, γ^*, which therefore can be immediately derived by a simple matrix inversion of G_{ik}. The *reciprocal base vectors* $\vec{a}^*$, $\vec{b}^*$, $\vec{c}^*$ are defined as:

$$\vec{a}^* = \frac{\vec{b} \times \vec{c}}{V}, \quad \vec{b}^* = \frac{\vec{c} \times \vec{a}}{V}, \quad \vec{c}^* = \frac{\vec{a} \times \vec{b}}{V}, \tag{2.8}$$

where V denotes the *volume of the unit cell* in the direct lattice (V^* for the reciprocal lattice), which equals the square root of the determinants of direct metric tensor (reciprocal metric tensor for V^*, respectively) [93]. From these relations the fundamental properties of the reciprocal lattice follow: $\vec{a}\cdot\vec{a}^* = \vec{b}\cdot\vec{b}^* = \vec{c}\cdot\vec{c}^* = 1$ as well as $\vec{a}\cdot\vec{b}^* = \vec{a}\cdot\vec{c}^* = \vec{b}\cdot\vec{c}^* = \vec{b}\cdot\vec{a}^* = \vec{c}\cdot\vec{a}^* = \vec{c}\cdot\vec{b}^* = 0$ and for the volumes: $V^* = V^{-1}$. A given vector in reciprocal space

$$\vec{H}_{hkl} = h\vec{a}^* + k\vec{b}^* + l\vec{c}^* \tag{2.9}$$

stands perpendicular to a plane of the direct lattice, which is defined by its intersection with the direct basis vectors, *i.e.*, 1/h, 1/k, and 1/l, where the integer indices h, k, l are the *Miller indices* of the *net plane* (hkl)[11], as illustrated in Fig. 2.10a. The correlation of direct and reciprocal space can therefore be directly seen by the vectors $\vec{p}_1 = \frac{\vec{a}}{h} - \frac{\vec{b}}{k}$, $\vec{p}_2 = \frac{\vec{b}}{k} - \frac{\vec{c}}{l}$ and $\vec{p}_3 = \frac{\vec{c}}{l} - \frac{\vec{a}}{h}$, which are in-plane vectors and hence the normal vector $\vec{n} = \vec{p}_1 \times \vec{p}_2$, which is $\vec{n} = h(\vec{b}\times\vec{c}) + k(\vec{c}\times\vec{a}) + l(\vec{a}\times\vec{b})$, lies parallel to $\vec{H}_{hkl}$ defined above. The length of the reciprocal lattice vector $|\vec{H}_{hkl}|$ is the reciprocal value of the lattice spacing d_{hkl} of (hkl): $d_{hkl} = \frac{1}{|\vec{H}_{hkl}|}$ [94, 95]. The plane normals and hence the reciprocal lattice vectors are of fundamental importance in crystallography, since they allow one to unambiguously represent a given crystal system by poles. The spherical projection of a (cubic) crystal structure is demonstrated in Fig. 2.10b. Moreover, the reciprocal lattice is directly correlated with the phenomenon of diffraction, which is outlined in the next section.

[11] In the strict sense (hkl) denotes only the *one* plane at axis intersection 1/h, 1/k, and 1/l and the entirety of parallel planes of same spacing is denoted as {hkl}. However, as common in XRD literature, the notation *(hkl)* is used throughout this work for the manifold of planes of same spacing d_{hkl} and for the corresponding diffraction peaks

2.2.2 Fundamentals of x-ray diffraction

The amplitude of the diffracted wave

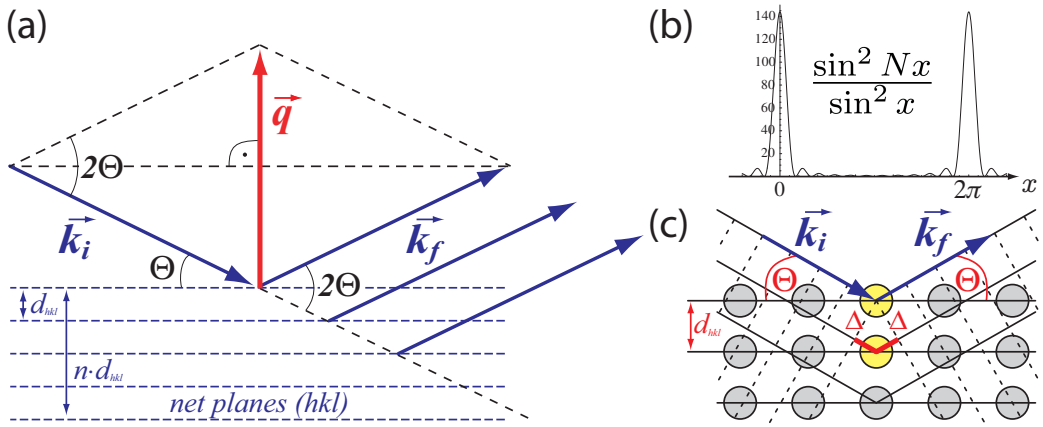

Figure 2.11: (a) Definition of the scattering vector $\vec{q}$ as basis of the derivation of Bragg's law. (b) Plot of the N-slit interference function for N=12. (c) Graphical derivation of Bragg's law via the path difference $2\Delta = 2d_{hkl}\sin\Theta$ of diffracted beams from two neighbouring lattice planes separated by d_{hkl}. Constructive interference takes place for $2\Delta = n\lambda$ with the integer diffraction order n leading to $n\lambda = 2d_{hkl}\sin\Theta$.

The scattering techniques applied in this work are based on the *elastic scattering* of hard x-rays with an energy of typically 10.5 kV, where the energies of incident and diffracted beams are equal, *i.e.*, $|\vec{k_i}| = |\vec{k_f}| = k = \frac{2\pi}{\lambda}$, where $\vec{k_i}$ and $\vec{k_f}$ are the wave vectors of the incoming and diffracted beams, respectively. Most diffraction phenomena in x-ray diffraction can be well described by the *kinematical scattering theory* [96] based on *Thomson scattering* [97] neglecting multiple scattering and assuming the total amplitude of the scattered wave given by a simple summation over all partial waves[12]. In the framework of this theory, the amplitude A_1 of an elastically scattered incident plane wave emitted by *a single electron* at position $\vec{r_e}$ is given by [96, 99]:

$$A_1 = A_0 \frac{1}{4\pi\varepsilon_0}\frac{e^2}{mc^2}\frac{P}{R_0}e^{i(\vec{k_f}-\vec{k_i})\cdot\vec{r_e}} = A_0 r_0 \frac{P}{R_0}e^{i\vec{q}\cdot\vec{r_e}}, \tag{2.10}$$

where A_0 is the amplitude of the incoming wave, $\frac{1}{4\pi\varepsilon_0}\frac{e^2}{mc^2} = r_0 \approx 2.82 \times 10^{-15}$ m is the Thomson scattering length (classical electron radius), P the

[12]The amplitude of the scattered wave is inversely proportional to the mass of the scattering particle, therefore contributions of the atomic nuclei can be neglected [98].

polarization factor and R_0 the distance to the observer, which is of relevance since a spherical wave is emitted. The change in direction of $\vec{k}_i$ to $\vec{k}_f$ was expressed by the *scattering vector* $\vec{q}$ (or: *momentum transfer*):

$$\vec{q} = \vec{k_f} - \vec{k_i} \tag{2.11}$$

in the second step and geometric considerations immediately yield *Bragg's law* as illustrated in Figs. 2.11a and 2.11c:

$$|\vec{q}| = 2k \sin\Theta = \frac{4\pi}{\lambda} \sin\Theta, \tag{2.12}$$

$$n\lambda = 2d_{hkl} \sin\Theta, \tag{2.13}$$

where n herein denotes the order of diffraction and Θ is the *Bragg angle* defined in Fig. 2.11a. The *polarization factor* P takes into account the polarization of the incident beam and depends on the scattering geometry as well as on the kind of the x-ray source. It is defined by the angle between the direction vector of the polarization $\vec{p}$ and $\vec{k_f}$ via $P = \sin^2[\angle(\vec{p}, \vec{k_f})]$ [100]. For specular x-ray diffraction (see Sec. 3.1.1) it is 1 in the synchrotron experiments carried out in this work, since herein the x-ray beam is highly polarized and the electric field vector $\vec{E}$ lies *in* the scattering plane. For off-specular diffraction in the synchrotron experiments performed in grazing incidence geometry (see Sec. 3.1.2) it can be expressed as $P = \cos^2\beta \cos^2\phi + \sin^2\beta$, with the angle ϕ being the in-plane angle and β being the out-of-plane angle, as defined in Fig. 3.3 for the sample system [100]. For unpolarized light, as provided by laboratory x-ray tubes, it is $P = \sqrt{0.5(1 + \cos^2 2\Theta)}$ [96].

For a *complete atom* to be considered (amplitude A_2) , the amplitudes of all single electrons (Equ. 2.10) – expressed by their density distribution – have to be added via integration:

$$A_2 = A_0 r_0 \frac{P}{R_0} \int_{-\infty}^{+\infty} \rho(\vec{r'}) e^{i\vec{q}\cdot(\vec{R_n}+\vec{r_j}+\vec{r'})} d^3\vec{r'} = A_0 r_0 \frac{1}{R_0} f(q) e^{i\vec{q}\cdot(\vec{R_n}+\vec{r_j})}, \tag{2.14}$$

where $\vec{R_n}$ is the position of the origin of the n^{th}-unit cell of the crystal, $\vec{r_j}$ the position of atom j in the unit cell, $\vec{r'}$ the position of the electrons of atom j in unit cell n over which the integration is performed, and $f(q)$ is the *atomic form factor* given as:

$$f(q) = \int_{-\infty}^{+\infty} \rho(\vec{r'}) e^{i\vec{q}\cdot\vec{r'}} d^3\vec{r'}, \tag{2.15}$$

which is the Fourier transform of the electron density of a single (spherical) atom and is a tabular value for the distinct chemical elements. Since the

intensity of diffraction scales with the square of the amplitude, it scales with the square of the number of electrons within the atom, which leads to comparably low scattering intensities in the case of (mostly carbon and hydrogen based) organic molecules.

Next, the atoms j within *one unit cell* are added, which yields for N_c atoms in a cell:

$$A_3 = A_0 r_0 \frac{P}{R_0} \sum_{j=1}^{N_c} f_j(q) e^{i\vec{q}\cdot(\vec{R_n}+\vec{r_j})} = A_0 r_0 \frac{P}{R_0} F(\vec{q}) e^{i\vec{q}\cdot\vec{R_n}}, \tag{2.16}$$

where $F(\vec{q})$ is the *structure factor*[13]

$$F(\vec{q}) \;=\; \sum_{j=1}^{N_c} f_j(q) e^{i\vec{q}\cdot\vec{r_j}}. \tag{2.17}$$

It is of central importance in x-ray diffraction, since it correlates the atomic positions in the unit cell with the intensities of the reflections. Mathematically, $F(\vec{q})$ has the form of a Fourier transform. However, since the intensity as the measured quantity is proportional to the square of $F(\vec{q})$, the phase information is lost and the inverse transformation to obtain the atomic positions from the peak intensity is not directly possible, which is known as the *phase problem in structure determination.*

Finally, the amplitude of the *whole crystal* A_4 can be derived by a summation over all N unit cells of the crystal. Assuming a crystal with unit cell axes $\vec{a_x}$, $\vec{a_y}$ and $\vec{a_z}$ parallel to the x, y, z-axis, respectively, $\vec{R_n} = n_1\vec{a_x} + n_2\vec{a_y} + n_3\vec{a_z}$ being the position of the origin of the n^{th}-unit cell and N_1, N_2, N_3 being the total number of unit cells in the three directions, A_4 can be derived to:

$$A_4 \;=\; A_0 r_0 \frac{P}{R_0} F(\vec{q}) \sum_{n_1=0}^{N_1-1} \sum_{n_2=0}^{N_2-1} \sum_{n_3=0}^{N_3-1} e^{i\vec{q}(n_1\vec{a_x}+n_2\vec{a_y}+n_3\vec{a_z})} \tag{2.18}$$

$$\;=\; A_0 r_0 \frac{P}{R_0} F(\vec{q}) J_{N_1}(\vec{q}\cdot\vec{a_x}) J_{N_2}(\vec{q}\cdot\vec{a_y}) J_{N_3}(\vec{q}\cdot\vec{a_z}), \tag{2.19}$$

where J_N is the *N-slit interference function.* Hence, the intensity in a scattering experiment is proportional to the square modulus of J_N. For a one-dimensional crystal composed of N cells, it can be derived by forming the geometric sum in equation 2.18:

$$|J_N(\vec{q}\cdot\vec{a_x})|^2 = |\sum_{n=0}^{N-1} e^{in\vec{q}\cdot\vec{a_x}}|^2 = |\frac{1-e^{iN\vec{q}\cdot\vec{a_x}}}{1-e^{i\vec{q}\cdot\vec{a_x}}}|^2 = \frac{\sin^2\frac{Nq_xa_x}{2}}{\sin^2\frac{q_xa_x}{2}}, \tag{2.20}$$

[13]Instead of defining $F(\vec{q})$ as sum over the atomic form factors, it can equivalently be defined as $F(\vec{q}) = \int_{uc} \rho(\vec{r}) e^{i\vec{q}\cdot\vec{r}} d^3\vec{r}$, *i.e.*, as the integral over the total charge distribution of the unit cell (uc).

where the component of the scattering vector in x-direction q_x was introduced in the last step. The relevant function of type $\frac{\sin^2 Nx}{\sin^2 x}$ is plotted for N = 12 in Fig. 2.11b and it can be clearly seen that distinct maxima arise at multiples of 2π, which become a series of delta functions for N$\rightarrow \infty$. Therefore, the amplitude of the diffracted wave is only *not* vanishing in certain, well-defined directions and equation 2.18 directly leads to the *Laue equations* as they were derived by Max Theodor Felix von Laue, which have to be satisfied simultaneously for the intensity to be a maximum [101]:

$$\vec{q} \cdot \vec{a_x} = 2\pi h, \tag{2.21}$$

$$\vec{q} \cdot \vec{a_y} = 2\pi k, \tag{2.22}$$

$$\vec{q} \cdot \vec{a_z} = 2\pi l. \tag{2.23}$$

Most importantly, this is only the case if $\vec{q}$ is a reciprocal lattice vector $\vec{H}_{hkl}$, as can be seen from the definition of the reciprocal lattice (Equ. 2.8). Moreover, from these equations the physical meaning of the reciprocal lattice becomes clear: An arbitrary set of integers *h, k, l*, *i.e.*, an arbitrary $\vec{H}_{hkl}$ (Equ. 2.9) leads to a scattering vector $\vec{q}$ that satisfies the Laue equations, therefore the *allowed values* for constructive interference form a three dimensional lattice, which is the reciprocal lattice, exhibiting base vectors pairwise orthogonal to the direct vectors defining the diffracting crystal itself.

In real diffraction experiments the experimentally determined intensity deviates from the calculated intensity and several corrections have to be applied to account for properties of both the x-ray beam[14] (*e.g.* its polarization) and the geometry of the scattering experiment (*e.g.* specular diffraction or experiments in grazing incidence geometry). This is done by multiplying the calculated intensity with several intensity factors. The most important are: (i) The *Lorentz factor L*, which takes into account the influence of the limited resolution of the experiment due to the divergence of the incident and diffracted beam. L depends on the way that the reciprocal lattice points pass through the Ewald-sphere, *i.e.*, the sphere of reflection, and therefore varies with the experimental method. For specular diffraction experiments, it is determined by $L = 1/\sin(2\Theta)$ and for grazing incidence geometry it is determined by $L = 1/(\cos\alpha_i \sin\phi \cos\beta)$ with α_i being the (small) incident angle [100]. (ii) The *area factor A*, which takes into account the active area of the incident beam on the sample and which depends on the incident angle α_i. The active area is then $\sim 1/\sin\alpha_i$, where slits limiting the incident and diffracted beam have to be considered. (iii) The *rod intersection factor R*,

[14]The beam can be regarded as monochromatic in the synchrotron experiments carried out in this work in good approximation.

which accounts for the finite size of the crystal scattering rods (see below) in surface diffraction. The intersection of rod and Ewald sphere depends on the out-of plane angle β (see Fig. 3.2) at fixed detector slit size. At a given β the detector integrates over $\Delta q_\perp$ of $q_\perp$, *the vertical component of the momentum transfer* leading to $\Delta q_\perp \approx \frac{2\pi}{\lambda}\Delta\beta\cos\beta$ for a small divergence of the incident beam, where $\Delta\beta$ denotes the (constant) ratio of out-of-plane width of the detector slit and the distance between sample and detector [100]. This leads to a rod intersection factor of $R \sim \cos\beta$. The measured intensity I_{exp} is related to the calculated intensity I_{calc} by multiplying the latter with the intensity factors.

Kinematic and dynamic diffraction

In the case of specular diffraction, where the angle of incidence and diffraction are equal and $q_x = q_y = 0$, Equ. 2.18 reduces to:

$$A_4 = A_0 r_0 \frac{P}{R_0} F(q_z) N_1 N_2 \sum_{n_3=0}^{N_3-1} e^{in_3 q_z a_z} = A_0 r_0 \frac{P}{R_0} F(q_z) N_1 N_2 \frac{1 - e^{iN_3 q_z a_z}}{1 - e^{iq_z a_z}} \tag{2.24}$$

and equals Equ. 2.20, where the maxima are located at values of $q_z = \frac{2\pi l}{a_z}$ with integer l (see Fig. 2.11b). This directly provides the lattice spacing a_z normal to the sample surface, which equals a unit cell parameter in orthogonal crystal systems. Moreover, the interference function exhibits minima with distances

$$\Delta q_z^{Laue} = \frac{2\pi}{N_3 a_z} = \frac{2\pi}{D_L}, \tag{2.25}$$

where D_L denotes the *coherent film thickness* perpendicular to the surface. Incoherently scattering domains lead to an attenuation of the oscillations. Therefore, the presence of pronounced Laue oscillations around Bragg peaks in specular x-ray diffraction experiments (Fig. 2.12) acts as an indicator for high film quality [102].

From Equ. 2.18 fundamental properties of diffracting patterns from thin films can be deduced. For a film of monolayer thickness, N_3 has to be set to 1, which makes the diffraction independent of the component of $\vec{q}$ along the surface normal, *i.e.*, from the momentum transfer perpendicular to the surface $q_\perp$. This means, that in contrast to an infinite three-dimensional crystal forming a point lattice in reciprocal space, scattering from a monolayer leads to a two-dimensional lattice of rods perpendicular to the surface in reciprocal space [99, 103]. In a reciprocal space map (see Sec. 3.1.2) the rods from monolayer diffraction can be seen as lines along $q_\perp$. In the experimentally important case of thin multilayer films, a situation occurs, in

which the measured intensity along the rods goes through a minimum between the Bragg points. This can again be seen from the rapidly varying interference function (Equ. 2.20) at high values of N, which cannot be resolved in a real experiment. The numerator of $I(q_z) \sim \frac{\sin^2 \frac{N_3 q_z a_z}{2}}{\sin^2 \frac{q_z a_z}{2}}$ can then be approximated by $\frac{1}{2}$ away from the Bragg points (*i.e.*, for $q_z a_z \neq 2\pi$), which leads to $I(q_z) \sim \frac{1}{2 \sin^2 \frac{q_z a_z}{2}}$ being independent of the value of N_3. Therefore the intensity between the Bragg points is non-zero and declines with the square of the q_z-distance from the Bragg points. The rods in the diffraction pattern are then denoted as *crystal truncation rods*, since they represent the folding of the sharp Bragg points from the infinite crystal with the $\frac{1}{q_z^2}$-tails originating from the inverse Fourier transform of the surface termination by a step-function. This implies that a deviation from a perfectly terminated film due to the roughness of real surfaces can be deduced from the shape of the crystal truncation rod [99, 103, 104].

Not all features that are observed in the x-ray diffraction results presented in this work can be satisfyingly described by the kinematical theory. The second important diffraction theory is the *dynamical scattering theory*, which represents the exact solution of Maxwell's equations for the electromagnetic wave fields and can be well applied for highly perfect systems. It includes multiple scattering, polarization effects as well as refraction and reflection effects at interfaces, but, in contrast to the kinematic approach, it is inappropriate to deal with imperfections giving rise to diffuse scattering in the vicinity of Bragg peaks [96]. The *distorted-wave Born approximation* (DWBA) [105] is a combination of both theories, which dynamically takes into account refraction effects at smooth interfaces and kinematically treats lateral inhomogeneities. It allows one to describe the phenomenon of maxima of diffuse scattering whenever $\alpha_i \approx \alpha_c$ or $\alpha_f \approx \alpha_c$, where α_i and α_f are the incident and exit angles, respectively and α_c is the critical angle of total reflection. These maxima occur for instance in reciprocal space maps at an exit angle of α_c and are called the *Yoneda peaks* [96, 106, 107] and are of purely dynamical nature [98]. For the experimentalist, a constant α_f position of the Yoneda peaks at varying in-plane scattering angle (see Sec. 3.1.2) is useful to assure the correct sample alignment in reciprocal space maps.

Reflection and refraction of x-rays

At low incident angles α_i of the incoming wave vector $\vec{k_i}$ the wavelength depending *refractive index* n of the penetrated medium must not be neglected. In general, the change of propagation direction upon entering from a medium

with n_0 into a medium with n can be described by Snell's law:

$$\frac{\cos\alpha_i}{\cos\alpha_t} = \frac{n}{n_0}, \tag{2.26}$$

where α_t denotes the angle of the refracted beam measured from the surface of the medium. In contrast to *normal dispersion* as found for visible light, where n increases with decreasing wavelength in most media, x-rays exhibit *anomalous dispersion* with n decreasing for decreasing wavelength and $n < 1$. That also means that the x-ray wavelength *increases* to λ/n upon entering the medium and that refraction therefore happens *away* from the plane normal. In the medium, exponential damping from incident intensity I_0 to I occurs, which follows the *law of Lambert-Beer*:

$$I = I_0 e^{-\mu(\lambda)l}, \tag{2.27}$$

where $\mu(\lambda)$ is the wavelength dependent *linear attenuation coefficient* and l the path in the medium. For x-rays in homogenous media, far away from absorption edges and impinging at grazing angles α_i, the refractive index can be expressed as [107]:

$$n = 1 - \delta + i\beta = 1 - \frac{\lambda^2}{2\pi} r_e \varrho_e + i\frac{\lambda}{4\pi}\mu(\lambda), \tag{2.28}$$

where δ and β are the dispersion and absorption terms, respectively, and ϱ_e denotes the electron density of the medium. From the dispersion part in Equ. 2.28, it follows for a single interface between vacuum ($n = 1$) and a certain medium via Snell's law that $\cos\alpha_i = (1-\delta)\cos\alpha_t$ and in the case of $\alpha_t = 0$, the incident angle becomes the *critical angle of total external reflection*[15] α_c and can be approximated as

$$\alpha_c \approx \sqrt{2\delta} = \lambda\sqrt{\frac{r_e \varrho_e}{\pi}} \tag{2.29}$$

This expression allows one to estimate the electron density of the medium and consequently the corresponding *mass density* ϱ_m via

$$\varrho_e = \frac{\alpha_c^2 \pi}{\lambda^2 r_e}, \quad \varrho_m = \frac{A\varrho_e}{N_A Z}, \tag{2.30}$$

[15]Since α_i and α_t are very small around the critical angle for x-rays, $\cos\alpha \approx \frac{1}{2}(1-\frac{\alpha^2}{2})$ holds for both angles leading via Snell's law (with $\beta = 0$) to $(1-\frac{\alpha_i^2}{2}) = (1-\frac{\alpha_t^2}{2})(1-\delta)$ and for $\alpha_t\delta \approx 0$ to $2\delta \approx \alpha_i^2 - \alpha_t^2$, which reduces in the case of total reflection, where $\alpha_t = 0$, to $\alpha_c \approx \sqrt{2\delta}$.

where Z is the atomic number, A is the mass number and N_A is the Avogadro constant. In experiments α_c is taken as the incident angle at which the total reflected intensity becomes 50% of the incident intensity [98].

At the vacuum/medium interface the parallel component of the wave vector is conserved and the complex reflection and transmission coefficients r and t, respectively, are given by the *Fresnel formulae*[16]:

$$r = \frac{k_{i,z} - k_{t,z}}{k_{i,z} + k_{t,z}} = \frac{\sin\alpha_i - \sin\alpha_t}{\sin\alpha_i + \sin\alpha_t}, \tag{2.31}$$

$$t = \frac{2k_{i,z}}{k_{i,z} + k_{t,z}} = \frac{2\sin\alpha_i}{\sin\alpha_i + \sqrt{n^2 - \cos^2\alpha_i}}, \tag{2.32}$$

where $k_{i,z} = k\sin\alpha_i$ and $k_{t,z} = nk\sin\alpha_t = k\sqrt{n^2 - \cos^2\alpha_i}$ denote the z-components of the incoming and transmitted beam. The intensities of the reflected (Fresnel reflectivity) and the transmitted beam (Fresnel transmission) are $R_F = |r|^2$ and $T_F = |t|^2$, respectively. It can be shown (without absorption) that R_F is 1 for $\alpha_i < \alpha_c$ and that it decreases rapidly for $\alpha_i > \alpha_c$, whereas T_F exhibits a maximum at $\alpha_i = \alpha_c$ since the reflected and transmitted waves interfere constructively enhancing the transmitted amplitude by a factor of two. For both cases absorption leads to $R_F < 1$ for $\alpha_i < \alpha_c$ as well as to a reduction of the enhancement of T_F for $\alpha_i = \alpha_c$ [107]. Furthermore, the value of $k_{t,z} \simeq ik(\alpha_c^2 - \alpha_i^2)^{1/2}$ for $\alpha_i < \alpha_c$ and the amplitude A of the wave (propagating in the x-z plane) therefore becomes $A \sim e^{ik_{t,z}z} = e^{-zk(\alpha_c^2-\alpha_i^2)^{1/2}} = e^{-z/\Lambda}$, where the *penetration depth* Λ was introduced, at which A decreased to $1/e$. Λ is therefore extremely low for $\alpha_i < \alpha_c$ and can be approximated by [108]:

$$\Lambda \simeq \frac{\lambda}{2\pi(\alpha_c^2 - \alpha_i^2)^{1/2}}, \tag{2.33}$$

which leads to typical values of Λ of some nanometers. In contrast to the significant damping along the z-direction, the wave vector component in the medium along the x-direction $k_x, t = k\cos\alpha_i$ provides a wave propagating along the surface[17] [108], which is referred to as *evanescent wave* in literature [107, 109]. These relations highlight the strengths of x-ray diffraction at gracing angles: It allows one to perform highly surface sensitive Bragg scattering and to determine the structural properties of ultra-thin films with strongly reduced substrate contributions.

[16]Equ. 2.31 gives the Fresnel formulae for s-polarized light with the electric field vector lying in the plane of the surface. The corresponding formulae for p-polarization do not differ significantly for x-rays due to $n \approx 1$ [107]

[17]Note that these equations for k_x, t and k_z, t do not take into account absorption resulting from $\beta > 0$, which is however low for organic thin films.

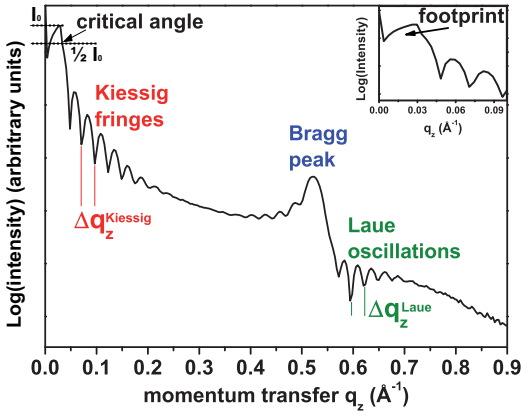

Figure 2.12: Specular scan on a thin film of hexabenzocoronene (see Fig. 2.1b) on SiO_x illustrating the distance between two consecutive minima (or maxima) of the Kiessig fringes and Laue oscillations, $\Delta q_z^{Kiessig}$ and Δq_z^{Laue}, respectively. Inset: zoomed representation of the low q_z-region demostrating the footprint effect.

In the case of a thin film on a substrate, interference effects occur between the beams reflected at the film surface and at the film/substrate interface due to the different optical path of the beams leading to a *phase difference* Δ between the beams. This leads to a sequence of minima and maxima of the reflected intensity, which are denoted as *Kiessig fringes* [110, 111]. The intensity exhibits a maximum whenever Δ is an integer multiple (m) of the wavelength[18]: $\Delta = m\lambda$. From simple geometric considerations, taking into account Snell's law and the approximation $\alpha_t = \sqrt{\alpha_i^2 - \alpha_c^2}$ it follows:

$$\Delta = m\lambda = 2D_K \sin\alpha_t \approx 2D_K\alpha_t = 2D_K\sqrt{\alpha_i^2 - \alpha_c^2} \tag{2.34}$$

$$\alpha_{i,m}^2 = \alpha_t^2 + (\frac{\lambda}{2D_K})^2 m^2, \tag{2.35}$$

which allows one to graphically determine the layer thickness D_K and the critical angle α_c from the angle positions $\alpha_{i,m}$ with maximal intensity. Plotting the squares of $\alpha_{i,m}$ versus the squares of the Kiessig fringe order the linear slope yields the layer thickness and the axis intersection determines α_c and, consequently, the refractive index of the layer. Expressed in terms of momentum transfer in reciprocal space this relation can be written as:

$$\Delta q_z^{Kiessig} = \frac{2\pi}{D_K}, \tag{2.36}$$

where $\Delta q_z^{Kiessig}$ denotes the q_z-spacing of the fringes. Note that this expression is similar to Equ. 2.25 for the Laue oscillations although they are of different physical origin and contain complementary information on the investigated film. Kiessig fringes are independent of the crystallinity of the film

[18] In the original work H. Kiessig considered a nickel film on a glass substrate, therefore a phase jump at the nickel/glass interface had to be taken into account, since for x-rays glass is optically denser than nickel [111].

and provide the *total film thickness*, whereas the Laue oscillations yield the number of *coherently scattering* lattice planes of *crystalline* matter. Hence, if the two values are in the same range, a crystalline arrangement throughout the film can be deduced. The two types of oscillations are illustrated in Fig. 2.12 together with the *footprint effect* at low angles accounting for the experimental projection of the incoming beam onto the sample surface, which may be larger than the sample size and has to be corrected if intensities are considered [98].

The investigation of multilayer systems is a more demanding task, since multiple interfaces between layers of different n have to be taken into account, which collectively determine the resulting reflected beam. This problem can be treated with a formalism introduced by Lyman G. Parratt [107, 112]. Herein, a recursive scheme is applied taking into account the Fresnel coefficients at the downward interface j (Equ. 2.31) $r_{j,j+1} = (k_{z,j} - k_{z,j+1})/(k_{z,j} + k_{z,j+1})$ with $k_{z,j} = k(h_j^2 - \cos^2 \alpha_i)^{1/2}$ being the z-component of the wave vector in layer j, the lowermost layer and vacuum having index N and 1, respectively. Therefrom, a recursive formula for the amplitude ratio of reflected to transmitted wave at interface j can be derived, starting with the boundary condition that the substrate is infinitely thick and therefore cannot provide a beam from the interior (N+1). Hence, after N iterations, the overall amplitude of the reflected beam is obtained. This formalism can be extended to account for interface roughness between the adjacent layers by simply replacing the Fresnel coefficients for sharp interfaces with modified coefficients comprising the *root-mean square* (rms) roughness (see Sec. 3.4), if the roughness is much lower than the respective layer thickness [107]. Therefore, using this model, a measured spectrum of a multilayer film can be fitted to extract the layer thicknesses, the vertical electron density profile as well as the interface roughnesses.

Line profile analysis

Already in 1918 Paul Scherrer established a correlation between the width of Bragg reflections and the size of the scattering crystal. Hence, he demonstrated that x-ray diffraction can be used to access information on the microstructure of solid state matter and derived a formula that correlates the *integral breadth* in 2Θ of a Bragg peak ($\beta_{2\Theta}$) with the crystallite size along the scattering vector [113, 114], where the integral breadth is defined as the width the peak would have, if modeled by a rectangular box with same maximum intensity I_0 and the same integral intensity $I_{int} = \int_{-\infty}^{+\infty} I(2\Theta) d2\Theta$, *i.e.*, $\beta_{2\Theta} = I_{int}/I_0$. Apart from using this definition to determine $\beta_{2\Theta}$, it can be extracted from a fit of the peak with an appropriate fit function. In x-ray

diffraction the *Voigt-function* $f_V(2\Theta)$ is widely used to represent experimental data [109, 115]. It is a convolution of a Cauchy (Lorentz) function f_C and a Gaussian function f_G with the two as limiting cases. It is defined as:

$$f_V(2\Theta) = \frac{\beta_V}{\beta_C \beta_G} \int_{-\infty}^{+\infty} f_C(\xi) f_G(2\Theta - \xi) d\xi, \tag{2.37}$$

where β_V, β_C and β_G denote the integral breadths of the Voigt, Cauchy and Gaussian profile, respectively and the shape of the Voigt function depends only on β_C and β_G, since β_V depends on those values. Since fitting of a given profile with $f_V(2\Theta)$ is a demanding task, a simplified version, the *pseudo-Voigt function* was introduced, which is defined as:

$$f_{pV}(2\Theta) = \eta f_C + (1 - \eta) f_G, \tag{2.38}$$

where the weight parameter η describes the Cauchy ratio in the convoluted profile. From η and the *full width at half maximum* $2w$, the integral breadth can be directly deduced via $\beta_{pV}(2\Theta) = (\eta\pi + (1 - \eta)\sqrt{\pi \ln 2})w$, which has been performed in all cases where integral breadths were used in this work. Using the *Scherrer formula*, the *out-of-plane crystalline coherence length* D_S, *i.e.*, the size of coherently diffracting domains, can be estimated:

$$D_S \approx \frac{\lambda}{\beta_{2\Theta} \cos\Theta} = \frac{2\pi}{\Delta q_z}, \tag{2.39}$$

where Δq_z denotes the integral peak breadth, here expressed in terms of momentum transfer. This relation can be directly derived from the integration of the square of the interference function with $D_S = N_3 a_z$. In the above formulation the Scherrer formula is valid for cube-shaped and monodisperse crystallites only. However, already in this simple form it can act as valuable (rough) estimate for the dimensions of crystalline domains. Similar expressions for various differently shaped crystallites including spheres or tetrahedra can also be derived. In the realistic case of a broad rather than a monodisperse distribution a *size distribution function* $g(D)$ can be introduced indicating the probability $g(D)dD$ that the value of D of an individual crystallite falls into the range dD. The size parameter derived from the Scherrer formula accounts for the ratio of the fourth central statistical moment $\langle D^4 \rangle$ over the third moment $\langle D^3 \rangle$ of $g(D)$, where $\langle D^x \rangle = \int D^x g(D) dD$ and it is denoted as $\langle D \rangle_V = \langle D^4 \rangle / \langle D^3 \rangle$, *the volume-weighted average crystallite size*. Therefore, the size parameter D_S obtained by the Scherrer formula is generally to be understood as volume-averaged mean [109].

Apart from broadening effects due to the finite size of the scattering crystallites, x-ray diffraction experiments always exhibit *instrumental broadening*, which is independent of the sample microstructure. Experimental

factors like beam monochromatization, beam divergence etc., broaden the Bragg diffraction peaks. The influence of instrumental broadening can be determined using well defined, untextured standard samples of minimal microstrain and large enough crystallite size. In the present work synchrotron radiation was used for all scattering experiments and the upper limit of instrumental broadening was estimated via the integral breadth of the Ag(111) Bragg peak of a silver single crystal ($\beta_{2\Theta} = 0.0382 \pm 0.0003°$), which is low compared to the breadth of typical peaks of organic layers that are in the range of 0.2°. Therefore a constant value of instrumental broadening over the whole investigated angular range could be assumed in good approximation.

In realistic thin films distortions of the crystal lattice will always be present, which are caused by lattice defects contracting or expanding bond lengths, which leads to strain fields in the lattice with extensions over large distances. Therefore, the lattice spacing occurring in Bragg's law has no sharp value and must be accounted for by a distribution, which leads to a broadening of the reflections around d_0, which is denoted as *microstrain broadening*[19]. It follows that the integral breadth of a recorded reflection is therefore a convolution of instrumental broadening, finite-size and strain induced broadening. However, it can be shown that (after correction for instrumental broadening) the *integral breadth due to finite-size broadening* β_S can be separated from the *integral breadth due to strain broadening* β_D , since the latter scales with $\tan\Theta$, whereas $\cos^{-1}\Theta$ occurs in the Scherrer formula [109, 116]. Williamson and Hall established in 1953 a method to graphically separate β_S from β_D by a plot of:

$$\beta^*_{2\Theta} = \beta^*_S + \beta^*_D = 1/\langle D\rangle_V + 2ed^*, \tag{2.40}$$

where $\langle D\rangle_V$ denotes the volume-weighted average thickness of the crystallites along the scattering vector and e denotes the *maximum (upper limit) strain* that is proportional to the crystal lattice distortion [109, 117, 118]. The parameters marked with (*) are expressed in reciprocal units: $\beta^*_{2\Theta} = \beta_{2\Theta} cos(\theta)/\lambda$, $d^* = 2sin(\theta)/\lambda$. This kind of analysis is denoted as *Williamson-Hall analysis (WHA)*. It must be emphasized that absolute values determined by WHA have to be treated with caution [119], however, in this work WHA was mainly applied to investigate *relative changes* of crystallite size and microstrain, which allows one to draw qualitative conclusions on the growth behaviour under well defined conditions like thermal treatment (Sec. 5.1) or co-deposition of two materials (Sec. 5.2 and 5.7).

[19]Note that the dimensions of the affected volume is low compared to Λ. In contrast, *macrostrains* exceeding the Λ-scale cause a shift of the Bragg reflection rather than a simple broadening around d_0 [109]

Chapter 3

Experimental methods

In this chapter the experimental methods applied in this work are introduced. The main experimental tools were x-ray diffraction in various measurement geometries as well as ultraviolet photoelectron spectroscopy, atomic force microscopy and vibrational spectroscopy. Detailed information on the specific experimental setups and the instrumental parameters applied can be found in Chap. 4.

3.1 X-ray diffraction techniques

The fundamentals of x-ray diffraction and reciprocal space have been introduced in Sec. 2.2. There it was shown that the momentum transfer in a scattering experiment can be vectorially expressed by the difference of scattered and incident wave vectors. Since the considerations were restricted to elastic scattering, *i.e.*, $k_i = k_f = k = 2\pi/\lambda$, there exists a well defined limited region of reciprocal space that can be accessed via x-ray diffraction experiments for $\vec{k_i}$ and $\vec{k_f}$ not penetrating through the sample. This region is illustrated in Fig. 3.1 as uncolored interior of a half sphere of radius $2k$, whereas the inaccessible regions of radius k are colored in yellow (termed *Laue-zones*)[1]. This figure shows the two main experimental geometries applied in this work in different colors:

(i) The vectors colored red in Fig. 3.1 illustrate the case of *specular x-ray diffraction* (XRD) symmetric ($\alpha_i = \alpha_f$) with respect to the sample surface (frequently termed as $\Theta/2\Theta$ scan), which is by far the most commonly used technique (see Sec. 3.1.1) [109, 121]. The length of the scattering vector $\vec{q}$ along the surface normal (usually termed q_z in $\Theta/2\Theta$ scans) is varied and

[1]Note that there are additional inaccessible regions around the y-axis in Fig. 3.1 [120] which were not drawn to maintain clarity.

Bragg peaks are observed whenever $\vec{q}$ matches a reciprocal lattice vector according to Bragg's law (Equ. 2.12), *i.e.*, the out-of-plane order is investigated. If the sample is tilted at fixed $\vec{q}$ in the vicinity of the Bragg angle Θ around the y-axis with $\vec{q}$ hence forming a circle around the origin of reciprocal space, the scan is denoted as *rocking scan* and allows one to investigate the shape of reciprocal lattice points and to deduce information on the mosaicity of the sample. At low incident angles (with the detector, therefore, near the primary beam) the scattering vector $\vec{q}$ is small (far below the (001) reciprocal lattice point in Fig. 3.1) and the technique is then usually called *x-ray reflectivity* (XRR) probing the vicinity of the origin of reciprocal space. It allows one to deduce electron densities, layer thicknesses and interface roughnesses of thin films and multilayer samples (according to the formalism derived in Sec. 2.2.2). Apart from reciprocal lattice points on the z-axis, any experimentally accessible position of reciprocal space can be investigated. This is demonstrated by the vectors colored violet in Fig. 3.1 with $\vec{q}$ pointing to a position in the xz-plane apart from the z-axis, which is done with the same $\vec{k_i}$ as above, but different $\vec{k_f}$.

(ii) The vectors colored blue in Fig. 3.1 show the geometry of *grazing incidence diffraction* (GID) where $\vec{k_i}$ impinges on the sample surface below α_c. This allows one to make use of the enhanced surface sensitivity due to the evanescent wave being present and the strikingly reduced value of the penetration depth Λ (see Sec. 2.2.2). If α_f is similar to α_i the vertical component of momentum transfer (usually termed $q_\perp$ instead of q_z in GID) is small and the scan almost takes place within the xy-plane. The scattering vector $\vec{q}$ (with its projection on the plane $q_\parallel$) is then varied along the vicinity of the border of the Laue-zone. Thus, with GID, information on the in-plane arrangement of the sample can be obtained (*in-plane diffraction*). Moreover, the grazing incidence geometry allows one to record maps of the reciprocal space by simultaneously varying $q_\parallel$ *and* $q_\perp$, a technique, which is termed gracing incidence *reciprocal space mapping* (RSM). In such maps features like the crystal truncation rod or even rods from monolayer films can be directly visualized (see Sec. 3.1.2).

In polycrystalline samples with complete isotropic crystallite orientation the condition $\vec{q} = \vec{H}_{hkl}$ is always fulfilled if Bragg's law is fulfilled. This is generally the case in *powder diffraction*. However, if the crystallites exhibit a certain preferential orientation, which is termed *texture*, this is no more the case. In the important case of a polycrystalline thin film with crystallites being preferentially oriented with respect to a certain direction in the sample reference frame, the anisotropy of crystallite orientation is named *fiber-texture* (also often referred to as *two dimensional powder*) with the *fiber-axis* as

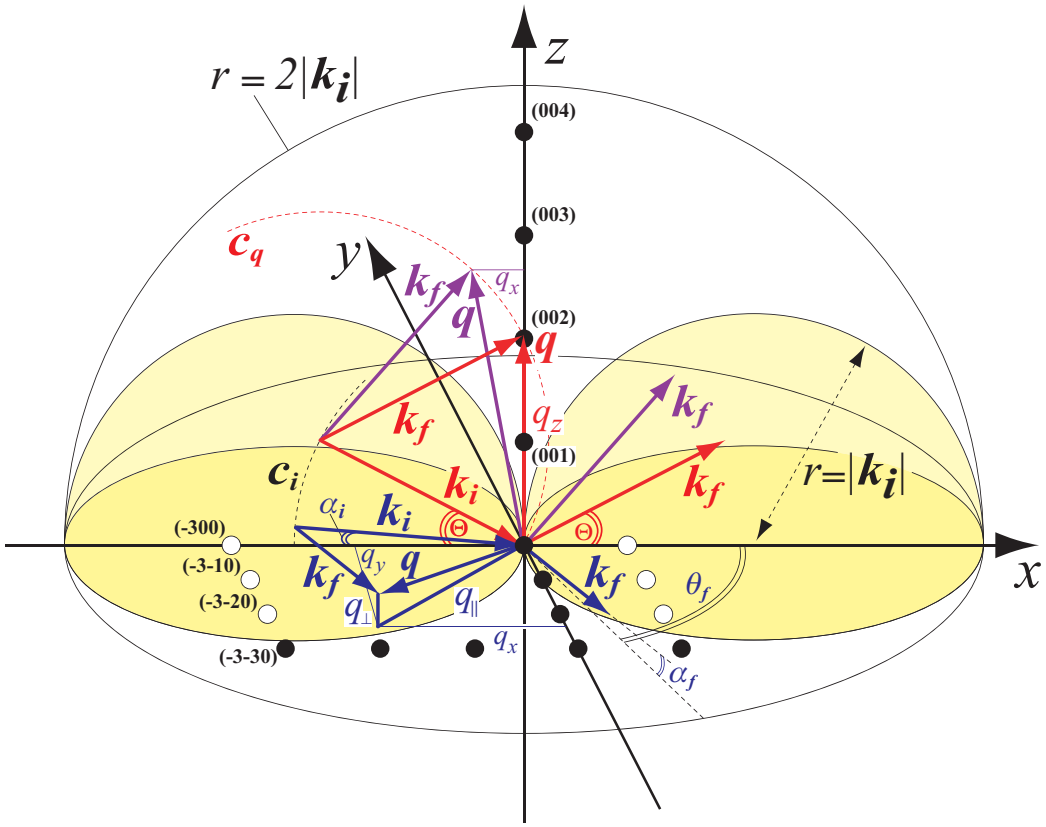

Figure 3.1: Schematic of the wave vectors $\vec{k_i}$ and $\vec{k_f}$, the scattering vector $\vec{q}$, its parallel and vertical components $q_\parallel$ and $q_\perp$ (q_z) respectively, for the most important experimental geometries XRD and GID (RSM). The uncolored regions of the half-sphere of radius $2k_i$ is the experimentally accessible region in reflection, whereas the yellow half-spheres (Laue zones) are only accessible in transmission; points with indices (hkl) denote reciprocal lattice points of a cubic crystal structure that are accessible (black) or inaccessible (white) at the given sample orientation. For fiber-textured films the lattice points lie on circles around the fiber axis. The XRD (or XRR at low Θ) arrangement of specular diffraction is illustrated in red, the GID (RSM) arrangement in blue. XRD scans are performed with q_z varying along the z-axis, rocking scans with q_z fixed in space and the sample rotating around the y-axis, GID scans in the vicinity of the Laue zones at low $q_\perp$ and reciprocal space maps by varying both $q_\perp$ and $q_\parallel$. Violet vectors illustrate a more general situation of $\vec{q}$ being apart from the z-axis in the xz-plane.

axis of preferential orientation. The structural investigations performed in this work deal with thin films on substrates being flat but not inducing preferential azimuthal order of the adsorbate crystallites. Therefore, the substrate surface normal is the most likely direction of the fiber axis, which was observed for PEN, PQ as well as PFP (see Sec. 5). For specular XRD investigations on fiber textured films this means that only the peak series originating from net planes perpendicular to the fiber axis (*e.g.*, the $(00l)$-series) can be observed. However, for RSM or GID investigations the presence of a fiber axis means that the off-axis reciprocal lattice points lie on circles around the axis collectively intersecting the reciprocal space map in RSM or the scan path in GID experiments, respectively. Therefore, the sample does not need to be azimuthally rotated as would be the case for the investigation of single crystals.

3.1.1 Specular x-ray diffraction

The fundamental relationships of specular XRD were introduced in Sec. 2.2.2 in terms of $\vec{q} = \vec{k_f} - \vec{k_i} \equiv \vec{H}_{hkl}$ and the underlying geometry in reciprocal space was outlined in the previous section. For the general case depicted in Fig. 3.1 (violet vectors) lattice planes inclined to the surface plane can be probed, which again lie perpendicular to $\vec{q}$. The components q_x, and q_z of the scattering vector are then [98]:

$$q_x = \frac{2\pi}{\lambda}(\cos\alpha_f - \cos\alpha_i), \tag{3.1}$$

$$q_z = \frac{2\pi}{\lambda}(\sin\alpha_i + \sin\alpha_f), \tag{3.2}$$

expressed by α_i, α_f in the sample coordinate system as introduced in Fig. 3.1 with $\alpha_i + \alpha_f = 2\Theta$. For symmetric specular diffraction (red vectors in Fig. 3.1) with $\alpha_i = \alpha_f$, *i.e.*, for a scan along the specular rod $(00l)$, these equations simplify to:

$$q_x = 0, \tag{3.3}$$

$$q_z = \frac{4\pi}{\lambda}\sin\Theta. \tag{3.4}$$

A specular XRD scan is generally the first step for the structural investigation of a thin film, since untextured (3D-powder like) samples can be easily distinguished from fiber-textured (2D-powder like) films. From the breadth of the Bragg peaks the microstructure of the film can be investigated via the Scherrer formula, or, if a peak series is being found, via WHA (Sec. 2.2.2).

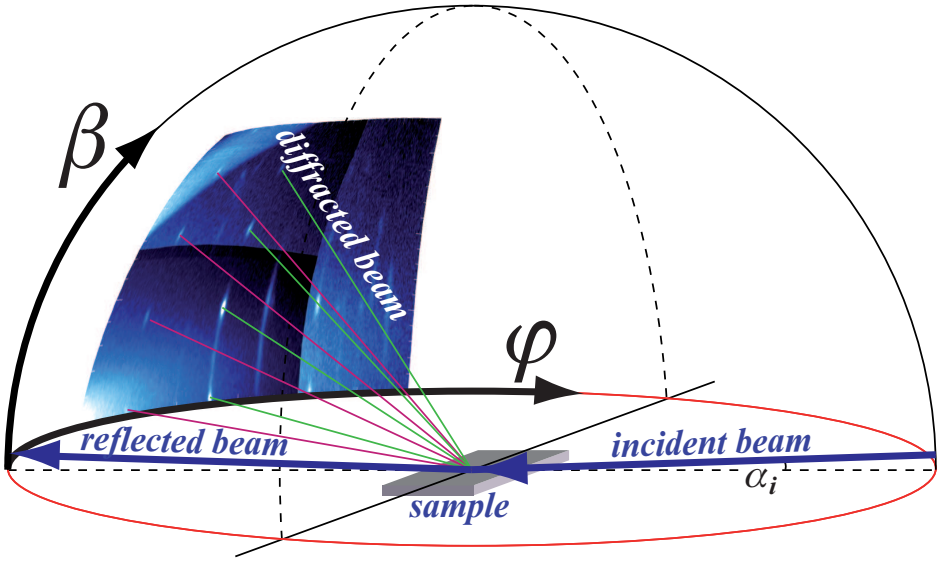

Figure 3.2: Schematic illustration of the geometry of a RSM experiment performed with a point detector moving on a half sphere together with the corresponding angles φ and β, which are the spherical coordinates of the sample coordinate system. Since the experiment is performed under grazing incidence conditions with $\alpha_i < \alpha_c$ most of the incident intensity is totally reflected.

3.1.2 Grazing-incidence x-ray diffraction

In the most general case of $\vec{k_i}$ impinging under angles α_i w.r.t. the xy-plane, under θ_i w.r.t. the xz-plane and of $\vec{k_f}$ being detected under α_f w.r.t. the xy-plane and under θ_f w.r.t. the xz-plane, the three components of $\vec{q}$ are given by [98]

$$q_x = \frac{2\pi}{\lambda}(\cos\alpha_f \cos\theta_f - \cos\alpha_i \cos\theta_i), \tag{3.5}$$

$$q_y = \frac{2\pi}{\lambda}(\cos\alpha_f \sin\theta_f + \cos\alpha_i \sin\theta_i), \tag{3.6}$$

$$q_z = \frac{2\pi}{\lambda}(\sin\alpha_i + \sin\alpha_f), \tag{3.7}$$

which can be simplified for the case of $\vec{k_i}$ being oriented in the xz-plane with $\cos\theta_i = 1$. The relevant coordinate of in-plane diffraction investigations of fiber textured films is $q_\parallel = \sqrt{q_x^2 + q_y^2}$, as outlined above. This is the case depicted in Fig. 3.1 (blue vectors).

A central aim of this work is the determination of unit cell parameters using grazing incidence RSM. In the experimental setup used for RSM

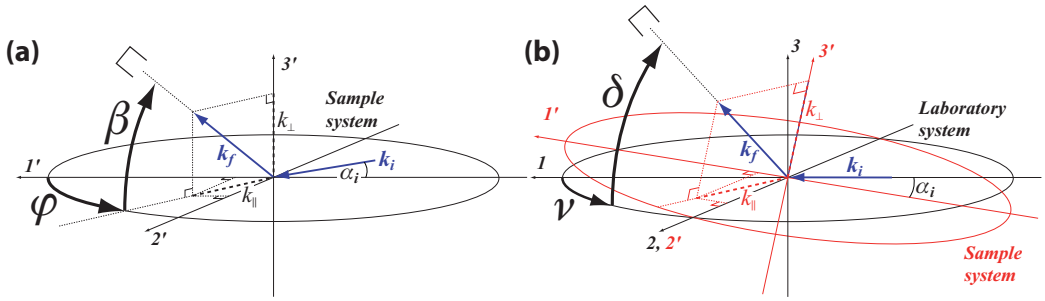

Figure 3.3: (a) Angles φ and β of the diffracted beam $\vec{k_f}$ in the sample coordinate system for an incident beam $\vec{k_i}$ impinging under the angle α_i w.r.t. sample plane. (b) The same situation depicted in the laboratory system with angles ν, δ. Vectors in the figure are printed bold.

(Sec. 4.2.1) a point detector is moved on along two angles to record a reciprocal space map under gracing incidence conditions; the principal geometry is illustrated in Fig. 3.2 in the *sample coordinate system* with spherical coordinates ϕ and β. Since the fixed angle of incidence[2] α_i is chosen below α_c most of the incident intensity is reflected under $\alpha_f = \alpha_i$. At certain angles (φ, β), which equal (θ_f, α_f)[3] in Fig. 3.1, Bragg's law may be fulfilled resulting in a peak in the map. However, in the present experimental setup the detector movement is not directly performed along φ and β of the sample coordinate system (right-handed axes 1′, 2′, 3′), since the primary beam is fixed in space and the sample has to be rotated around axis 2′ to account for α_i. This rotation is the transformation between the sample system and the *laboratory coordinate system* (axes 1, 2, 3) with spherical coordinates ν and δ, which are the independent directions of detector movement. This type of setup is referred to as *2+2 type diffractometer* [122]; the two coordinate systems are illustrated in Fig. 3.3.

Since the map is recorded as tuples (ν, δ), a transformation to the sample coordinate system becomes necessary. Points $\vec{r} = (x, y, z)$ in the laboratory system are transformed into the sample system $\vec{r'} = (x', y', z')$ using the spherical coordinates:

$$\begin{aligned} x' &= \cos\varphi \ \cos\beta, \\ y' &= \sin\varphi \ \cos\beta, \\ z' &= \sin\beta, \end{aligned}$$

[2]Note that since the experiment is performed under fixed α_i no specular XRD scan can be carried out by simply scanning along β at $\varphi = 0$.

[3]This different notation is used to outline the difference between general considerations and specific experimental circumstances.

by a rotation of the system around the common axis 2 by the angle $-\alpha_i$ under the use of the transformation operation

$$\vec{r} = \mathbf{R}_2^{-\alpha_i}\ \vec{r}\,', \tag{3.8}$$

where $\mathbf{R}_2^{-\alpha_i}$ denotes the rotation matrix

$$\mathbf{R}_2^{-\alpha_i} = \begin{pmatrix} \cos\alpha_i & 0 & -\sin\alpha_i \\ 0 & 1 & 0 \\ \sin\alpha_i & 0 & \cos\alpha_i \end{pmatrix}. \tag{3.9}$$

This yields the spherical coordinates in the laboratory system:

$$\begin{aligned} \nu &= \arctan\left(\frac{r_2}{r_1}\right) = \arctan\left(\frac{\cos\beta\ \sin\varphi}{\cos\alpha_i\ \cos\beta\ \cos\varphi - \sin\alpha_i\ \sin\beta}\right), \qquad (3.10) \\ \delta &= \arctan\left(\frac{r_3}{\sqrt{r_1^2 + r_2^2}}\right), \\ &= \arctan\left(\frac{\cos\alpha_i\ \sin\beta + \sin\alpha_i\ \cos\beta\ \cos\varphi}{\sqrt{\cos\beta^2\ \sin\varphi^2 + (\cos\alpha_i\ \cos\beta\ \cos\varphi - \sin\alpha_i\ \sin\beta)^2}}\right), \end{aligned}$$

and for the reversed transformation:

$$\begin{aligned} \varphi &= \arctan\left(\frac{r_2'}{r_1'}\right) = \arctan\left(\frac{\cos\delta\sin\nu}{\cos\alpha_i\ \cos\delta\ \cos\nu + \sin\alpha_i\ \sin\delta}\right), \qquad (3.11) \\ \beta &= \arctan\left(\frac{r_3'}{\sqrt{r_1'^2 + r_2'^2}}\right), \\ &= \arctan\left(\frac{\cos\alpha_i\ \sin\delta - \sin\alpha_i\ \cos\delta\ \cos\nu}{\sqrt{\cos\delta^2\ \sin\nu^2 + (\cos\alpha_i\ \cos\delta\ \cos\nu + \sin\alpha_i\ \sin\delta)^2}}\right). \end{aligned}$$

Closed circular paths of constant $\beta < 90°$ in the sample system with φ from 0 to 360° are *small circles* on the sphere and equal paths of constant momentum transfer perpendicular to the sample $q_\perp$ (as necessary for GID scans).

To derive the coordinates of the scattering vector $\vec{q}$ (defined in the sample system) from a given set of detector angles (ν, δ) the wave vector of the primary beam $\vec{k_i} = \frac{2\pi}{\lambda}\vec{e_1}$, which lies on axis 1 of the laboratory system (Fig. 3.3b) has to be transformed into the sample system, which is again performed via the rotation around the common axis 2 using the transformation

$$\vec{k}_i = \frac{2\pi}{\lambda}\ \mathbf{R}_2^{-\alpha_i}\vec{e}_1. \tag{3.12}$$

Analogously, the representation of the scattered vector $\vec{k}_f$ can be obtained in a similar way by subsequent rotations of the system by the two angles ν and δ (Fig. 3.3a) according to

$$\vec{k}_f = \frac{2\pi}{\lambda} (\mathbf{R}_2^{-\alpha_i} \cdot (\mathbf{R}_2^{\delta} \cdot (\mathbf{R}_3^{-\nu} \vec{e}_1))), \tag{3.13}$$

which finally yields, together with the general relation $\vec{q} = \vec{k}_f - \vec{k}_i$, the expression of the components of the scattering vector in dependence of the coordinates of the laboratory system:

$$\begin{aligned} q_{\parallel} &= \frac{2\pi}{\lambda}\sqrt{\sin^2\nu + (\cos\nu\cos\alpha_i\cos\delta + \cos\nu\sin\alpha_i\sin\delta - \cos\alpha_i)^2}, \\ q_{\perp} &= \frac{2\pi}{\lambda}(\sin\alpha_i - \cos\nu\cos\delta\sin\alpha_i + \cos\nu\cos\alpha_i\sin\delta), \end{aligned} \tag{3.14}$$

which is necessary for the correct representation of maps in reciprocal space if recorded with the specific type of goniometer.

However, a further step is necessary to fully evaluate reciprocal space maps [123]. The position of a certain reflection (hkl) in terms of $(q_{\parallel}, q_{\perp})$ has to be derived in order to compare it with a measured reflection. For the general case of a triclinic coordinate system this is preferentially performed in an orthogonal representation, which is achieved through the use of the transformation matrix [122, 124, 125]

$$\mathbf{B} = \begin{pmatrix} a^* & b^*\cos\gamma^* & c^*\cos\beta^* \\ 0 & b^*\sin\gamma^* & -c^*\cos\alpha\sin\beta^* \\ 0 & 0 & \frac{2\pi}{c} \end{pmatrix} \tag{3.15}$$

with the transformation

$$\vec{H}_{hkl} = \mathbf{B} \cdot \hat{\vec{H}}_{hkl}, \tag{3.16}$$

where $\hat{\vec{H}}_{hkl}$ is a reciprocal lattice vector in the crystal coordinate system, $\vec{H}_{hkl}$ is its orthogonal representation and a^*, b^*, c^*, α^*, β^*, γ^* are the reciprocal unit cell parameters obtained by inversion of the metric tensor (Equ. 2.7). To correlate a certain reflection with a measured reciprocal space map it is mandatory to orient the reciprocal lattice in a well defined way, *e.g.*, with its fiber axis $\vec{G}_{hkl}$ (as orientation vector) along the axis $3'$. This is done via two rotations around axes $1'$ and $2'$ by angles ψ and χ:

$$\psi = \arctan\left(\frac{G_{hkl}}{G_{hkl,1}}\right), \tag{3.17}$$

$$\chi = \arctan\left(\frac{G_{hkl,3}}{\sqrt{G_{hkl,1}^2 + G_{hkl,2}^2 + G_{hkl,3}^2}}\right), \tag{3.18}$$

where $G_{hkl,1}$, $G_{hkl,2}$ and $G_{hkl,3}$ denote the components of the *orientation vector* $\vec{G}_{hkl}$. The orthogonalized reciprocal vector $\vec{H}_{hkl}$ can be used to derive the scattering vector via Bragg's law:

$$\vec{q} = \begin{pmatrix} \cos\chi & 0 & \sin\chi \\ 0 & 1 & 0 \\ -\sin\chi & 0 & \cos\chi \end{pmatrix} \cdot \begin{pmatrix} \cos\psi & \sin\psi & 0 \\ -\sin\psi & \cos\psi & 0 \\ 0 & 0 & 1 \end{pmatrix} \cdot \vec{H}_{hkl}, \quad (3.19)$$

which directly yields $(q_{\parallel}, q_{\perp})$ as a function of the indices h, k, l via the general expressions $q_{\parallel} = (q_1^2 + q_2^2)^{\frac{1}{2}}$ and $q_{\perp} = |q_3|$. This formalism has been implemented within the scope of this work into a software package *Recmap* using the 4^{th} generation programming language *IDL* from *ITT Visual Information Solutions*, which is based on *Stereopole* [125]. It allows one to graphically compare measured to calculated reflections within reciprocal space maps and was used to analyze and process the maps presented in this work.

All x-ray diffraction experiments were carried out at the beamline W1 of the synchrotron radiation source HASYLAB, for a detailed description of the beamline and the diffractometer see Sec. 4.2.1.

3.2 Ultraviolet photoelectron spectroscopy

Photoelectron spectroscopy (PES) is *the* established experimental tool for the investigation of electronic properties of COMs and interfacial energetics [50, 54, 57, 62, 126, 127]. The basic concepts have been addressed in detail in various textbooks and review articles [128–130] and will be summarized to the needed extent in the following. The basic phenomenon of photoemission was already reported in 1887 by H. Hertz [131] and explained by A. Einstein in 1905 by postulating the quantum nature of light [132], where the basic equation of photoemission is:

$$E_{kin} = h\nu - \phi_s, \quad (3.20)$$

where E_{kin} is the kinetic energy of the photo-electrons, ν the frequency of the incident (monochromatic) light and ϕ_s the work function of a (metallic) sample.

Ultraviolet photoelectron spectroscopy (UPS), *i.e.*, photoelectron spectroscopy using ultraviolet light mostly in the *vacuum-ultraviolet* (VUV) region (6.20 - 124 eV according to ISO-DIS-21348), is a highly surface sensitive tool and the information depth can be quantified with the *electron escape depth*, which is depending on the kinetic energy of the photoelectrons and therefore on the incident light frequency in a photoemission experiment via

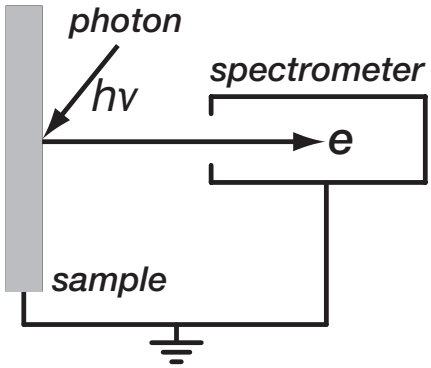

Figure 3.4: The principle of a photoemission experiment: The sample is irradiated with monochromatic light in the VUV region (UPS), electrons are ejected out from the sample via the photoelectric effect and the electron energy distribution is measured with a spectrometer. Sample and spectrometer are interconnected hence aligning their Fermi levels in thermodynamic equilibrium.

Equ. 3.20. In the energy range used for the present UPS investigations of around 20 eV the information depth is in the range of a few Å and is therefore in the typical monolayer range of organic molecules. This high surface sensitivity allows one to access information on the coverage and it even allows one to reliably estimate the growth mode (see Sec. 2.1.2) of organic adsorbates: If the substrate (or underlayer) features within UPS spectra are not attenuated in the range of nominal monolayer coverage, three dimensional growth can be concluded. Photoelectron spectroscopy using soft x-rays is denoted as *x-ray photoelectron spectroscopy* (XPS) and exhibits a significantly larger information depth of typically a few organic layers therefore allowing for depth profiling of thin films. Moreover, the reversed process of PES, where electrons of defined energy impinge on the sample, denoted as *inverse photoelectron spectroscopy* (IPES), can be used to investigate *unoccupied states* by the detection of the bremsstrahlung from the decelerated electrons.

A typical PES spectrum of an organic semiconductor is depicted in Fig. 3.5, where the ranges accessible by UPS, XPS and IPES are indicated. Since XPS and IPES were not performed in this work the discussion will be restricted to UPS in the following. In the *valence electron region* emission from the individual molecular levels appear in UPS, which allows one to derive the hole injection barrier $\Delta_h = E_F^{kin} - E_{homo}^{kin}$ from the difference in kinetic energy between the *electrons emitted from the Fermi level* E_F^{kin} of a metal substrate and the HOMO emission onset E_{homo}^{kin}. At low kinetic energies (close to zero) the spectrum is dominated by secondary electrons, *i.e.*, electrons that have been inelastically scattered during the escape process. Below the energy of the *secondary electron cutoff* (SECO) the electrons have insufficient kinetic energy to escape from the sample. In the *elastic case* the kinetic energy of a photoelectron emitted from a state with *binding energy* E_B is given in

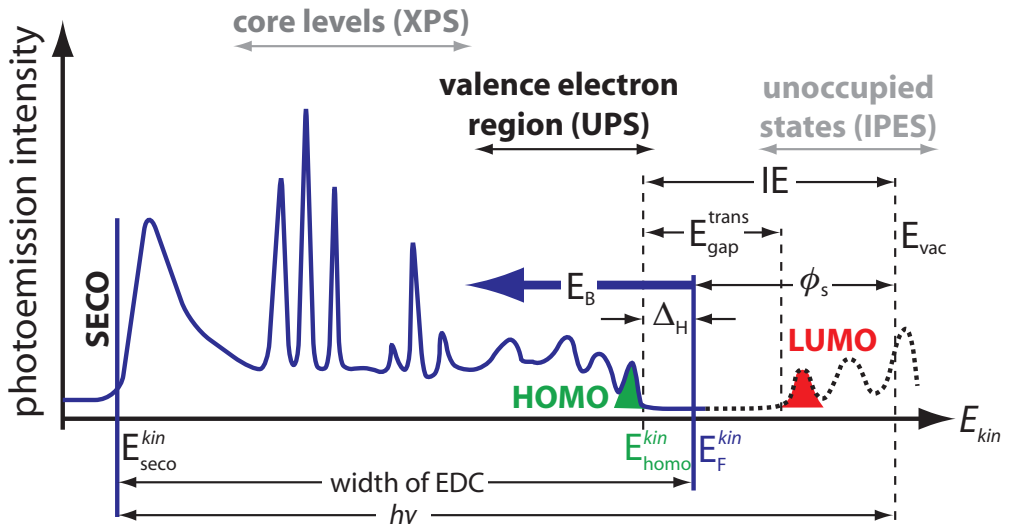

Figure 3.5: Schematic of a typical spectrum of photoemission intensity vs. photoelectron kinetic energy (E_{kin}) of an organic semiconductor as measured by PES. E_B denotes the binding energy measured from the Fermi energy E_F^{kin}, ϕ_s the sample work function, E_{vac} the vacuum level, E_{gap}^{trans} the transport gap of the semiconductor, Δ_h the hole injection barrier, E_{seco}^{kin} and E_{homo}^{kin} the kinetic energetic positions of the SECO and the HOMO level, respectively.

analogy to Equ. 3.20 by

$$E_{kin} = h\nu - \phi_s - E_B, \tag{3.21}$$

where E_B is defined *relative* to the Fermi energy E_F. The value of the sample work function can be deduced from the width of the *energy distribution curve* (EDC), which is defined as the difference in kinetic energy between E_F^{kin} and the *kinetic energy of the SECO* (E_{seco}^{kin}), *i.e.*,

$$\phi_s = h\nu - (E_F^{kin} - E_{seco}^{kin}). \tag{3.22}$$

As outlined in Sec. 2.1.4 the *ionization energy* IE is an important parameter of organic materials, which can be derived in analogy to ϕ_s (see Fig. 3.5) via

$$IE = h\nu - (E_{homo}^{kin} - E_{seco}^{kin}). \tag{3.23}$$

Note that the measurement of E_{seco}^{kin} is usually performed with a defined bias voltage U_{bias} applied to the sample for E_{seco}^{kin} to appear at $E_{kin} > 0$. Moreover, in most cases the work function of the spectrometer ϕ_{spec} will be different from ϕ_s, *i.e.*, for $\phi_{diff} = \phi_s - \phi_{spec} < 0$ the SECO position would

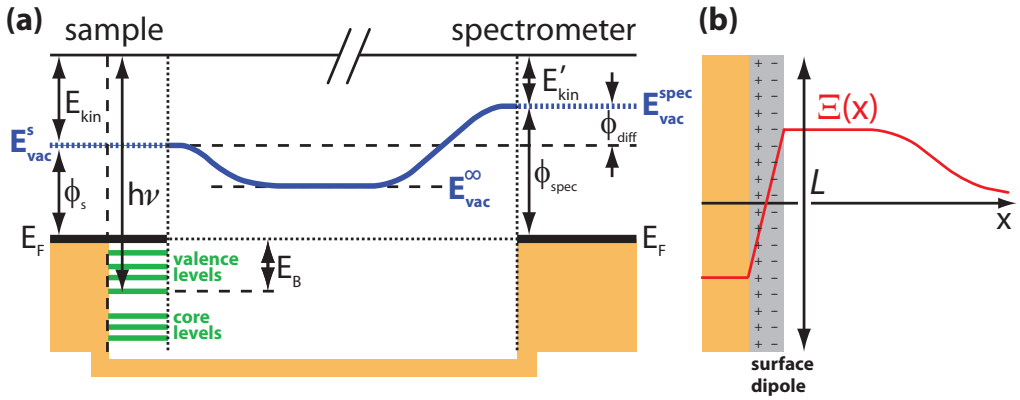

Figure 3.6: (a) Schematic energy level diagram for the interconnected sample and spectrometer in a PES experiment demonstrating the vacuum level characteristics and the influence of the spectrometer work function ϕ_{spec} [127].(b) Electrostatic potential $\Xi(x)$ in the vicinity of a dipole layer of extension L.

be experimentally inaccessible without biasing the sample. With an applied bias the SECO position consequently is given by $E_{seco}^{kin} = \phi_{diff} + eU_{bias}$. Since the Fermi levels of sample and detector are aligned in thermodynamic equilibrium (Fig. 3.4) the *kinetic* energy value of the Fermi energy is given by $E_F^{kin} = h\nu - \phi_{spec} + eU_{bias}$ finally leading with the expression for E_{seco} to Equ. 3.22.

The influence of the spectrometer work function ϕ_{spec} on the kinetic energy is illustrated in Fig. 3.6a: Due to $\phi_s \neq \phi_{spec}$ the kinetic energy of a photoelectron emitted from a level with binding energy E_B measured with the spectrometer is given by $E'_{kin} = E_{kin} - \phi_{diff} = h\nu - E_B - \phi_{spec}$. Therefore E_B can be determined independent from the specific sample work function with ϕ_{spec} being constant for a given experimental setup[4]. The vacuum levels in the proximate vicinity of sample and spectrometer have well defined values of E_{vac}^s and E_{vac}^{spec} that are experimentally accessible via ϕ_s and ϕ_{spec}. This vacuum level *just outside* of the medium cannot serve as *invariant* reference level as it is well established for metals exhibiting different work functions depending on the crystal face, with therefore different vacuum levels converging to a common value E_{vac}^{∞} (Fig. 3.6a) at infinite distance [50, 57, 133]. The difference in the work function of different metal crystal faces is mostly due to different surface dipoles by electrons spilling out into the vacuum, as explained in Sec. 2.1.3. Such dipoles impact the vacuum level, which will be made use of in Sec. 5.3 in terms of intrinsic dipoles present in PEN and PFP.

[4]Note that E_B is *practically* determined via its definition as kinetic energy difference from E_F.

This surface dipole with a given lateral extension L raises the electrostatic potential $\Xi(x)$ that stays essentially constant for distances $x \ll L$ away from the sample, since the dipole can be regarded as infinitely extended in good approximation (Fig. 3.6b). For distances $x \gg L$ the value of $\Xi(x)$ decreases $\sim x^2$ as the dipole can be regarded as point dipole in good approximation converging to an essentially constant value at infinite distance, as do E^s_{vac} and E^{spec}_{vac} to E^{∞}_{vac} (Fig. 3.6a). It shall be emphasized that the value of E^{∞}_{vac} is experimentally *inaccessible* since the measured kinetic energy E'_{kin} only depends on the potential difference.

The detailed treatment of the photoionization process as transition from a N to a $N-1$ electron system must comprise initial and final state, since the photo-hole interacts with the electronic structure of the sample. The transition probability w for an electron in the process of photoexcitation is given in the dipole approximation (where the radiation wavelength is large compared to the excited volume) by *Fermi's Golden Rule* [128]:

$$w \propto \frac{2\pi}{\hbar} |\langle \Psi_f | H | \Psi_i \rangle|^2 \delta(E_f - E_i - h\nu), \tag{3.24}$$

where Ψ_f is the final state and Ψ_i the initial state wave function, H is the Hamilton operator, E_f and E_i are energies of final and initial states, and $\langle \Psi_f | H | \Psi_i \rangle$ is the transition matrix element, respectively. In the simplest approximation it can be derived to

$$\langle \Psi_f | H | \Psi_i \rangle = \langle \phi_{f,E_{kin}} | H | \phi_{i,k} \rangle \langle \Psi^k_{f,R}(N-1) | \Psi^k_{i,R}(N-1) \rangle, \tag{3.25}$$

where $\phi_{f,E_{kin}}$ denotes the wave function of the emitted electron, $\phi_{i,k}$ the wave function of the initial orbital k and $\Psi^k_{i,R}(N-1)$ and $\Psi^k_{f,R}(N-1)$ the wave functions of remaining (R) initial and final state electrons, respectively. Herein, the wave function of the initial state was expressed as $\Psi_i(N) = C\phi_{i,k}\Psi^k_{i,R}(N-1)$ and the wave function of the final state as $\Psi_f(N) = C\phi_{f,E_{kin}}\Psi^k_{f,R}(N-1)$, where C is an anti-symmetrizing operator [128]. Neglecting the impact of the ionization process on the wave function of the remaining electrons, which is referred to as *Koopmans' theorem* [134], this equation can be solved and the measured binding energy corresponds to the binding energy of the undisturbed system. However, final state effects cannot be neglected and particularly the screening of the photo-hole by the surrounding medium leads to reduction of the Coulomb attraction[5] between electron and hole. This effect is most important for highly polarizable media

[5]Note that the effect of attraction between electron and hole *generally* impacts the measured value of E_{kin}.

like metals and consequently also an issue in thin organic films on metal substrates, where the emission from energy levels of multilayers are measured at lower E_{kin} than the energy levels of (sub-)monolayers, which has to be taken into account for an adequate interpretation of PES results [54, 57, 135].

3.3 Vibrational spectroscopy

Prevalently throughout this work the structural investigations by means of XRD have been corroborated with vibrational spectroscopy, where *Fourier-transform infrared spectroscopy* (FT-IR) was applied in transmission geometry. In general, infrared spectroscopy allows one to access information on the vibrational behaviour of chemical bonds and on intermolecular interactions using the wavelength-dependent attenuation of a transmitted (or reflected) infrared beam: If the incident infrared energy equals the vibrational energy of a certain intramolecular bond, vibration energy can be resonantly absorbed from the incident beam, which is detected with an infrared spectrometer [27, 136–138]. The number f of degrees of freedom of a molecule comprising N atoms is $f = 3N - 6$, since each atom can perform translation in three directions of space for the translation (3N), minus three combined movements of translation of the *whole* molecule and three for its rotation around the mass center[6]. It is evident that molecules in solid state as in the thin organic films investigated in this work only exhibit vibrational degrees of freedom. For both, rotation and vibration to be active in the infrared, a change of the dipole moment of the molecule must occur according to the selection rule for dipole radiation [27].

In a *dispersive* infrared spectrometer a prism or grating is used to geometrically disperse the infrared radiation to a scanning slit/photodiode combination. The slit isolates a certain frequency range for a certain integration time, which finally yields the infrared absorption spectrum. Obviously, using this kind of setup most of the radiation remains undetected at a time, which leads to long accumulation times in this type of spectrometer. Significant progress was achieved by using interferometric methods in spectroscopy, where the *whole* spectrum can be recorded all of the time. The FT-IR spectrometer comprising a Michelson interferometer (Fig. 3.7) is such a device, which is based on the interference of two beams from a common source, that are produced by a beam splitter [136, 138]. The two partial beams are both reflected at mirrors and the intensity of the reunited beam is depending on the path difference between the beams, therefore giving a maximum, if the

[6]Note that for linear molecules $f = 3N - 5$, since the rotation around the long axis does not lead to a movement of the atoms.

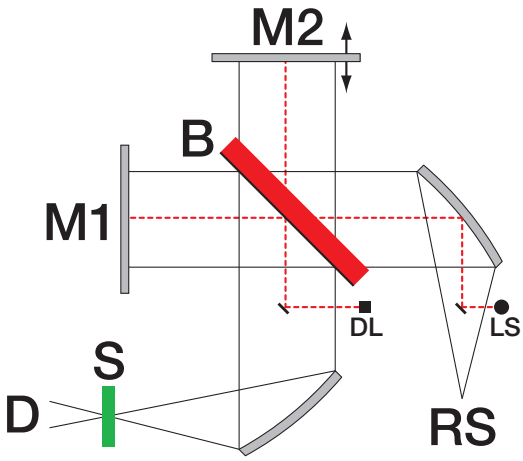

Figure 3.7: Schematic view of the optical path in a FT-IR spectrometer comprising a radiation source (RS), a detector (D), a sample (S) measured in transmission and a Michelson interferometer with a beam splitter (B), a fixed (M1) and a moving mirror (M2). The beam path drawn in dotted red is the path of the calibration laser with source (LS) and detector (DL).

beams add coherently. One of the two mirrors is moved and the signal at the detector therefore becomes a function of mirror displacement. This detector function containing all information on the incident spectrum, which is denoted as the *interferogram*, is given for a *monochromatic* source by [136]:

$$I(x) = 2RTI(\nu)(1 + \cos 2\pi\nu x), \tag{3.26}$$

where R is the reflectance of the beam splitter, T its transmittance, $I(\nu)$ the incident intensity at frequency ν and x the path difference. The interference of monochromatic light is used in the FT-IR spectrometer as reference signal by means of a He-Ne laser with the same beam path through the interferometer as the infrared light (see Fig. 3.7). The zero crossings of the cosine function in Equ. 3.26 of the laser interferogram serve as trigger for the sampling of the infrared interferogram at therefore fixed values of x. Moreover, it allows one to accurately set the point of zero path difference of the polychromatic infrared light source (like the *globar source* used in the present measurements), which is denoted as *center burst* exhibiting maximal intensity at the detector. For this general case of a *polychromatic* source $A(\nu)$, the interferogram is given by:

$$I(x) = \int_0^\infty A(\nu)(1 + \cos 2\pi\nu x)d\nu, \tag{3.27}$$

and taking into account the extreme values for zero path difference ($I(0) = 2\int_0^\infty A(\nu)d\nu$) and large path difference ($I(\infty) = I(0)/2$) for the Michelson interferometer, the interferogram can be written as:

$$F(x) = I(x) - I(\infty) = \int_0^\infty A(\nu)\cos(2\pi\nu x)d\nu. \tag{3.28}$$

The interferogram can be inverted[7] using the theory of Fourier transformation and therefore can the spectrum of the polychromatic source be regained:

$$A(\nu) = 2 \int_0^\infty F(x) \cos(2\pi\nu x) dx, \tag{3.29}$$

which allows one to extract the information on frequency-dependent absorption by a given sample through comparison with a reference scan of the free beam path. Hence, if the reference scan is performed on the substrate used for thin film investigations, the absorption solely from the thin film is being recorded.

Within the FT-IR investigations on thin organic films presented in this work a splitting D of vibrational modes was observed, which is usually referred to as *Davydov splitting* [13, 140, 141]. It occurs if molecules of nonequivalent orientations are present in the unit cell of the crystal, as it is for instance the case in the herringbone structure (see Fig. 2.1). In this case, vibrational states of individual molecules can split into differently polarized normal vibrations [142]. The theoretical treatment in the simplest approximation, which however was reported to reproduce experimental data considerably well [140], this splitting is treated as exclusively based on the interaction between the dipoles and is therefore proportional to the dipole-dipole interaction potential V_{dd}:

$$D \propto V_{dd} = \frac{1}{4\pi\varepsilon_0} \frac{\vec{p_1}\vec{p_2} - 3(\vec{p_1}\vec{e_r})(\vec{p_2}\vec{e_r})}{r^3}, \tag{3.30}$$

where $\vec{p_1}$ and $\vec{p_2}$ are the vibration-related dynamic dipole moments and $\vec{e_r} = \vec{r}/r$ is the unit vector of the inter-dipolar distance r. In the investigation of phase separation in co-deposited thin films the disappearance of Davydov splitting, if present in the pure film, can provide evidence for the intercalation of the compounds (see Sec. 5.2).

3.4 Atomic force microscopy

Shortly after the invention of the Scanning Tunneling Microscopy (STM) [143], which allowed for the first time to resolve features of *conducting* samples on an atomic scale, the *Atomic Force Microscope* (AFM) was introduced [144]. Its basic concept is to measure the force between a sharp tip on a flexible cantilever and the surface of a sample. In principle, the deflection of the

[7] The practical computation of transformation is carried out via the *Fast Fourier Transform* (FFT) [139] allowing to reduce the computational efforts dramatically.

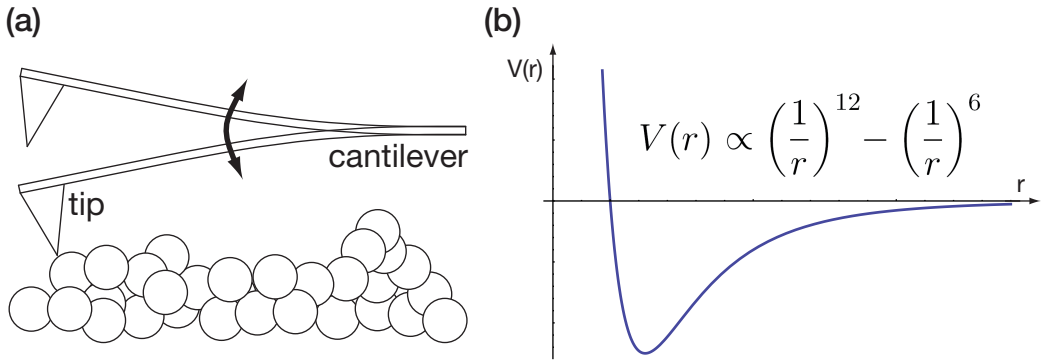

Figure 3.8: (a) Schematic view of the basic principle of tapping mode AFM. The oscillating cantilever is moved horizontally and vertically by piezo elements. (b) The Lennard-Jones potential.

cantilever is the measurement signal from which the morphology of the surface is deduced by linewise scanning. Most often (and in the instrument used for the measurements presented in this work) the bending of the cantilever is measured *optically* with the aid of a laser beam reflected from the cantilever into a position-sensitive (four-segment) photodiode [145, 146]. There exist a large number of different techniques based on this basic principle, which differ by the specific measurement signal. All AFM images presented in this work were recorded using *tapping mode AFM* [147, 148], which is based on a cantilever that initially oscillates free near its resonant frequency with an amplitude typically in the range of tens of nanometers (schematic see Fig. 3.8a). This method relies on the change of the free oscillation amplitude of the cantilever due to the tapping of the surface with the tip: The device comprises a feedback system, which detects the perturbation of the oscillation amplitude upon approach and contact with the sample. Driven by piezo crystals, the cantilever laterally scans the sample and a varying morphology on the scan path leads to varying tip-sample interactions, which modify the oscillation amplitude of the cantilever away from a given setpoint. This variation is used to vertically adjust the tip-sample distance to regain the setpoint value of the amplitude via the feedback system, which finally generates a topographic image of the sample; the basic principle is illustrated in Fig. 3.8a. In contrast to *contact mode AFM*, where the tip is in continuous contact with the sample, tapping mode highly reduces the lateral forces on the sample, and the vertical forces can be held low to induce only small and reversible deformations, while the resolution is mainly limited by the tip radius [147].

As outlined in Sec. 2.1.3 the interaction between electrically neutral atoms can be well described with the Lennard-Jones potential (Equ. 2.1) comprising

an attractive (van der Waals) term $\sim r^{-6}$ and a repulsive part $\sim r^{-12}$, *i.e.*, for large distances the potential is attractive and upon decreasing distance it turns repulsive at a certain point (see Fig. 3.8b). However, to describe the interaction between complex structures like the tip and the sample in AFM investigations, the van der Waals attraction must be treated using more advanced expressions for the interaction by taking into account the macroscopic nature of tip and sample [145]: The sample is modelled as flat continuum with a certain atomic density yielding (via the so-called Hamaker integration) an attractive potential term $\sim r^{-3}$ for a (tip-) atom at vertical distance r above the surface, from which various expressions for different tip shapes can be derived [149–151]. Moreover there exists a large variety of further tip-surface interactions depending on the respective materials: Electrostatic forces, magnetic forces and capillary forces due to a water meniscus formed between tip and surface upon measurements in ambient air [152].

An operation mode of the tapping mode AFM that allows one to access information beyond the sample morphology is *AFM phase imaging*, which has been used in the study presented in Sec. 5.1 to discriminate different chemical compounds (Fig. 5.6). In AFM phase imaging, the phase difference between the cantilever excitation and its oscillation is monitored in addition to the topography data. The recorded phase lag is very sensitive to variations of material properties like the elastic properties of the surface and can serve as valuable qualitative tool to map local stiffness variations on the sample surface [145, 153].

An important parameter that can be deduced from AFM micrographs is the *surface roughness*, which quantifies height variations of a given surface. It is most often expressed in terms of the *root mean square (rms) roughness*, *i.e.*, by the standard deviation of the data:

$$\sigma_{rms} = \sqrt{\frac{1}{N}\sum_{j=1}^{N}(z_j - \overline{z})^2}, \tag{3.31}$$

where z_j is the height value of pixel j of the surface z=z(x,y) in an AFM micrograph consisting of N pixels, and $\overline{z} = \frac{1}{N}\sum_{j=1}^{N} z_j$ is the mean height [154]. For a correct determination of σ_{rms} the AFM micrographs have to be base-plane corrected prior to the calculation to account for non-linearities of the piezo motors of the instrument.

Chapter 4

Materials and Experimental Setups

In the following chapter the investigated molecular systems and the substrates used in this work are introduced and details of the experimental setups described in Sec. 3 are given.

4.1 Materials

In the following, a short outline of the fundamental properties of the organic materials used in this work is given. The chemical structures of the organic compounds are given in Fig. 4.1 and their empirical formulae as well as the respective manufacturers, where the materials were purchased are listed in Tab. 4.1.

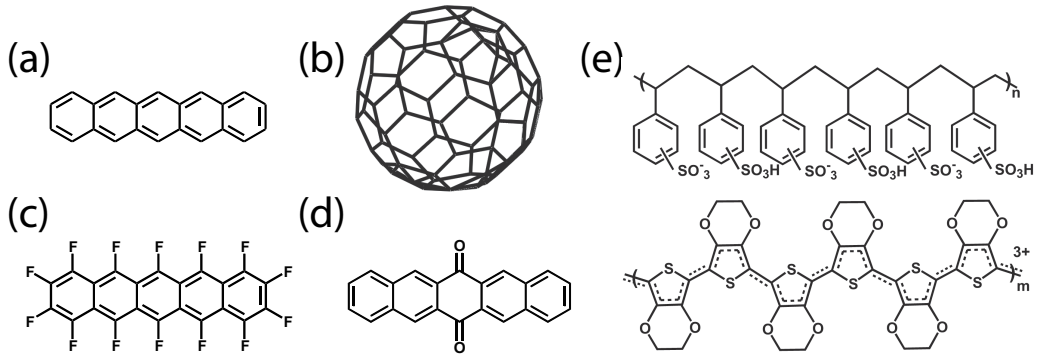

Figure 4.1: Chemical structure of the molecules investigated in this work: (a) PEN ($C_{22}H_{14}$), (b) C60 (C_{60}), (c) PFP ($C_{22}F_{14}$), (d) PQ ($C_{22}O_2H_{12}$) and (e) PEDOT:PSS; for more details see Table 4.1.

Pentacene (PEN) (Fig. 4.1a) is one of the most thoroughly investigated conjugated organic molecules in the context of organic electronics. It can be regarded as *the* benchmark material in applications in novel electronic devices due to its high charge carrier mobility (μ_{FET}) for holes of up $5.5\,\mathrm{cm^2V^{-1}s^{-1}}$ in OFETs (which is almost comparable to amorphous silicon) [12, 155–162]. In contrast to this strikingly high hole mobility, the electron mobility reported so far was only $0.04\,\mathrm{cm^2V^{-1}s^{-1}}$ [163]. The structural and energetic properties of its functional heterojunctions (*e.g.*, as active layer in OPVCs) are the main focus of this work.

Fullerene (C60) is the spherical configuration of carbon consisting of 12 pentagons and 20 hexagons ("soccer ball configuration" [164]) and is among the most prominent organic n-type semiconductors and is widely used in the field of organic electronics (Fig. 4.1b) [51, 165, 166]. In its crystalline state (*e.g.*, on a PEN buffer layer) it was reported to exhibit a field-effect mobility for electrons of up to $4.9\,\mathrm{cm^2V^{-1}s^{-1}}$, which is the highest value for COMs reported so far [165]. Furthermore, in combination with PEN, C60 was reported to form an efficient heterojunction in organic photovoltaic cells based on *layered* thin organic films [18, 20, 22].

In order to successfully design complementary circuits in organic electronics, *i.e.*, switch organic thin film transistors with either positive or negative gate voltages, there is a particular need for efficient electron conducting (n-type) materials. Moreover, substituting organic molecules with electron-withdrawing side groups (*e.g.*, by adding fluorine or oxygen to known p-type cores) may stabilize the anionic form of the molecules and enable efficient electron conduction [167]. The impact of the complete fluorination of PEN to perfluoropentacene (PFP) (Fig. 4.1c) [23–25, 168–171] represents a further central part of this work (Sec. 5.2 and 5.3). PFP can be regarded as very promising n-type material, since it was reported to exhibit an electron mobility of $0.22\,\mathrm{cm^2V^{-1}s^{-1}}$ in OFETs, and it appears to be particularly well-suited for OFET design due to its crystalline growth behaviour on SiO_x, which is generally used as gate dielectric in OFETs [23–25] (see Sec. 5.2 and 5.3).

An oxidized modification of PEN with two oxygen atoms doubly-bond to the center carbon atoms of the PEN backbone is 6,13-pentacenequinone (PQ) (see Fig. 4.1d). Its electronic structure, structural arrangement and its interplay with PEN in PEN/PQ heterostructures is thoroughly investigated in this work (see Sec. 5.4, 5.5 and 5.7), since PQ may serve as n-type OSC in OPVCs as found from the energy level alignment with PEN presented in Sec. 5.4. Moreover, high chemical purity of PEN films and crystals was reported to be an important prerequisite for efficient applications in literature, since impurities have a tremendous impact on the charge carrier mobility. It was reported that the presence of (PQ as oxidized PEN derivative) leads to

a significant reduction of the charge carrier mobility in PEN single crystals at concentrations as low as 0.68% [77].

Intrinsically conducting polymers (ICPs) are commonly used as electrodes in organic electronics. Nowadays, the most widely used ICP is poly(3,4-ethylenedioxythiophene)/ poly- (styrenesulfonate) (PEDOT:PSS) (Fig. 4.1e) exhibiting relatively high work function values of 4.8 to 5.7 eV, depending on the formulation and the preparation parameters [172], which makes it highly suitable as hole-injection layer in devices [173]. Within this work, commercially available PEDOT:PSS in the PEDOT to PSS weight ratio of 1:20 (brand name Baytron P CH8000) was used as electrode and substrate in the investigations of photovoltaic cells based on PEN and C60 heterostructures.

Table 4.1: List of molecular acronyms, empirical formulae, names and sources of the organic compounds investigated in this work.

Acronym	**Empirical formula**	**Name**	**Source**
PEN	$C_{22}H_{14}$	pentacene	Sigma-Aldrich
C60	C_{60}	carbon-60 (Buckminsterfullerene)	Sigma-Aldrich
PFP	$C_{22}F_{14}$	perfluoropentacene	Kanto Denka Kogyo Co., Ltd.
PQ	$C_{22}O_2H_{12}$	6,13-pentacenequinone	Sigma-Aldrich
PEDOT:PSS		poly(3,4-ethylenedioxythiophene)/ poly(styrenesulfonate)	H. C. Starck

4.2 Experimental setups

In this section the experimental setups used within this work and the experimental procedures are described.

4.2.1 X-ray diffraction at HASYLAB W1

All x-ray diffraction experiments presented in this work were carried out at the beamline W1 of the synchrotron radiation source HASYLAB (Hamburg, Germany) that is based on the positron storage ring DORIS III, which exhibits a circumference of 289 m, a positron energy of 4.45 GeV and an initial beam current of 120 mA. For the beamline W1, a 16-period wiggler is used as insertion device with a sample to source distance of 46 m. The beam is

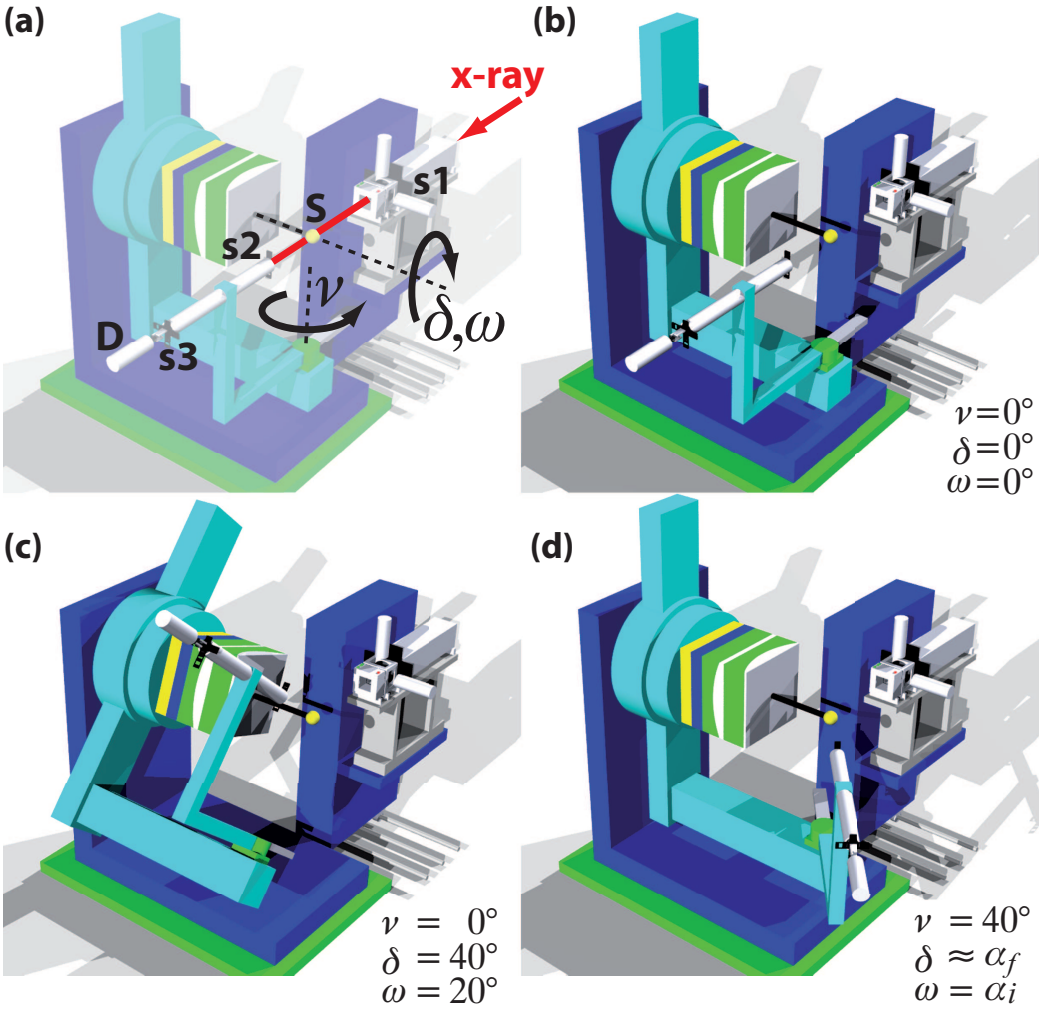

Figure 4.2: (a) Outline of the diffractometer at the beamline W1 at HASYLAB illustrating the primary rotation axes for the sample (S) rotation by an angle ω and for the detector movement by angles ν, δ as defined in Sec. 3.1.2. The x-ray beam is passed through a primary (s1) and secondary (s2), (s3) slit system. (b) The detector directly in the primary beam defining $\nu = \delta = 0$. (c) The diffractometer during a specular scan ($\nu = 0$) with $\delta = 40°$ ($= 2\Theta$) and $\omega = 20°$ ($= \Theta$). (d) The diffractometer during a GID scan with ω defining α_i, the horizontal detector angle ν set to 40° and angle δ being set slightly above the surface horizon. The detector angles ν, δ can be transformed into the angles of the sample system φ, β, *i.e.*, to the sample in-plane angle and α_f, by Equ. 3.11. For recording reciprocal space maps the detector scans linewise along ν at stepwise increasing δ for a fixed value of $\alpha_i = 0.15°$.

monochromatized using a Si(111) single crystal monochromator and the (focused) beam size at the sample position is $1.6 \times 4\,\mathrm{mm}^2$ (flux: $\approx 2 \times 10^{11}$ photons/s/mm^2). The intensity of the primary beam is measured by a monitor detector in order to correct for intensity variations of the incident beam. The energy of the x-ray beam was set to 10.5 keV ($\lambda = 0.11808\,\mathrm{nm}$) in all experiments. The beamline is equipped with a heavy-load 6-circle diffractometer (see Fig. 4.2) using a NaI(Tl)-detector. The primary beam hitting the sample is vertically and horizontally defined by a primary slit system (s1). The diffracted beam enters an evacuated flight tube (to reduce the background noise due to air scattering) through a vertically defining slit (s2) and enters the detector (D) at the end of the tube through a vertically and horizontally defining slit system (s3). For alignment, the sample can be moved vertically and horizontally and can be tilted around the axis of the primary beam. In experiments the *sample* is rotated around the (horizontal) normal of the primary beam (angle ω in Fig. 4.2a) to set the angle of beam incidence α_i. The *detector* can be moved horizontally and vertically (angles ν, δ in Fig. 4.2a) allowing for symmetric specular scans (ν=0, $\omega = 2\delta$, see Fig. 4.2c) and scans in gracing incidence geometry (see Fig. 4.2d). For GID scans, a fixed value of $\omega = \alpha_i$ below the critical angle of total external reflection α_c is set ($\alpha_i = 0.15°$ throughout this work) and the detector is moved horizontally at fixed angle β *above the sample horizon* ($\beta = 0.5°$ for the GID scans in this work). As becomes clear from Figs. 4.2 and 3.3, this movement must be performed through a simultaneous movement (calculated by the diffractometer software) of the detector by the angles ν and δ, since the laboratory and the sample coordinate system do not match in the specific device (see Fig. 3.3). Reciprocal space maps (see Fig. 3.2) are however recorded directly as function of the detector angles ν and δ: Linescans along ν at successively increased δ are performed to reduce the scan time (and transformation into φ and β is performed *a posteriori*), since the movement of both motors for each measured pixel of the map to record directly in the sample coordinate system (φ, β) is time-consuming. The beamline exhibits an autoabsorber device that automatically reduces the beam intensity if necessary, which allows to measure reflectivity curves right from $\delta = 0°$ (primary beam position). Note that an azimuthal rotation of the sample was not necessary in GID and RSM investigations within the present work, since only fiber-textured samples have been investigated. If single crystals or textured films on single crystalline substrates are investigated, the diffractometer can be equipped with an optional Eulerian cradle.

4.2.2 UPS at HASYLAB and BESSY

The UPS experiments presented in Sec. 5.1, 5.4 and 5.3 were performed at the FLIPPER II end station at the synchrotron radiation source HASYLAB (Hamburg, Germany) [174]. The experimental setup consists of four valve-separated UHV chambers allowing for sample transfer without breaking the UHV conditions. It provides a sample magazine for the storage of eight samples and a fast entry load-lock. The end-station comprises two film deposition chambers (base pressure of 2×10^{-9} mbar), which allow preparing organic/organic heterostructures (Sec. 5.4) without the danger of cross-contamination during the evaporation process. They are equipped with a quartz microbalance to monitor the nominal film thickness during film deposition. The third chamber (base pressure 1×10^{-10} mbar) is used as preparation chamber for single crystal substrates and is equipped with a heatable manipulator, an ion source for Argon ion sputtering, a quartz microbalance and three metal evaporators. The fourth chamber (base pressure 2×10^{-10} mbar), which is used for the UPS experiments, exhibits an electron analyzer and a Low-energy electron diffraction (LEED) device. The UPS spectra were recorded with a double-pass cylindrical mirror analyzer with the energy resolution set to 150 meV (measured as 80% to 20% intensity drop at a metal Fermi-edge); the photon energy was set to 22 eV. The angle between the incident synchrotron radiation and the entrance of the analyzer is built fixed to 90°. All the UPS spectra were recorded angle-integrated (analyzer acceptance angle 12° - 24° and 56° - 68°) with the angle between detector and surface normal of the sample set to 50°. The SECOs were measured with the sample biased at a voltage of -3.00 V.

The UPS experiments presented in Sec. 5.8 were performed at the end-station SurICat (beamline PM4) at the synchrotron light source BESSY (Berlin, Germany) [175]. The UHV system consists of interconnected sample preparation (base pressure: 5×10^{-9} mbar) and analysis (base pressure: 1×10^{-10} mbar) chambers. The UPS spectra were recorded with a hemispherical electron energy analyzer (Scienta SES 100) with 120 meV energy resolution using 32 eV excitation energy.

4.2.3 UHV-chamber

The samples that have been investigated in this work (except those investigated by UPS) were prepared in a custom built ultra-high vacuum (UHV) chamber that has been constructed and assembled by the author of this work; the chamber is illustrated in Fig. 4.3. It is divided into a separately pumped load-lock and main chamber, where the basic evacuation of both parts is

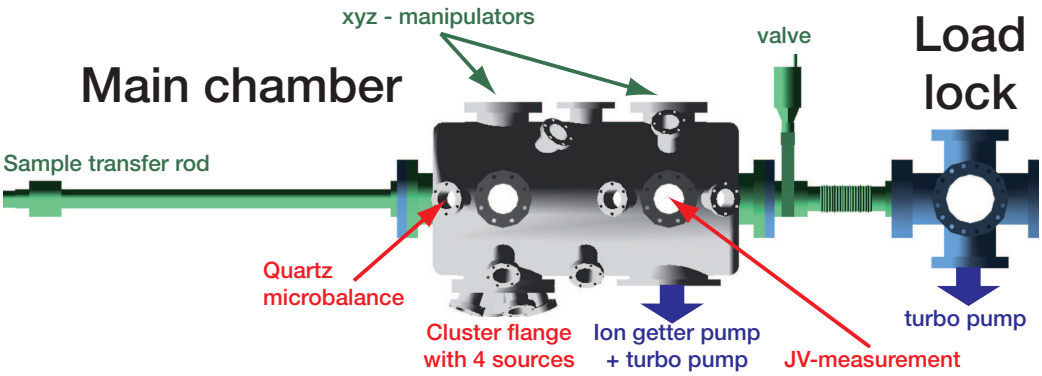

Figure 4.3: Outline of the UHV-chamber built for sample preparation and current vs. voltage characterization of OPVCs. The most important parts are labeled, illumination of the OPVCs is performed through the opposite window of the JV-measurement position.

performed with a turbo molecular pump (Varian Turbo-V301) and the main chamber can be additionally pumped with an ion getter pump (Vacion Plus 150) to maintain UHV conditions during vented load-lock conditions. The chamber was mainly used without baking (which is necessary to obtain UHV conditions) therefore reaching pressure values in the range of 5×10^{-8} mbar. The sample transfer is performed with a magnetic transporter (1 m linear + rotary motion) using the Omicron sample transfer system. The pressure is measured with a cold-cathode gauge (Pfeiffer IKR 261) and the nominal film thickness is recorded with a custom-built quartz microbalance. The source chemicals for film deposition can be simultaneously evaporated from four independent custom-built sources (ceramic crucibles, resistively heated with a tungsten wire, mounted on electric feedthroughs). A shutter mounted on a rotary feedthrough allows to close an individual source for the purpose of defined co-deposition of two compounds. The metal top contacts of the devices are analogously produced via thermal evaporation of the source material, however, through a shadow mask providing pads of 0.5 and 1 mm diameter. The chamber allows to record current density versus voltage curves (JV-curves) of OPVCs under UHV conditions. Therefore the top contact of the device is contacted with a gold wire and the bottom contact closes the circuit via the chamber wall to a Keithley 2400 SourceMeter (using a LabView-based software environment); the approach of the gold wire can be controlled via a CCD camera. The illumination for OPVC characterization is performed from the bottom of the sample (ITO coated glass) from the outside of the chamber using a halogen lamp (for details see Sec. 4.3).

4.3 Experimental details

This section provides details on the specific measurement conditions of the studies presented in chapter 5 and on the various substrates for thin film deposition used in this work.

Substrates

For the preparation of the conducting polymer substrates used for the study in Sec. 5.1 an aqueous dispersion of PEDOT:PSS [weight ratio of 1:20 (Baytron P CH8000, provided by H. C. Starck Gmbh & Co. KG)] [172], was spin cast onto freshly cleaned (ultra-sonicated in acetone, isopropanol (both at 50°C), rinsed in deionised water and UV/O_3 treated for 30 min) indium-tin oxide (ITO) coated glass substrates ($8 \times 8\,mm^2$ size) under ambient conditions; the polymer films were annealed at 200°C for 5 min in ambient air and served as a high work-function electrodes in the device studies.

The SiO_x substrates for the samples investigated in Sec. 5.1, 5.2, 5.3 and 5.7 were (100) p-doped silicon wafers (Siegert Consulting, prime grade) with a native oxide layer cut into 10×10 mm coupons; the study presented in Sec. 5.5 was performed on similar silicon wafers, however in this case with a thermally grown oxide layer of 50 nm (rms roughness for both types: 0.15 nm determined by AFM). These substrates were used as received, and their cleanliness was confirmed by AFM investigations prior to organic film deposition; the SiO_x substrate of same type used for the study presented in Sec. 5.4 was cleaned by sonication in methanol and acetone before placement in the UHV system, and was heated to 300°C *in vacuo* prior to the deposition of the organic materials. The native silicon oxide substrates for the investigations in Sec. 5.8 was a silicon wafer cleaned in H_2O_2 (30%)+H_2SO_4 (99.99%) (3:1), etched with hydrofluoric acid, and re-oxidized by exposure to oxygen at atmospheric pressure for one hour.

The Au substrates for PEN deposition in Sec. 5.8 were *in-situ* sputtered Au films on native SiO_x coupons; the highly oriented pyrolytic graphite (HOPG) samples (grade ZYB) in the same study were purchased at GE Advanced Ceramics and *ex-situ* cleaved using adhesive tape.

The Ag(111) single crystal substrate used for the study presented in Sec. 5.4 was cleaned by repeated Ar-ion sputtering and annealing cycles until a clear Low Energy Electron Diffraction (LEED) pattern could be observed prior to the deposition of the organic materials.

Sample preparation

The organic thin films were either obtained by vacuum deposition from resistively heated ceramic crucibles (Sec. 5.2, 5.7 and 5.5) or from custom-made pinhole sources (Sec. 5.1, 5.8, 5.3 and 5.4). The substrate were held at room temperature, the base pressure during the film deposition was $\leq 3\times10^{-7}$ mbar except for the samples studied by UPS, where the base pressure was $\leq 2\times10^{-9}$ mbar. The *film mass-thickness* (θ) was measured *in-situ* by a quartz microbalance in all cases; the error of the θ-measurement was determined to be below 10% via AFM investigations of PEN sub-monolayer covered SiO_x samples. Hence, all indicated values for coverages correspond to nominal film thicknesses; no correction was made for possible differences in sticking coefficients on the different substrates. The organic materials of high purity were used unpurified as received from the manufacturer except for the studies presented in Sec. 5.8 (PEN: gradient-sublimation cleaned two times) and Sec. 5.4 (PEN and PQ: purified once by vacuum sublimation)[1].

The heating experiments on the thin films of PEN and C60 presented in Sec. 5.1 were performed under helium atmosphere; a constant temperature was held for 120 min at each step using a Lakeshore 330 temperature controller; the XRD measurements were performed after the samples had again cooled down to room temperature in the protective gas.

The PEN single crystals for the study presented in Sec. 5.8 were grown[2] *ex-situ* using the method described in Ref. [77]. They were mounted on metal sample holders with conducting adhesive tape, and cleaved *in-situ* (in the preparation chamber) by peeling off adhesive tape stuck to the crystal surface[3]. The exposure of the PEN single crystal samples to oxygen (purity 5N) was done in the analysis chamber via a leak-valve. Thin film samples were exposed to oxygen and air (both up to atmospheric pressure) in the preparation chamber.

All sample preparation steps and measurements were performed at room temperature.

[1]The purification of PEN and PQ was done by J. Pflaum, Universität Stuttgart, 3. Physikalisches Institut, 70550 Stuttgart, Germany.

[2]The PEN single crystal was provided by T. T. M. Palstra, Materials Science Center, Rijksuniversiteit Groningen, NL-9747 AG Groningen, The Netherlands.

[3]PEN molecules crystallize in a layered structure with a herringbone arrangement such that the hydrogen orbitals of one molecule interact strongly with the π-system of neighboring molecules. The interactions *between* the layers are less strong, as they are hydrogen-hydrogen interactions. Therefore, the crystal easily cleaves along the a-b plane (perpendicular to the c° direction); the molecular packing is illustrated in Fig. 2.1.

XRD measurements

All x-ray diffraction measurements presented in this work were performed at the beamline W1 at the synchrotron radiation source HASYLAB (Hamburg, Germany); the wavelength was set to $\lambda = 1.1808\,\text{Å}$. The upper limit of instrumental broadening of the setup was estimated by the 2Θ-width of the (111) reflection of a Ag(111) single crystal to $0.0382 \pm 0.0003°$; line profiles were fitted using pseudo-Voigt functions. The GID measurements were performed at an incident angle of the primary beam (α_i) of 0.15°; the detector angle (α_f) was set to 0.5°. The reciprocal space map measurements were performed using a scintillating point detector with square entry slits set to 1 mm side length. The correction of the deviation of diffractometer and sample coordinate systems was performed *ex-situ* via data treatment; the simulation of the peak positions and the visualisation was performed using the software *Recmap*. The reciprocal space maps are composed of 120 longitudinal scans in Sec. 5.2 and 100 longitudinal scans in Sec. 5.6 (450 points each). For the supporting x-ray diffraction texture analysis measurements mentioned in Sec. 5.5, a Philips MRD 4-circle goniometer with a Cu-Kα tube was used (data not shown).

UPS measurements

The photoemission experiments of the studies presented in Sec. 5.1, 5.4 and 5.3 were performed at the FLIPPER II end-station at HASYLAB (Hamburg, Germany) [174]. For the UPS measurements on non-metallic substrates, the position of the substrate Fermi-energy was determined using a freshly evaporated and sputtered Au-film. The error of all given values of binding energies and SECO positions is estimated to $\pm\,0.05\,\text{eV}$. All spectra shown were measured with the sample kept in dark and no spectral shift was observed when the samples were illuminated with white light from laboratory lamps, thus ruling out surface photovoltaic effects during the UPS measurements.

The photoemission experiments presented in Sec. 5.8 were performed at the end-station SurICat (beamline PM4) at the synchrotron light source BESSY GmbH. The UHV system consists of interconnected sample preparation (base pressure: $1\times10^{-8}\,\text{mbar}$) and analysis (base pressure: $5\times10^{-10}\,\text{mbar}$) chambers. Sample transfer between the chambers proceeded without breaking UHV conditions. The excitation energy for UPS was 25 eV in this case, and the spectra were collected with a hemispherical electron energy analyzer (Scienta SES 100) with an energy resolution of 140 meV (80%-20% intensity drop at the Au Fermi-edge). The PEN single crystal samples were irradiated with a laser (frequency-doubled Nd:YVO_4, 532 nm wavelength, 40 mW

power) during UPS measurements in this study, in order to avoid charging [176] of the thick crystals (ca. 20 μm).

AFM and scanning electron microscopy investigations

The AFM investigations were performed with a Veeco Nanoscope in *TappingMode* under ambient conditions recording topography and phase micrographs. Step heights (h) were analyzed using elevation histograms of AFM micrographs considering areas of at least 5×5 μm. The scanning electron microscopy (SEM) investigations presented in Sec. 5.5 were carried out by S. Rogaschewski (HU-Berlin) with a Cambridge Instruments S360 SEM. In order to avoid charging problems during SEM measurements, the organic thin-film samples were coated with a 3 nm Au film.

OPVC characterization

Current density versus voltage curves (JV-curves) on the OPVCs described in Sec. 5.1 were recorded immediately after device preparation without breaking the vacuum using a Keithley 2400 general-purpose SourceMeter (Keithley Instruments Inc.) under illumination through the supporting ITO- coated glass substrate with a halogen lamp (Solux, Light Bulbs Etc Inc., 12 V, 50 W, 4700 K with 10° beam spread) providing $\sim 100\,\mathrm{mW/cm^2}$ (P_{inc}) at the sample position. The top-contact for the I-V measurements were vacuum sublimed samarium pads contacted with a flexible gold wire.

Vibrational spectroscopy measurements

Fourier-transform infrared absorption spectroscopy measurements (FT-IR) (resolution $2.0\,\mathrm{cm^{-1}}$ in Sec. 5.2, 5.7, 5.1, 5.3 and $2.8\,\mathrm{cm^{-1}}$ in Sec. 5.5) were performed with a Bruker IFS-66v spectrometer under near-normal transmission geometry using a globar source (mid-IR: 7500-30 $\mathrm{cm^{-1}}$) and a liquid N_2 cooled mercury cadmium telluride (MCT) detector. Reference scans were done on SiO_x substrates covered with the powder of the respective pure materials.

Chapter 5

Results and Discussion

As outlined in Chap. 1, the goal of this work is the thorough structural, energetic and morphological characterization of PEN heterostructures with C60, PFP and PQ using a multi-technique approach in order to judge on the respective application potential for organic electronic devices (experimental details see Sec. 4.3). First, a survey on PEN/C60 heterostructures is presented in Sec. 5.1 correlating the energetic, structural and morphological properties with the performance of both layered and bulk-heterojunctions in OPVCs. In Sec. 5.2 PEN/PFP heterostructures are investigated comprising the structure solution of an unknown PFP thin film polymorph and the characterization of both layered and PEN:PFP mixed crystal structures obtained by co-deposition. The effect of PEN+PFP intercalation is described in Sec. 5.3, where it is shown that the IE of organic films with molecules exhibiting intramolecular polar bonds can be tuned through the mixing ratio of the compounds. The third presented PEN heterostructure is the combination with PQ, where UPS results are shown in Sec. 5.4 demonstrating a highly molecular-orientation dependent IE and a mutual energy level offset well capable for the use as heterojunction in OPVCs. Consequently, the structural and morphological properties of PEN/PQ layered and bulk-heterostructures are characterized in Sec. 5.5. In this context, the structure of an unknown PQ polymorph is solved using RSM, which is shown in Sec. 5.6. Finally, the impact of PQ as impurity in PEN films is analyzed by structural investigations in Sec. 5.7, where it is shown that PQ does not intercalate with PEN but rather forms phase-separated patches or accumulates at PEN grain boundaries. Since PQ presence in PEN films can also be possibly caused by oxidative processes, PEN single-crystals and thin films are exposed to O_2 and water as well as to reactive oxygen species, which is described in Sec. 5.8. It is shown by UPS and FT-IR that the first two do not react noticeably with PEN, whereas the latter produce volatile reaction products instead of PQ.

5.1 Structural and electronic properties of pentacene/fullerene heterojunctions

In this study the performance differences of layered and bulk-heterojunction based organic solar cells composed of the prototypical p- and n-type organic semiconductors PEN and C60 are correlated to the physical properties of the heterostructures. The electronic structure of layered and co-deposited thin PEN and C60 films on the conducting polymer substrate PEDOT:PSS was investigated with UPS. Layered structures of C60 on PEN pre-covered PEDOT:PSS exhibited an offset of the HOMO levels of 1.45 eV. In contrast, co-deposited films of PEN and C60 showed a reduced HOMO-level offset of 0.85 eV, which increased to 1.45 eV by pre-coverage of the substrate with a thin PEN layer. In this case, the PEN-HOMO level was Fermi-level pinned at 0.35 eV binding energy and charge transfer between PEN and PEDOT:PSS decreased the vacuum level 0.75 eV. In addition, the morphology and crystal structure of the respective systems have been investigated by AFM, XRD and FT-IR, which indicated pronounced phase separation of PEN and C60 in the co-deposited films. XRD revealed crystalline growth of PEN in all investigated cases forming crystallites that exceeded the nominal film thickness by an order of magnitude, whereas C60 was crystalline only if grown on the PEN pre-covered substrates. AFM investigations allowed to correlate morphology and structure revealing micro- and nanophase separation between PEN and C60. This work is submitted for publication (Ref. [177]).

5.1.1 Introduction

Significant efforts have been directed towards improving the understanding of organic/organic heterostructure interfaces, since numerous applications are based on the combination of different organic compounds [8, 9, 11, 12]. Concerning OPVCs, the combination of preferentially hole and electron conducting materials in a layered or a mixed-bulk morphology has been shown to be suitable for the fabrication of efficient solar cells [10, 178]. Alternatively, OPVCs based on bulk-heterojunctions (see Sec. 2.1.4) formed via *co-deposition* have been reported to show enhanced device performance compared to layered heterojunctions, like in case of phthalocyanines combined with 3,4,9,10-perylene tetracarboxylic bis-benzimidazole [10] or C60 [88, 92, 179–181], which could be explained through improved charge transport as well as increased exciton dissociation efficiency at the bulk heterojunction [178]. However, no comprehensive study on the comparison of layered and bulk-heterojunctions for PEN and C60 exists, although it is well established

that PEN exhibits phase separation in case of co-deposition [182, 183] and that PEN based co-deposited OPVCs show auspicious performance results [184].

The present work was motivated by the experimental finding that bulk-heterojunction OPVCs based on PEN and C60 co-deposited films (PEN:C60) show significantly lower efficiency compared to the respective layered structures (Fig. 5.1). This is surprising, since one would expect PEN and C60 to exhibit phase separation, therefore maximizing the common donor/ acceptor interface and the energy levels to be suitable for efficient exciton dissociation. The aim of this comprehensive study is to identify the key parameters, which lead to this unexpected result. This issue was addressed by (i) the thorough investigation of the electronic properties of layered and co-deposited PEN:C60 heterojunctions on the application relevant conducting polymer electrode PEDOT:PSS (see Sec. 4.1) using UPS (see Sec. 3.2). This is of highest interest, because the energy level alignment at interfaces plays a crucial role for the dissociation of photo-generated excitons as well as for the injection of charge carriers, which can act as bottleneck for organic device performance [12, 49, 54, 57, 185, 186]. (ii), the structural properties of layered and co-deposited heterostructures were investigated using x-ray diffraction (see Sec. 3.1), since efficient bulk-heterostructures require phase separation at the length scale of the exciton diffusion length, continuous paths of the pure materials to the electrodes as well as lowermost defect densities [10, 49, 92, 187]. (iii), controlled heating experiments of PEN:C60 bulk-heterostructures were performed and the impact on the structural order was investigated, since post-fabrication annealing is a commonly applied tool to increase the device performance through structural rearrangement [10, 188]. Finally (iv), AFM (see Sec. 3.4) was used to study the morphology of the investigated hetero-systems in conjunction with FT-IR spectroscopy (see Sec. 3.3) measurements to challenge the interpretations deduced from XRD and AFM.

5.1.2 Solar cell characteristics

Layered (C60/PEN) and 1:1 co-deposited (PEN:C60) OPVCs of PEN and C60 were investigated *in vacuo* by current versus voltage measurements (see Sec. 2.1.4); representative I-V curves are shown in (Fig. 5.1), the inset depicts the respective device geometry and the nominal layer thicknesses. For the C60/PEN OPVC (blue curve in Fig. 5.1) an open circuit voltage (V_{OC}) of 0.24 V, a short circuit current density (J_{SC}) of 4.15 mA/cm^2 and a fill factor $FF = P_{max}/(J_{SC}V_{OC})$ of 33% were found, where $P_{max} = Max(JV)$ denotes the maximum power of the OPVC. This yields a power conversion efficiency

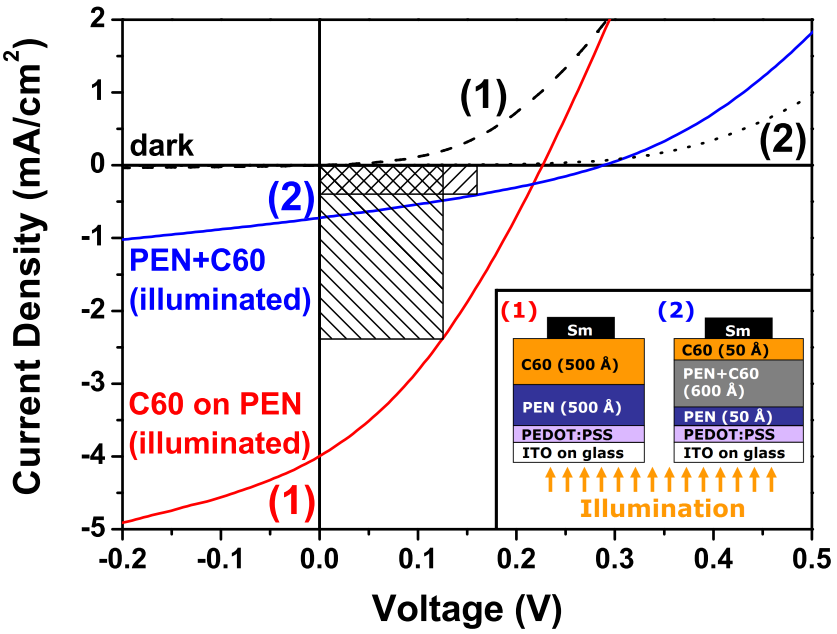

Figure 5.1: Representative current versus voltage characteristics of a layered C60 on PEN (curves labeled 1) and a bulk-heterostructure based PEN:C60 OPVC (curves labeled 2) in dark (black) and under illumination (colored curves), the inset shows a cartoon of the OPVC structures. The shaded rectangles (areas: $P_{max} = Max(JV)$, intersection with the I-V curves at the maximum power point) in the power generating fourth quadrant indicate the fill factor. Device (2) exhibits a short circuit current density about six times lower than the layered structure (for details see text).

$\eta_P = J_{SC}V_{OC}FF/P_{inc}$ of 0.29%. For the bulk-heterojunction OPVC (red curve in Fig. 5.1) a slightly increased value for V_{OC} of 0.29 V and a significantly reduced value for J_{SC} of 0.73 mA/cm^2 ($FF = 31\%$) and for $\eta_P = 0.05\%$ was observed. The result for the C60/PEN OPVC is comparable to published data [18, 21] taking into account the absence of a bathocuproine (BCP) exciton blocking layer in this OPVC [189]. However, the bulk heterojunction OPVC showed reduced values for J_{SC} and η_P by almost a factor of six. To investigate whether this result is caused by a modification of the electronic structures of PEN and C60 in the case of co-deposition UPS experiments were carried out on the pure, layered and co-deposited samples of PEN and C60.

5.1.3 Electronic structure

Figure 5.2 shows thickness dependent UPS spectra of layered and co- deposited PEN and C60 films. From the SECO the sample work function can be derived and the emission onset of the highest occupied molecular orbital (HOMO) yields the hole injection barrier Δ_h (see Sec. 3.2). The deposition of PEN with a nominal thickness (θ_{PEN}) of 128 Å on the PEDOT:PSS substrate ($\phi = 5.30\,\text{eV}$) decreased the vacuum level by 0.75 eV (see Fig. 5.2a). This shift of the vacuum level can be attributed to an interfacial charge transfer since PEN is Fermi-level pinned on conducting polymer substrates with high work functions [59, 61]. The PEN spectrum in the valence electron region with the onset of the HOMO derived peak at 0.35 eV binding energy (BE) is consistent with earlier reported spectra of PEN on PEDODT:PSS [59]. The subsequent deposition of C60 with a nominal thickness (θ_{C60}) of up to 16 Å on top of the PEN underlayer did not further change the position of the SECO, *i.e.*, C60 seems vacuum level aligned with PEN[1]. However, further deposition of up to 64 Å C60 increased the vacuum level by 0.15 eV. In the valence electron region the emission feature of the C60 HOMO level became apparent with the peak onset at 1.80 eV BE. The PEN features were gradually attenuated by the C60 deposit and almost vanished at $\theta_{C60} = 64\,\text{Å}$; the position of both the C60 and the PEN HOMO-levels stayed essentially constant for all values of θ_{C60}. Therefore, it can be concluded that C60 and PEN exhibit a HOMO level offset (Δ_{homo}) of 1.45 eV in the layered arrangement C60/PEN on PEDOT:PSS. This is a relatively large value for Δ_{homo}, which is a crucial energetic parameter for efficient exciton dissociation in OPVCs [49]. A recent UPS study of C60/PEN on polycrystalline Au substrates yielded similar results for the energy level offsets [191].

In the case of co-deposition of PEN and C60 in a volume ratio of 1:1 on PEDOT:PSS (see Fig. 5.2b) a small increase of the sample work function to $\phi = 5.20\,\text{eV}$ was found for a nominal film thickness $\theta_{co} \leq 16\,\text{Å}$, which can be deduced from the shift of the SECO to higher kinetic energy. This is the same trend as found in a previous study of pure C60 on PEDOT:PSS [192]. Further PEN:C60 deposition of up to $\theta_{co} = 64\,\text{Å}$ did not change ϕ [2].

[1]The reversed deposition sequence of PEN on C60 pre-covered PEDOT:PSS is less relevant for OPVC application. However, the results are interesting from a fundamental point of view, since evidence for a lack of thermodynamic equilibrium between the PEN top-layer and the substrate was found, which will be subject of a forthcoming study [190].

[2]The IE of PEN seems remarkably large (5.50 eV) in the co-deposited film on pristine PEDOT:PSS. PEN and C60 exhibit pronounced phase separation (see below) with *local* vacuum levels above the respective patches. In UPS experiments an area averaged surface potential is measured [193, 194]. Therefore, the IE of PEN in the co-deposited film cannot be properly determined with the present data.

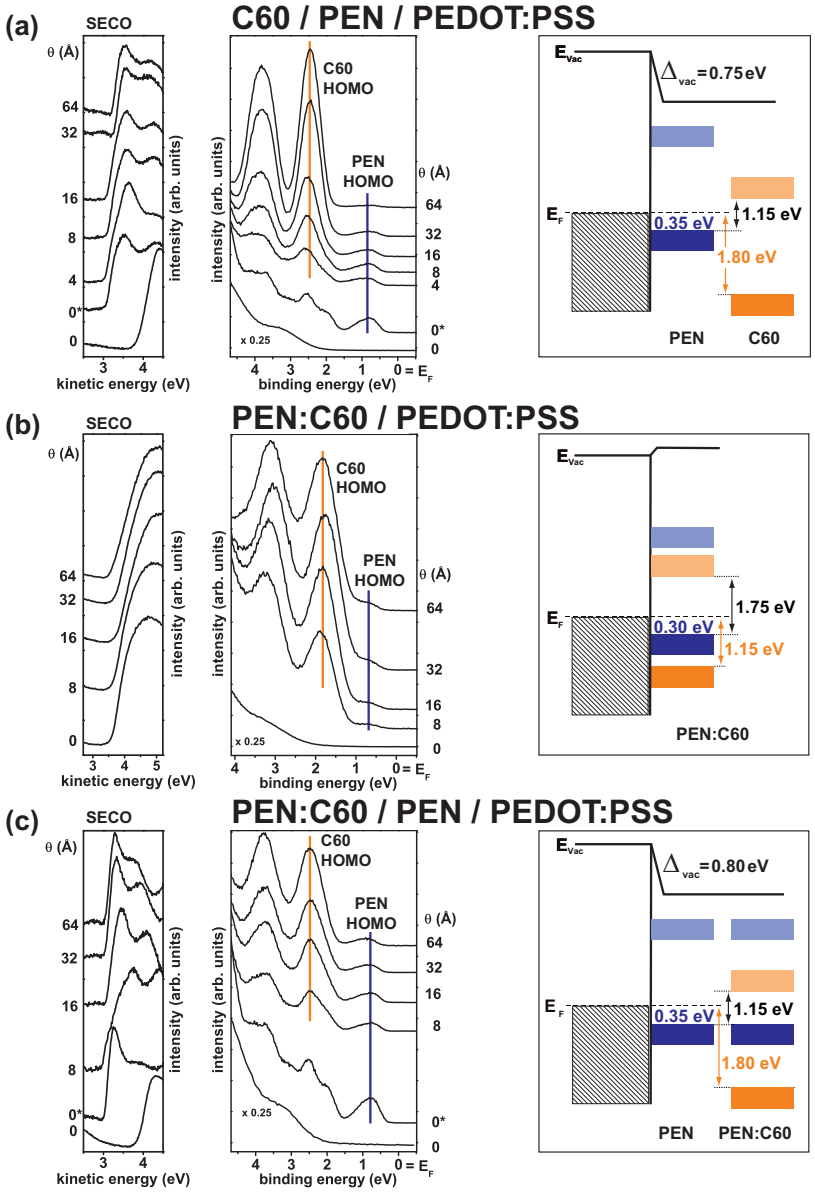

Figure 5.2: (a) Thickness dependent UPS spectra of C60 on PEN pre-covered PEDOT:PPS, (b) of PEN:C60 on bare and (c) on PEN pre-covered PEDOT:PSS. Left: SECO, middle: valence orbital region, right: schematic energy level diagram (dark and light colored rectangles depict HOMO and LUMO levels, respectively; LUMO positions estimated via the transport gaps). E_F denotes the Fermi energy, Δ_{vac} the vacuum level shift and 0* the spectrum of the 128 Å PEN pre-coverage layers.

In the valence electron region a superposition of the emission features was observed that can be attributed to PEN and C60. For θ_{co} up to 64 Å the onset of the PEN HOMO emission was found at 0.30 eV BE, which is essentially the same value as found for the pure PEN film (see above). However, the onset of the C60 HOMO emission was at 1.15 eV BE in case of co-deposition, which leads to a reduced value for Δ_{homo} of 0.85 eV. Taking into account the reported values for the PEN and C60 transport gap (E_g^T) of 2.2 eV [54] and 2.6 eV [195], respectively, the offsets of the lowest unoccupied molecular orbital (LUMO) levels can be estimated to 1.05 eV for C60 on PEN and to 0.45 eV for PEN:C60, respectively.

One crucial prerequisite for efficient exciton dissociation at the donor/ acceptor interface is that the exciton energy (E_{ex}) is larger than the offset in the HOMO position of the donor and the LUMO position of the acceptor (see Sec. 2.1.4). For C60 on PEN this offset is 1.15 eV, whereas for PEN:C60 on pristine PEDOT:PSS an offset of 1.75 eV can be derived, which is already in the range of E_{ex} of PEN, as estimated from the optical gap (1.90 eV) [182]. Therefore the dissociation efficiency for excitons generated in PEN at a bulk-heterojunction interface to C60 grown on *bare* PEDOT:PSS may be far lower than at a layered heterojunction of C60 grown on a PEN underlayer. The change of the HOMO-LUMO level offset due to PEN pre-coverage is a consequence of the substrate work function shift due to the Fermi-level pinning of PEN. Hence, it appears reasonable to pre-cover the PEDOT:PSS substrate with PEN prior to PEN:C60 co-deposition in order to achieve energetics suitable for efficient bulk-heterojunction OPVCs.

The results of UPS investigations of a co-deposited PEN:C60 film on PEDOT:PSS *pre-covered with 128 Å PEN* are shown in Fig. 5.2c. The SECO position stayed constant upon PEN:C60 deposition after the initial decrease of ϕ by 0.80 eV due to the PEN coverage of the substrate. In the valence electron region again a superposition of the PEN and C60 HOMO features was found with emission onsets at 0.35 eV BE and 1.80 eV BE, respectively. The HOMO level positions stayed constant up to the final θ_{co} of 64 Å. These values are identical to the case of C60/PEN and the HOMO level offset for PEN:C60 structure *on PEN* was again 1.45 eV.

Hence, the different OPVC performance of the two device structures shown in Fig. 5.1 cannot be explained by different energy levels. Therefore, structural reasons may account for the different performance of the respective devices. This question was addressed via x-ray diffraction experiments on SiO_x as model substrate.

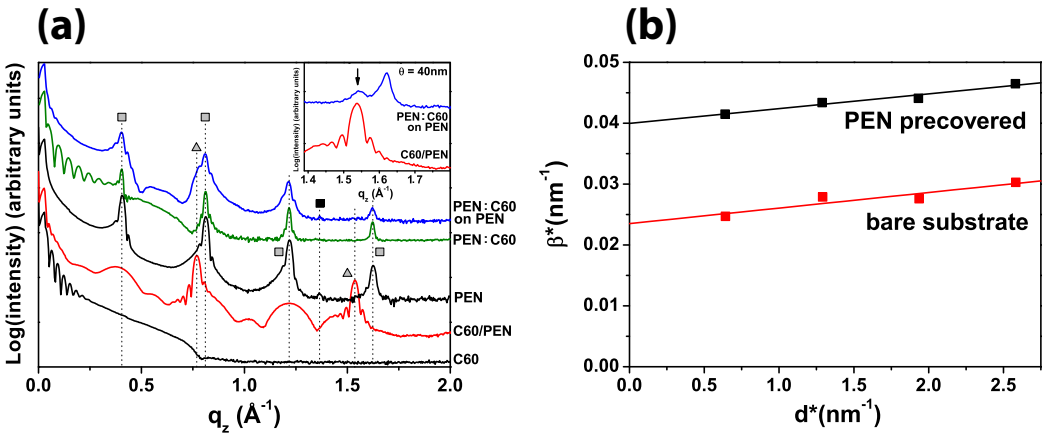

Figure 5.3: (a) Specular x-ray diffraction results on films of nominally (from bottom to up): 20 nm C60, 30 nm C60 on 3 nm PEN, 10 nm PEN, 20 nm PEN:C60 and 20 nm PEN:C60 on 3 nm PEN and (b) a Williamson-Hall analysis of the PEN reflections in the co-deposited films. Peaks of the PEN thin film phase are labeled with grey squares, reflections from C60 with triangles and the black square denotes the (1-10) peak of a PEN bulk phase [196]. q_z denotes the perpendicular momentum transfer with respect to the substrate plane, β^* and d^* denote the 2Θ-integral peak breadth and the lattice spacing, respectively, expressed in reciprocal units. The inset in (a) shows a zoomed representation around the (004) peak of the C60 film on the PEN underlayer compared to the spectrum of a PEN:C60 film ($\theta_{co} = 40$ nm) on PEN.

5.1.4 Structural properties

Specular x-ray diffraction investigations (see Sec. 3.1.1) were performed on pure C60 ($\theta_{C60} = 20$ nm) and PEN ($\theta_{PEN} = 10$ nm) films, on a C60 film ($\theta = 30$ nm) on a thin PEN underlayer ($\theta_{PEN} = 3$ nm) as well as on co-deposited PEN:C60 (total $\theta_{co} = 20$ nm) films on the bare and the PEN pre-covered substrate, the results are shown in Fig. 5.3a. The pure C60 film showed pronounced thickness oscillations (*i.e.*, Kiessig fringes, see Sec. 2.2.2) corresponding to a layer thickness of 21 ± 1 nm which stem from a smooth film of a thickness almost equal to the nominal film thickness. No Bragg peak could be observed thus indicating amorphous growth of C60 on bare SiO_x. In contrast, on the approximately two monolayer thick PEN underlayer (broad PEN features marked with shaded squares in Fig. 5.1.4a) the C60 film exhibited the (002) and (004) peaks of hexagonally close packed C60 [197], *i.e.*, crystalline C60 through an ordering effect by the PEN underlayer growing in a c* axis orientation [165]. This effect can be explained by the characteristic distance of neighbouring identical molecules in the (001) plane

of the pentacene thin film phase [198, 199] (0.9637 nm), which leads to a varying surface potential in the periodicity of the lattice constant a of the hexagonal C60 polymorph (1.0009 nm) that initiates crystalline C60 growth in the specific polymorph, providing strong indications for hetero-epitaxy of C60 and PEN. The intensity of the Kiessig fringes (corresponding to a film thickness of 33 ± 1 nm) is dramatically reduced in case of C60 on PEN, however the thickness oscillations nicely correlate to the total nominal film thickness. From the spacing of the Laue-oscillations (see Sec. 2.2.2) in the vicinity of the first three C60 peaks (see inset in Fig. 5.3a) the coherent film thickness can be derived to 24 ± 1 nm, which indicates coherent out-of-plane order throughout almost the complete C60 film. The growth of PEN in the thin film phase (001-texture) on the SiO_x substrate is demonstrated for the pure PEN film in Fig. 5.3a. In the PEN:C60 film on bare SiO_x thickness oscillations corresponding to a smooth film of 13 ± 1 nm and a series of pronounced Bragg peaks were found that correspond to the lattice spacing of the *00l*-series of the PEN thin film phase, though no indication of crystalline C60 could be observed. However, for the PEN pre-covered film the (002) reflection of C60 can clearly be observed as shoulder of the PEN (001) peak; at a nominal film thickness of $\theta = 40$ nm even the (004) reflection can be found sufficiently separated from the PEN (004) peak (see inset in Fig. 5.3a). This allowed to determine the *out-of-plane crystalline coherence length* of the crystalline C60 portion to 17 ± 2 nm (estimated by the Scherrer formula, see Sec. 2.2.2), *i.e.*, almost half of the nominal film thickness.

The microstructure of the PEN portion of the co-deposited film is an application relevant parameter, since defects or grain boundaries are limiting factors of device performance [162]. The investigation of the microstructure was performed applying a Williamson-Hall analysis (WHA) (see Sec. 2.2.2); the results are shown in Fig. 5.3b. From WHA values of 42 ± 2.5 nm and 25 ± 0.5 nm for $\langle D \rangle_V$ of the PEN:C60 films on the bare and PEN pre-covered substrate, respectively, were found. The microstrain was in both cases identical with $e = 0.0025 \pm 0.0005$. Interestingly, this value is the same (within the error margin) as the value found for a pure PEN film of $\theta = 30$ nm ($e = 0.0018 \pm 0.0005$) in different study (see Sec. 5.7). An analogous analysis was done for the film of $\theta = 40$ nm and yielded values of $\langle D \rangle_V = 87 \pm 12$ nm ($e = 0.0038 \pm 0.0008$) and $\langle D \rangle_V = 45 \pm 1$ nm ($e = 0.0015 \pm 0.0003$) on the bare and PEN pre-covered substrate, respectively.

In summary, these XRD results indicate that (i) PEN:C60 films exhibit phase separation, (ii) PEN grows in the thin film phase polymorph and forms islands with a height exceeding the nominal PEN mass thickness (i.e., $\theta/2$) in the co-deposited films by factors of 4 and 2 for the bare and the PEN pre-covered substrate, respectively, (iii) the PEN islands in the PEN:C60

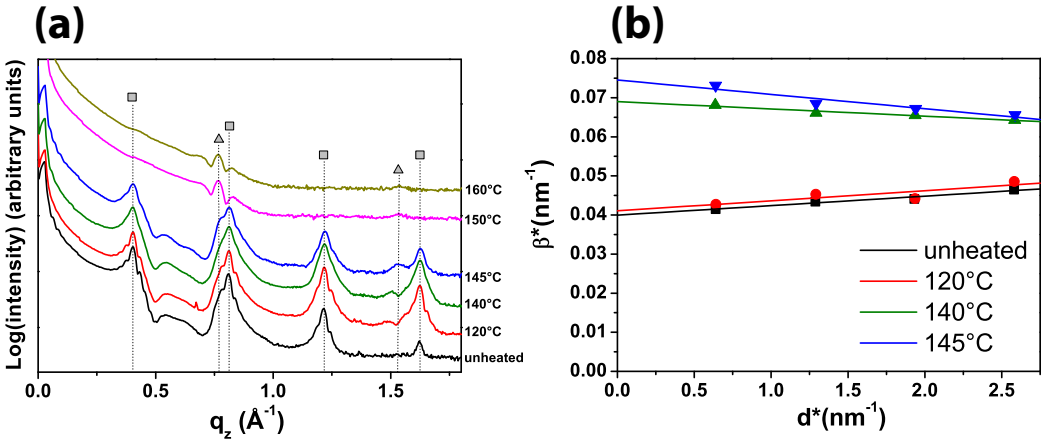

Figure 5.4: Specular x-ray diffraction measurements on annealed PEN:C60 structures ($\theta_{co} = 20\,\text{nm}$) on PEN pre-covered SiO_x substrates (a) and the corresponding Williamson-Hall analysis (b). Peaks in (a) of the PEN thin film phase *00l*-series are labeled with grey squares, the (002) and (004) reflections from C60 with triangles.

films exhibit structural order comparable to pure PEN films and (iv) PEN pre-coverage leads to an on ordering effect on C60 in the PEN:C60 film, as was also found for the layered structure of C60 on PEN.

It has been reported that post-fabrication annealing of films of OPVC material pairs [10, 200] and pure C60 layers [188] was able to impact the structural, surface and electrical properties, which can lead to a device efficiency improvement. Therefore, the impact of annealing on the PEN:C60 film deposited on the PEN underlayer was investigated; the XRD results are shown in Fig. 5.4a. From the specular scans it becomes evident that annealing increases the order in the C60 portion, since the as prepared film does not exhibit the second order reflection of C60, which however can be observed in all spectra of the annealed samples. Interestingly, the corresponding (002) lattice spacing derived from the (004) reflection is significantly reduced from 0.843 nm in the sample annealed at 120° C to 0.817 nm for annealing temperatures $\geq$ 145° C, which then equals the value found for the pristine C60 film on PEN. At annealing temperatures higher than 145° C no more PEN features are found. The present WHA analysis (Fig. 5.4b) reveals that heating up to 120° C did not significantly change the value of $\langle D \rangle_V$ determined to $24.5 \pm 1\,\text{nm}$. Moreover no change of the strain value could be observed. Between 120° C and 140° C the value of $\langle D \rangle_V$ is significantly reduced to $14.5 \pm 1\,\text{nm}$, and further to $13.5 \pm 1\,\text{nm}$ for 145° C thus indicating desorption

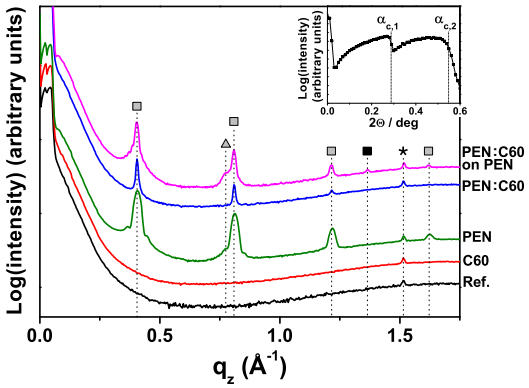

Figure 5.5: Specular x-ray diffraction on PEDOT:PSS coated ITO (from bottom to up): Reference PEDOT:PSS (CH8000) on ITO, 20 nm C60, 20 nm PEN, 40 nm PEN:C60, 40 nm PEN:C60 on 3nm PEN. PEN thin film phase peaks are labeled with grey squares, reflections from C60 with triangles and the black square denotes the (1-10) peak of a PEN bulk phase.

of PEN from the film. From these findings a PEN desorption temperature *higher* than 120° C (at ambient pressure) can be deduced hence demonstrating the possibility to make use of post fabrication annealing of PEN:C60 heterostructures at this temperature. Note, that annealing of the PEN:C60 film on a bare substrate (i.e., without PEN pre-coverage) up to 150° C did not provide evidence for a crystallisation of C60 (not shown).

To investigate the validity of the above findings for the application relevant substrate PEDOT:PSS on ITO coated glass, specular XRD measurements were performed on pure C60 ($\theta = 20$ nm) and PEN ($\theta = 20$ nm) films and on a co-deposited PEN:C60 (total $\theta = 40$ nm) film on the bare substrate and on a thin PEN underlayer ($\theta = 3$ nm); the results are shown in Fig. 5.5. Evidence for amorphous growth of C60 in the pure and co-deposited film on the bare PEDOT:PSS substrate was observed as well as (00l) textured growth of PEN in the thin film phase. In the case of the PEN pre-covered substrate, the (002) reflection of the hexagonal C60 polymorph was observed in complete analogy to the findings on SiO_x. Note that the low angle region of the spectra two critical angles ($\alpha_{c,1}$, $\alpha_{c,2}$) can be observed that can be attributed to the PEDOT:PSS layer as well as to the underlying ITO/glass substrate, respectively. This allows to estimate the mean electron density of the PEDOT:PSS layer to $\varrho_{el,1} = 0.51\,\mathrm{e\ Å^{-3}}$ (see Sec. 2.2.2).

5.1.5 Morphology

Moreover, AFM investigations were performed using topography and phase imaging in order to correlate the results from the structural investigations to morphological properties, representative micrographs are depicted in Fig. 5.6. A film of C60 on the PEN pre-covered SiO_x substrate exhibited a granular morphology (RMS roughness = 3.1 nm) comparable to previous reports [19, 21] with an island density of $(90 \pm 10)\mu m^{-2}$, which was about 30 times lower

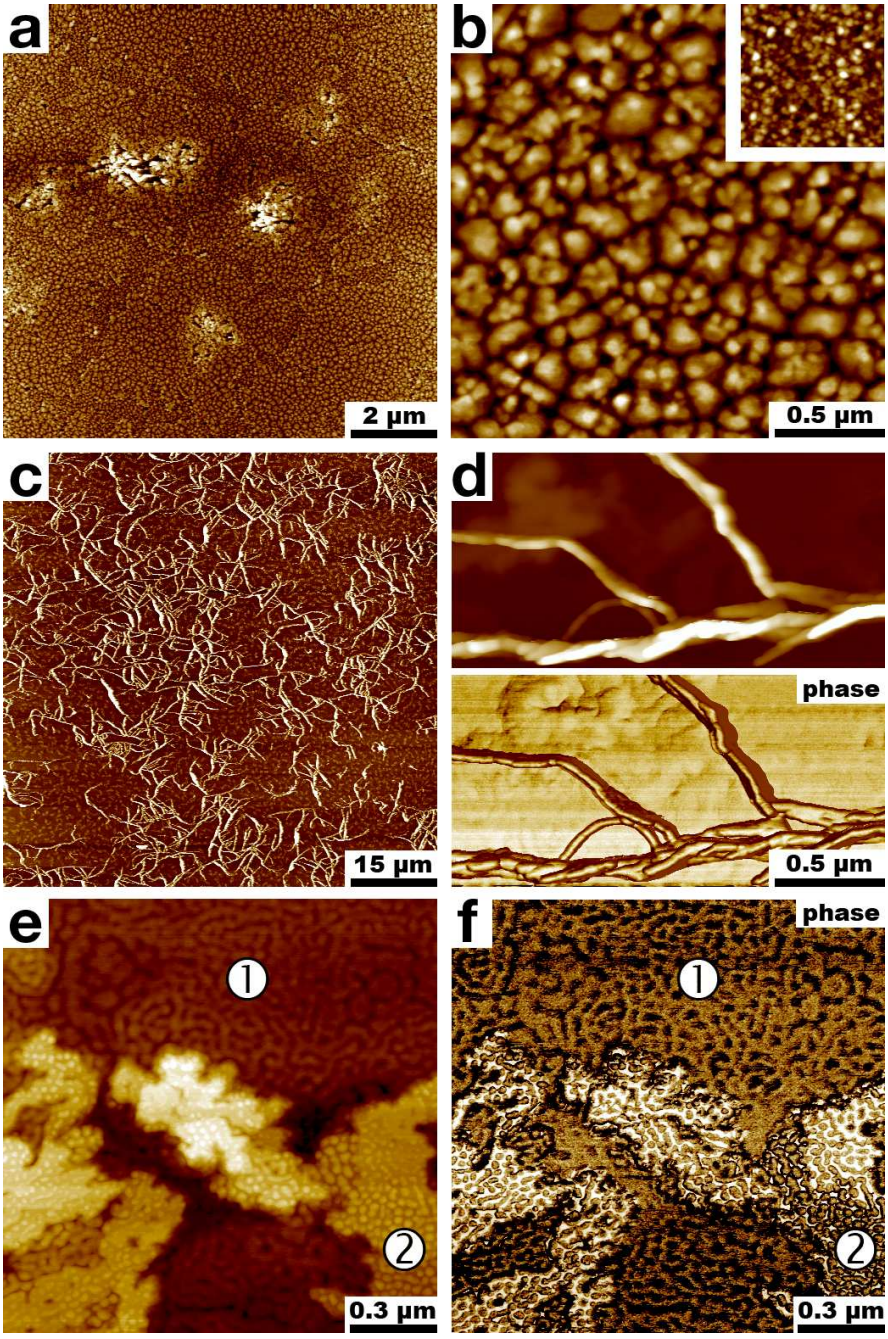

Figure 5.6: AFM micrographs of nominally 30 nm C60 on a 3 nm PEN underlayer (a, b) and on the bare SiO_x substrate (inset in (b), same scale) and of 20 nm PEN:C60 on 3 nm PEN covered SiO_x (c-f). Colours correspond to height levels up to: 2 nm in (a-b), 200 nm in (c-d) and 20 nm in (e-f) and to phase values of up to 90° in (d) and (f). Areas of interest are labeled with (1) and (2), for details see text.

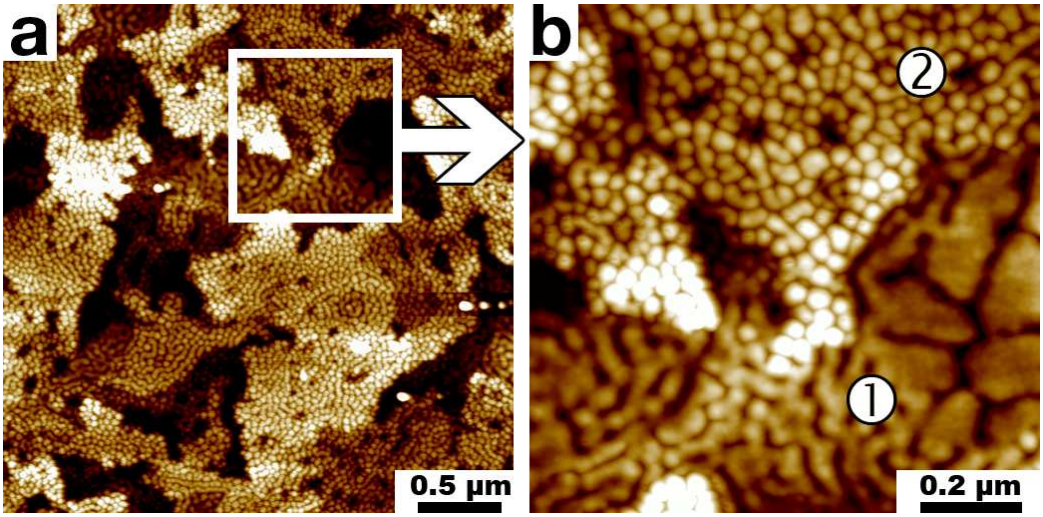

Figure 5.7: AFM micrograph of nominally 20 nm thick PEN:C60 films on a 3 nm PEN underlayer after annealing at 150° C for 120 min (a) and a zoomed view (b), colours correspond to height levels of up to 20 nm.

than for C60 on the bare substrate (RMS roughness = 1.6 nm, see inset in Fig. 5.6b). AFM topography micrographs of the PEN:C60 film on the PEN pre-covered substrate are shown in Fig. 5.6c-e. The most apparent feature is a needle-like network with an elevation of up to 200 nm exhibiting an internal structure best visible in the corresponding phase image (Fig. 5.6d). The area between these islands (Fig. 5.6e) exhibits a variety of morphologies: Areas of meandered lamellae (1) as well as areas of round islands (2) embedded within a smooth matrix. These morphologies strikingly resemble patterns often found in phase-separated block copolymers and polymer blend films [201–203]. AFM phase imaging can provide high contrast due to variations in local attractive forces and stiffness and can therefore be used as tool to discriminate between areas covered by different chemical compounds in blended films [204–206]. The phase image in Fig. 5.6f reveals comparably the same phase angle values (ϕ) in the meandered lamellae (1) and the round islands (2), however with high contrast to the surrounding smooth matrix in (2) (white areas in Fig. 5.6e) with a variation of $\Delta\phi \approx 20°$. This finding is interpreted as nanophase separation between C60 (islands) and PEN (matrix) in area (2).

The assignment of the morphological features to the distinct materials can be corroborated via AFM investigation of the PEN:C60 on PEN sample heated to 150°, where the desorption of PEN was confirmed via XRD (see section 5.1.4). In large area AFM micrographs no more needle-like crystallites

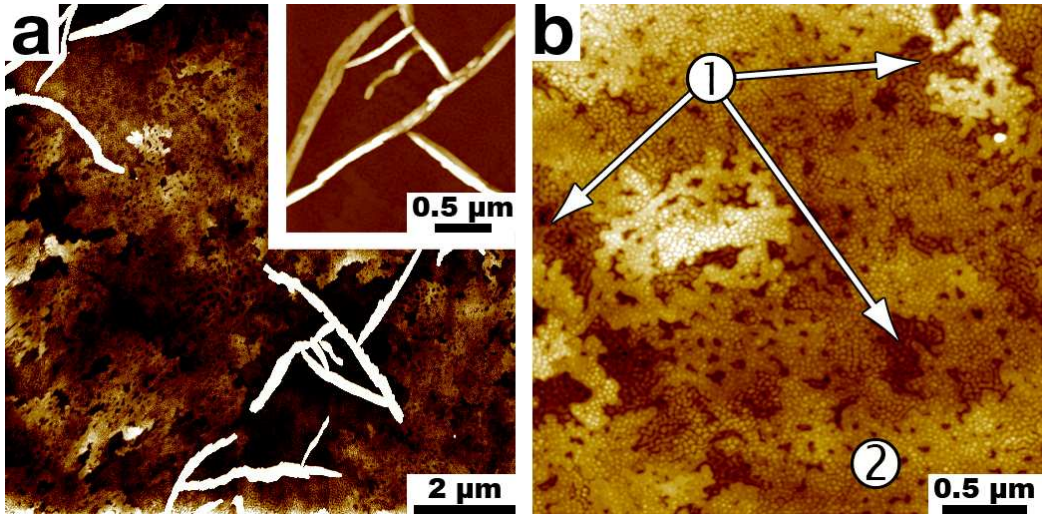

Figure 5.8: AFM micrographs of a nominally 40 nm thick PEN:C60 film on a PEDOT:PSS substrate covered with 3 nm PEN underlayer. Colours correspond to height levels of 30 nm in (a, b) and to 200 nm (inset in (a)).

like in Fig. 5.6c-d could be observed, whereas the close-view on the structure of the remaining film in Fig. 5.7 almost perfectly resembles the morphology of the as prepared film, however without the smooth matrix surrounding the round islands. In the corresponding phase images $\Delta\phi$ of neighbouring features did not significantly vary as was the case for the as prepared film. These findings are evidence that both, the needle-like crystallites with high elevation and the smooth surrounding matrix of the round islands consist of PEN. Moreover, after the annealing process no significant number of pores was observed instead of the PEN matrix, which points to the nanophase-separated PEN portion not penetrating deep into the C60 film and therefore not forming continuous paths to the substrate.

An AFM investigation of the PEN:C60 film ($\theta = 20$ nm) on PEN pre-covered PEDOT:PSS substrates yielded essentially the same results. Again, needle-like structures of up to 200 nm were found surrounded by a film of low elevation exhibiting again the two different morphologies already found in the film on SiO_x; representative micrographs are shown in Fig. 5.8. However, areas (2) appear to contain more holes on PEDOT:PSS than in the case of growth on SiO_x whereas the island density of the round islands was essentially the same. These small differences in morphology are due to the higher surface roughness of PEDOT:PSS (RMS ≈ 1.2 nm) compared to SiO_x (RMS ≈ 0.2 nm) leading to an increased defect density of the PEN underlayer.

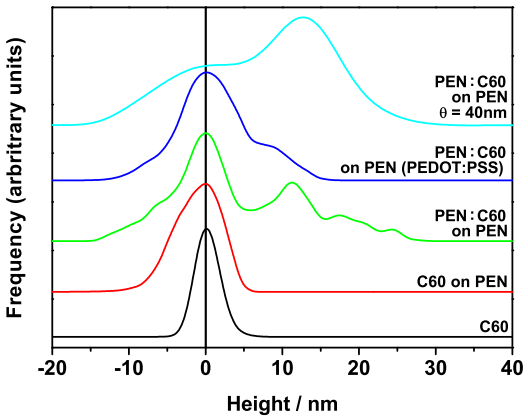

Figure 5.9: Elevation histograms deduced from AFM micrographs. If not explicitly stated differently: SiO_x substrates, nominal film thickness $\theta = 20\,\text{nm}$. The histograms are shifted vertically for clarity.

From all investigated samples elevation histograms of the AFM micrographs were derived as shown in Fig. 5.9. The films of pure C60 on the bare and the PEN pre-covered substrate did not exhibit characteristic step heights, whereas all co-deposited PEN:C60 films on SiO_x showed pronounced overlapping peaks. In the case of the PEN:C60 film on the PEN pre-covered SiO_x substrate ($\theta = 20\,\text{nm}$) the dominating island height (h) was determined to $\approx 11\,\text{nm}$, the same film on the PEDOT:PSS substrate exhibited a slightly lower value of $h \approx 9\,\text{nm}$. Interestingly, the film of twice the nominal film thickness on SiO_x only showed an increase of h to $\approx 13\,\text{nm}$, whereas the frequency ratio to the peak at the origin was reversed thus indicating preferential lateral instead of vertical growth at increasing θ.

5.1.6 Vibrational spectroscopy

From XRD crystalline growth of PEN in the thin film polymorph was deduced for the co-deposited films and the AFM investigations revealed that C60 islands partly grow enclosed within a PEN matrix. Since XRD investigations are exclusively sensitive to crystalline portions of a sample, information on the structural arrangement of possibly amorphous PEN portions is inaccessible via XRD. Therefore a FT-IR investigation was performed on the pure and co-deposited films, since FT-IR probes both crystalline and amorphous sample portions and is additionally sensitive to polymorphism [182]. Two PEN fingerprint ranges are shown in Fig. 5.10. The vibrations of the PEN thin film reference sample ($\theta = 20\,\text{nm}$) at $729.5\,\text{cm}^{-1}$, $737.5\,\text{cm}^{-1}$ and $903.5\,\text{cm}^{-1}$ can be assigned to the C-H out-of-plane bending modes [207, 208]. Together with the XRD results these vibrations are assigned to PEN in the thin film phase (additional pronounced vibrations at 833.0, 954.0, 1296.5 and $1344.0\,\text{cm}^{-1}$). The PEN vibrations of the nominally 3 nm thick (≈ 2 monolayers) underlayer for the crystalline C60 film appear at the same frequencies, except for the

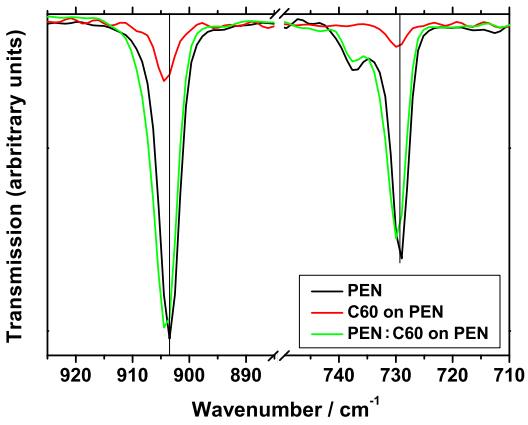

Figure 5.10: FT-IR results of films of PEN ($\theta = 20\,\text{nm}$), C60 ($\theta = 30\,\text{nm}$) on 3 nm PEN and PEN:C60 ($\theta = 40\,\text{nm}$) on 3 nm PEN.

two strong C-H out-of-plane bending modes in Fig. 5.10, which are shifted by $+0.5\,\text{cm}^{-1}$ to $730.0\,\text{cm}^{-1}$ and by $+1\,\text{cm}^{-1}$ to $904.5\,\text{cm}^{-1}$ compared to the PEN reference. This may indicate a different molecular arrangement of PEN in the ultrathin film[3]. The most pronounced vibrations assigned to C60 were observed at 1182.5, 1429.0 and $1539.5\,\text{cm}^{-1}$ in *all* investigated samples, *i.e.*, amorphous and crystalline grown C60 could not be distinguished in FT-IR. In contrast, the two PEN peaks of the co-deposited film (Fig. 5.10) were found shifted compared to the PEN reference at 730.0 and $904.0\,\text{cm}^{-1}$, the full width at half maximum of the two peaks fitted with a Cauchy function was 3.1 and $3.9\,\text{cm}^{-1}$ for the pure PEN film and 3.7 and $4.5\,\text{cm}^{-1}$ for the co-deposited film. Since in WHA the crystalline PEN portion in the co-deposited film exhibited comparable crystalline quality and the same structure as the pure PEN film, this broadening points to a superposition of features from crystalline and amorphous PEN, which cannot be experimentally resolved. This finding supports the AFM interpretation of round C60 islands being embedded into a matrix of amorphous PEN while crystalline PEN grows in large needle-like islands.

[3]In a recent XRD study almost upright molecular arrangement was shown for the PEN monolayer [209] and in a different work PEN was reported to exhibit a thickness driven orthorhombic to triclinic phase transition [210]. The unit cells proposed in both studies are equal within the error margin, hence one may speculate that the vibrations found in the FT-IR investigation can be assigned to this specific polymorph. Another explanation would be the bimodal growth behaviour of PEN films in thin film and bulk phase, which was recently shown to be undetectable by XRD at low nominal film thickness [211]. Therefore the shifted vibration of the ultrathin film could dominantly stem from the thin film phase, whereas the thick PEN film shows a superposition of thin film and bulk phase features. Admittedly, this cannot be decided from the present data and more work concerning this question is necessary.

5.1.7 Summary and discussion

Using various complementary experimental techniques, a comprehensive picture of electronic, structural and morphological properties of PEN and C60 heterostructures could be derived. Starting with the experimental finding of OPVCs based on co-deposited PEN:C60 films showing poor performance compared to layered structures of C60/PEN the possible reasons were systematically investigated: (i) unfavourable interface energetics, (ii) structural disorder, (iii) lack of phase separation and (iv) degree of surface corrugation.

(i) The UPS results (Fig. 5.2) prove that PEN pre-patterning of the PEDOT:PSS substrate leads to an identical HOMO-LUMO level offset between PEN and C60 in the layered case and in the bulk heterojunction. This was explained by vacuum level alignment of C60 on both PEDOT:PSS and PEN, whereas PEN was Fermi-level pinned on PEDOT:PSS leading to a decreased substrate work function for C60. Therefore, PEN pre-covered substrates allow for a more favourable HOMO-LUMO level offsets for bulk heterojunction based OPVCs, which is crucial for the exciton dissociation process at the PEN-C60 interface. However, the finding of identical HOMO-LUMO level offsets in case with PEN pre-coverage cannot explain the exceedingly different OPVC performance (in Fig. 5.1).

(ii) Structural investigations with XRD (Fig. 5.3) revealed that PEN pre-coverage has an ordering effect on C60, which formed amorphous films on the bare substrates (SiO_x and PEDOT:PSS), and crystalline films on the PEN thin film phase (001) plane with C60 in its hexagonal crystal structure growing with the (001) plane of C60 parallel to the contact. The same was found in the case of co-deposition, where PEN grew (almost upright standing) (001) textured in the thin film phase independent of the PEN pre-coverage and C60 was crystalline on the PEN pre-covered substrates only. From WHA it became clear that the crystalline PEN portion exhibits a coherence length far larger than the nominal PEN mass thickness, thus indicating pronounced 3D growth. This is an unexpected growth behaviour for this specific polymorph, since the PEN thin film phase morphology on amorphous substrates is known to be fairly flat. Via WHA in defined *ex-situ* heating experiments (Fig. 5.4) a lower limit for the annealing temperature not affecting the PEN microstructure while improving the structural order in the C60 portion of 120°C was determined and it could be demonstrated that annealing up to 150°C leads to desorption of PEN.

(iii) The growth behaviour of the pure and co-deposited films on PEDOT:PSS (Fig. 5.5) was shown to be very similar to that on SiO_x. The finding of PEN growth in both the pure and the co-deposited films in the same polymorph is strong evidence for phase separation with C60. This is

further supported by the fact that C60 itself exhibited crystalline growth in a known polymorph on PEN.

(iv) AFM investigations revealed a needle-like network of crystallites with up to 200 nm height (Fig. 5.6), which could be assigned to PEN due to the XRD finding of the PEN coherence length exceeding the nominal film thickness. This morphology has not been observed before for the PEN thin film phase, which usually grows showing pronounced monomolecular steps of ca. 1.5 nm height that correspond to the (001) lattice spacing. The areas between the PEN needles are covered by two distinguishable morphologies of *meandered lamellae* and *round islands* surrounded by a smooth matrix. Evidence for PEN and C60 nanophase separation was found through pronounced contrast in the AFM phase images. The assignment was corroborated by an AFM investigation of the PEN:C60 on PEN sample annealed at 150° (Fig. 5.7), in which the PEN features in the XRD scans had vanished: No needle-like crystallites and no smooth PEN matrix surrounding the round islands was then observed, while the morphology of the areas attributed to C60 was not modified through the annealing process. In contrast to the smooth C60/PEN films, the co-deposited films with $\theta = 20\,\text{nm}$ exhibited a preferred island height of $\approx 11\,\text{nm}$ deduced from the elevation histograms (Fig. 5.9); a film of $\theta = 40\,\text{nm}$ showed a preferred island height of $\approx 13\,\text{nm}$. Note, that this value is in good agreement with the coherence length of the C60 crystallites deduced from the peak breadth analysis in XRD ($17 \pm 2\,\text{nm}$) taking into account that preferred island height values are measured *relatively* between areas labeled (1) and (2) in the micrographs, which both are expected to grow on doubling the nominal film thickness. The morphology of the application relevant films on PEDOT:PSS (Fig. 5.8) appeared to be essentially the same compared to the films grown on the model substrate SiO_x.

The FT-IR investigations (Fig. 5.10) revealed a shift and a broadening of the PEN C-H out-of-plane bending modes of the co-deposited film compared to a pure PEN reference, which are explained by a superposition of features from PEN portions with different molecular arrangement. Since the PEN crystalline quality in the PEN:C60 film (Fig. 5.3) was comparable to the pure PEN film, this shift can be explained by a superposition of contributions from the needle-like crystallites (thin film phase) and amorphous PEN portions in nanophase-separated areas.

These findings provide a comprehensive answer to the question, *why* the OPVC based on the co-deposited structure showed poor performance results: (i) The distance between the needle-like PEN islands is in the length scale of μm and their height exceeds the surrounding C60 areas by more than one order of magnitude. This minimizes the common interface necessary for

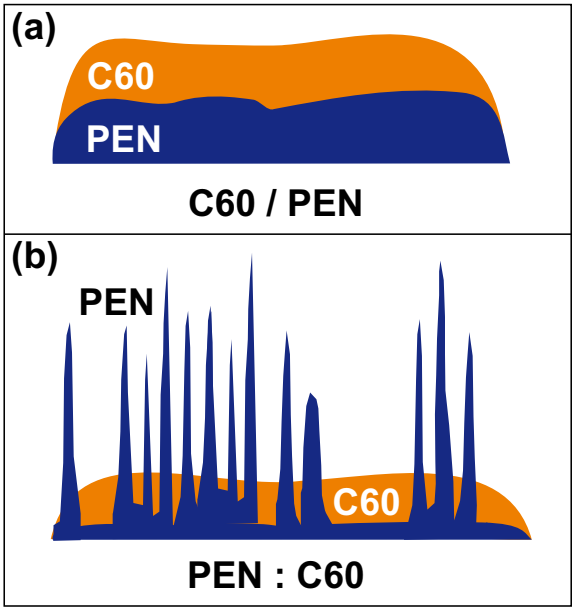

Figure 5.11: Schematic drawing of growth models deduced from the experimental results for (a) a layered film of C60 on PEN and (b) a co-deposited film of PEN:C60 on a thin PEN underlayer: Pure C60 forms a smooth layer on a PEN pre-covered substrate, whereas, if co-deposited with PEN, a highly corrugated film surface is formed with PEN islands far exceeding the surrounding C60 areas.

an efficient exciton dissociation (cartoon see Fig. 5.11). (ii) The areas exhibiting nanophase separation most probably do not form continuous PEN paths to the substrate, which is however crucial for the performance of bulk-heterojunction based OPVCs. (iii) The PEN underlayer of $\theta = 3\,\mathrm{nm}$ is too thin to significantly contribute to light harvesting and exciton dissociation at the PEN/C60 interface, since exciton quenching occurs in defect-rich ultrathin films.

In this study it was demonstrated that a multi-technique view on the physical properties is crucial for a correct interpretation of device performance results. Morphological issues were identified to be responsible for the poor device performance of PEN:C60 co-evaporated OPVCs.

5.2 Perfluoropentacene thin films and heterostructures with pentacene

In this study, synchrotron x-ray diffraction reciprocal space mapping was performed on PFP thin films on SiO_x in order to determine the crystal structure of a novel, substrate-induced thin film phase to be monoclinic with unit cell parameters: $a = 15.76 \pm 0.02$ Å, $b = 4.51 \pm 0.02$ Å, $c = 11.48 \pm 0.02$ Å, $\beta = 90.4 \pm 0.1°$. Moreover, layered and co-deposited heterostructures of PFP and PEN were investigated by specular and grazing-incidence x-ray diffraction, atomic force microscopy and Fourier-transform infrared spectroscopy. For a ca. three monolayer thick PFP film grown on a PEN underlayer, a slightly increased lattice spacing was found. In contrast, co-deposited PEN:PFP films form a new mixed crystal structure with no detectable degree of phase separation. These results highlight the structural complexity of these technically relevant molecular hetero-junctions for the use in organic electronics.
This work is published as Ref. [168].

5.2.1 Introduction

The fundamental electronic properties and the crystallographic structure of PFP have already been investigated to some extent [24, 169–171]. For potential device applications, both aspects are highly important because charge injection efficiency and transport properties critically depend on the molecular orientation in organic thin films [70, 212–215]. Thin films of PFP grow fiber-textured on SiO_x with a (100) lattice spacing (d_{100}) of 15.7 Å, which is notably larger than the value of 15.5 Å determined for a single crystal by x-ray diffraction [24, 170]. This suggests the existence of a *PFP thin film phase* on SiO_x with yet unknown lattice parameters. An analogous growth behaviour has been observed for PEN where several polymorphs have been observed including a long-debated thin film phase that was successfully solved by x-ray diffraction only recently [198, 199, 216]. In addition, the structural properties of devices based on a combination of PEN and PFP in layered and blended structures, reported to exhibit ambipolar behaviour in OFETs [23], are still unexplored.

In this study, x-ray diffraction reciprocal space mapping (RSM) (see Sec. 3.1.2) was applied using synchrotron radiation to derive the lattice parameters of the PFP thin film phase. This highly surface-sensitive technique allows to solve crystal structures of thin films while minimizing radiation damage issues [122]. Moreover, using specular and grazing incidence x-ray diffraction (GID) (see Sec. 3.1) (i) a PFP on PEN bilayer structure of ca.

three monolayers thickness was investigated to explore the growth behaviour in the region of the organic-organic interface as well as (ii) a PEN:PFP (1:1) co-deposited film in order to investigate the potential of such blended films as bulk heterojunction for organic photovoltaic devices. Complementary investigations were AFM (see Sec. 3.4) and FT-IR spectroscopy (see Sec. 3.3); both methods have been helpful to explore polymorphism and phase separation in organic thin films [81, 182, 183].

5.2.2 Structural properties

Thin films of pure PEN PFP and co-deposited PEN:PFP (total $\theta = 300\,\text{Å}$) as well as a thin layered film of PFP on PEN ($\theta = 50\,\text{Å}$ PEN + $50\,\text{Å}$ PFP) were investigated by specular XRD and GID; the results are summarized in Fig. 5.12. The pure PEN film was in the PEN thin film phase, exhibiting a (001) fiber texture ($d_{001} = 15.45 \pm 0.05\,\text{Å}$). In addition, a weak contribution of a (1-10) and (022) orientation of the PEN bulk phase [196] was observed in the specular scan, which agrees with previous studies [182, 209, 217–219]. The pure PFP film exhibited a similarly textured growth behaviour, however with a larger lattice spacing of $d_{100} = 15.75 \pm 0.05\,\text{Å}$, which deviates from the respective value in the PFP single-crystal structure [23, 170]. These data clearly reveal that thin PFP films on SiO_x grow in a crystal structure different from the PFP single crystal, *i.e.*, in a substrate-induced *PFP thin film phase*.

In order to determine this unknown structure, an x-ray diffraction reciprocal space map study was performed; the results are depicted in Fig. 5.13 together with a simulated pattern. The crystal structure was found to be monoclinic with the unit cell parameters $a = 15.76 \pm 0.02\,\text{Å}$, $b = 4.51 \pm 0.02\,\text{Å}$, $c = 11.48 \pm 0.02\,\text{Å}$, $\beta = 90.4 \pm 0.1°$. The most significant deviation from the single crystal structure is the $0.25\,\text{Å}$ elongated unit cell axis a, as well as the reduced monoclinic angle, which is only slightly off 90°[4]. The cell volume is $V = 816.0\,\text{Å}^3$ and therefore slightly larger than in case of the single crystal structure ($V = 797.0\,\text{Å}^3$). Hence, in analogy with the PFP single-crystal structure space group $P2_1/c$ and two non-equivalent molecules per unit cell ($Z = 2$) can be assumed for the PFP thin-film phase. These changes from bulk to thin-film phase are analogous to the PEN case. Using force field calculations[5] the molecular orientation of PFP in the unit cell was modelled;

[4]Peaks that differ by indices $\pm l$ cannot be resolved individually due to the low deviation of β from 90°. However, the oval peak-shape and the dependency of its longer diameter on the peak order allows to determine the split corresponding to a maximum error of $\Delta\beta = 0.1°$.

[5]The force field calculations have been performed by *Dmitrii Nabok*, Chair for Atomistic

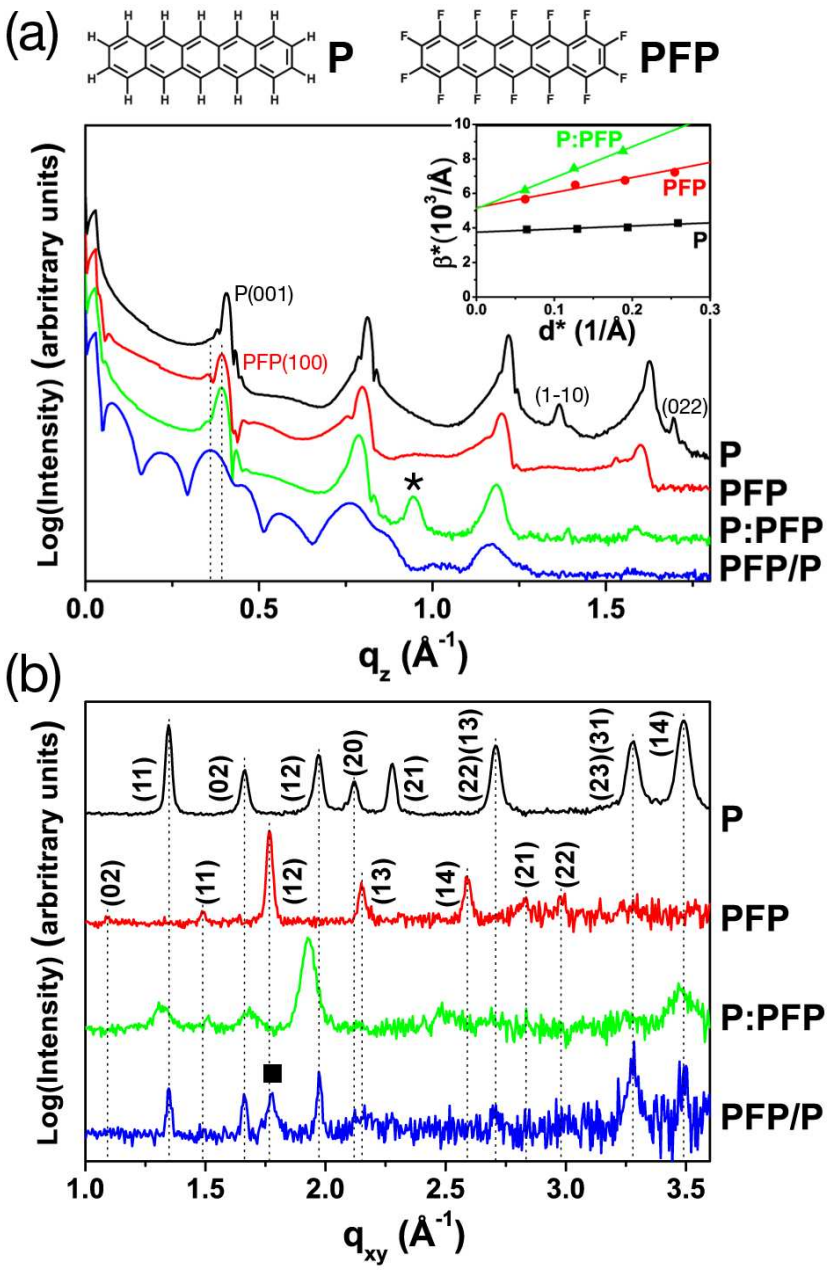

Figure 5.12: Specular (a) and GID (b) scans of PEN PFP, and co-deposited PEN:PFP films of $\theta = 300\,\text{Å}$ and of a $50 + 50\,\text{Å}$ thick layered PFP/PEN film. The peaks are labeled with the respective indices; q_z and q_{xy} denote the perpendicular and lateral momentum transfer with respect to the substrate plane. The inset in (a) shows the result of a Williamson-Hall analysis of the specular peaks-series, β^* and d^* denote the 2Θ-integral peak breadth and the lattice spacing, respectively, expressed in reciprocal units.

the derived structure is shown in Fig. 5.14 in comparison to the PFP bulk phase in top-view on the texture plane (100). The two structures are most similar with angles between the plane normals of the unequal molecules of 74.35° and 75.31° for the thin film and bulk phase, respectively.

The specular scan of the co-deposited PEN:PFP film (Fig. 5.12a) also shows a series of Bragg reflections up to the fourth order with a lattice spacing of $d_{001} = 15.95 \pm 0.05\,\text{Å}$ as well as a pronounced peak at $q_z = 0.945 \pm 0.007\,\text{Å}^{-1}$ momentum transfer (marked with a star in Fig. 5.12a), which corresponds to a lattice spacing of $6.65 \pm 0.05\,\text{Å}$ and which exhibits an *out-of-plane crystalline coherence length* of $130 \pm 13\,\text{Å}$ (estimated by the Scherrer formula, see Sec. 2.2.2). The observed d-value cannot be explained by any known crystal structure of PEN or PFP, hence it can not be decided whether it stems from an additional distinct polymorph or a different orientation of the specific polymorph, which yields the (100) series[6].

The microstructure of the pure PEN, PFP and the PEN:PFP co-deposited films was investigated with a Williamson-Hall analysis (WHA) (see Sec. 2.2.2); the results are shown in the inset of Fig. 5.12. From WHA, values of $312 \pm 9\,\text{Å}$, $216 \pm 8\,\text{Å}$ and $219 \pm 17\,\text{Å}$ were observed for $\langle D \rangle_V$ of the PEN, PFP and PEN:PFP films, respectively. The film of PFP shows five times more strain ($e = 4.4 \times 10^{-4}$) than the pure PEN film and the co-deposited film even ten times more. From these findings it can be concluded that the PFP film (prepared under the same conditions as the PEN film) contains a significantly larger number of defects that leads to the elevated microstrain compared to the PEN film. The reduced value of $\langle D \rangle_V$ at equal θ in case of PFP also points to a reduced crystalline quality of the film. The co-deposited PEN:PFP film shows the same $\langle D \rangle_V$ value as the pure PFP film, however with a dramatically increased value of the microstrain. Together with the increased lattice spacing determined from the specular scan, this finding of severely disturbed crystal growth can be seen as evidence for intercalated growth of PEN and PFP, *i.e.*, the growth of a mixed crystal structure in case of co-deposition. This assumption is, in fact, corroborated by GID (Fig. 5.12), where the mixed film exhibited a severely altered spectrum with no detectable features of the pure films, as well as by the FT-IR results (Fig. 5.16) through the loss of spectral features specific for the pure film.

Modelling and Design of Materials, Montanuniversität Leoben, Franz-Josef-Straße 18, A-8700 Leoben, Austria.

[6]In case of the PFP series in the specular scan the labels are chosen differently to the case of PEN since the PFP single crystal structure (most similar to the PFP thin film structure) is defined with the lattice parameter a as the longest edge length (instead of c in case of the PEN thin film structure). The GID spectrum of the PEN:PFP film resembles the PEN-GID spectrum; therefore, the labelling order of PEN is applied in this case.

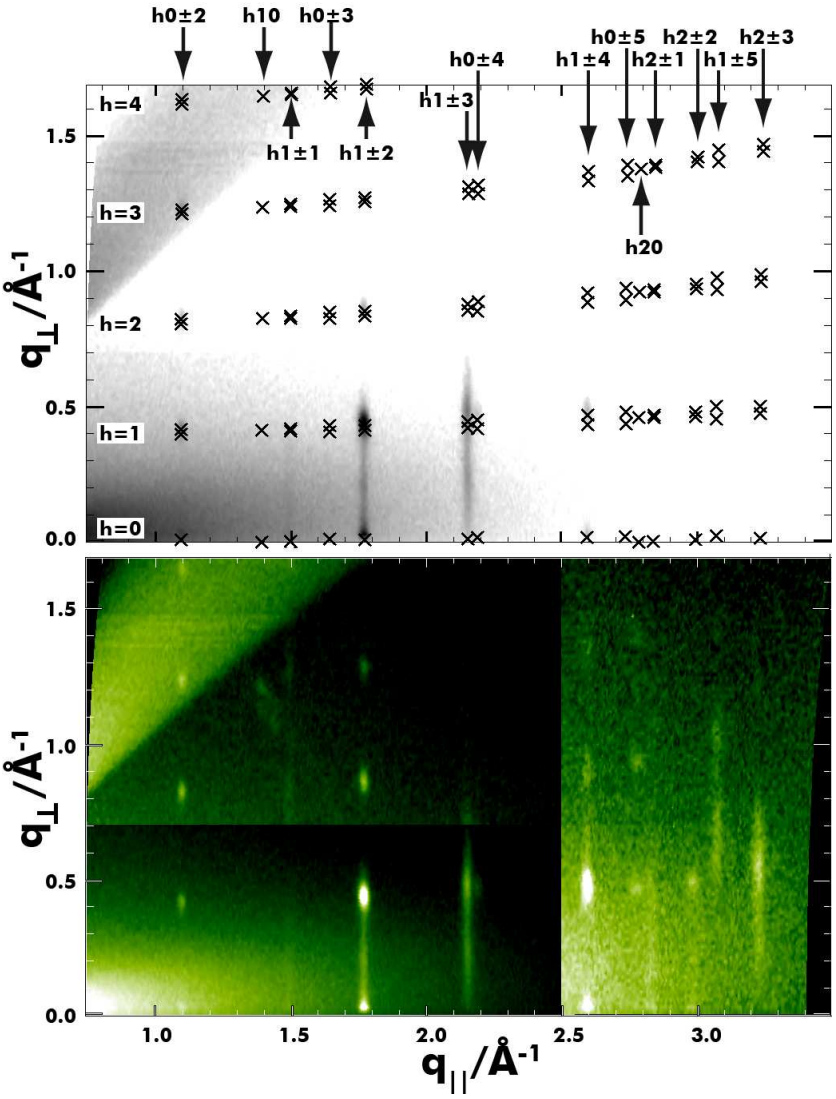

Figure 5.13: Experimental (bottom) result of a RSM investigation on a 300 Å thick PFP film on SiO_x below a simulated pattern (top); $q_{\parallel}$ and $q_{\perp}$ denote the in-plane and out-of-plane component of the momentum transfer q. The series of different indices h and equal indices k, $\pm l$ are found vertically aligned along $q_{\perp}$. The split between peaks with indices $\pm l$ stems from the monoclinic unit cell angle β being slightly off 90°; the respective peak with negative index l appears at lower $q_{\perp}$. The experimental map was divided into three parts, because different scaling had to be applied due to the high background at low values of momentum transfer.

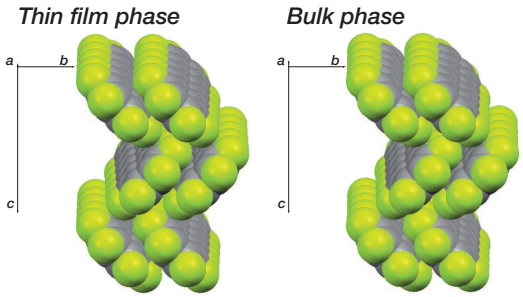

Figure 5.14: Comparison of the most similar polymorphs of PFP: Thin film phase structure (left) as derived by force field calculations for the experimental unit cell parameters and bulk phase structure (right), both viewed on the (100) texture plane; carbon atoms are colored grey, fluorine atoms green.

The thin layered sample of nominally 50 Å PFP on 50 Å PEN shows thickness oscillations (Kiessig fringes, see Sec. 2.2.2) corresponding to a layer thickness of 52 ± 5 Å and a series of three Bragg peaks that correspond to a lattice spacing of $d_{100} = 16.2 \pm 0.2$ Å. This demonstrates that the thin PFP film on the PEN underlayer grows with a more upright molecular arrangement than in case of the thick PFP film on SiO_x. A similar growth behaviour has been reported for ultrathin PEN layers on SiO_x [209, 220]. It is well known that PEN films follow the Stranski-Krastanov growth mode on SiO_x, characterized by islands growing on closed underlayers [220, 221]. Specular x-ray diffraction on a reference sample of the PEN underlayer yielded Kiessig fringes that correspond to a slightly lower layer thickness of 40 ± 5 Å (not shown). Therefore it is suggested to assume that the PEN underlayer dominates the thickness oscillations with a PFP top-layer dominantly forming islands[7].

GID investigations were performed on the same set of samples in order to investigate the in-plane structure of the films; the results are shown in Fig. 5.12b. The PEN film exclusively shows reflections originating from the thin film phase, and the peak positions agree with the calculated values. The GID spectrum of the pure PFP film is similar to a calculated powder pattern of the single crystal structure; however, all measured peaks deviate by an amount of at least one peak half-width from this structure. Therefore it appears reasonable to assume a similar structure of the PFP thin film phase with analogous indexing, which could be justified by the results of the RSM measurement (Fig. 5.13). The GID pattern of the co-deposited PEN:PFP film shows reflections that can not be explained by any known PEN or PFP structure (they do, however, resemble the pattern of the PEN thin film phase). This is strong evidence that PEN and PFP form a mixed

[7]Note that, in contrast, a layered PFP/PEN film of $\theta = 500 + 500$ Å shows a simple superposition of the pristine spectra with a PFP lattice spacing equal to the PFP thin film phase (not shown).

crystal structure in case of co-deposition, which is corroborated by the FT-IR results (Fig. 5.16). However, it is not possible to derive the unit cell dimensions from the present data; a RSM investigation in this regard will be subject of a forthcoming study. The majority of the PEN-GID reflections can also be found in the pattern of the thin layered PFP/PEN sample, which points to a high crystalline quality of the PEN underlayer. In addition, the most intense PFP reflection of the pristine film (marked with a square in Fig. 5.12b) also occurs in the spectrum of the layered sample, however slightly shifted to higher values of momentum transfer. This corresponds to a decreased d-value, which fits to the increase of the c^* value deduced from the specular scan if the unit cell volume is expected to be constant. Moreover, the PFP peak is much broader than the vicinal peaks of PEN which corresponds to a lower crystalline coherence length in the film plane, as expected in case of island growth.

5.2.3 Morphology

In order to investigate the film morphology, AFM measurements were performed on all investigated samples; representative micrographs are shown in Fig. 5.15. The PFP thin-film morphology matches the results of previous studies [23, 170]. Pronounced steps with a height (h) of 16 ± 2 Å were found and a visible integrated film volume[8] of $9 \times 10^{-3} \mu m^3$ per μm^2 area was measured (Fig. 5.15a), which is less than a third of the nominal deposited volume. Therefore, the PFP layer can be considered as completely closed at this value of θ without significant voids reaching down to the substrate. The co-deposited PEN:PFP film (Fig. 5.15b) exhibits a morphology very different from the pure PEN and PFP films. A highly corrugated morphology was found with a needle-like network and terraced areas (see inset in Fig. 5.15b) with $h = 17 \pm 2$ Å, which are attributed to steps of the (100) series found in the specular x-ray diffraction scan, *i.e.*, nearly upright standing molecules. The mean height of the needle-like crystallites *above* the terraced structure was 110 ± 20 Å, which agrees well with the value of $D = 130 \pm 10$ Å derived for the peak corresponding to $d = 6.65 \pm 0.05$ Å. On closer inspection, the needle-like crystallites exhibit characteristic angles of $132 \pm 10°$ and even a zigzag shape at several positions. Together with the low lattice spacing this is evidence for the long molecular axes being close to parallel to the substrate in this morphology. It points to domain boundaries between

[8]Using computational image analysis (Veeco NanoScope v5.3) the observed volume *above* a certain height level was analyzed and compared to the nominally deposited volume per unit area (μm^2) of films with $\theta = 300$ Å and 50 Å ($3 \times 10^{-2} \mu m^3$ and $5 \times 10^{-3} \mu m^3$, respectively).

symmetry-equivalent domains at the vertices, as also found for the morphology of lying alpha-sexithiophene [222]. The terraced structure possibly grows substrate-induced up to a certain critical thickness at which the film grows preferentially forming the needle-like structure (note that significant strain is present in the film). This hypothesis, however, needs to be further investigated for films with various θ-values.

The morphology of the layered PFP/PEN structure is shown in Fig. 5.15d and the PEN underlayer is depicted in Fig. 5.15c. PFP on PEN exhibits a terraced morphology very similar to PFP grown on SiO_x. The analysis of the film volume above the height level marked with an arrow in Fig. 5.15d yields a volume of $3 \times 10^{-3} \mu m^3$, which is evidence that at least one layer of PFP is fully closed under the islands. Note, that the thickness oscillations found in the specular scan in Fig. 5.12a corresponding to a layer thickness (52 ± 5 Å) can not stem from PEN alone, for which 40 ± 5 Åwas found. It equals θ of the PEN film although the AFM micrographs (Fig. 5.15c) proved the growth of islands. This indicates that PFP forms a closed interface on the thin PEN layer, *i.e.*, a wetting of the underlayer that gives rise to the thickness oscillations corresponding to an increased layer thickness. This finding is of high relevance for device applications based on bilayer structures, since it points towards maximum contact area at the PFP/PEN interface.

5.2.4 Vibrational spectroscopy

In addition, all samples were investigated by FT-IR as vibrational spectroscopy is highly sensitive to changes of the molecular environment [223–225], i.e the crystallization in different polymorphs and the molecular intercalation in case of mixed crystal structures. A characteristic part of the FT-IR spectra is shown in Fig. 5.16, and compared to a reference spectrum of PFP powder. In the region of C-H out-of-plane bending and stretching modes [207, 208], the most prominent PEN absorption (903.5 cm^{-1}, peak (1) in Fig. 5.16) in the spectrum of the co-deposited PEN:PFP film was shifted by +2.0 cm^{-1} with respect to the pure PEN film. This points to a different molecular environment of PEN molecules in the PEN thin film phase and the co-deposited film, since this shift is too low to be attributed to strong interactions like inter-molecular charge transfer. Moreover, in a recent study a comparable shift of this vibration of PEN in its bulk and thin-film phase was observed [182]. Vibrations of the pure PFP film were found at 920.0 cm^{-1}, 933.0 cm^{-1}, 974.5 cm^{-1}, and 980.0 cm^{-1} (peaks labeled (2)-(5) in Fig. 5.16), which was assigned to C-F in-plane stretch modes through comparison with

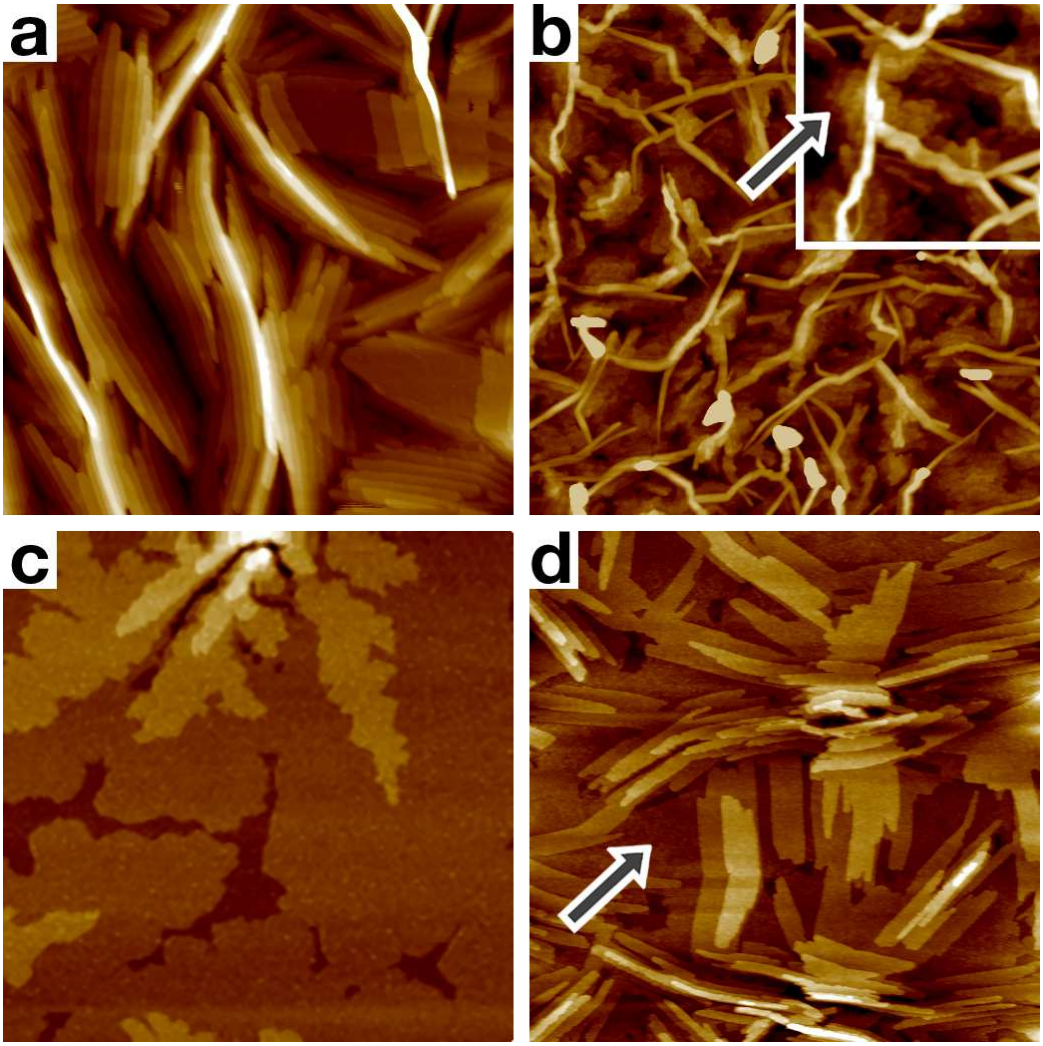

Figure 5.15: AFM micrographs of a PFP (a) and a co-deposited PEN:PFP (b) film of $\theta = 300\,\text{Å}$, of a PEN film of $\theta = 50\,\text{Å}$ (c), and a layered PFP/PEN film of $\theta = 50 + 50\,\text{Å}$ (d). The images show an area of $3 \times 3\,\mu m$, colours correspond to height levels of 200 Å range in (a) and (b), and 100 Å range in (c) and (d). The inset in (b) shows a $1 \times 1\,\mu m$ zoom. The arrow in (b) points to a region with steps of molecular height; in (d) the basis height level for a volume analysis of the PFP layer is marked (see text).

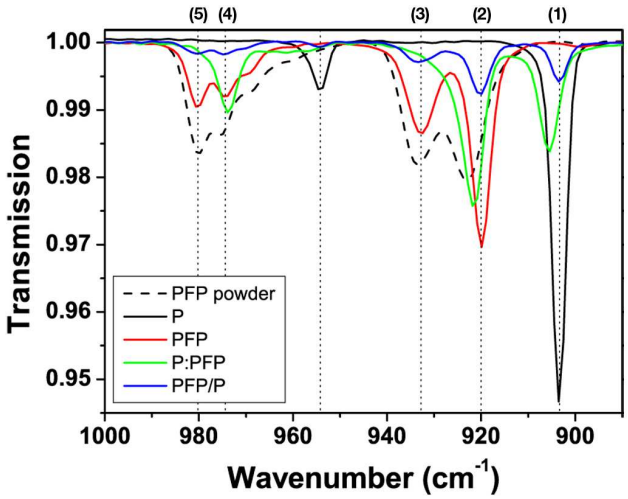

Figure 5.16: FT-IR spectra of a PEN, PFP, a co-deposited PEN:PFP film and a layered PFP/PEN film in comparison to a PFP reference. Vertical lines mark the peaks of the pure PEN and PFP films.

a calculated theoretical spectrum of PFP [226][9]. Peaks (2) and (3) are significantly shifted with respect to the PFP powder reference, which can be explained by the structural difference of the PFP thin-film phase and the bulk crystal structure. These peaks are also noticeably shifted with respect to the thin PFP film on a PEN underlayer, which supports the finding of the slightly different layer spacing observed by specular x-ray diffraction. The PFP single crystal structure exhibits a herringbone arrangement with two inequivalent molecules in the unit cell; the same holds for the PFP thin film structure. Therefore it is reasonable to suggest that peaks (2), (3) and (4), (5) are components of a Davydov-split peak (see Sec. 3.3) in both PFP powder and thin film [13, 142, 227]. For the co-deposited PEN:PFP film, only *two* single peaks can be observed in the vicinity of peaks (2) and (4), respectively, which is direct evidence for the intercalation of PEN and PFP in case of the co-deposited film. Since this film has been shown to be crystalline by x-ray diffraction, this evidences the growth of a mixed crystal of PEN:PFP with one PFP molecule per unit cell. Moreover, this result indicates that there exist no relevant film portions of pure *and* crystalline PFP, since even at $\theta = 50\,\text{Å}$ the missing peaks (3) and (5) are very well pronounced in the spectrum of the thin layered film.

[9]Calculation was performed by Georg Heimel (Institut für Physik, HU-Berlin, Germany) using Gaussian 03, Rev. C.02 using the modified Perdew-Wang (mPW) exchange functional, the Lee-Yang-Parr correlation functional (LYP) and the 4-31G** basis set (mPWLYP/4-31G**).

5.2.5 Summary

In conclusion, the unit cell parameters of the PFP thin-film phase on SiO_x were determined and the growth behaviour of PFP in heterostructures with PEN was explored. On a PEN underlayer, PFP exhibits a slightly larger lattice spacing compared to the PFP thin-film phase and forms a large area interface with P. Importantly, PFP was shown to form a mixed crystal if co-deposited with PEN with no detectable phase separation. The dependence of the PFP thin film crystal structure on the substrate has direct implications for the application of the n-type semiconducting material PFP in thin film transistors. For PEN it is already well established that the electron bandwidth depends on the specific crystal polymorph, which directly impacts the charge carrier mobility [228]. In analogy, a dependence of the charge-carrier mobility on the specific PFP polymorph can be expected. Therefore, the results demonstrate that polymorphism in PFP has to be taken into account when comparing charge carrier mobility values from different device structures.

5.3 Tuning the ionization energy of organic semiconductor films: The role of intramolecular polar bonds

In the previous section it was demonstrated that pentacene and perfluoropentacene form a mixed crystal structure comprising standing molecules in the case of co-deposition. For these prototypical conjugated organic molecules it is demonstrated in the following how the surface termination of ordered organic thin films with intramolecular polar bonds (i.e., -H versus -F) impacts the ionization energy. It is shown that the mixing of these differently terminated molecules on a molecular length scale allows continuously tuning the ionization energy of thin organic films between the limiting values of the two pure materials. This study shows that surface engineering of organic semiconductors via adjusting the polarity of intramolecular bonds represents a generally viable alternative to the surface modification of substrates to control the energetics at organic/(in)organic interfaces.
This work is published as Ref. [229].

5.3.1 Introduction

The mechanisms that govern surface and interface energetics of metals and conventional inorganic semiconductors are generally well understood today. In contrast, fairly little is known about the impact of surface termination on the electronic structure of organic semiconductor surfaces and the energy level alignment at organic/(in)organic heterojunctions. Recently, it was shown that an inhomogeneous charge-distribution within individual π-conjugated molecules impacts the ionization energy of and the charge injection barriers into organic thin films [70]. It was suggested that polar end-group substitution of a molecule should permit predictably adjusting the IE of ordered layers. Moreover, the proposed model also predicts that the IE of mixed ordered molecular layers, comprising two molecular species with different polar end-groups, should assume a value in between those of layers comprising only one compound.

In the present study, both is experimentally demonstrated: **(1)** IE tuning via molecular orientation and intramolecular polar bonds, and **(2)** IE tuning by appropriate mixing of two molecular species. For that purpose, the prototypical organic semiconductors PEN and PFP (see Sec. 4.1) were used. In thin films, both molecules have an almost upright standing orientation on SiO_x substrates [24, 168, 171, 198, 199, 216], a common gate dielectric in organic field effect transistors. In such PFP films the surface is terminated by

strongly polar bonds; the strongly electronegative fluorine carries a negative partial charge [δ^-] compared to the backbone carbon atoms [δ^+] leading to a surface dipole moment ($\vec{\mu}$) pointing towards the molecular cores. In PEN, only a small positive partial charge [δ^+] on the hydrogen atoms compared to the conjugated backbone [δ^-] exists. The latter thus leads to a (small) surface dipole pointing in the opposite direction compared to PFP (both molecules do not exhibit any external net dipole moment). The existence of a (molecular orientation dependent) surface dipole layer affects the IE [70] (see Sec. 2.1.3 and 3.2), since it causes a jump in the electrostatic potential energy, hence shifting the vacuum level (E_{vac}) [50, 57, 230].

5.3.2 Electronic structure

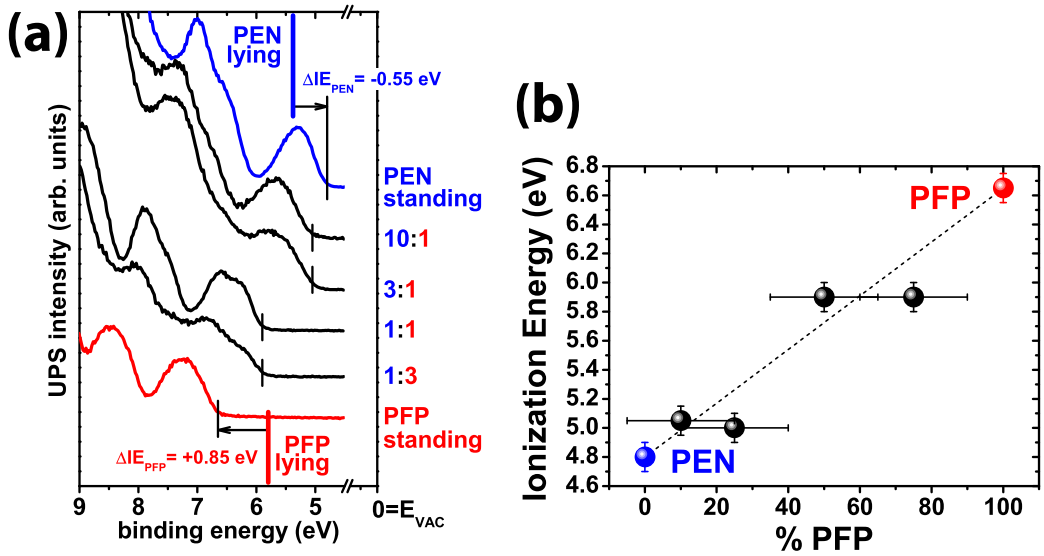

Figure 5.17: (a) UPS spectra of pure and mixed films of standing PEN and PFP on SiO_x. The vertical lines indicate the photoemission onsets (*i.e.*; the IE values of lying PEN and PFP on Au(111) [169] are given for comparison). (b) Ionization energies deduced from the UPS spectra of (a) in dependence of the PFP ratio.

(1) The UPS (see Sec. 3.2) results for PEN and PFP films of nominally 3.2 nm thickness on SiO_x substrates (ca. 2 layers of *standing* molecules) demonstrate the effect of surface termination of organic solids by polar intramolecular bonds on their IE; values of *lying* molecular layers of PEN and PFP on Au(111) [169] are indicated for comparison (Fig. 5.17a). Clearly, highly orientation dependent IEs for both molecules are observed, however,

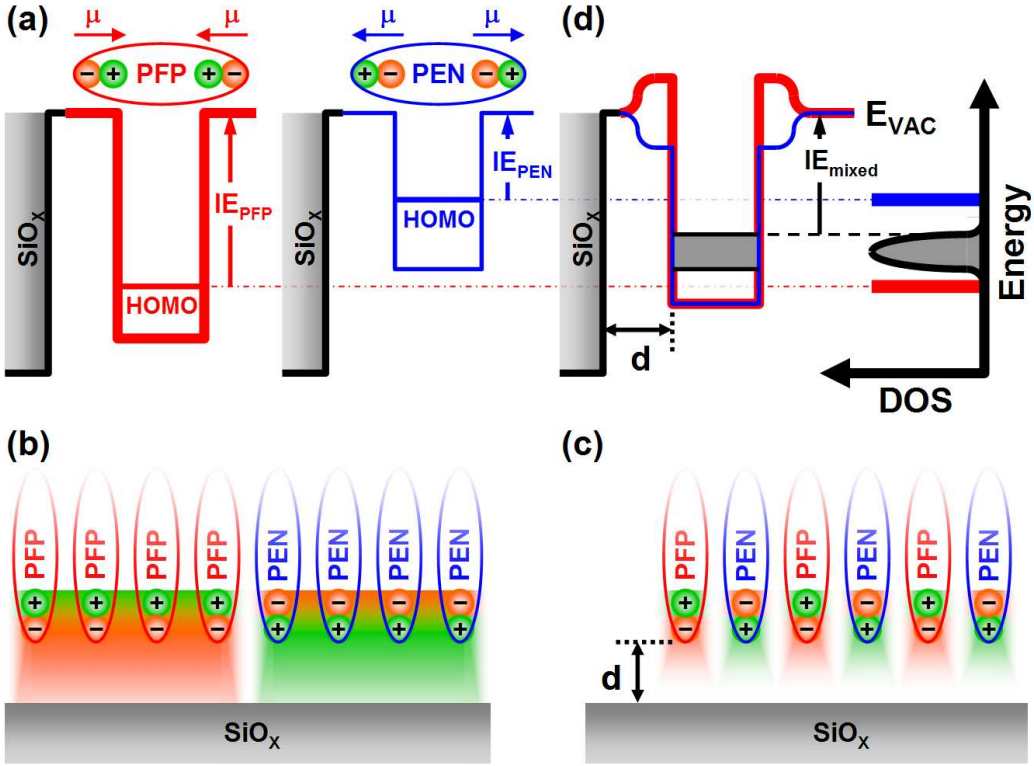

Figure 5.18: (a) Schematics of the pure film energetics; (b) the electrostatic potential at the organic/SiO_x interface for the (hypothetical) case of large-scale phase separation, and (c) molecular-level mixing, where orange (green) indicates regions of higher (lower) electron potential energy; the white area between molecules and substrate indicates an intermediate value. (d) Schematic of the mixed film energetics. For details see text.

with opposite trends between standing and lying orientation: For PEN, the IE of the standing molecules (4.80 eV) is *lower* than that of lying molecules (5.35 eV) [169], whereas the layer of standing PFP exhibits a *higher* IE value (6.65 eV) than that of lying molecules (5.80 eV) [169]. The oppositely oriented dipolar surface terminations of PEN and PFP films (due to different intramolecular dipolar bonds exposed at the surface) strongly impacts the IEs values in the anticipated way: The difference between the lying/standing IE for PEN layers is $\Delta IE_{PEN} = -0.55$ eV while for PFP this difference is $\Delta IE_{PFP} = +0.85$ eV.

(2) The remarkably high IE difference between standing PEN and PFP of 1.85 eV suggests that mixing the two molecules in different ratios should allow a gradual shift of the thin film IE between the values of pure PEN

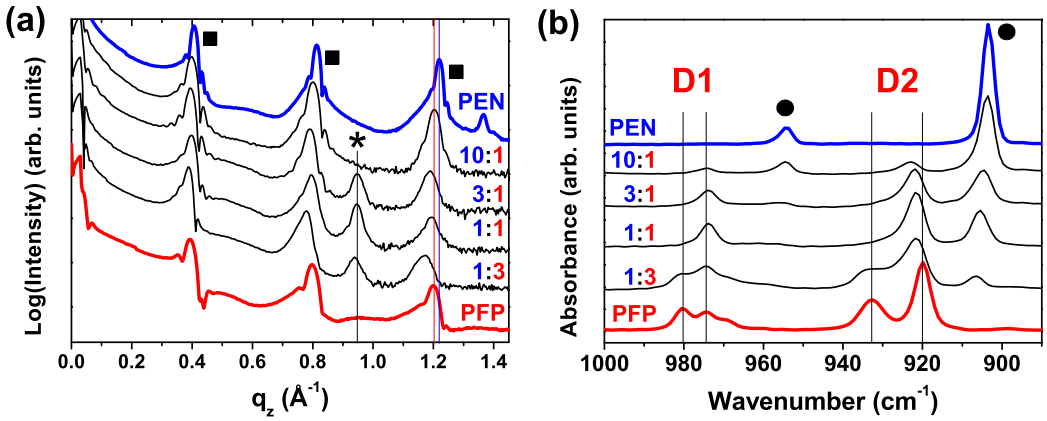

Figure 5.19: (a) XRD data on films of pure and mixed (3:1, 1:1 and 1:3) PEN and PFP; q_z denotes the vertical momentum transfer; squares indicate peaks originating from standing molecules; the star marks a second molecular orientation in the mixed films. (b) FT-IR spectra of the respective samples; D1 and D2 denote two Davydov-split peaks of PFP, the circles mark C-H vibrations of PEN that are not split.

and PFP, thus 'dialling in' the overall IE of the organic semiconductor film. In order to demonstrate this effect, two requirements must be met by the samples: (i) the molecules in mixed film must still adopt a standing orientation, and (ii) mixing of PEN and PFP must occur on the molecular length-scale. Long-range phase separation, *i.e.,* adjacent patches of pure PEN and PFP, would lead to *individual* vacuum level alignment of the PEN and PFP patches with the SiO_x substrate, thus simply yielding a superposition of the respective UPS spectra, as schematically shown in Fig. 5.18a-b. Only if the lateral distance between the two different molecular species is sufficiently small (Fig. 5.18c), *i.e.*, in the range of the molecule-substrate adsorption distance (d), the interface layer of alternating dipoles leads to the formation of a *common* electrostatic potential on the length scale of d, which is then aligned with the surface potential of the SiO_x substrate [231]. Only in this case an overall IE_{mixed} between the extreme cases of the pure films can be observed (Fig. 5.18c-d).

5.3.3 Structural properties

Crystalline mixed (on a molecular length-scale) PEN and PFP thin films were realized via vacuum co-deposition of PEN and PFP on SiO_x; the error of the mixing ratio is estimated to 15%. For the investigated mixing ratios XRD (see Sec. 3.1) results (Fig. 5.19a, experimental values in Tab. 5.1) show a peak

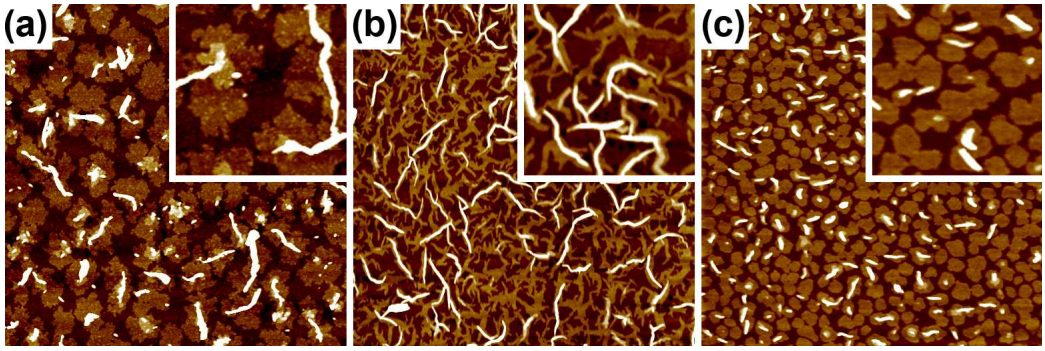

Figure 5.20: AFM micrographs of the set of samples of the UPS investigations showing mixed films of PEN:PFP with mixing ratios of 3:1 (a), 1:1 (b) and 1:3 (c); the image area is $5 \times 5\,\mu m^2$; the inset area is $1.2 \times 1.2\,\mu m^2$ colours correspond to a height scale of 5 nm.

series corresponding to *standing* molecules with an increased lattice spacing compared to the pure PEN and PFP thin film phases [23, 168, 198, 199]. In addition, XRD provides evidence for the presence of a differently oriented (almost lying) mixed film phase with a lattice spacing independent of the mixing ratio (marked with a star in Fig. 5.19a), which is attributed to a 1:1 phase of PEN and PFP. FT-IR spectroscopy (see Sec. 3.3) proves the intercalation of PEN and PFP on the molecular scale, because the Davydov-splitting of lines D1 and D2 found in pure PFP films (D1 and D2 in Fig. 5.19b) is removed in mixed films[10].

5.3.4 Morphology

To get an insight into the morphology of the investigated structures AFM investigations (see Sec. 3.4) were carried out on the same set of co-deposited samples of 3.2 nm nominal thickness, on which the UPS investigations were performed[11]; representative AFM micrographs are shown in Fig. 5.20. Apparently there exist two different morphologies, which can be assigned to the two crystalline orientations found by specular XRD. More than 85% of the exposed sample surface area exhibits the standing molecular orientation with characteristic steps of 1.5±0.2 nm height (as measured by elevation histograms), which is in agreement with the lattice spacing of *standing* molecules

[10]The mixed film with PFP majority (1:3) seems to contain a certain portion of pure crystalline PFP, as evidenced by the remaining Davydov-components at higher wavenumbers in Fig. 5.19b.

[11]The AFM investigations were done by Rolf Kniprath (HU-Berlin).

Table 5.1: Experimental results of the various experiments. This table summarizes the values deduced from the UPS, XRD and FT-IR experiments on films of nominal thickness (χ); IE denotes the ionization energies; d(S) the lattice spacing of the dominant (standing) diffraction series, d(L) the spacing of the peaks marked with a star in Fig. 5.19a (lying orientation), D(S) and D(L) the out-of-plane crystalline coherence length deduced from the Scherrer-formula [113] for the standing and lying orientations, respectively; ν_i denote vibrations found in the FT-IR spectra of Fig. 5.19b; increasing indices i are chosen for increasing wavenumber values.

	χ (nm)	IE (eV)	d(S)	d(L)	D(S) (nm)	D(L)	ν_1	ν_2	ν_3	ν_4 (cm^{-1})	ν_5	ν_6
PEN/Au[a]		5.35										
PEN	3.2	4.80										
PEN	30		1.545		39.8		903.5			954.1		
10:1	3.2	5.05										
10:1	30		1.570		24.8		904.0			954.5		
3:1	3.2	5.00										
3:1	30		1.590	0.66	25.1	22.0	904.8	922.1			974.0	
1:1	3.2	5.90										
1:1	30		1.580	0.66	24.5	25.1	905.6	921.6			973.9	
1:3	3.2	5.90										
1:3	30		1.615	0.67	24.4	19.4	906.6	921.7	934.1		974.3	980.8
PFP	3.2	6.65										
PFP	30		1.575		23.7			920.0	932.8		974.3	980.4
PFP/Au[a]		5.80										

[a] The values for the lying conformation on Au(111) were taken from Ref. [169], as the IE value of flat-lying monolayers plus 0.2 eV screening to account for interface effects [135].

deduced from XRD (lattice spacing d(S) in Tab. 5.1); no characteristic steps were observed for the second needle-like morphology. Detailed AFM investigations revealed that more than 95% of the SiO_x substrate for all samples was covered by the organic layers. However, since the needle-like structure exists in all three samples and since it exhibits pronounced characteristic angles (most apparent in case of the 1:1 film, which was already reported for thick films of $\chi = 30\,\mathrm{nm}$ [168], see Sec. 5.2) this morphology is assigned to the sample portion giving rise to the XRD-peak (marked with $*$ in Fig. 5.19a) corresponding to lying molecules (lattice spacing *d(L)* in Tab. 5.1). The elevation histograms of the AFM micrographs yield a coverage of the second layer of the standing morphology of 65±3 % for the 3:1, of 50±3 % for the 1:1 and of 65±3 % for the 1:3 mixed film thus pointing to an increase of the lying morphology in the 1:1 case (note that the corresponding XRD-peak in Fig. 5.19a is also increased compared to the other ratios). The area ratio of the lying morphology is 9±3 % (3:1), 15±3 % (1:1) and 8±3 % (1:3).

As evidenced by the combination of XRD, FT-IR and AFM, mixed films of PEN and PFP could be achieved via co-deposition and can therefore be used to experimentally verify prediction **(2)**: a gradual change of the IE depending on the mixing ratio was observed (Fig. 5.17). Since the IE is a *macroscopic* material property, the *internal* electronic structure of the mixed organic semiconductor bulk is not directly accessible (Fig. 5.18d). The lying morphology with an area ratio of less than 20% found by XRD and AFM contributes very little to the UPS signal, since UPS is an area-averaging (over ca. $1\,\mathrm{mm}^2$) surface sensitive technique. However, it gives rise to a larger error bar of the IE values (Fig. 5.17b) and accounts for the deviations from a strict linear dependence of the IE on the PEN:PFP mixing ratio. The IE values deduced from the UPS spectra are summarized in Fig. 5.17b and Tab. 5.1.

5.3.5 Electrostatic modeling

In more detail, lying PEN and lying PFP exhibit the *same* surface termination, *i.e.*, the negatively charged π-system. Therefore, the difference in IE (0.45 eV) can *not* be attributed to polar intramolecular bonds. Subtracting this value from the difference in IE between the respective standing layers (1.85 eV) yields the contribution of the different surface termination in that case (1.40 eV). Applying the Helmholtz equation, one can deduce from this difference in potential energy a difference in the surface dipole area-density of ≈0.01 Debye per bohr^2 between pure layers of PEN and PFP. In order to assess the molecular-scale electrostatics at the organic/vacuum and organic/substrate interfaces in mixed PEN:PFP films on SiO_x, the following model system for the surface termination of the molecular films was consid-

ered: For PFP molecules, a negative point charge represents the F-atoms and a positive point charge represents the closest C-atoms on the backbone; for PEN, the reverse is assumed, *i.e.*, a positive point charge for the H-atoms terminating the surface of layers of standing molecules and a negative point charge for the closest C-atoms on the backbone. The separation of these charges in the direction perpendicular to the surface of layers of standing molecules (z-direction) was chosen to be 2 bohr. The electrostatic potential for a single row (arranged perpendicular to the surface normal) of 24 of such dipoles (separated by ≈ 10 bohr ≈ 5 Å $\approx$ intermolecular distance) was then calculated; this proved to be sufficient to eliminate "edge"-effects for the potential around the central 12 dipoles in this row, which are considered in the following (Fig. 5.21). To capture the two-dimensional aspect of a surface, the problem was treated in two-dimensional electrostatics, *i.e.*, the structure described above can be thought of being infinitely extended into and out of the plane of drawing. Note that, in two-dimensional electrostatics, the potential, V, of a point charge is $V(r) \propto -2\ln(r)$ rather than the familiar $V(r) \propto 1/r$. In this model, the above-mentioned surface dipole density translates into values of $\pm 0.01\, q_e$, respectively, for all point charges; q_e denotes the elementary charge. V was then calculated by numerically summing the contributions of all point charges.

In Fig. 5.21a, the potential energy for electrons, $E = -q_e V$, above the surface of a model for a mixed (1:1) and macroscopically phase separated PEN:PFP film is shown. The patches are assumed to consist of 4 molecules each, and their respective surface termination is represented by four adjacent dipoles pointing in the same direction. In Fig. 5.21b, the same is shown for the case of mixing at the molecular scale, *i.e.*, adjacent dipoles are of opposite direction. Locally, above the plus-terminated domains (Fig. 5.21a) or molecules (Fig. 5.21b), one observes regions of lower potential energy and above the minus-terminated portions, one observes regions of higher potential energy. At some distance from the dipole-terminated surfaces, the differences in local surface potential average out (*i.e.*, the fluctuations are below an experimentally accessible value of 20 meV) and a common vacuum level, E_{vac}, is established. Importantly, this distance is much larger in the case of macroscopic phase separation ($D = 55$ bohr in Fig. 5.21a) than in the case of mixing at the molecular scale ($d = 14$ bohr) in Fig. 5.21b), *i.e.*, it scales linearly with the area of the domains of pure PEN and PFP. Now, the two mixed organic semiconductors are brought in contact with a substrate at an average molecule-substrate distance in the range of several Å $\approx d$ (Fig. 5.21c-d). Clearly, a common E_{vac} is already established in the case of molecular-level mixing, while the local surface potential below the phase separated films is still strongly inhomogeneous (fluctuations in the order of 0.3 eV). As vac-

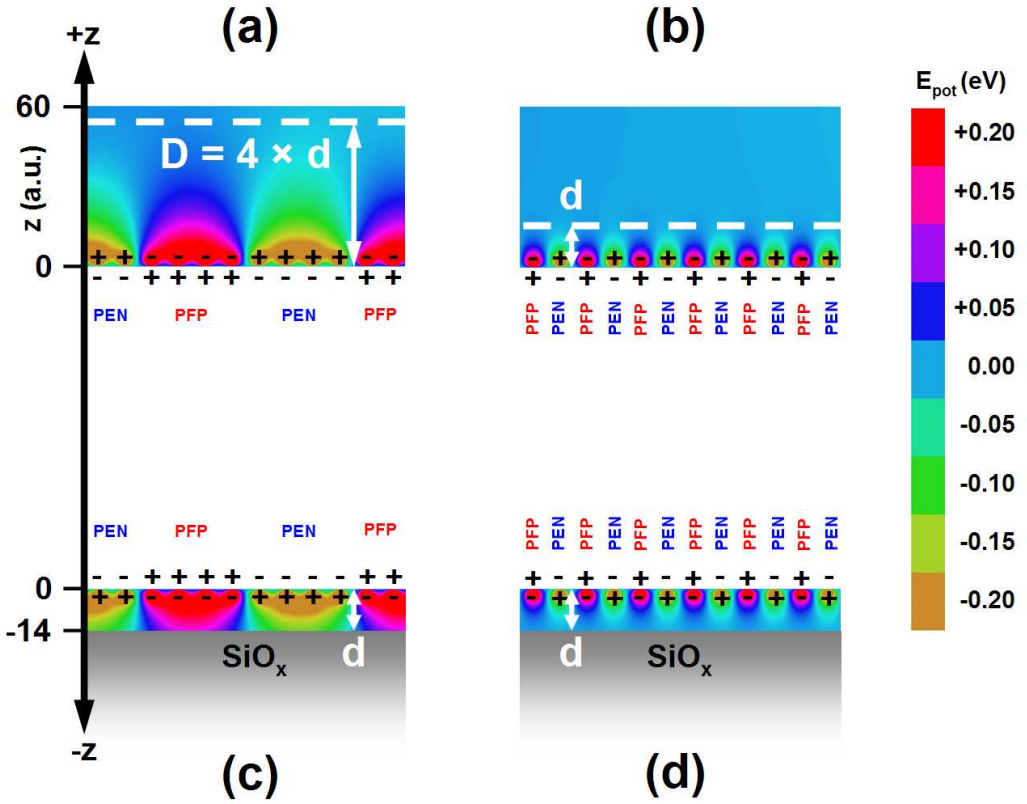

Figure 5.21: Electrostatic potential energy for electrons in atomic units (see color bar) above the surface of the model for a macroscopically phase separated mixed (1:1) PEN:PFP film of standing molecules (a). The same is shown in (b) for the case of mixing at the molecular scale. D and d indicate the approximate distance at which a common vacuum level is established; distances are given in bohr (atomic units). The local interface potential at the contact region between the mixed organic semiconductor and a SiO_x substrate is shown in (c) and (d) for the cases of large-scale phase separation and mixing at the molecular level, respectively.

uum level alignment prevails at the interface between most organic molecular films and SiO_x, the common vacuum level below the molecular film aligns with the vacuum level above the (homogenous) SiO_x in the case of molecular mixing. In the case of phase separation, vacuum level alignment occurs for each domain of pure PEN or PFP individually[12].

[12]All electrostatic calculations were carried out by Georg Heimel (HU-Berlin)

5.3.6 Summary

In conclusion, it was shown that the surface termination of ordered organic thin films with intramolecular polar bonds can be used to tune their IE. The collective electrostatics of these oriented bonds also explains the pronounced orientation dependence of the IE. Furthermore, mixing of differently terminated molecules on a molecular length scale allows continuously tuning the IE of thin organic films between the limiting values of the two pure materials. This study shows that surface engineering of organic semiconductors via adjusting the polarity of intramolecular bonds represents a viable alternative to the surface modification of substrates to control the energetics at organic/(in)organic interfaces.

5.4 Molecular-orientation dependent energy levels of pentacene and pentacenequinone

Ultraviolet photoelectron spectroscopy was used to investigate the energy level alignment at contacts between PEN and Ag(111) in the presence of interfacial PQ. Depending on the metal pre-coverage with PQ, evidence for three distinctly different interface morphologies and molecular orientations was found, which significantly change of the energy level alignment, in particular the ionization energies. Consequently, the hole injection barrier between PEN and Ag(111) varied between 1.1 eV (pristine Ag) and 0.45 eV (5.4 nm PQ precoverage on Ag). In addition, the UPS results suggest that PQ can act as deep trap for electrons in a PEN matrix. Depending on the exact mutual orientation of PQ and PEN, the depth of these traps can be in the range of 0.2 eV to 0.75 eV. Most of this work is published as Ref. [185][13].

5.4.1 Introduction

Besides application-oriented studies, significant research efforts are directed towards an understanding of fundamental physical properties of organic molecular crystals and thin films, particularly with regard to the nature of charge transport and charge carrier mobility. In order to access the intrinsic mobility of charge carriers, samples of exceptional high purity are needed [232]. Besides structural defects, chemical impurities can significantly complicate the evaluation of intrinsic material properties [233]. Particularly, chemical defects can act as deep charge carrier traps. The presence of 6,13-pentacenequinone (PQ) in a PEN matrix has been identified as a "key" chemical defect lowering carrier mobility [77]. Moreover, in order to measure charge carrier mobilities, or to fabricate field effect transistors, contacts between the organic material and metal electrodes are ubiquitous. The importance of the energy level alignment at organic/metal interfaces has been pointed out in many studies [54, 57] (see Sec. 2.1.3). One may speculate that some PQ is formed on the surface of PEN crystals due to photo-oxidation, as, *e.g.*, was shown for tetracene single crystals [233]. If that were the case, the energy level alignment at interfaces between PEN and metals may be altered significantly by the presence of interfacial PQ. The aim of the present study was to investigate the energy level alignment between PEN and PQ with respect to the applicability as OPVC and the effects of PQ presence on the interface energetics between an electrode material (Ag) and PEN.

[13]The data analysis of this section was led by Norbert Koch.

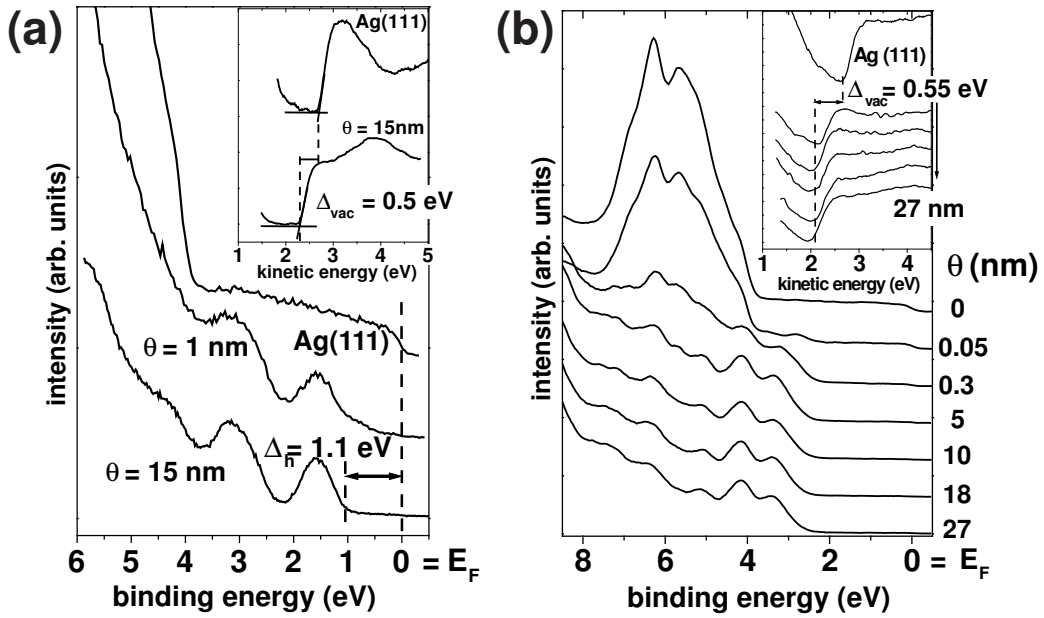

Figure 5.22: (a) Molecular structure and UPS spectra for increasing coverage (θ) of (a) PEN on Ag(111), and (b) PQ on Ag(111). Insets: secondary electron cutoffs.

5.4.2 Electronic structure

PEN on Ag(111)

The energy level alignment (see Sec. 3.2 and 2.1.3) of PEN on polycrystalline Ag has been reported before [59, 234]. In Fig. 5.22a the results obtained for PEN on Ag(111) are briefly summarized. For a nominal coverage (θ_P) of 15 nm, the peak derived from the PEN HOMO is centered at a binding energy (BE) of 1.5 eV. The HOMO low-BE onset is found 1.1 eV below E_F of Ag; this value corresponds to the hole injection barrier (Δ_h) at the interface. At lower θ_{PEN}, this value for the barrier approaches 1.0 eV, which is attributed to more efficient photo-hole screening close to the metal surface, observed for essentially all metal/organic interfaces without strong chemical interactions (see Sec. 3.2). The sample work function (ϕ) changed from 4.45 eV for pristine Ag(111) to 3.95 eV for 15 nm PEN, inferred from the change in kinetic energy of the SECO shown in the inset of Fig. 5.22a. Due to the weak interaction between Ag and PEN, this interface dipole is attributed to the "push-back" effect of electrons spilling out into vacuum for the clean Ag surface (see Sec. 2.1.3). The IE of PEN was determined to be 5.0 eV for this sample. A physisorption-like interaction between Ag and PEN can be assumed since

no charge-transfer (*e.g.*, from Ag to the PEN lowest unoccupied molecular orbital) induced new spectral intensity can be seen below the HOMO-derived peak. The first few layers of PEN are most likely oriented with their long molecular axes parallel to the Ag surface [235], however, a change to an almost vertical orientation of PEN molecules at higher θ_{PEN} can be expected [236].

PQ on Ag(111)

The evolution of photoemission spectra for PQ deposited on Ag(111) is shown in Fig. 5.22b. For a PQ coverage (θ_{PQ}) of 27 nm the emission feature centered at 3.4 eV can be attributed to be derived from the PQ HOMO. The onset is found 2.6 eV below E_F; this value also corresponds to Δ_h. As expected, spectra at lower θ_{PQ} are shifted towards lower BE (due to better screening efficiency, see above), such that Δ_h equals 2.4 eV for $\theta_{PQ} = 0.3$ nm. The sample work function changed from 4.45 eV for pristine Ag(111) to 3.9 eV, very similar to PEN/Ag(111). This points towards a similarly weak interaction between PQ and Ag, which is further supported by the lack of photoemission features in the energy gap of PQ throughout the deposition sequence. The IE for PQ in the 27 nm thick film is 6.5 eV. It is reasonable to assume that also the first few layers of PQ are oriented with their long molecular axes parallel to the Ag surface, supported by the fact that the photoemission (PE) intensity of the substrate (close to E_F) is already substantially quenched at $\theta_{PQ} = 0.3$ nm. For higher θ_{PQ}, a transition towards vertically inclined PQ molecules is possible. Furthermore, island growth of PQ after monolayer formation can be proposed, since close inspection reveals that the reduction of the photoemission signal from the substrate is less efficient for coverages beyond 0.3 nm. Even for $\theta_{PQ} = 27$ nm a low PE intensity can be seen at E_F. In order to investigate the influence of the presence of PQ on the energy level alignment at interfaces between Ag and PEN, Ag(111) surfaces were pre-covered with PQ layers of three different thicknesses before the deposition of PEN.

PEN on PQ pre-covered Ag(111)

The lowest PQ pre-coverage of only 0.05 nm (denoted as *case 1* in the following) has negligible influence on the observed energy levels of PEN films on Ag(111) (see Fig. 5.23a). The HOMO-onset for the PQ sub-monolayer is found at 2.35 eV below E_F. For *case 1*, the sequence of spectra for different film thicknesses of PEN is virtually identical to that obtained for PEN deposited on clean Ag(111). Already at low θ_{PEN}, a clear PE signature of

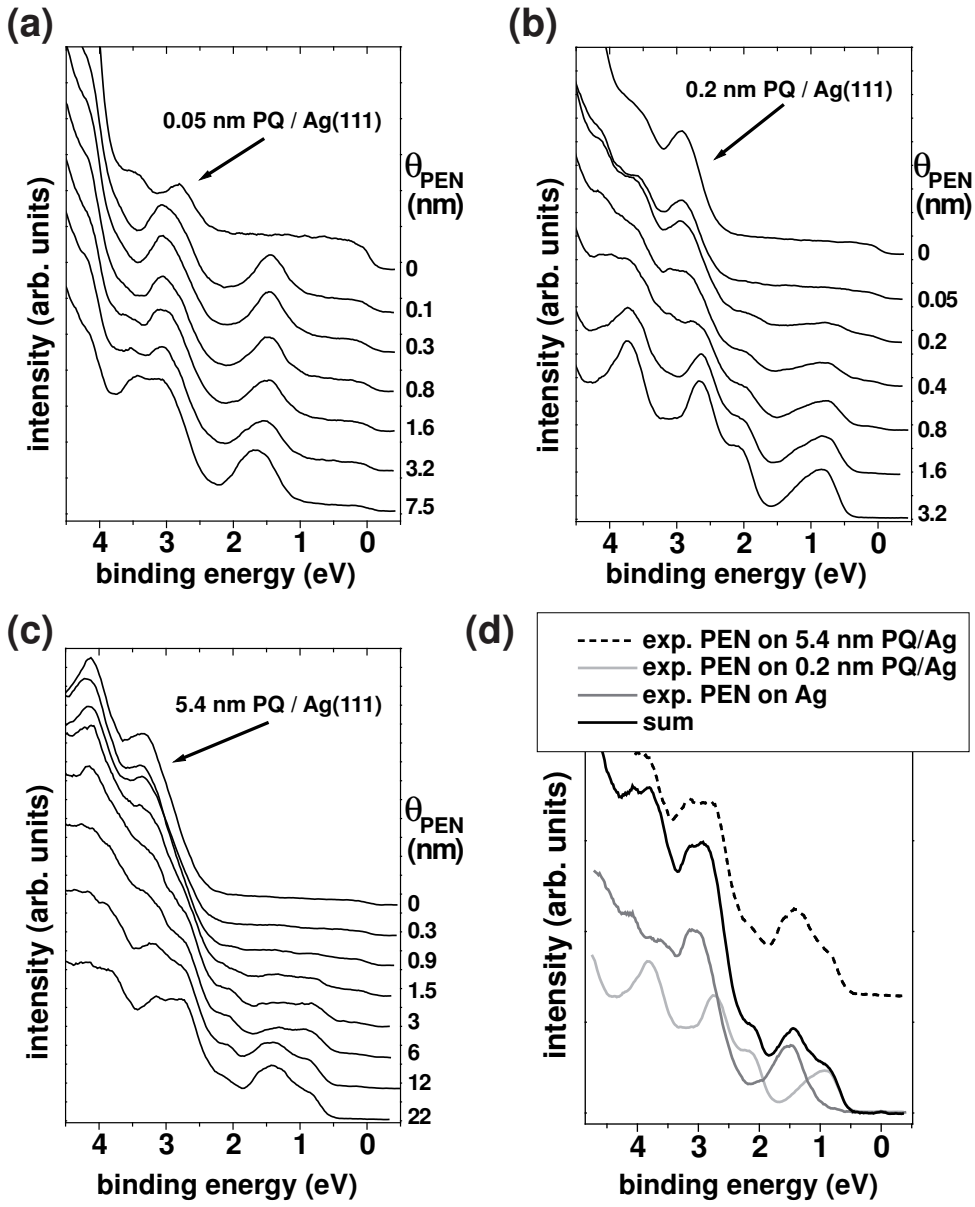

Figure 5.23: UPS spectra for increasing PEN coverage (θ_{PEN}) on Ag(111) pre-covered with (a) *case 1*: 0.05 nm PQ, (b) *case 2*: 0.2 nm PQ, and (c) *case 3*: 5.4 nm PQ. (d) Experimental (dashed) and simulated (thick solid) UPS spectra of PEN on 5.4 nm PQ/Ag(111). For details see text.

the PEN HOMO is visible, with the center at 1.45 eV BE and the low BE-onset at 1.0 eV. Increasing θ_{PEN} leads to the expected screening-related shift towards higher BE, and the position of the HOMO-onset reaches 1.15 eV for $\theta_{PEN} = 7.5$ nm. Consequently, the offset between the HOMOs of PQ and PEN is 1.35 eV at low θ_{PEN} and 1.2 eV at high θ_{PEN}. Note that the lineshape of the HOMO-derived peak at monolayer-range coverage (ca. 0.3 nm) is rather symmetric, and becomes only slightly asymmetric for higher coverages. The lineshape of monolayer PEN/Ag(111) resembles that reported for PEN on highly oriented graphite [81, 175], indicating flat-lying PEN molecules. Since a finite PE intensity at E_F is still observed for $\theta_{PEN} = 7.5$ nm, it can be concluded that PEN growth results in the formation of multilayer islands, with a few uncovered patches of Ag being present. The overall lineshape and peak intensity ratios of the high coverage PEN film corresponds well to PE spectra obtained for PEN samples, where the long molecular axes of PEN are oriented *parallel* to the substrate surface [81, 175]. The total change in the SECO position for this sequence is 0.55 eV, *i.e.*, a final of ϕ 3.9 eV is obtained.

Increasing the PQ pre-coverage of Ag(111) to 0.2 nm (ca. one monolayer, denoted as *case 2*) leads to a remarkable change in the energy level position and morphology of subsequently deposited PEN films (Fig. 5.23b). The HOMO-onset for PQ is found at 2.4 eV BE. In contrast to *case 1*, the intensity of PEN-derived spectral features is lower at comparable nominal θ_{PEN}. In addition, the lineshape of the HOMO-derived PE feature is highly asymmetric, and the intensity ratios of individual features from PEN are rather different in comparison to Fig. 5.23a. PE spectra of this kind have been reported for PEN samples, where the long molecular axes are almost *perpendicular* to the substrate surface, *e.g.*, pentacene films on SiO_x [81, 175]. For these two reasons, it can be concluded that the same molecular orientation of PEN prevails in the present sample. Virtually no PE intensity at E_F is observed for $\theta_{PEN} = 3.2$ nm, suggesting a close-packed molecular film. Most strikingly, the HOMO-onset of PEN is now found at 0.45 eV BE ($\theta_{PEN} = 3.2$ nm, corresponding to ca. two upright standing molecular layers of PEN), *i.e.*, ca. 0.7 eV lower than for PEN/Ag(111) and PEN/0.05 nm PQ/Ag(111) (*case 1*). Consequently, the HOMO-offset (Δ_{homo}) between PQ and PEN for this sample is 1.95 eV. The total change in the SECO position for this sequence is 0.5 eV, *i.e.*, a final ϕ of 3.95 eV is obtained, resulting in an IE of 4.4 eV.

In the third set of experiments, Ag(111) was pre-covered with 5.4 nm PQ prior to the deposition of PEN (Fig. 5.23c, *case 3*). Since at this PQ coverage multilayers are present, the HOMO-onset for PQ is found at 2.45 eV BE. The spectra obtained for PEN on top of this PQ layer do not resemble

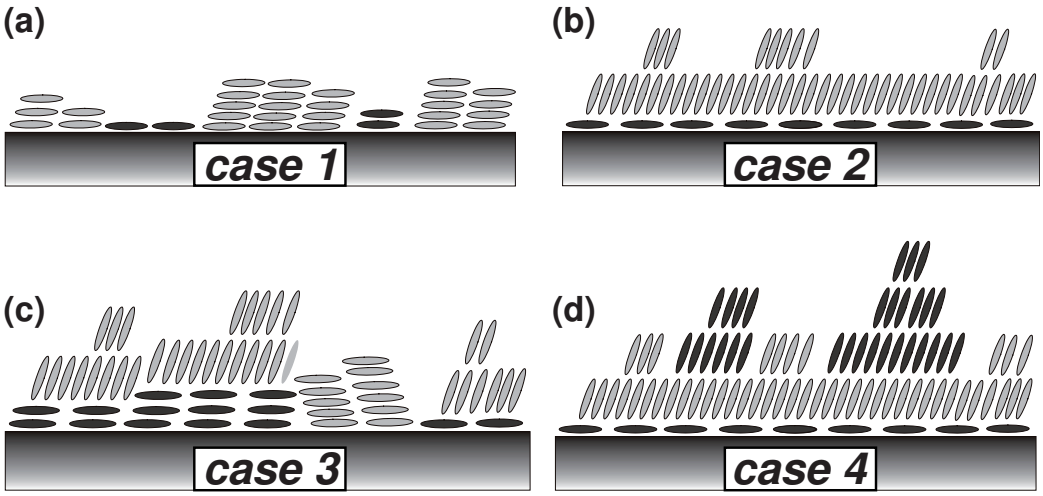

Figure 5.24: Schematic morphology and molecular orientation for (a) PEN on 0.05 nm PQ/Ag(111), (b) PEN on 0.2 nm PQ/Ag(111), (c) PEN on 5.4 nm PQ/Ag(111), and (d) for PQ on 3.2 nm PEN/0.2 nm PQ/Ag(111). Dark: PQ, light: PEN.

any of the two former cases. Rather than just a single new spectral feature between the PQ HOMO and E_F, two features are now observed, centered at ca. 0.85 eV and 1.35 eV BE. The low BE onset of these features is 0.45 eV below E_F at low coverage, and at 0.55 eV for $\theta_{PEN} = 22$ nm. It is unreasonable to assume that a chemical reaction between PEN and PQ leads to the splitting of the PEN HOMO-derived feature at low BE. Rather, a more complex organic/organic heterolayer morphology, in conjunction with the molecular orientation-dependent energy level alignment shown for the two previous cases, *case 1* and *case 2*, can be invoked to explain the spectra of Fig. 5.23c. In fact, these spectra can be reproduced by a superposition of spectra obtained for *case 1* (PEN on 0.05 nm PQ/Ag(111), which is virtually identical to PEN on pristine Ag(111)) and *case 2* (PEN on 0.2 nm PQ/Ag(111)). This is demonstrated in Fig. 5.23d, where the experimentally obtained PE spectrum for PEN on 5.4 nm PQ/Ag(111) is compared to the sum of appropriately scaled bottom-most spectra from Fig. 5.23a (contribution from Ag substrate subtracted) and Fig. 5.23b. From this it can be concluded that the nominally 5.4 nm thick PQ film on Ag(111) must be discontinuous, exposing some bare Ag areas. Interestingly, this was not the case for the 0.2 nm PQ film on Ag(111), where only one type of PEN energy levels was seen. A possible explanation for this could be a morphology change for PQ on Ag(111) after the completion of a monolayer. Details shall

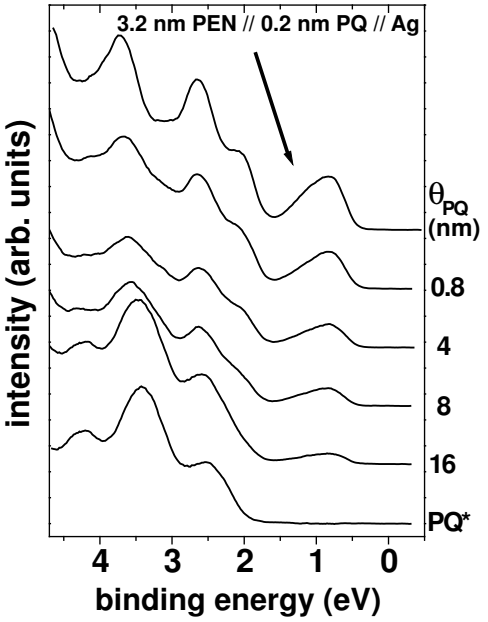

Figure 5.25: UPS spectra for increasing PQ coverage (θ_{PQ}) on 3.2 nm PEN/0.2 nm PQ/Ag(111); *case 4*. The spectrum denoted as PQ* is the result of the subtraction of an appropriately scaled PEN spectrum from the spectrum with $\theta_{PQ} = 16$ nm exhibiting a *lower* HOMO-onset of 1.95 eV BE in comparison to 2.6 eV for PQ/Ag(111).

be investigated in future studies. Schematics of the three sample morphologies proposed above, including deduced relative molecular orientation, are depicted in Fig. 5.24a-c.

PQ on a PEN monolayer on PQ pre-covered Ag(111)

In order to further investigate the impact of relative molecular orientation at organic/organic heterojunctions on the interface energetics, PQ was deposited onto the closed PEN layer existing on 0.2 nm PQ pre-covered Ag(111) (denoted as *case 4*). The starting point thus was the sample whose PE spectrum is shown as bottom-most in Fig. 5.23b, *i.e.*, *case 2*. Increasing θ_{PQ} on this sample leads to an attenuation of PEN features (most notably seen for the PEN HOMO in Fig. 5.25), and at $\theta_{PQ} = 16$ nm the spectrum resembles mostly that of PQ, except for a still weak emission originating from the PEN HOMO (centered at ca. 0.8 eV BE). This obvious PE signature of PQ (to be compared with Fig. 5.22b) becomes clearer after subtraction of an appropriately scaled PEN spectrum. The resulting spectrum is indicated by PQ* in Fig. 5.25. Notably, the HOMO-onset of this PQ layer grown on PEN is at 1.95 eV BE, in contrast to the 2.6 eV obtained for PQ of comparable thickness on pristine Ag(111). This energy difference of 0.65 eV parallels that obtained for the PEN on pristine and differently PQ pre-covered Ag surfaces of ca. 0.7 eV, as recognized in comparing Fig. 5.23a to Fig. 5.23b. Δ_{homo} (between PQ and PEN) for PQ on 3.2 nm PEN/0.2 nm PQ/Ag(111) is thus

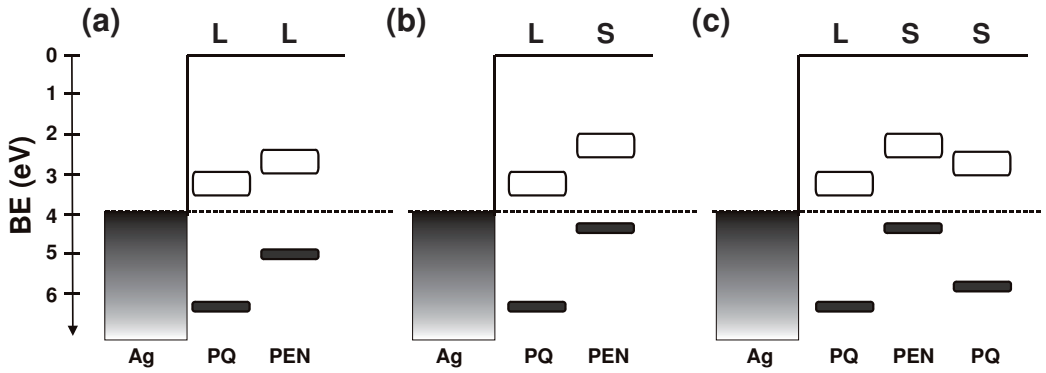

Figure 5.26: Summary of experimentally observed energy level diagrams of PEN and PQ hetero-layers on Ag(111) demonstrating the orientation dependence of the IE. (a) *case 1*, (b) *case 2*, and (c) *case 4*; *case 3* is a mixture of (a) and (b). The open symbols for the LUMO levels were chosen broader than the HOMO levels since they were not directly measured in this study. According to the schematic in Fig. 5.24 L and S denote layers of lying and standing molecules, respectively.

1.95 eV - 0.45 eV = 1.5 eV. Interestingly, within the error-bar due to screening effects (±0.1 eV), this value is very similar to those found for PEN and PQ grown separately on Ag(111) (ca. 1.5 eV; Fig. 5.22a and Fig. 5.22b) and PEN grown on 0.05 nm PQ/Ag(111) (1.35 eV; Fig. 5.23a; *case 1*). All these values are markedly smaller than the HOMO values measured for *case 2* (PEN on 0.2 nm PQ/Ag(111)) and one of the components of *case 3* (PEN on 5.4 nm PQ/Ag(111)), which were 1.95 eV (Fig. 5.23b) and 2.00 eV (Fig. 5.23c), respectively.

A summary of all energy level alignment scenarios observed in the study of PEN/PQ hetero-interfaces on Ag(111) is shown in Fig. 5.26. In this figure, the ionization energies and binding energy values for the HOMO levels have been measured. The position of the pentacene LUMO level (*i.e.*, electron transport level) was estimated by using the transport gap of 2.2 eV [67, 237] instead of the optical gap. However, these values posses a large error bar, since orientation dependance as well as changes in molecular polarization cannot readily be assessed for these levels. For PQ, only the optical gap is known (ca. 2.94 eV [238]). The position of the electron transport level was estimated by assuming a similar difference between optical and charge transport gap, *i.e.*, 0.4 eV, as reported for PEN [67, 237]. Fig. 5.26 displays clearly that PQ incorporated into a PEN matrix can act as deep trap for electrons, with trap depths ranging from 0.2 to 0.75 eV in this simple model, depending on mutual orientation (compare according morphologies from Fig. 5.24).

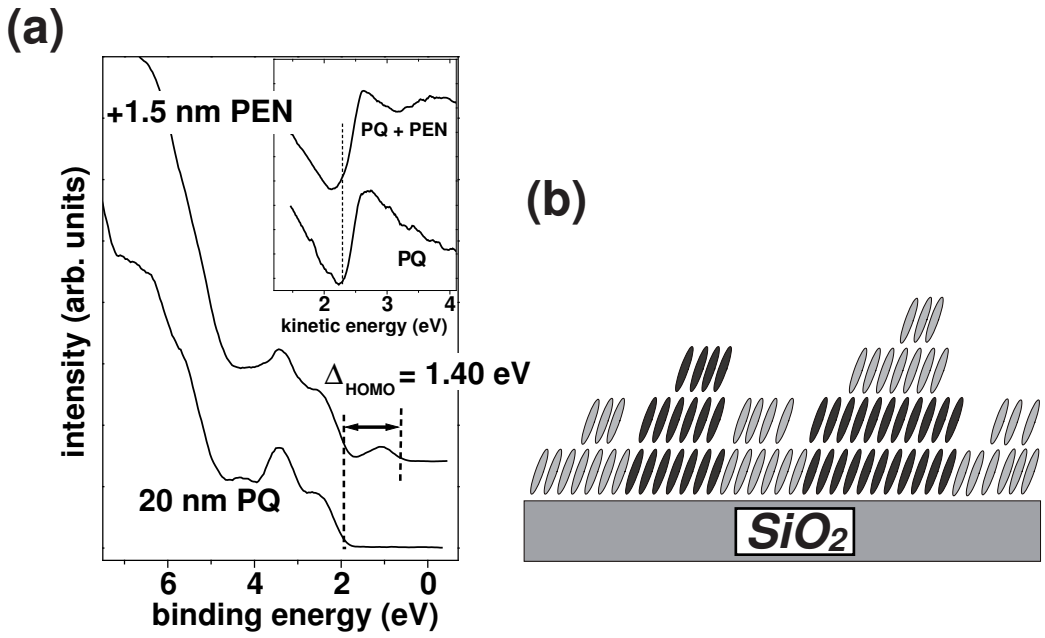

Figure 5.27: (a) UPS spectra for 20 nm PQ on SiO_x prior (bottom) and after deposition of 1.5 nm of PEN (top). Inset: secondary electron cutoff. (b) Schematic morphology and molecular orientation for PEN/PQ/SiO_x. Dark: PQ, light: PEN.

PEN on PQ pre-covered SiO_x

While molecular orientation behavior can be rather complicated on metal surfaces, as pointed out above, a substrate was chosen, where molecular orientation is the same for mono- and multilayers, *i.e.*, silicon oxide (SiO_x). An almost standing orientation of PEN and PQ on SiO_x is well documented (See Sec. 5.2, 5.5 and 5.6). In a first step, 20 nm PQ were deposited onto SiO_x (bottom curve in Fig. 5.27a). Then 1.5 nm PEN were deposited top (top curve in Fig. 5.27a), and photoemission features of both materials can be distinguished. The HOMO-offset was 1.4 eV, again very close to the value obtained for *case 1* (PEN on 0.05 nm PQ/Ag(111)). No change in the position of the secondary electron cutoff was observed (inset of Fig. 5.27a). Fig. 5.27b shows a schematic representation of the sample morphology and molecular orientation. It is reasonable to propose that non-interacting PEN and PQ (residing *side-by-side* like in Fig. 5.24a), as well as PEN/PQ heterostructures where molecules are growing *on* each other as depicted in Fig. 5.27b, exhibit Δ_{homo} of ca. 1.4 eV. Thus, only for the case where PEN molecules grow in an almost

perpendicular orientation relative to PQ (Fig. 5.24b and c) a larger Δ_{homo} of 1.95 eV (Fig. 5.23b) is found. These values of Δ_{homo} seem to be highly suitable for efficient exciton dissociation in OPVCs based on this material pair.

As evident from Fig. 5.26, the IE of pentacene depends dramatically on the molecular orientation, *i.e.*, the IE value changed from ca. 5.0 eV (lying configuration) to ca. 4.4 eV (almost standing), for both monolayer and multilayer range. As outlined in Sec. 2.1.3 the value if IE is *intrinsically* depending on the molecular orientation in molecular assemblies. The observed difference in IE between the differently oriented molecular films found here can be explained by the surface dipole *built into* the molecular layers due to *collective electrostatic effects*. The difference in IE for lying and standing PEN was calculated to 0.6 eV [70], which is in perfect agreement with the difference in the observed IE values deduced from UPS in this study. The same trend is found for PQ (Fig. 5.26).

5.4.3 Summary

The influence of PQ at interfaces between PEN and Ag(111) on the energy level alignment was investigated within this study. Three different precoverages of PQ on Ag(111) led to three markedly different interface energetics scenarios. (i) Submonolayer θ_{PQ} did not change the energy level alignment between PEN and Ag(111) compared to the case of PEN on the pristine metal surface. (ii) Ca. one monolayer coverage of PQ on Ag lowered the hole injection barrier between PEN and Ag(111) by 0.7 eV. (iii) Multilayer θ_{PQ} resulted in a mixture of the two former cases. These differences were explained by different mutual molecular orientations at the investigated organic/organic hetero-junctions. Furthermore, the photoemission results show that PQ can form deep traps for electrons in a PEN matrix, with depths ranging from 0.2 eV to 0.75 eV, depending on molecular orientation. On the other hand, the large values found for Δ_{homo} may allow for efficient exciton dissociation in PEN/PQ based OPVCs, which will be investigated in detail in the next section. Moreover, the impact of the molecular orientation on the value of the ionization energy was demonstrated for both PEN and PQ, which was attributed to the different film surface termination in the cases of lying and standing molecular constituents. As shown in the previous section this effect can be applied to systematically tune the IE.

5.5 Heterostructures of 1:1 co-deposited pentacene/pentacenequinone films

PEN and PQ have been vacuum co-deposited onto SiO_x in order to control phase separation in thin films for the application as bulk heterojunctions in OPVCs, since suitable values of Δ_{homo} were found in the previous section. Structural investigations by means of AFM and SEM revealed pronounced phase separation of the two materials at length scales that turned out to be tuneable by the variation of the deposition rate. XRD provided evidence for polymorphism in pure films of PEN and PQ on SiO_x. While pure films exhibited both the bulk and thin film phase, the bulk phase is mainly suppressed within the co-deposited films (PEN:PQ). This was corroborated by FT-IR spectroscopy results. SEM investigations of pure and co-deposited films indicated that PQ bulk crystallites of up to 200 nm height form continuous paths to the substrate and grow within a matrix formed of PEN and PQ thin film phases. The obtained heterojunction morphologies thus appear interesting for the application in organic-based photovoltaic cells.
This work is published as Ref. [182].

5.5.1 Introduction

Considerable efforts have been made to investigate the structure of PEN thin films, since the intermolecular arrangement governs the highly anisotropic transport properties of oligoacenes [219]. In addition, chemical impurities in PEN films and crystals were identified to have a tremendous impact on the charge carrier mobility. For instance, the presence of PQ leads to a significant reduction of charge carrier mobility in PEN single crystals at concentrations as low as 0.68% [77]. In Sec. 5.4 it was suggested that PQ can form deep traps for electrons within a PEN matrix with depths depending on the mutual molecular orientation. This may explain, to some extent, why the electron mobility reported for pentacene is notoriously lower than that of holes [163, 239–241]. However, no information is available on the impact of the presence of PQ on the resulting structure and morphology of PEN thin films. Even slight changes in intermolecular arrangements can lead to a number of shallow traps in thin films causing inferior charge carrier mobilities [242]. The intrinsic electronic properties of sequentially deposited PEN and PQ thin films on SiO_x have been investigated by UPS (see Sec. 5.4), which revealed an energy level offset between the particular HOMO levels of 1.4 eV. Together with the values found for the respective optical band gaps of 1.8 eV (PEN) and 2.8 eV (PQ) [182] and the value of the pentacene electron

affinity of ca. 2.7eV [237] the estimated energy level arrangement appears suitable for the use in bulk-heterojunction photovoltaic devices produced by co-deposition [9, 49, 178, 180, 243]. The morphology as well as the structural properties of co-deposited films are herein decisive in order to evaluate the applicability as interpenetrating donor/acceptor network within this field of application.

The investigation of the structural properties of thin films composed of PEN and PQ is also of particular interest from a more fundamental viewpoint: While both molecules have similar length, are rigid and planar, the crystal structures of pure PEN and PQ differ significantly. Several polymorphs have been observed for PEN, which can be distinguished by the spacing of the (001) cleavage planes, ranging from 1.41 to 1.44 nm for PEN single crystals (bulk phase) and 1.54 nm for thin films thermally evaporated on SiO_x substrates (thin film phase) [198, 199, 216]. The molecules form a layered structure perpendicular to this plane and adopt a herringbone arrangement within such a plane. The PQ single crystal structure also exhibits a comparable layered structure along the (020) cleavage planes, however, with a smaller spacing of 0.89 nm [244]. For PQ, the molecular planes are parallel within the layers, *i.e.*, no internal herringbone structure exists. However, the long molecular axes and planes of molecules in neighboring layers are tilted with respect to each other. It is therefore important to know, whether PEN and PQ – somewhat similar on a molecular level but largely different in their crystal structure – form a mixed crystal (intercalation-like) or whether phase separation prevails if both compounds are simultaneously present during the crystallization process. This question is addressed in the present study, by investigating the morphology and structure of PEN and PQ thin films prepared by co-deposition.

5.5.2 Morphology of thin PQ films

In contrast to the case of PEN, where extensive growth studies have already been carried out for sub-monolayer [17, 39, 209, 221, 245–247] and for multilayer films [14, 218], no systematic investigation on PQ thin film growth has been reported yet. Thin films of PQ on SiO_x ($\kappa = 0.1$ nm/min) have been analyzed by means of AFM at various film thicknesses, and representative results for a nominal sub-monolayer film ($\theta = 0.8$ nm) and a film in the multilayer range ($\theta = 3.2$ nm) are shown in Fig. 5.28a and b, respectively. In both cases, pronounced island growth of Volmer-Weber type was found, as no indication for the presence of a wetting layer could be found. This is in contrast to the Stranski-Krastanov type growth reported for PEN thin films on SiO_x, where at least one complete layer is being formed on which island

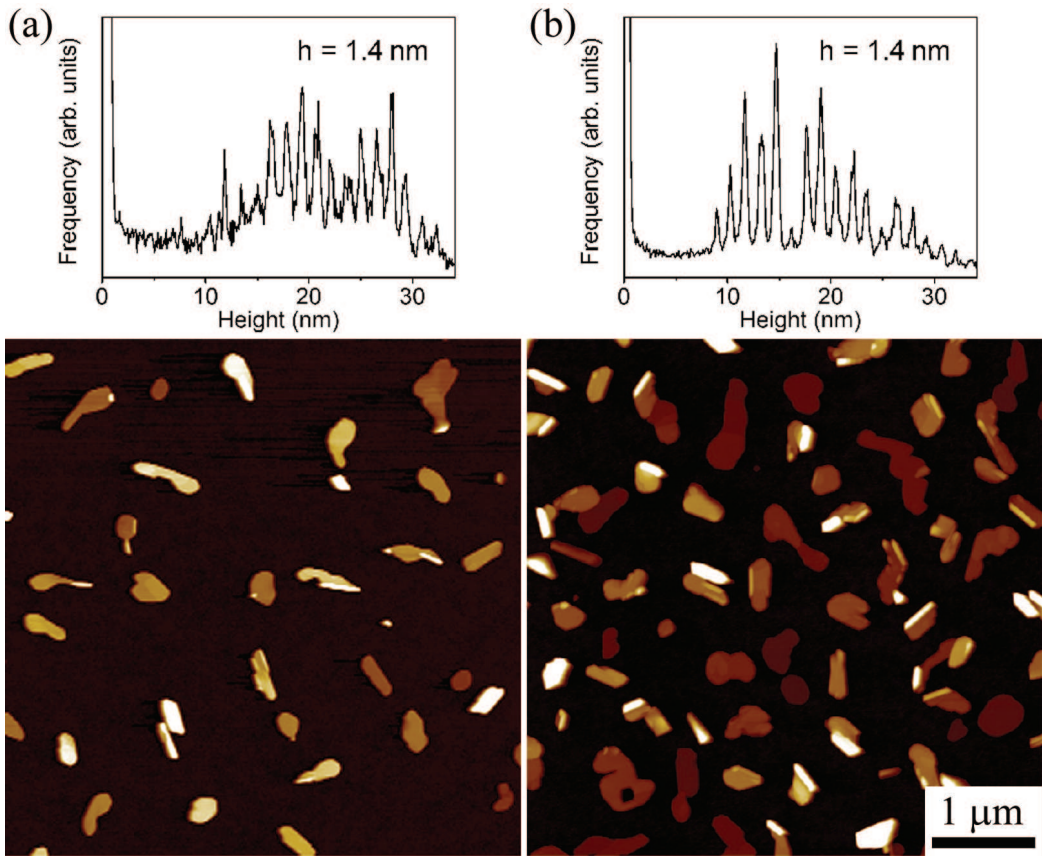

Figure 5.28: AFM height images of PQ films of $\theta = 0.8\,\mathrm{nm}$ (coverage 10%, island density (N) = 1.4 μm^{-2}) (a) and $\theta = 3.2\,\mathrm{nm}$ (coverage 30%, N = 2.3 μm^{-2}) (b) on SiO_x ($\kappa = 0.1\,\mathrm{nm/min}$) together with the corresponding elevation histograms showing stepped terraces of height h.

are built up [220]. The PQ sub-monolayer film exhibits an area coverage of only 10% (due to the instant formation of multilayer islands) and an island density (N) of 1.4 μm^{-2}. For comparison, a PEN film of same nominal thickness had a coverage of 50%, and N = 5.5 μm^{-2}. These values are increased to 30% coverage and N = 2.3 μm^{-2} for the PQ film of nominally 4 monolayer thickness ($\theta = 3.2\,\mathrm{nm}$). The pronounced island growth indicates that PQ molecules have a large diffusion constant on the SiO_x surface and that the growth is dominated by intermolecular interaction of PQ molecules as opposed to the interaction between the molecules and the substrate. The AFM micrographs reveal the presence of two different kinds of island morphologies: (1) smooth, plane islands with comparable dimensions within the substrate plane (mean height ca. 15 nm) that show pronounced internal steps, as well

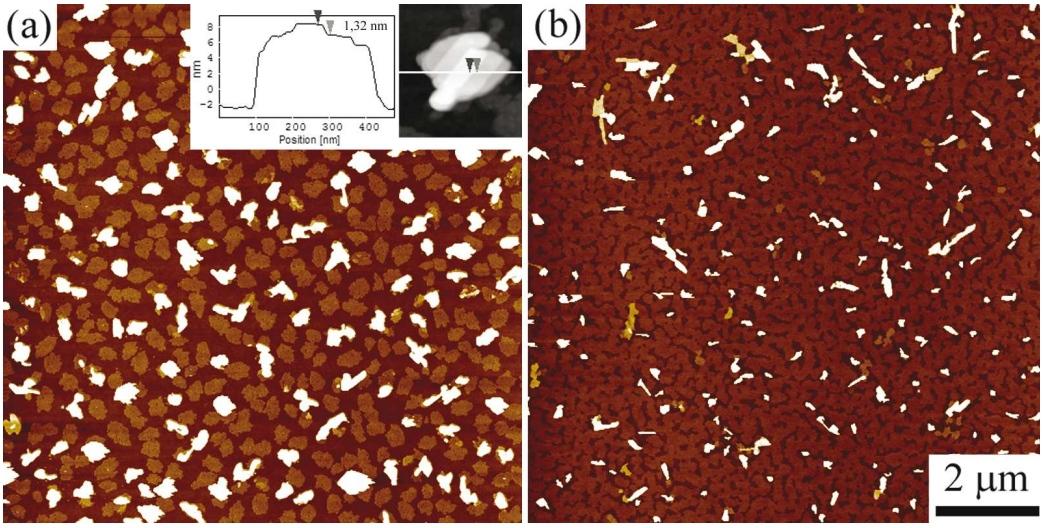

Figure 5.29: AFM height images of 1:1 co-deposited PEN:PQ films of total $\theta = 1.6$ nm deposited at rates of total (a) 0.1 nm/min and (b) 6 nm/min on SiO_x. The inset in (a) shows a zoomed view of a typical island assigned to PQ exhibiting terraces with a step height of ca. 1.4 nm.

as (2) needle-like crystallites of up to 100 nm height without detectable internal steps. From the corresponding elevation histograms the internal step heights of the islands of type (1) were determined to h = 1.4±0.2 nm. Note, that this step height agrees with the reported value of 1.27 nm found for the interplanar spacing of the (001) net planes within a thin film phase of PQ by XRD [248]. As will become apparent from additional studies presented below, the two distinctly different morphologies are attributed to two coexisting different PQ polymorphs, *i.e.*, the bulk phase and a substrate-induced thin film phase (see Sec. 5.5.6).

5.5.3 Morphology of thin PEN:PQ films

In order to investigate the early stage of the growth of PEN:PQ co-deposited films (ratio PEN:PQ = 1:1) on SiO_x, samples of $\theta = 1.6$ nm were prepared at two different deposition rates, *i.e.*, κ of total 0.1 nm/min (Fig. 5.29a) and 6 nm/min (Fig. 5.29b) and investigated by means of AFM. In the case of low κ two types of morphologies can be distinguished: Approximately 50% of the substrate is covered by flat islands of 1.8±0.4 nm height, which closely resemble the morphology of thin films of PEN only (see Fig. 5.31a). This step height is comparable to the reported values of 1.54 nm [198, 199, 216] for the (00l) lattice spacing of the PEN thin film phase and 1.61 nm [209]

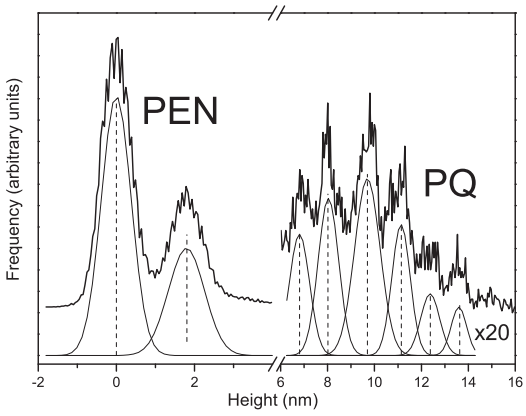

Figure 5.30: Elevation histogram of the AFM height image in Fig. 5.29a together with gaussian fits. The peak at the origin represents the substrate level; at a mean step height of 1.8±0.4 nm contributions from the PEN monolayer can be found. Steps of 1.4±0.2 nm at elevated heights result from PQ multilayers.

for the PEN monolayer thickness[14]. In addition, ca. 13% of the surface is covered by islands of average total height of ca. 10 nm with internal steps and somewhat different shape (N = 1.7 μm^{-2}, see inset in Fig. 5.29a). They are assigned to PQ due to their similarity to films of pure PQ (Fig. 5.28. The step heights were determined from the corresponding AFM height histograms (Fig. 5.30). For higher deposition rates of 6 nm/min an increased density of PEN monolayer islands was found, as expected by previous work [249]. The same effect was observed for the islands assigned to PQ (coverage 8%, N = 3.2 μm^{-2}), which exhibit an average island height that is nearly doubled to 17 nm (compared to 10 nm for the film prepared with κ=0.1 nm/min). The intrinsic PQ step height was identical to the low-κ sample. In addition, a higher κ apparently leads to an increase of the relative amount of the islands that exhibit the characteristic PQ steps. From the AFM investigations in the sub-monolayer range of co-deposited thin films, indications for pronounced phase separation of PEN and PQ are being obtained, which is substantiated in the following sections.

5.5.4 Morphology of thin layered films

The results of the previous section pose the question whether PEN and PQ islands grow next to or on top of each other. This issue was addressed through sequential deposition of the two materials (without breaking the vacuum). Growth parameters were adjusted in order to achieve equal island densities of the PEN ($\kappa = 1$ nm/min) and PQ ($\kappa = 1$ nm/min) underlayer (Fig. 5.31a and c). In both cases of sequential deposition (PQ on PEN (Fig. 5.31b) and

[14]The height information obtained from AFM was assumed to be more reliable in case of intrinsic steps as in the case of steps between PEN and SiO_x due to the different mechanical properties of the materials in the latter case (intrinsic PEN steps of multilayer films however exhibit a mean step height of 1.6 nm).

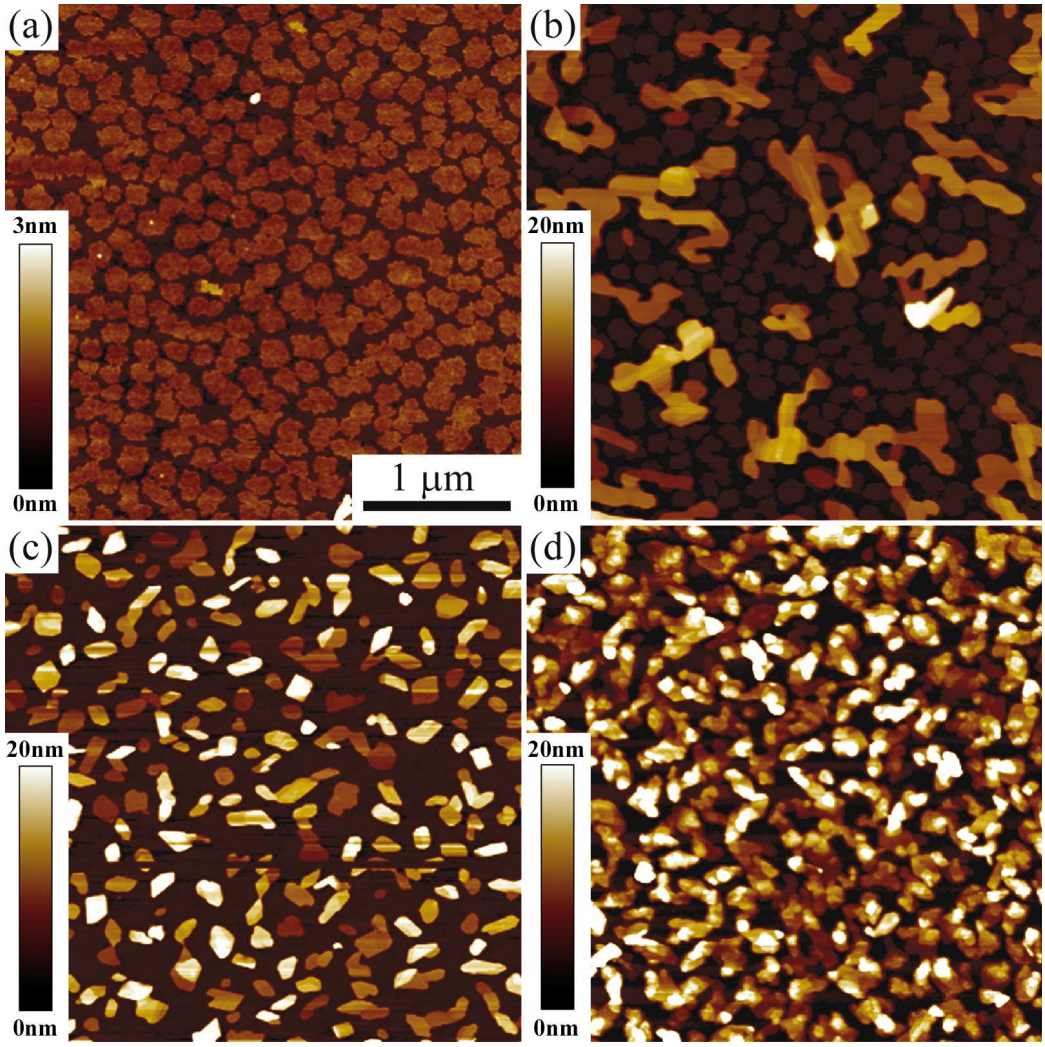

Figure 5.31: AFM height images of layered PEN and PQ films with comparable island densities (different κ). (a) PEN film of $\theta = 1\,\mathrm{nm}$ ($\kappa = 1\,\mathrm{nm/min}$), and (b) 2 nm thick PQ film ($\kappa = 0.1\,\mathrm{nm/min}$) on top. (c) underlayer film of 3.2 nm PQ ($\kappa = 6\,\mathrm{nm/min}$) for (d), a PEN film of $\theta = 1\,\mathrm{nm}$ (0.1 nm/min).

PEN on PQ (Fig. 5.31d)) the later evaporated compound was apparently found to be growing on top of the first. In addition, the respective islands of both materials adopt the shape of the underlying layer. The characteristic step heights found in both layered samples are in agreement with the values found for co-deposited films (Fig. 5.29). Note that the island-coalescence for overlayer PQ on PEN is more pronounced than for the reverse case. This is in contrast to the morphology found for co-deposited samples, and may thus indicate that PQ islands in Fig. 5.31 grow next to islands of PEN.

Interestingly, no evidence for the appearance of the needle-like phase could be found in the case of sequential evaporation of PQ onto a sub-monolayer of PEN.

5.5.5 30 nm thick PEN, PQ and PEN:PQ films

For devices, the relevant film thicknesses are larger than those presented so far. Therefore, the morphology and the structure of $\theta = 30$ nm thin films of pure PEN and PQ films ($\kappa = 0.5$ nm/min) as well as co-deposited samples (P:PQ ratio 1:1,total $\kappa = 0.5$ nm/min and 6 nm/min) on SiO_x was investigated by AFM (Sec. 3.4), XRD (Sec. 3.1) and FT-IR (Sec. 3.3). For pure PEN films ('sample PEN') the AFM micrograph in Fig. 5.32a shows the well known stepped terrace-like morphology of the thin film phase [14, 218, 245, 246, 250] with typical steps of h = 1.6±0.2 nm, which were obtained via AFM step height analysis during different stages of the growth process (inset in Fig. 5.32a). For the pure PQ film ('sample PQ', Fig. 5.32b) a total coverage of only 65% of the substrate surface was found despite the nominal film thickness of about 20 monolayers. This observation of incomplete SiO_x coverage by PQ agrees with the findings presented for the $\theta = 0.8$ and 3.2 nm films (Fig. 5.28). Again, a two phase morphology is apparent, which consists of both the planar phase (1) areas and elevated needle-like structures of phase (2) (here up to 200 nm high), as already found for the thin PQ films (Fig. 5.28). Analogously the two morphologies are assigned to areas grown in the thin film and in bulk phase, respectively. The analysis of the elevation histogram (inset in Fig. 5.32b) yields a frequency maximum for island heights of ca. 40 nm (PQ thin film phase) covering 40% of the substrate. By integrating the respective areas of the histogram the volume ratio between the two phases can be estimated to be 1:1. The morphology of the co-deposited film ('sample PEN:PQ', Fig. 5.32c) shows areas of granular structure (height range < 20 nm) together with islands of needle-like shape (heights up to 200 nm). From a comparison to the results for the morphology of pure PEN films (Fig. 5.32a), pure PQ films (Figs. 5.28 and 5.32b) as well as PEN:PQ films (Fig. 5.29), the islands marked in Fig. 5.32d are assigned to islands of the PQ bulk phase, the planar islands marked in Fig. 5.32e to islands of the PQ thin film phase and the stepped structures showing again steps of h = 1.6±0.2 nm in Fig. 5.32f to PEN thin film phase islands. For the pure PQ film 15% of the surface area was covered by the PQ bulk, whereas this amount reduces to 8% in case of PEN:PQ films. This indicates that the process of co-deposition of the two materials leads to preferred growth of PQ within the thin film phase.

In order to obtain more information on the vertical composition of the

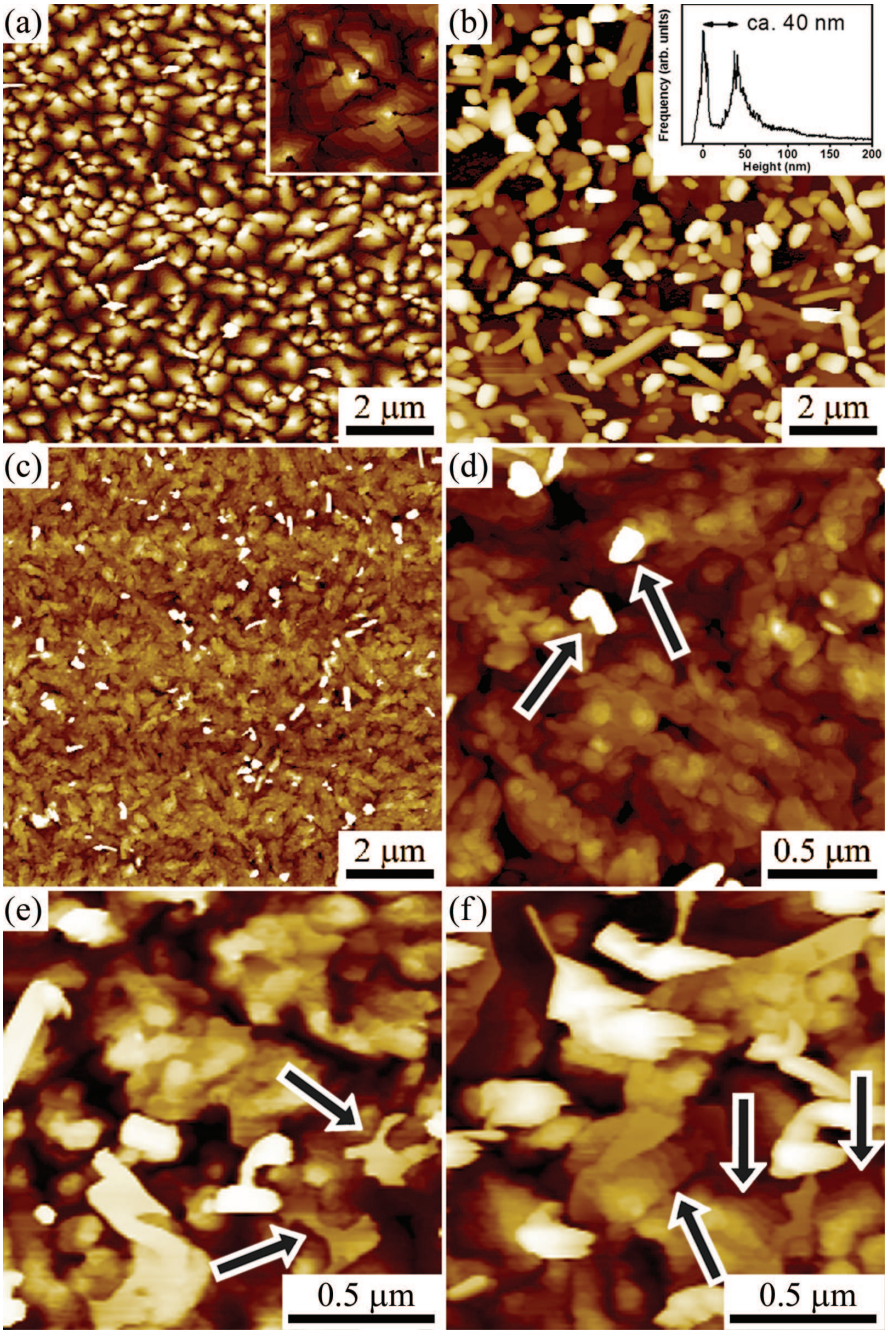

Figure 5.32: AFM height image of samples PEN (a), PQ (b) and of PEN:PQ ($\kappa = 0.5\,\mathrm{nm/min}$) on SiO_x (c) together with zoomed representations (d-f). The inset in (a) shows a $2.5\times2.5\mu m$ image of intermediate θ of 5 nm, the inset in (b) shows the elevation histogram of the pure PQ film. Arrows in (d-f) point to islands assigned to: the PQ-bulk phase (d), the PQ thin film phase (e) and the PEN thin film phase (f) (see text).

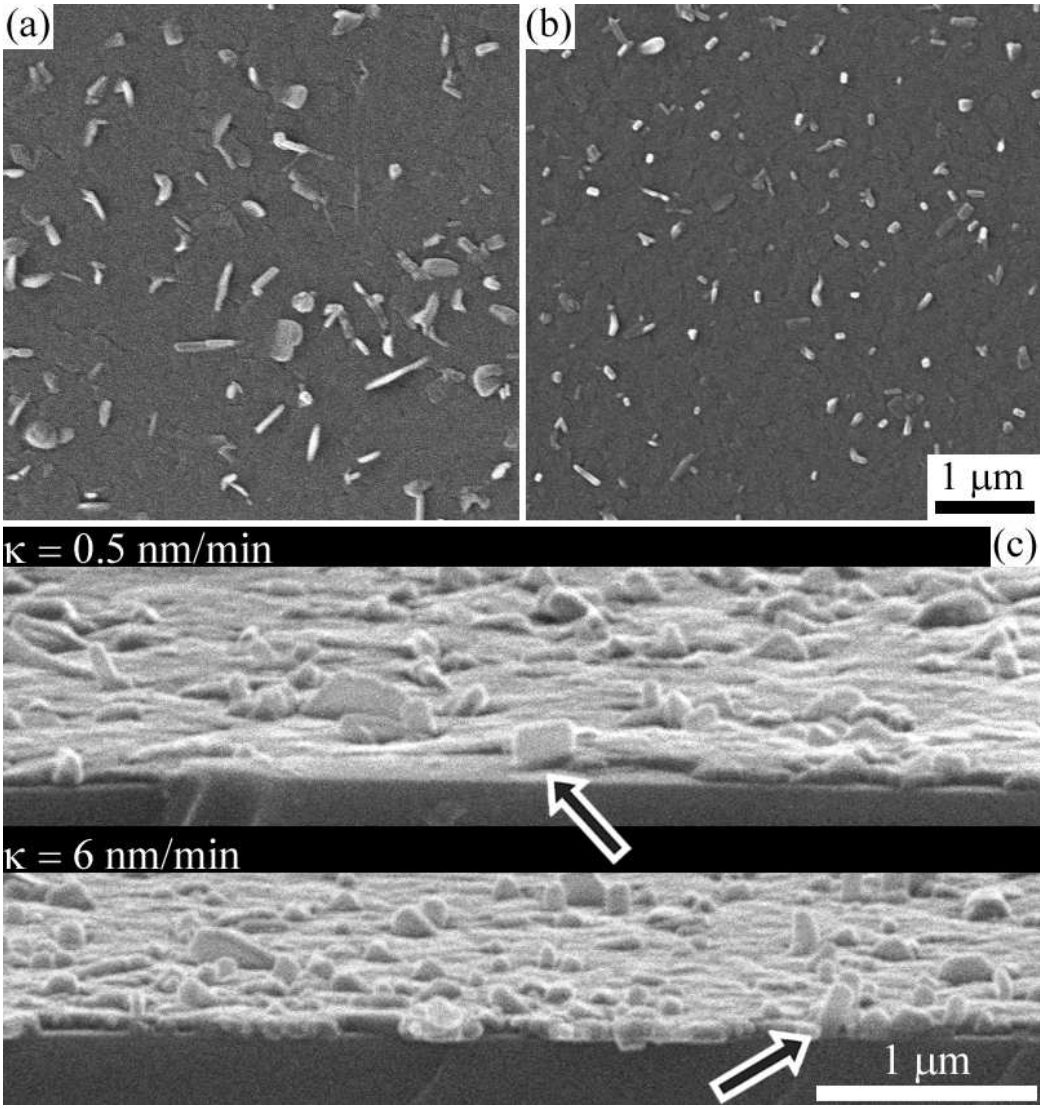

Figure 5.33: SEM micrographs of co-deposited PEN:PQ films of 30 nm nominal thickness at different deposition rates κ of total 0.5 nm/min (a) and 6 nm/min (b) under top view. The images in figure (c) show the cut-edge of the two samples and were recorded under a sample inclination of 80°.

PEN:PQ film, the two PEN:PQ samples deposited at different κ were investigated by SEM. For that purpose, samples were broken along a preferential direction of the Si wafer to allow for cross-section viewing along edges. Figs. 5.33a-b show on-top views of different κ samples and images of the cross-section view (for a sample tilt of 80°) are shown in Fig. 5.33c. As already inferred from the AFM investigations, the SEM top-view sup-

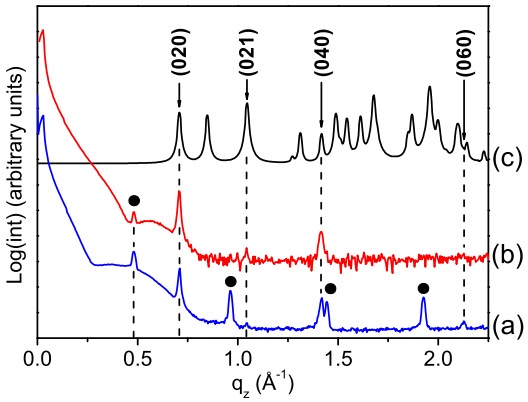

Figure 5.34: Specular XRD scan of (a) 3.2 nm (AFM in Fig. 5.28b) and (b) 30 nm (AFM in Fig.5.32b) PQ on SiO_x compared to a calculated PQ powder spectrum (CSD refcode PENTQU) [251]. Curve (c) is normalized with respect to the (020) reflection in (b); (060) is hidden in the shoulders of neighbouring peaks.

ports the notion of pronounced phase separation of PEN and PQ within the co-deposited film. One can clearly distinguish needle-like crystallites, which were assigned to the PQ bulk (at low κ: 8% coverage, island density 3 μm^{-2}). These needles seem to be embedded within a closed and rather smooth film (composed of PEN and PQ thin film phases, which cannot be distinguished by SEM). From the cross-section view the height of the PQ bulk islands can be estimated (sample islands marked by arrows in Fig. 5.33c) to ca. 200 nm, whereas the thickness of the surrounding PEN/PQ film matrix is estimated to be ca. 20 nm. The investigation of several crystallites in the vicinity of the cut edge indicates a direct growth on the substrate within the resolution limits of SEM (ca. 10 nm). The increase of the deposition rate κ to 6 nm/min yields a reduced value of 0.8 ± 0.2 μm for the inter-island distance and reduces the area covered by PQ bulk islands by a factor of about two. In this case the island density is nearly doubled to $5 \mu m^{-2}$, which is also apparent in the SEM micrograph shown in Fig. 5.33b.

5.5.6 Structural properties

Already from the investigation of the thin film morphologies strong indications for polymorphism of PQ in both pure and co-deposited films was found, *i.e.*, growth within a PQ thin film and the bulk phase can be proposed. In order to pin down this assumption, specular x-ray diffraction scans have been performed on that same set of samples. The pure PQ films of $\theta = 3.2$ nm (curve *a* in Fig. 5.34) and 30 nm (curve *b*) exhibit indeed polymorphic growth within a thin film and the bulk phase. A preferred orientation of the bulk (0k0) net planes parallel to the substrate was found, which is inferred from a comparison with a calculated powder spectrum [251, 252]. Within the film of $\theta = 3.2$ nm reflections of the bulk (0k0)-series were found up to k = 6 (reflec-

tion condition k = 2n due to the monoclinic space group $P2_1/b$) as well as a small contribution of the (021) plane (intensity ratio between (021) and (020) ca. 1:100). The thick film of $\theta = 30$ nm shows contributions of the same orientation, and all bulk peak positions were found in perfect agreement with the calculated spectrum of the PQ bulk (experimental values are listed in Tab. 5.2). The orientation of PQ molecules with respect to the plane (020) is illustrated in Fig. 5.35 (viewed along the axes of the unit cell) and the plane is identified as a cleavage plane of the crystal. The reflection found at the lowest momentum transfer (marked with a circle in Fig. 5.34) corresponds to the lattice spacing (d_{hkl}) of $d_{001} = 1.305$ nm for (001) planes of the PQ thin film phase, which was already proposed from the step height analysis from the AFM micrographs (h = 1.4±0.2 nm). Reflections of this orientation are found up to fourth order in the thin, whereas only the first order can be clearly seen in the spectrum of the PQ film of 30 nm nominal thickness. Considering the van der Waals length of a single PQ molecule of 1.61 nm it can be estimated that PQ molecules are tilted by ca. 36° with respect to the substrate surface normal for the thin film polymorph. Note that the result deviates by 0.035 nm from a previously reported value [248] for the lattice spacing d_{001} of the PQ thin film phase. For the pure PEN film ($\theta = 30$ nm) reflections were found that can be assigned to the $(00l)$-series of the PEN thin film phase (square symbols in Fig. 5.36) with a characteristic d_{001} layer thickness of 1.55 nm(Tab. 5.2). In addition, two weak contributions of the PEN bulk structure [196] can be found. Thus, the results obtained from x-ray diffraction nicely support the AFM-based proposal for the polymorphism in pure PQ films.

Turning towards the co-deposited film (low κ) two series of Bragg peaks are found, which can be assigned to the respective thin film phases of PEN and PQ (Fig. 5.36, curve PEN:PQ). However, no significant contributions from the respective bulk phases are observed. In contrast to PEN, where the same number of reflections appears as for the pure film (but with reduced intensity), the peaks of the PQ thin film phase are now found up to (004). This finding matches the results from morphological investigations, where preferred growth of the PQ thin film phase was found for co-deposition (an increase of ca. 50% if compared to the pure film). In more detail, the complete disappearance of the PQ bulk (020) reflection in the specular scan points to a differently or significantly less textured growth of the PQ bulk crystallites in the co-deposited film, since PQ bulk crystallites are clearly visible in both AFM and SEM micrographs of the co-deposited film. The method of choice to assess this issue is the *x-ray diffraction pole figure technique* (XRD-PF), where the goniometer is fixed to the momentum transfer of a certain d_{hkl} and the plane normal to the sample surface is being tilted

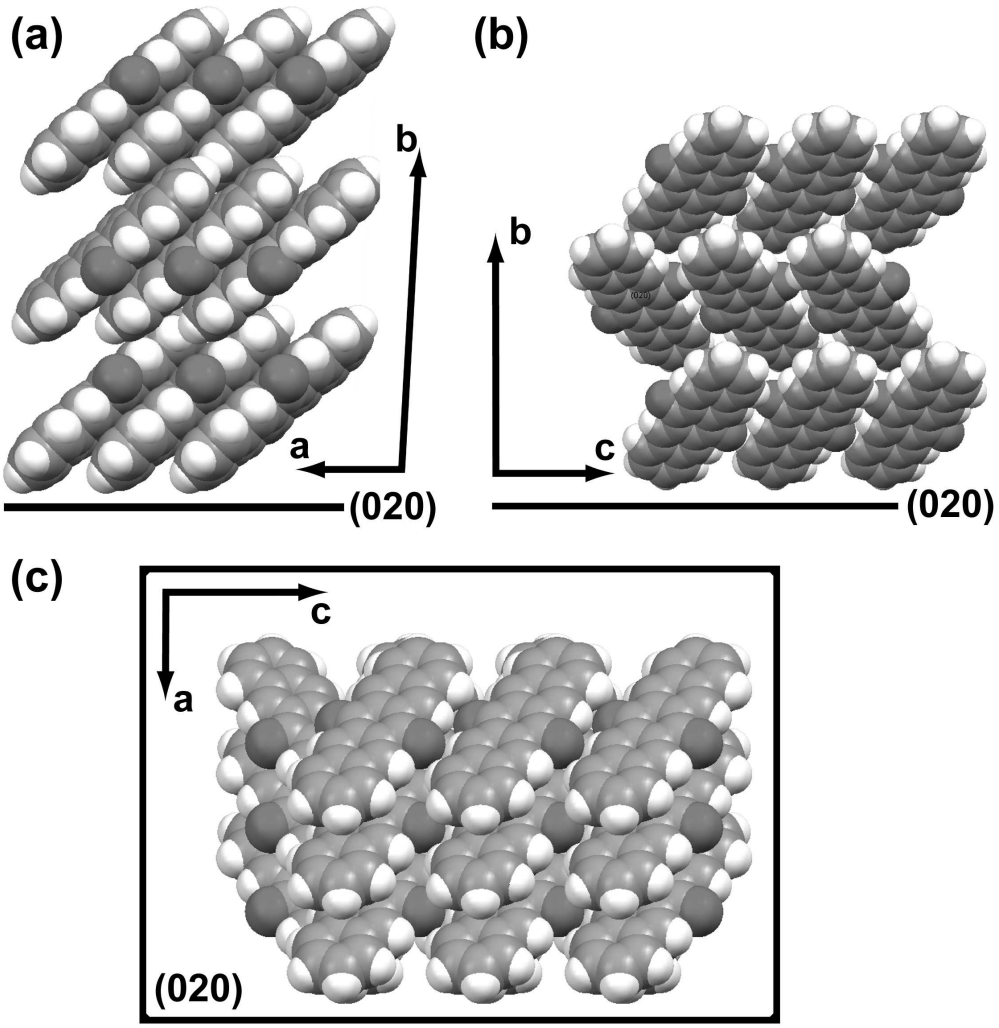

Figure 5.35: The bulk structure of PQ viewed in projection on the ab-plane (a), the bc-plane (b), and the ac-plane of the unit cell together with the position of the (020) net plane that was found as most intense reflection within XRD (Fig. 5.34), visualisation performed by MERCURY [251].

with respect to the scattering vector by an angle ψ. Such experiments were performed, however, for XRD-PF scans in the range $0° < \psi < 85°$ for the (020) and (140) reflections of the PQ bulk (the latter is the most intense peak of the powder spectrum) no evidence for the respective Bragg peaks could be found. Therefore, it can be concluded that the bulk phase needle-like crystallites observed with AFM and SEM do not grow significantly textured in case of co-deposition. One can thus think of the bulk crystallites as "powder" of

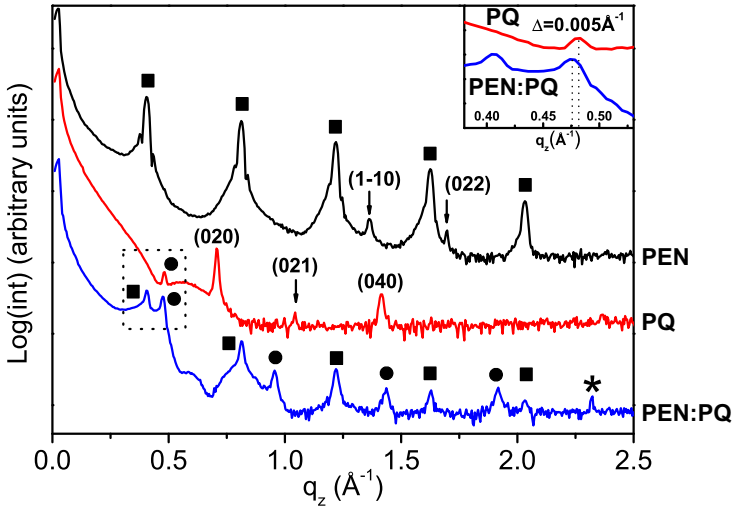

Figure 5.36: XRD scans of samples PEN, PQ and PEN:PQ. Bulk phase reflections are indicated with Miller indices, peaks from the thin film phase $(00l)$-series are indicated with a square (PEN) and a circle (PQ), respectively. The star marks a second-order reflection of the silicon (004) plane. The inset shows a zoomed representation of the dotted area illustrating a shift of the PQ (001) thin film phase reflection of 0.005Å^{-1} in the PEN:PQ sample compared to pure PQ.

too low scattering intensity to be detected in the specific experimental setup. Interestingly, the (001) reflection in the spectrum of PEN:PQ is shifted by q_z=0.005Å^{-1} compared to the pure film, which corresponds to an increase of d_{001} of the thin film phase of 0.013 nm. This finding can be assigned to macrostrains induced in PQ by the co-existence with PEN, which hence leads to a slightly reduced inclination of the PQ molecules with respect to the substrate surface in this polymorph. All peak positions of x-ray diffraction results for films of $\theta = 30$ nm are summarized in Tab. 5.2. In addition, the out-of-plane crystalline coherence length (D_S) that was estimated using the Scherrer formula [113, 114] (see Sec. 2.2.2). The finding that the D_S-values of the PEN and PQ thin film phases do not differ significantly for pure ($\theta = 30$ nm) and co-deposited films (total $\theta = 30$ nm) is further evidence for pronounced phase separation in the latter. In the case of the co-deposited film at elevated κ of 6 nm/min (SEM micrograph in Fig. 5.33b) a specular x-ray diffraction scan yields a significant intensity increase of the PQ thin film phase (001) reflection in relation to the PEN thin film phase (001) reflection (not shown). This supports further the finding from the SEM investigations that an increase of κ decreases the amount of PQ within its bulk phase under

Table 5.2: Positions of the Bragg reflections found in the x-ray diffraction scans shown in Fig. 5.36. Reflections of planes (*hkl*) of the bulk phases are denoted as PEN(*hkl*) and PQ(*hkl*), reflections of the thin the thin film phases as TP(*hkl*) for PEN and TQ(*hkl*) for PQ, respectively. q_z indicates the momentum transfer, D_S the out of plane crystalline coherence length estimated by the Scherrer formula (see Sec. 2.2.2) and d_{hkl} the resulting plane spacing of lattice planes (*hkl*).

	Pentacene			6,13-pentacenequinone			Co-deposited		
	q_z	D_S	d_{hkl}	q_z	D_S	d_{hkl}	q_z	D_S	d_{hkl}
	(Å^{-1})	(Å)	(Å)	(Å^{-1})	(Å)	(Å)	(Å^{-1})	(Å)	(Å)
TP(001)	0.406	449	15.47				0.406	494	15.48
TQ(001)				0.482	469	13.05	0.477	502	13.17
PQ(020)				0.708	323	8.87			
TP(002)	0.813	446	7.73				0.815	461	7.71
TQ(002)							0.957	387	6.56
PQ(021)				1.041	103	6.04			
TP(003)	1.219	444	5.15				1.220	382	5.15
PEN(1-10)	1.364	391	4.61						
PQ(040)				1.416	274	4.44			
TQ(003)							1.434	298	4.38
TP(004)	1.626	425	3.87				1.627	391	3.86
PEN(022)	1.696	703	3.70						
TQ(004)							1.917	301	3.28
TP(005)	2.032	388	3.09				2.033	328	3.09

the given experimental circumstances.

5.5.7 Vibrational spectroscopy

FT-IR spectroscopy has already been successfully used in the study of polymorphism of organic molecular crystals [81, 253–256]. In contrast to XRD, where only contributions of crystalline domains can be detected, FT-IR provides additional information about the entire sample, since also non-crystalline phases contribute to IR absorption. By and large, these could be identified by changes in vibrational energies compared to crystalline phases. Therefore, FT-IR is highly sensitive to sample volumes that potentially contain non-crystalline or intercalated PEN and PQ. Fig. 5.37 shows the absorption spectra of the respective pure and co-deposited films on SiO_x compared

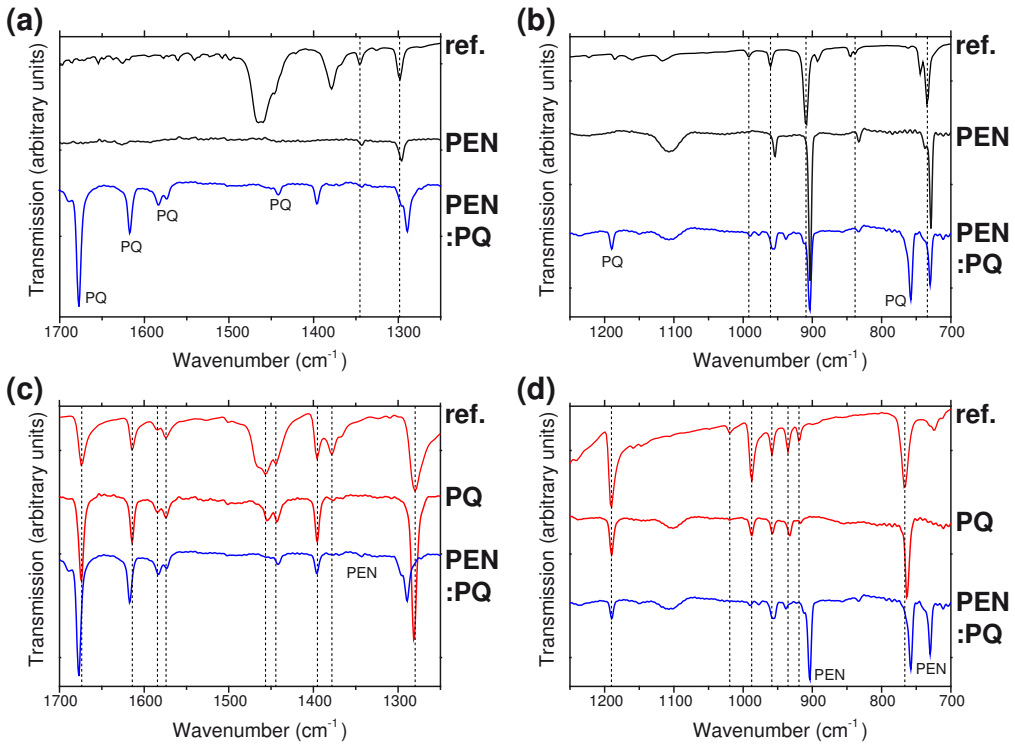

Figure 5.37: FT-IR spectra of samples PEN (a), (b) and PQ (c), (d) compared to sample PEN:PQ and a KBr reference spectrum provided by the manufacturer. Peaks originating from the second compound within the spectrum of PEN:PQ are marked as PEN and PQ, respectively.

to reference spectra provided by the manufacturer for the two materials (each corresponding to the respective bulk phases of PEN and PQ). The spectra presented in Fig. 5.37a and 5.37b of PEN show a significant shift of all absorptions compared to the bulk reference, which agrees with the finding of preferential growth in the PEN thin film polymorph. Compared to the PEN contributions in the spectra of sample PEN:PQ, the peak positions remain essentially unchanged (shifts ≤ 1 cm^{-1}), which agrees with the results from x-ray diffraction, where exclusively the PEN thin film phase was observed. This also corroborates the proposition of pronounced phase separation within co-deposited films of PEN and PQ, since IR spectroscopy is highly sensitive to a potential intercalation of PEN and PQ. For PQ rather the opposite behavior was observed, *i.e.*, the spectrum of the pure film matches well the reference (dominating bulk phase, as found in XRD), whereas certain PQ peaks in the spectrum of PEN:PQ are significantly shifted (dominating PQ thin film phase, shifts of up to 5 cm^{-1}). PQ peaks of the pure sample that show a

shift of max. 1 cm^{-1} compared to the reference are heavily shifted (up to to 5 cm^{-1}) in the co-deposited film (preferred thin film phase). Particularly, in the region of C-H out of plane bending and stretching modes [207, 208] the influence of the different molecular orientation within the polymorphs is apparent (P: 729(+1), 904(+1) and 954(±0) cm^{-1}, PQ: 763(-5), 933(+5), 958(±0) and 988(+2) cm^{-1}, shifts of pure materials relative to PEN:PQ in brackets). This also holds for the region of other vibrations of outer atoms like the C=O bond vibrations [77, 257, 258] of PQ (1674(+3) and 1614(+3) cm^{-1}), whereas the frequencies of carbon backbone vibrations like C-C ring stretch modes [259] (P: 1296(±0) and 1344(±0), PQ: 1190(±0), 1396(±0)) remain unchanged. The C-C stretch modes of the reference data in the region 1440-1540 cm^{-1} along the molecular axis of PEN are suppressed due to the almost perpendicular orientation of PEN molecules on SiO_x within the thin film phase [207, 260], whereas this is not true for PQ in the pure and co-deposited film (1443(+1), 1453(±0), 1574(-1) and 1584(-1) cm^{-1}), since the molecules have a higher inclination within the PQ thin film phase.

5.5.8 Summary

Using a number of experimental techniques evidence of pronounced phase separation in co-deposited thin films of pentacene and pentacenequinone was found. Pure films of PQ (Fig. 5.34) exhibit polymorphic growth on SiO_x in the thin film and bulk phase[15]. If sequentially deposited, both materials preferentially grow on top of each other. It was found that the presence of PEN (as underlayer in sequential deposition or if co-deposited) induces PQ growth preferentially in the thin film phase. The ratio between PQ bulk and thin film phases was found to be sensitive to κ (more thin film phase at increased κ). For co-deposited films of $\theta = 30\,nm$, no PQ bulk phase contributions could be found via XRD, although apparent in AFM and SEM images. This indicates non-textured growth of the PQ bulk phase needle-like crystallites on SiO_x. The lattice spacing d_{001} of the PEN thin film polymorph was insensitive to the presence of PQ, whereas d_{001} of the PQ thin film phase is increased by 0.013 nm in case of co-deposition, indicating a more upright orientation of the molecules. It was shown that the island density also in co-deposited films depends on the deposition rate κ. Therefore κ was identified as key parameter to control the length scale of phase separation obtained by co-deposition in this system. Moreover, FT-IR spectroscopy showed that no significant intercalation of PEN and PQ molecules takes place

[15]This finding demonstrates the influence of the specific "substrate" (*i.e.*, a PEN underlayer vs. SiO_x) for the growth of the different PQ polymorphs. In Sec. 5.6 it is shown that even different types of SiO_x substrates can dramatically change the polymorphic ratio.

during growth. The high degree of crystallinity found in both pure and co-deposited films and the pronounced phase separation meet the requirements of bulk heterojunction materials for photovoltaic applications. As device structure, a co-evaporated film of PEN:PQ sandwiched between PEDOT:PSS coated Indium Tin Oxide as transparent high work function electrode ($\phi \approx 5.1\,\mathrm{eV}$) [59] and samarium ($\phi \approx 2.7\,\mathrm{eV}$) [237] as low work function electrode seems to be reasonable. These preliminary experiments did however not yield reproducible current/voltage characteristics, most likely due to the highly corrugated surface of PEN:PQ films (Fig. 5.33).

5.6 The pentacenequinone thin film phase

In this section a full structure solution is performed for the unknown pentacenequinone thin film phase that was observed in Sec. 5.5. Thin films almost only composed of this specific polymorph could be fabricated and were investigated by RSM yielding triclinic unit cell parameters of $a = 4.691\,Å$, $b = 5.991\,Å$, $c = 13.454\,Å$, $\alpha = 77.83°$, $\beta = 84.13°$ and $\gamma = 81.11°$, with notably only one molecule per unit cell. Therefore, in contrast to its bulk crystal polymorph, pentacenequinone does not exhibit a herringbone arrangement in the thin film phase structure, which is suggested to depend on the process of crystal growth. From morphological results obtained by AFM investigations evidence for a correlation between an anisotropic island shape and the molecular tilt with respect to the substrate is proposed.
This work will be subject to a forthcoming publication [261].

5.6.1 Introduction

It was outlined in Sec. 5.5 that polymorphism was observed for PQ in terms of a bulk phase [244] and a thin film phase of which the d_{001} lattice spacing could be determined via specular x-ray diffraction. In this section, the attempt of a full structure solution is made using RSM (see Sec. 2.2.2) to determine (i) the unit cell parameters and (ii) to estimate the molecular packing in the unit cell using force field calculations[16], which have already been successfully applied for the solution of the PEN thin film phase [216, 262]. As observed in the spectrum of the pure PQ film in Sec. 5.5, which was grown on a SiO_x substrate with a 50 nm thermally grown oxide layer (Fig. 5.36), the film was dominated by the PQ bulk and only thin film phase reflections up to second order could be observed. In the corresponding AFM micrograph (Fig. 5.32) a highly corrugated film surface with two different kinds of morphologies was observed, which could be successfully assigned to the two phases. Subsequent investigations of PQ thin films however revealed that films almost exclusively consisting of the thin film phase with outstanding film quality can be obtained (here, SiO_x substrates with a ca. 2 nm thick native oxide layer were used). The exact origin of this different growth behaviour however remains speculative, since no more SiO_x substrates of the type used for the study in Sec. 5.5 are available for control experiments[17]. A possible reason

[16] As in Sec. 5.2, the force field calculations have been performed by Dmitrii Nabok, Chair for Atomistic Modelling and Design of Materials, Montanuniversität Leoben, Franz-Josef-Straße 18, A-8700 Leoben, Austria.

[17] It must be emphasized that both studies were performed *completely* on *one* set of samples cut from an individual wafer.

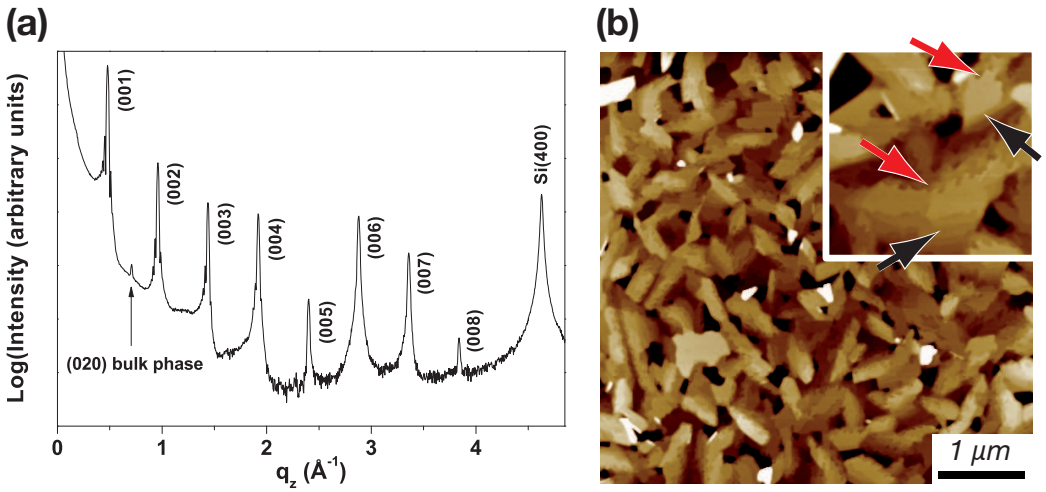

Figure 5.38: (a) Specular x-ray diffraction on a film of 30 nm PQ on SiO_x and (b) the corresponding AFM height micrograph; colors denote the height scale of 50 nm. Inset: zoomed area of $1 \times 1\,\mu m^2$; red arrows point to frayed and black arrows to even island sides (see text).

can be different hydrophilicity of the two types of substrates, which already was demonstrated to highly impact the PEN growth [221]. Note that in extensive investigations it could be ruled out that the deposition rate accounts for the different growth behaviour, since no evidence for a change of the ratio between the polymorphs could be observed for films deposited with $\kappa = 0.1$, 0.5, 1 and 2 nm/min; also a different impurity concentration can be ruled out since the same base material was used. Further investigations on this issue will be undertaken by defined hydrophilization of the substrate in the near future.

5.6.2 Full structure solution

Apart from the above open question the films of high thin film phase content can be perfectly used to determine the crystal structure via x-ray diffraction. Figure 5.38a shows a specular scan of a film of 30 nm PQ on SiO_x, where the $(00l)$ reflections ($d_{001} = 1.310$ nm) exhibiting pronounced Laue oscillations could be observed up to eighth order and only minor presence of PQ bulk was found[18]. The corresponding AFM micrograph (Fig. 5.38b) shows inter-

[18]The observation that the intensity of the higher orders do not reduce linearly (on the logarithmic scale), as found for PEN (Fig. 5.36), can be qualitatively understood by the molecular structure in *standing* PQ with the two center oxygen atoms, which leads to an increased intensity of the $(00l)$ reflections with even index l.

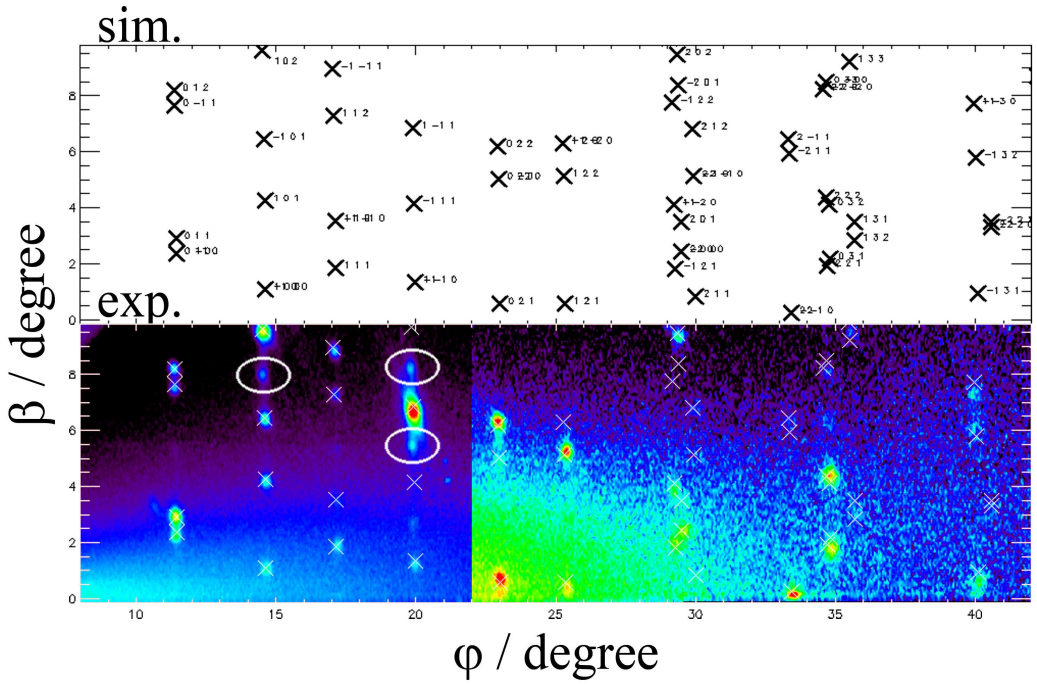

Figure 5.39: Result of the RSM investigation on a 30 nm PQ film on SiO_x with the corresponding simulated peak pattern; the angles φ and β are the angles of the sample system (see Fig. 3.2). The calculated peak positions are marked with crosses; peaks that do not originate from the PQ thin film phase are marked with circles. The map is vertically divided in two areas of different intensity scale.

connected, terraced islands with clear steps of $h = 1.4 \pm 0.2$ nm (determined by elevation histograms), which equals the value observed in Sec. 5.5 for thin film phase islands (therefore strongly supporting the assignment performed there). Again, the film is not closed as evidenced by the elevation histograms thus still indicating Volmer-Weber growth. Interestingly, the islands are elongated and have anisotropic edges: they preferentially exhibit *one* frayed (red arrows) and three even sides (black arrows in the inset of Fig. 5.38b). Assuming island comprising single grains this may point to anisotropic properties of the crystal faces forming the island edges in the island growth process, which depends on the ability of admolecules to diffuse along the island edges and to interdiffuse between the layers (see Sec. 2.1.2).

The results of the corresponding RSM investigation is depicted in Fig. 5.39 showing a reciprocal space map recorded under gracing incidence conditions exhibiting more than 30 clear reflections. The map can well be indexed using the software *Recmap* (see Sec. 3.1.2) assuming a triclinic crys-

tal structure with unit cell parameters $a = 4.691 \pm 0.02$ Å, $b = 5.991 \pm 0.02$ Å, $c = 13.454 \pm 0.02$ Å, $\alpha = 77.83 \pm 0.1°$, $\beta = 84.13 \pm 0.1°$ and $\gamma = 81.11 \pm 0.1°$. Note that the unit cell exhibits a volume of 364.2 Å^3, whereas the volume of the bulk unit cell is 718.2 Å^3 [244], which is almost the double of this value. The derived unit cell can therefore contain only *one molecule per unit cell* ($Z = 1$). This is surprising, since for the bulk phase $Z = 2$, which is necessary to host molecules arranged in a herringbone structure. However, due to the large number of reflections occurring in the map and the volume being almost the half of the bulk value there can be virtually no doubt on the validity of the unit cell parameters. A closer inspect of the PQ bulk structure (Fig. 5.35) reveals that PQ molecules exhibit a herringbone arrangement *between* the (020)-planes (*i.e.*, *along* the fiber axis), which is in extreme contrast to other rod-like molecules like PEN or PFP. There, the herringbone arrangement is found *in* the texture plane (001), *i.e.*, *perpendicular* to the fiber axis, and therefore concerns *lateral* neighbouring molecules with respect to the long molecular axis. Hence, one might argue that a PQ thin film structure similar to the PQ bulk can occur, in which the periodic molecular tilt between the adjacent layers along the bulk *b*-axis (Fig. 5.35b) is lost. Note that the layered growth of the islands happens by lateral attachment *to* existing layers and upwards diffusion *onto* existing layers (see Sec. 2.1.2), where the information on the arrangement of the underlayer might be differently important for different polymorphs, *e.g.*, if the underlayer molecules are more upright standing (as predicted by the thin film phase d_{001} spacing) compared to the bulk structure (Fig. 5.35a).

With the aid of force field calculations it was possible to model the molecular orientation of PQ in the unit cell and therefore to propose a molecular packing model of the PQ thin film phase. The derived structure is shown in Fig. 5.40 in comparison to the PQ bulk phase illustrating a similar, but more upright molecular orientation on the texture plane in comparison to the PQ bulk. The long molecular axis $\vec{m}$ is at an angle of $\angle(\vec{m}, \vec{a} \times \vec{b}) = 65.0°$ with respect to the fiber axis, which is in contrast to PEN and PFP, which exhibit an almost upright orientation on SiO_x in their respective thin film structures. The tilted growth behaviour of PQ may account for the anisotropy in island shape with one frayed side, since the interlayer diffusion may be influenced by the inclination of the layer side walls. However, further investigations and theoretic modelling will be necessary to pin down this assumption.

The film explored by RSM was additionally investigated by FT-IR, the result is depicted in Fig. 5.41 (curve *a*) in comparison to the spectra of the pure PQ film (curve *b*) and the PEN:PQ film (curve *c*) taken from Fig. 5.37, (where however the *total* nominal thickness was 30 nm with a PQ ratio of 50%). All peaks of (a) appear essentially unshifted compared to (c), since

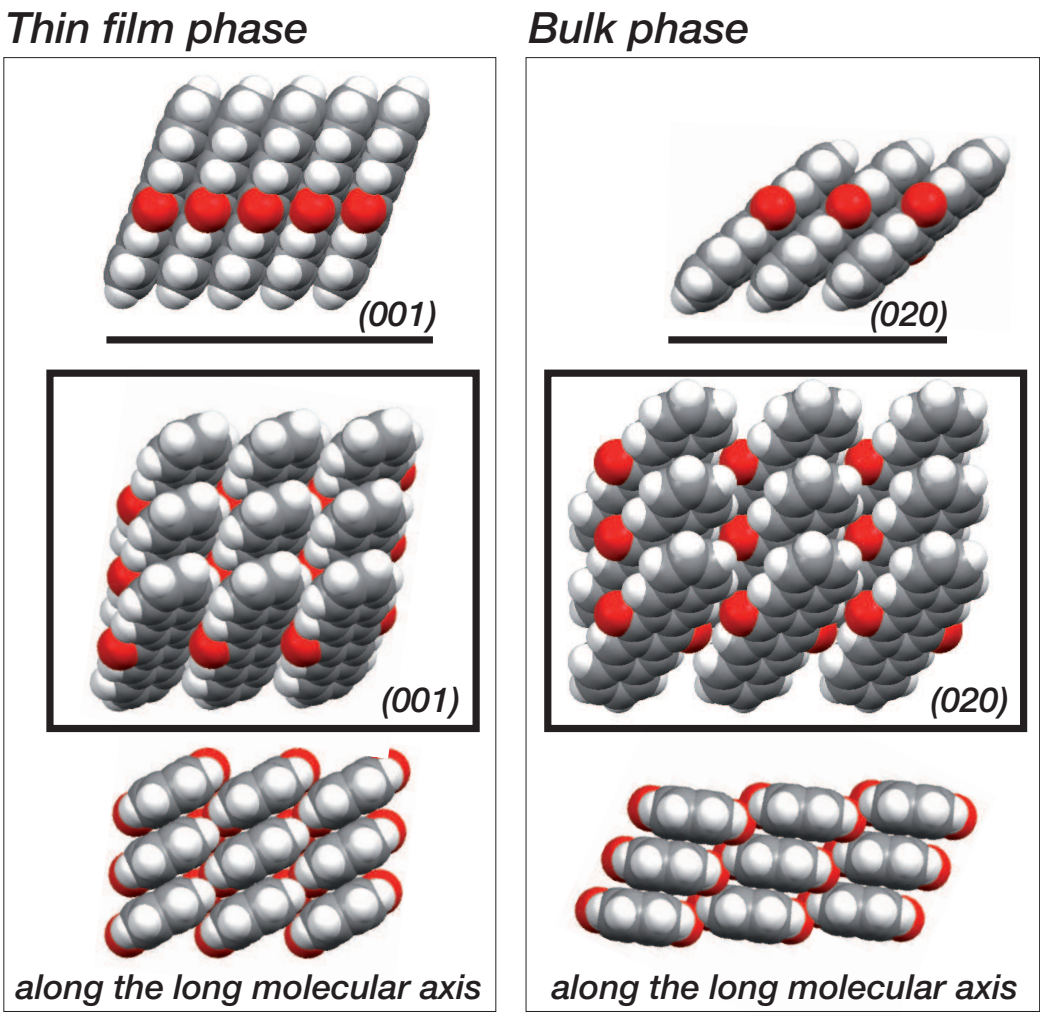

Figure 5.40: Comparison of the PQ thin film phase structure (left), as derived by force field calculations for the unit cell parameters obtained from RSM, with the PQ bulk phase (right). From top to bottom: View along the direction formed by the intersection of molecular and texture planes (001) and (020), respectively; top view on the texture planes; view along the long molecular axes. For the bulk phase one layer parallel to the (020) plane was taken into account therefore *not* showing the herringbone arrangement *between* the adjacent layers along the bulk *b*-axis (see Fig. 5.35b). Carbon atoms are colored in grey, hydrogen white and oxygen red.

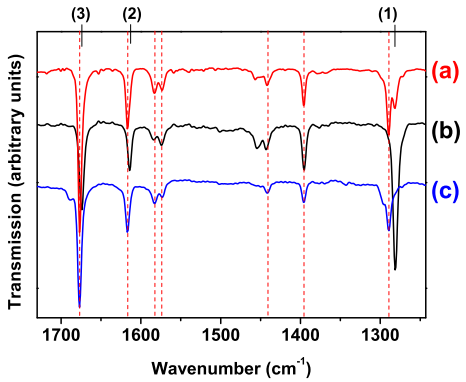

Figure 5.41: FT-IR investigations on (a) the PQ film investigated by RSM (thin film phase dominated) and the films investigated in Sec. 5.5, with (b) the pure PQ film (bulk dominated) and (c) the PEN:PQ film (thin film phase dominated); numbers label peaks of interest discussed in the text.

they are both thin film phase dominated samples (assignments and peak positions see Sec. 5.5). The spectrum (b) is the bulk phase dominated sample and peak (1) also can be found in spectrum (a) thus indicating a certain amount of PQ bulk also being present in the sample investigated by RSM, which can also be seen from the asymmetry of the peaks labeled (2) and (3) in spectrum (a).

5.6.3 Summary

In summary, the unit cell parameters of the unknown PQ thin film phase were determined and force field modelling yielded a reasonable model for the molecular arrangement of the PQ molecules in the unit cell. The thin film morphology explored via AFM exhibited island growth with terraced and surprisingly anisotropically shaped islands with *one* frayed side, which may be attributed to anisotropic inter-island diffusion caused by the tilted molecular arrangement with respect to the substrate in the PQ thin film phase.

5.7 Impact of low pentacenequinone concentration on pentacene thin film growth

Thin films of PEN have been vacuum co-deposited on SiO_x with low concentrations of PQ in order to investigate the impact on the PEN thin film structure. Within a range of 2-20% PQ concentration no intercalation of the compounds can be observed by means of XRD and FT-IR. The crystalline quality of the PEN films stays unchanged by the presence of PQ, whereas PEN bulk phase contributions are being suppressed at PQ concentrations $\geq$5%, which could be confirmed by means of AFM. From these results phase-separated PQ growth is suggested as well as PQ nucleation at PEN grain boundaries.
This work is published as Ref. [183].

5.7.1 Introduction

It was found that PQ is a main impurity in commercially available PEN and that its presence can significantly reduce the charge carrier mobility in PEN single crystals [77]. In addition, it was suggested that PQ can form deep traps for electrons within a PEN matrix, depending on the mutual molecular orientation (see Sec. 5.4). In Sec. 5.5 it was shown that PEN and PQ exhibit pronounced phase separation if co-deposited in a molar ratio of 1:1. However, up to now no attention has been directed to possible structural changes of PEN thin films due to the presence of low concentrations of PQ during PEN thin film growth. This issue is addressed by controlled vacuum co-deposition of PEN and PQ using films of nominally 30 nm thickness.

5.7.2 Structural properties

Specular x-ray diffraction (see Sec. 3.1.1) was performed on PEN:PQ co-deposited films with PQ concentrations of 50%, 20%, 10%, 5% and 2%, as well as on a reference film of pure PEN (see Fig. 5.42a). It is known that PEN can grow in different polymorphs depending on the film preparation conditions [217, 245]. In all spectra primarily the $00l$-series of a PEN structure characterized by a (001) net plane spacing that of (1.55 ± 0.01) nm was found, which is commonly referred to as *PEN thin film phase* [263], indicating a nearly upright standing molecular orientation. For the pure and PEN film containing 2% PQ additionally two reflections originating from the (1-10) and (022) net planes of another polymorph were found [196] (referred to as *bulk phase* in the following). Here the long molecular axes are parallel with respect to the substrate plane. In the latter case, the intensity of the bulk

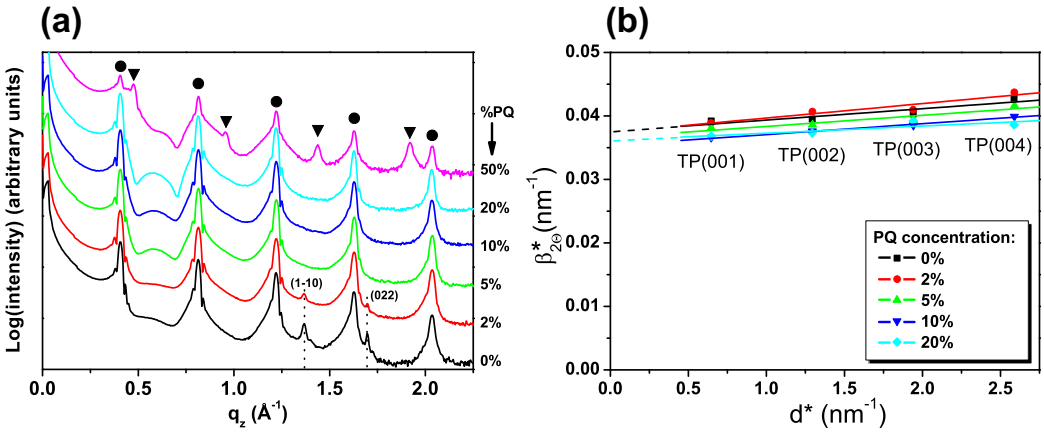

Figure 5.42: (a) Specular XRD scans of PEN:PQ co-deposited films on SiO_x at various molar ratios, q_z denotes the momentum transfer normal to the surface at the Bragg angle Θ, the plots are vertically shifted for clearness. Peaks assigned to the PEN and PQ thin film phases are marked with a circle and triangle respectively, peaks assigned to the PEN bulk phase are labeled with the corresponding indices. (b) Williamson-Hall plot of PEN films co-deposited with different amounts of PQ. The lines connecting the peak series are linear least-squares fits; TP denotes the PEN thin film phase.

contributions is reduced by 25%, and vanishes at PQ concentrations $\geq$5%. Interestingly, no peaks from PQ can be found even at concentrations as high as 20%. Instead, a broad feature arises between the PEN (001) and (002) reflections, which may be due to scattering from amorphous PQ. However, in the 1:1 case PEN and PQ grow in phase separated crystallites, exhibiting the two series of the respective thin film phases (see Sec. 5.5 and 5.6).

In order to investigate the microstructure of the mixed films a Williamson-Hall analysis (WHA) (see Sec. 2.2.2) has been performed. Being aware of the limitations of this simple model in deriving absolute values for $\langle D \rangle_V$ and the strain e [119], WHA was applied to explore *changes* within the PEN lattice due to low-concentrations of PQ. The line profiles of the PEN (00l) reflections were fitted using pseudo-Voigt functions; the result is shown in Fig. 5.42b. For pristine PEN a value of $\langle D \rangle_V = (26.6 \pm 0.6)$ nm was found, which is only slightly increased to (27.7$\pm$0.5) nm for the film containing 20% PQ. The value of the strain remains essentially constant for all PEN:PQ ratios. The slight increase of $\langle D \rangle_V$ can be attributed to the decrease of the PEN bulk phase amount, as the PQ ratio is increased (see Fig. 5.42a). This demonstrates that the PEN thin film phase crystallites grow essentially *undisturbed* despite the presence of 2-20% PQ, which is corroborated by the constant strain.

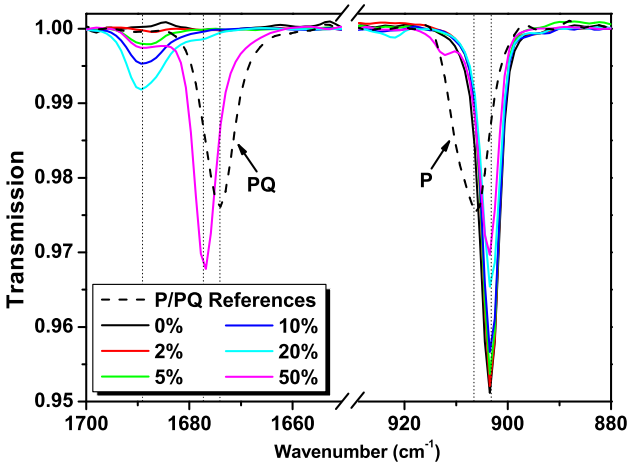

Figure 5.43: FT-IR spectra of PEN:PQ blended films of different PQ percentages compared to reference scans of the respective source materials used for evaporation.

5.7.3 Vibrational spectroscopy

In contrast to XRD, where only contributions of crystalline volume portions can be detected, FT-IR (see Sec. 3.3) provides information also on less ordered sample volumes. For instance, FT-IR can be used to study polymorphism of organic molecular crystals [81, 182]. It allows even to observe amorphous regions and can be highly sensitive to changes of the molecular environment, as would be induced by intercalation of PEN and PQ.

FT-IR was performed on the same set of samples that were investigated by XRD; characteristic parts of the spectra are shown in Fig. 5.43 in comparison to reference spectra of the pure materials. In the region of C-H out-of-plane bending and stretching modes [207, 208], the most intense PEN absorption (903.5 cm^{-1}) was shifted by -3.0 cm^{-1} with respect to the PEN reference. This is explained by the different molecular arrangement in the PEN powder and the vacuum deposited films (substrate induced PEN thin film phase)[19]. No shift of this mode was observed for PQ ratios up to 50%, which is further evidence for unchanged PEN growth in the presence of PQ. The same holds for other PEN vibrations (not shown). In the spectrum of the 50% PQ film the C=O stretching mode at 1676.9 cm^{-1} is blue-shifted by 2.7 cm^{-1} compared to the PQ reference [257, 258], which is explained by growth in the thin film polymorph [182], as found by XRD (Fig. 5.42a). However, at lower PQ concentrations, the intensity of this vibration is strongly reduced and a peak at 1689.2 cm^{-1} emerges, which has not been reported before. This indicates a different molecular environment of PQ (compared to the bulk and thin film phases) in the low-concentration cases. However, considerable PQ

[19]The intensity ratio of the (001) reflection of the thin film phase and the (1-10) reflection of the bulk phase in the spectrum of the pure PEN film was determined to ca. $1{:}10^{-4}$, therefore the bulk contribution might be undetectable with FT-IR.

intercalation into the PEN lattice can be ruled out, since this would alter the PEN lattice, and therefore also change the PEN absorption frequencies (which was not observed).

5.7.4 Morphology

In addition, all samples have been investigated by AFM (see Sec. 3.4); Fig. 5.44 displays micrographs of the pure PEN and the 20% PQ ratio sample. Appar-

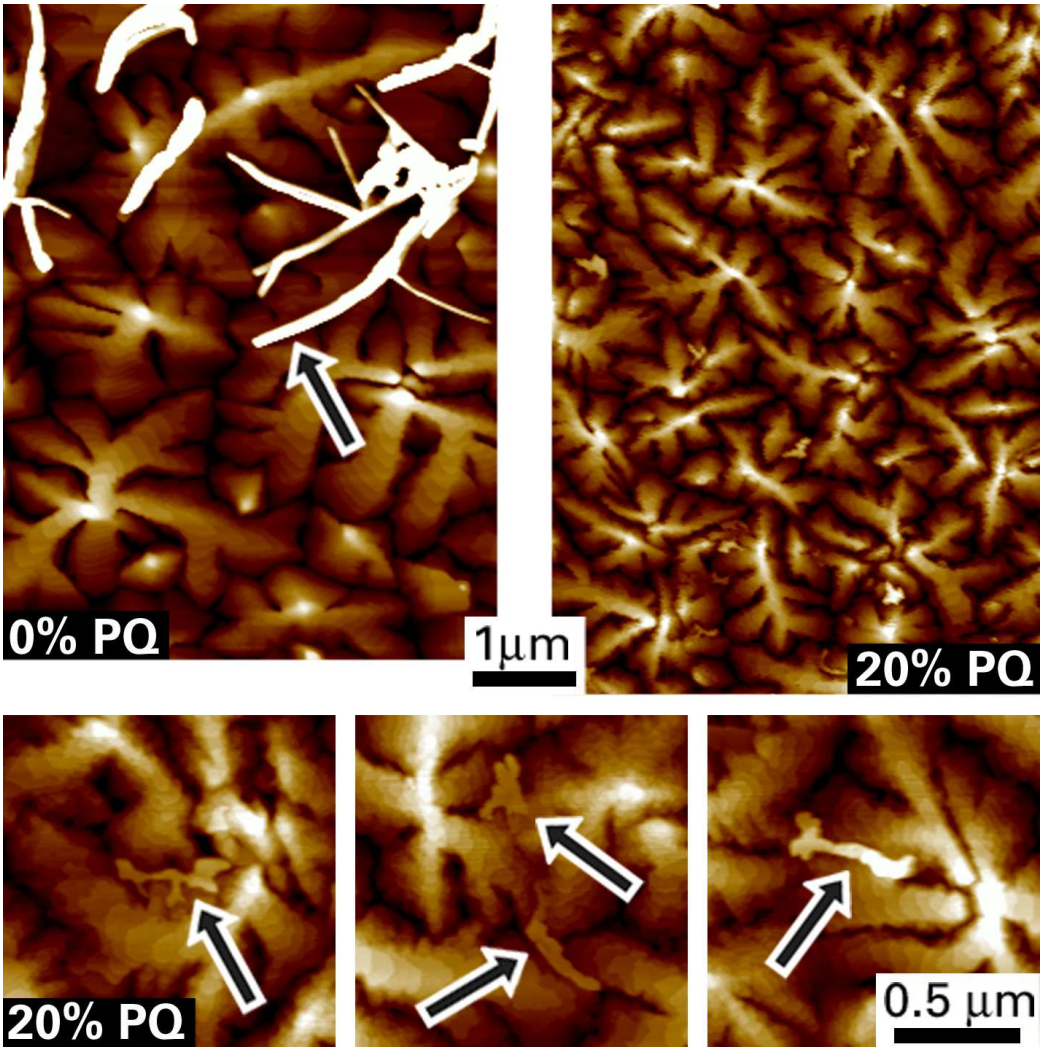

Figure 5.44: AFM micrographs of a pure PEN film compared to a co-deposited PEN:PQ film with 20% PQ ratio. The colors indicate a height range of 30 nm, arrows point to areas of interest (see text).

ently, the PEN island density increased for PQ concentrations $\geq 20\%$ (*e.g.*, 0% PQ: 0.4 μm^{-2}, 20% PQ: 0.9 μm^{-2}). Both films showed the expected morphology of the PEN thin film phase with characteristic steps of (1.6 ± 0.2) nm height. Apart from PEN thin film phase islands small areas of different morphology were found in both cases, assigned to: Areas of PEN bulk phase (pure PEN film) and PQ areas (co-deposited film with 20% PQ ratio)[20]. As the features assigned to PQ in the co-deposited film (Fig. 5.44) are being found at PEN grain boundaries, these sites can be expected to be preferred nucleation positions for PQ, since the findings from XRD and FT-IR provide strong evidence against intercalated growth of PEN and PQ, and a reduction of the lateral extension of the PEN islands was observed.

5.7.5 Summary

In conclusion, the influence of low-concentration PQ presence on PEN thin film growth has been investigated. Upon co-deposition with PQ, the proportion of the PEN bulk phase is reduced and even absent for PQ concentrations $\geq 5\%$. Within the investigated PQ concentration range, the crystalline quality of the PEN structure remains unchanged and no evidence for intercalated growth was found. Instead, it is suggested that PQ accumulates at PEN grain boundaries thus leading to additional complexity of grain boundary energetics with an expected impact on charge transport, which could now be studied systematically as function of PQ content. Moreover, it should be interesting to investigate possible charge- confinement on single PEN grains due to barriers provided by PQ.

[20]The flat features assigned to PQ areas in the co-deposited film are being found near grain boundaries and can not be observed in the pure PEN film, whereas the areas assigned to the PEN bulk phase in the pure PEN film can not be observed at PQ ratios $> 5\%$ in the co-deposited films.

5.8 The Interaction of oxygen and ozone with pentacene

Ultraviolet photoemission spectroscopy was used to investigate the effect of oxygen and air exposure on pentacene thin film electronic structure. It is found that O_2 and water do not react noticeably with pentacene on the timescale of several hours, whereas singlet oxygen and ozone readily oxidizes the organic compound. No evidence was obtained for irreversible intercalation of oxygen into pentacene or considerable p-type doping after re-evacuation. Infrared spectroscopy and atomic force microscopy are used to study the oxidation of pentacene thin films. The data suggest the oxidation of pentacene with reactive oxygen species to yield highly volatile reaction products as evidenced by significant mass-losses of the films observed by AFM.
This work is published as Ref. [264] and [175][21].

5.8.1 Introduction

The interplay between thin film structure/morphology and measured charge carrier mobility is of particular interest [77, 265, 266]. However, a reliable comparison between experimental results obtained in different laboratories is often hampered by the variation of sample preparation and the environmental conditions for mobility measurements [14, 267, 268]. Another issue is long term stability of devices made from organic materials, as oxidation is believed to be a major reason for early device failure [269, 270]. It has been observed that the measured conductivity of PEN thin films and single crystal surfaces depends on the residual oxygen or air pressure [271]. It was shown that oxygen can diffuse into PEN, and readily diffuses out again after re-evacuation [271]. Still to be addressed is the nature, on a molecular scale, of oxygen-induced changes in charge transport properties. It needs to be established to what extent and under which experimental conditions these changes are reversible. Additionally, it has been proposed that oxygen creates new (chemical) species in PEN films, some of which have states in the otherwise empty energy gap of PEN, and therefore act as traps for charges [269]. Consequently, a movement of E_F in the organic film towards the highest occupied molecular orbital (HOMO) is predicted, displaying p-type behavior of the organic semiconductor [272, 273]. The approach to resolve the above questions consists in using UPS (see Sec. 3.2) to follow changes in the E_F-position of PEN single crystals and thin films before and after exposure to oxygen and to air.

[21] The data analysis of this section was led by Antje Vollmer (BESSY, Berlin).

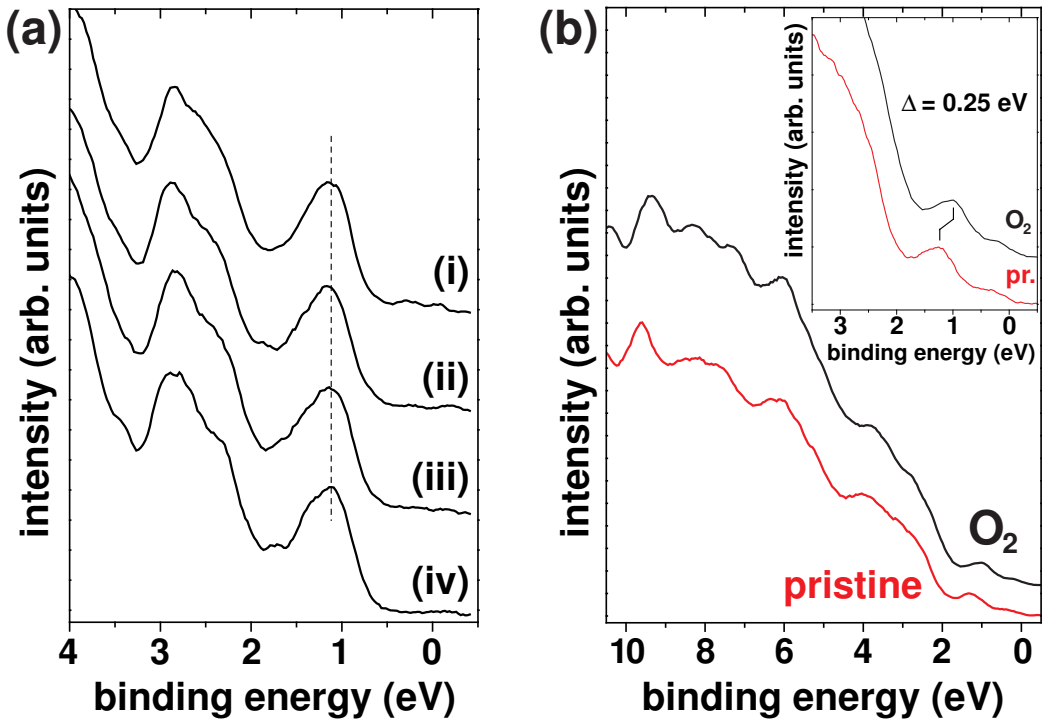

Figure 5.45: (a) UPS spectra of a PEN single crystal measured under the following conditions (and in this time sequence): (i) 3×10^{-8} mbar partial O_2 pressure, (ii) 32×10^{-9} mbar total residual pressure, (iii) 3×10^{-8} mbar partial O_2 pressure after exposure to 5×10^{-6} mbar O_2 for 30 min, and (iv) again at 2×10^{-9} mbar total residual pressure. (b) Extended BE scale UPS spectra of 12 nm PEN on Au before (pristine; bottom curve) and after (upper curve) exposure to one atmosphere of O_2 for 60 min. Inset: close-up of the near-E_F region, indicating the rigid shift Δ.

5.8.2 Electronic structure

The valence region UPS spectra (Fig. 5.45a) recorded on a PEN single crystal under different residual oxygen pressure during the measurement and total oxygen exposure clearly show that there is no influence of molecular oxygen on the position of the energy levels (at the given conditions). Note that the exposure to oxygen at 10^{-6} mbar for one second is sufficient for the (hypothetical) formation of a complete O_2 monolayer. If crystalline PEN were prone to undergo rapid oxidation, the dosing conditions used here would allow for the detection of such, since UPS is highly surface sensitive. A reaction of PEN with electron withdrawing oxygen would result in a loss of conjugation, which would be visible in a UPS spectrum as a decrease in the relative in-

tensity and shift towards higher binding energy of the emission derived from the HOMO [176] (the peak at 1.1 eV binding energy in Fig. 5.45a). All four spectra in Fig. 5.45a exhibit the same characteristic photoemission features of PEN, comparable to previous reports [58, 274]. If "doping" (*i.e.*, p-type) of PEN by O_2 were the case (to a significant degree), a clear shift of all levels towards lower binding energy (BE) would be observed [273, 275]. While changes in conjugation (due to a chemical reaction) would be difficult to be seen for concentrations smaller than a few percent, energy shifts due to doping can readily be seen for much smaller concentrations (below 0.3% [275]). However, the total *in situ* exposure of the single crystal to O_2 was rather limited (up to a pressure of 3×10^{-8} mbar; for experimental limitations), and one might argue that the single crystal was exposed to air for a very long period of time (several days) prior to the initial measurement. As the time required for oxygen molecules to insert in the PEN crystal is on the order of tens of minutes even at atmospheric pressure (the time constant for 15 μm thick crystals is approximate 100 minutes [271]), no noticeable changes in the spectrum could be observed. Therefore the following investigations have been performed on *in situ* deposited thin films of PEN.

A PEN film of 12 nm nominal thickness was deposited onto *in situ* sputtered polycrystalline Au. The corresponding UPS spectrum is shown on a wide energy range in Fig. 5.45b (bottom curve), and as a close-up in the figure inset. The Au Fermi-edge can still be discerned, since PEN exhibits pronounced island growth on Au [58]. The low BE-onset of the highest occupied molecular orbital (HOMO) is 0.8 eV below the Fermi-level (E_F), consistent with earlier reports [58, 274]. After exposure to O_2 at atmospheric pressure for one hour, the entire UPS spectrum was shifted 0.25 eV towards lower BE (Fig. 5.45b, upper spectrum, and inset) but the lineshape remained unchanged. This result would be consistent with p-type doping of PEN by oxygen that remains intercalated within the organic layer after re-evacuation. However, it has been suggested by Seki and Ishii [276] that oxygen adsorption below the organic film on the metal substrate surface changes its work function (ϕ). Therefore, the shift seen in Fig. 5.45b may be related to this change of substrate ϕ and/or a shift of the PEN molecular levels due to doping. The only way to differentiate between the two mechanisms is the use of substrates which are not influenced by oxygen. The surfaces of silicon oxide (SiO_x) and HOPG are suitable for the present purpose.

Fig. 5.46 shows UPS spectra of nominally 12 nm thick, pristine PEN films on SiO_x (i) and HOPG (iv). These two spectra differ in the relative photoemission intensities from some molecular levels, as one can see clearly for the feature at ca. 3 eV BE in particular. This is due to the fact that the long molecular axis of PEN is oriented almost vertically on SiO_x (when the

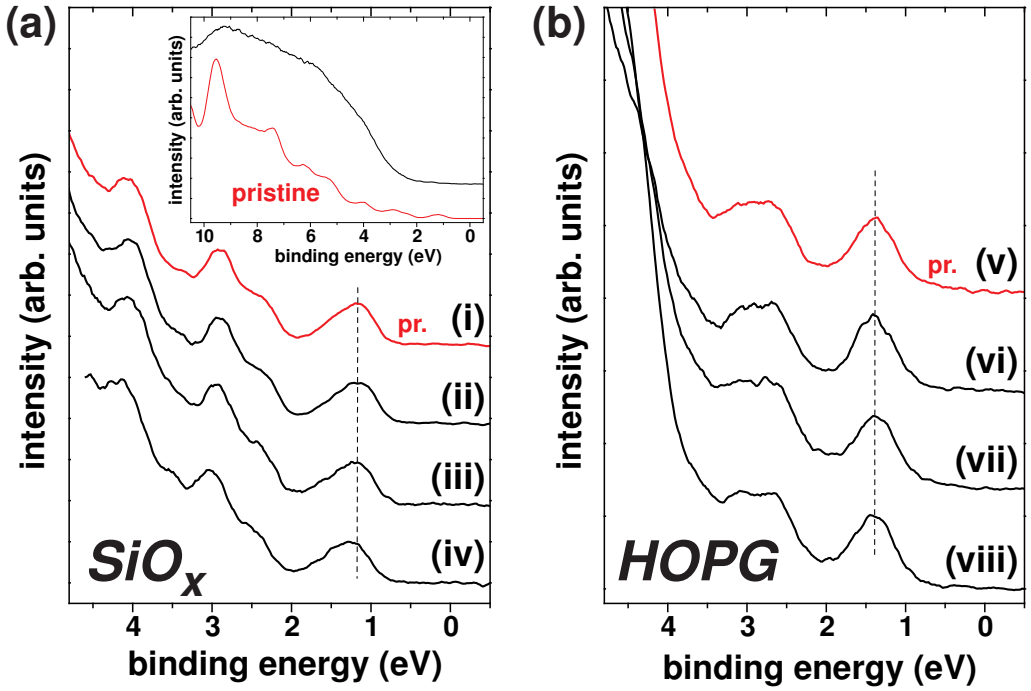

Figure 5.46: UPS spectra of 12 nm PEN films on SiO_x (left-hand side) and HOPG (right-hand side). (i) and (v): pristine. (ii) and (vi): after exposure to one atmosphere O_2 for 30 min (in dark). (iii) and (vii): after additional exposure to one atmosphere O_2 for 120 min (with visible light). (iv) and (viii): after additional exposure to ambient air for 60 min (with visible light). Inset: extended UPS spectra of the pristine PEN film on SiO_x (bottom), and after exposure to ambient air for 15 min with UV irradiation (top).

film is grown at room temperature [196]), while it is presumably parallel to the surface of HOPG [81, 277]. It is known that measured photoemission intensities depend strongly on molecular orientation [278]. The energy spacing of emission features in both films are identical, which is strong evidence for intact PEN being present on both surfaces. These two films were exposed to one atmosphere of pure oxygen in dark for 30 min. (Fig. 5.46 (ii) and (vi)). Subsequently, the samples were exposed to one atmosphere of pure oxygen for 120 min. (Fig. 5.46 (iii) and (vii)), this time irradiated with visible light (to test the influence of PEN optical excitation during exposure) from a halogen lamp (cutoff wavelength of the experimental chamber glass window: 300 nm). In the next step, both samples were exposed to ambient air for 60 min. (Fig. 5.46 (iv) and (viii)), again with visible light irradiation. Finally, exposure to ambient air for 15 min proceeded, with the samples being

additionally exposed to ultraviolet (UV) light (inset of Fig. 5.46) from a low-pressure Hg-lamp (placed ca. 10 cm away from the samples). Note that the applied exposure times are sufficient for complete diffusion of O_2 through the thin film (as mentioned above for thick single crystals [271]), and that after each exposure the samples were brought back to UHV conditions for the UPS measurements. Most notably, the spectra in Fig. 5.46a and Fig. 5.46b ((i) - (iv) and (v) - (viii)) are - within the experimental error - virtually identical in both energy position and lineshape, regardless of treatment.

The essence of these experimental results is that molecular oxygen and also water (from air) do not react with PEN (on the timescale of the experiments), as long as they come into contact in dark or under visible light. The surface sensitivity of UPS would unmistakably allow for the identification of such a reaction. Therefore it is reasonable to conclude that optically excited PEN (the optical gap of PEN is 1.85 eV [67], thus well contained in the spectrum of the halogen lamp used here) is not sufficient to promote a reaction. Oxygen possibly diffused into PEN at atmospheric pressure appears to diffuse out again rapidly after re-evacuation, and does not lead to irreversible changes (detectable by UPS) in the electronic structure, like, *e.g.*, p-type doping (as might have been suspected from the experiment with the Au substrate). Yet, charge traps predicted in several works may be present [270, 273], but at such low density that the Fermi-level position in PEN is not affected. The shift of ≤ 0.1 eV observed for spectrum (d) in Fig. 5.46. might point towards an effect of water adsorption on the SiO_x substrate properties. It can be ruled out that PEN itself is affected, since no shift is seen for PEN/HOPG (spectrum (viii)). In contrast, the inset of Fig. 5.46 demonstrates that the exposure of PEN to air in the presence of UV light leads to a rapid reaction of PEN, most probably an oxidation by singlet oxygen and/or ozone (produced by the UV light). Unfortunately, the reaction product is ill-defined, as can be seen from the featureless spectrum (upper curve in the inset of Fig. 5.46). Essentially the same spectrum was observed for the PEN/HOPG after air/UV exposure (spectrum not shown).

The comparison of the results on the different substrates allows to clearly differentiate between doping of PEN (*not observed* under the present experimental conditions) and a modification of the substrate properties (*observed* for the Au substrate) due to oxygen exposure. It cannot be excluded that oxygen- or water-induced changes occur at higher pressures (still reversible), which could not be experimentally achieved. The implication for devices comprising PEN and Au contacts (*e.g.*, field effect transistors [273]) is that upon exposure of the devices to oxygen/air a considerable lowering (increase) of the hole (electron) injection barrier from Au into PEN occurs (*i.e.*, from 0.8 eV to 0.55 eV for holes), which is not caused by doping.

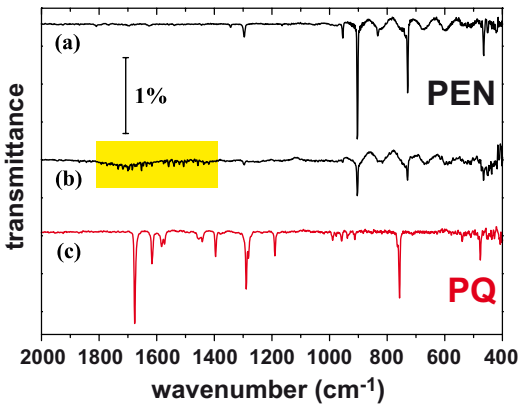

Figure 5.47: Infrared spectra of a 12 nm thick PEN film on SiO_x (a) in its pristine state and (b) after 13 h UV exposure in air. The wiggles below 1000 cm^{-1} are caused by the electronics of the spectrometer. (c) Infrared spectrum of a 12 nm thick 6,13-pentacenequinone film on SiO_x.

5.8.3 Vibrational spectroscopy

In order to investigate the chemical reactions occurring in PEN thin films in the presence of reactive oxygen species infrared spectroscopy experiments (see Sec. 3.3) have been performed[22] on PEN films as a function of exposure time to UV light from the low pressure Hg-lamp in ambient air. The IR spectrum of a 12 nm thick pristine PEN film on SiO_x (Fig. 5.47a) displays a number of strong absorption bands, which can be identified according to the literature [58]: 729 cm^{-1} and 903 cm^{-1} are out-of-plane C-H bending modes, 1296 cm^{-1} a ring stretching mode, and several peaks close to 3040 cm^{-1} (not shown) correspond to C-H in-plane stretching modes. A representative IR spectrum taken after 13 h exposure to UV radiation in air is shown in Fig. 5.47b. Absorption peaks characteristic of PEN have decreased in intensity, and only a very weak and ill-defined broad feature between 1600 cm^{-1} and 1800 cm^{-1} (region of the C=O stretching modes) appears in the spectrum, which may indicate the formation of a variety of oxidized intermediate species (the tiny sharp absorptions in this region are due to residual water vapour in the spectrometer). Interestingly, no absorptions characteristic of PQ can be identified in comparison to Fig. 5.47c, where the IR spectrum of a 12 nm thick PQ film is displayed. The absorption at 1676 cm^{-1} is assigned to the characteristic C=O stretching mode [275]. From these observations it can be concluded that PQ is not a stable intermediate that forms upon oxidation of PEN with reactive oxygen species, but that oxidation proceeds efficiently to form small, volatile reaction products.

[22]The FT-IR investigations were performed by H. Weiss, Universität Magdeburg, Chemisches Institut, D-39106 Magdeburg, Germany.

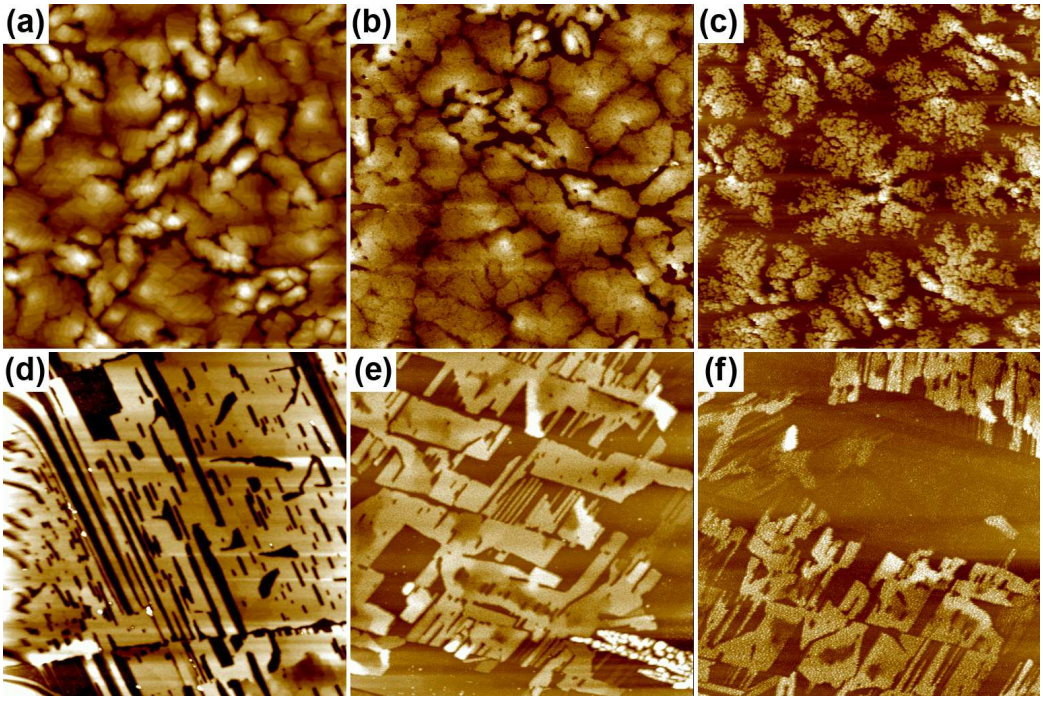

Figure 5.48: AFM images of a 12 nm thick PEN film on SiO_x in its pristine state (a), after 11 h (b) and 26.5 h (c) UV-exposure in air and of a pristine film on HOPG (d), after 13.3 h (e) and 22.3 h (f) UV-exposure in ambient air. (a-c: $6 \times 6\mu m^2$, d: $10 \times 10\mu m^2$ and e-f: $5 \times 5\mu m^2$; 40 nm height scale)

5.8.4 Morphology

In order to confirm the film mass-loss suggested by the intensity decrease of PEN related vibrations in the IR-investigation as well as to gain a deeper insight into the decay of the PEN films' morphology upon oxidation, AFM investigations (see Sec. 3.4) have been performed[23] under analogue conditions to the IR experiments. Fig. 5.48 gives the comparison of the PEN film in its pristine state and after UV-irradiation in air. For pristine SiO_x a three-dimensional growth with frayed pyramidal terraced structures is found (comparable to Fig. 5.32a).

Upon exposure to the reactive oxygen species the terraces of the PEN film become corrugated and sieve-like, hinting towards the lack of preferential mesoscopic reaction sites, such as step edges (Fig. 5.48a-c). The AFM images give evidence to the fact that the reactive oxygen species corrode the islands both at the edges as well as on the terraces, and that significant mass-loss

[23]The AFM investigations have been performed in cooperation with S. Rentenberger, Graz University of Technology, Austria.

occurs, due to the formation of volatile reaction products. The PEN film on the HOPG substrate (Fig. 5.48d-f) shows the same behaviour upon exposure to irradiation with UV-light in ambient air.

5.8.5 Summary

In extensive tests no reaction of PEN with molecular oxygen and water on the timescale of a few hours was observed, even if PEN is optically excited. More importantly, it was found that oxygen diffusion through PEN thin films (and single crystals) is reversible, and does not leave behind - after re-evacuation - electrically active electronic states that would lead to doping of the organic bulk material. This is evidenced by a lack of energy shifts in UPS spectra of PEN before and after exposure to O_2 and to air. Instead, it was found that the hole injection barrier at the Au/PEN interface is lowered by oxygen exposure. Finally, it was demonstrated that rapid oxidation of PEN occurs in air only in the presence of UV light, due to the formation of highly reactive singlet oxygen and/or ozone. In none of the investigated cases PQ was observed originating from PEN oxidation.

Chapter 6

Summary and Outlook

In this work the combination of PEN with C60, PFP and PQ within layered and co-deposited heterostructures was investigated in vacuum sublimed films. A thorough structural, energetic and morphological characterization was carried out in order to judge the respective application potential for the field of organic electronics. Throughout this work a multi-technique approach was followed utilizing XRD, FT-IR, AFM and UPS in order to access complementary information on both the structural and energetic properties of these PEN heterostructures.

For the heterostructures with C60 the poor performance results of bulk-heterojunction based OPVCs compared to layered ones could be attributed to morphological instead of energetic or structural issues, clearly demonstrating that in general a comprehensive multi-technique view on the physical properties is necessary to correctly interpret device performance results in the field of organic electronics. From the present results a systematic modification of preparation parameters and device structure may be feasible: An increase of the PEN underlayer thickness and a reduction of the PEN island separation distance *e.g.*, via a significant increase of the deposition rate or via substrate cooling could combine the benefits of the layered and the co-deposited structures. Experiments in this directions will be carried out in the near future.

The combination of PEN with PFP, *i.e.*, the heterojunction of the two maybe most auspicious OSCs, demonstrated that PFP nicely wets a PEN underlayer, which is of importance for OFET applications. Moreover, an unknown thin film polymorph of PFP could be solved using grazing incidence RSM. Bulk heterostructures of PEN and PFP were found to form a mixed crystal structure, which will be subject of a forthcoming investigation in terms of a full structure solution. In the present work, this blended structure of PEN and PFP mixed on a molecular scale could be successfully applied

to tune the ionization energy of thin films by a change of the mixing ratio, which was explained by the presence of intramolecular polar bonds (C-H and C-F for PEN and PFP, respectively). The corresponding UPS investigations could be effectively corroborated by electrostatic modelling to theoretically substantiate the findings. This study demonstrates that surface engineering of OSCs can be performed via adjusting the polarity of intramolecular bonds, which therefore represents a viable alternative to the surface modification of substrates to control the interface energetics.

The third investigated PEN heterostructure was the combination with PQ, where the electronic structure of PEN/PQ and PQ/PEN layered films was thoroughly investigated by UPS on application relevant substrates. Films with highly molecular-orientation dependent ionization energies were found, which could again be explained by the different surface termination of films comprising surface dipoles. This study insistently outlined the necessity for a detailed knowledge on the structural arrangement in functional organic layers, since the mutual molecular orientation was demonstrated to severely impact the energy level offsets between the respective compounds. Moreover, the observed energy level offset exhibited to be capable for the use as heterojunction for efficient exciton dissociation in OPVC applications. Therefore, pure, layered and 1:1 co-deposited films of PEN and PQ were thoroughly characterized by means of XRD, FT-IR and AFM, where pronounced phase separation in the case of co-deposition was observed suppressing (textured) growth of PQ in its bulk phase polymorph and promoting growth in an up to now unexplored PQ thin film polymorph. PQ was identified to be an interesting model material for the investigation of highly three-dimensional island growth, since even at high nominal coverages no closed film could be achieved, while the crystalline quality was found to be outstandingly high. This growth behaviour further offers the possibility, *e.g.*, in conjunction with subsequent PEN deposition, to use the intrinsically corrugated film morphology of pure PQ as electron acceptor in layered OPVCs with therefore intrinsically increased interfacial area. Layered devices of p-type oligomer materials or polymers on PQ underlayers will therefore be subject of further investigations. Furthermore, the thin film polymorph of PQ was successfully solved using grazing-incidence RSM, where force field calculations yielded a molecular arrangement markedly different to the bulk structure with an intriguing loss of the herringbone arrangement known from the PQ bulk. Morphological investigations using AFM revealed anisotropic island borders, which was suggested to be related to the dynamics of thin film growth. This finding of fundamental interest will be subject of further research efforts comprising investigations of a possible coverage/rate dependence of this anisotropic growth behaviour in order to alter the dynamics of island growth. Moreover, the im-

pact of PQ as impurity in PEN thin film growth was investigated in detail via structural investigations again following a multi-technique approach. It was shown that PQ does not measurably intercalate with PEN and rather forms phase-separated patches or accumulates at PEN grain boundaries. Finally, PQ presence in PEN films due to a possible oxidation of PEN to PQ under oxygen exposure was investigated owing to the relevance for real-world applications. Using UPS and FT-IR as experimental tools it was demonstrated that O_2 and water do not react noticeably with PEN on the timescale of hours, whereas singlet oxygen and ozone readily oxidizes the PQ films producing highly volatile reaction products instead of PQ from the oxidation process.

Within this work, several issues of fundamental and application relevance have been addressed. On the one hand, the material scientific knowledge on heterostructures of possibly trendsetting OSCs was enlarged, which could be of relevance for more technologically oriented future studies. Two unknown crystal structures were solved, which is of importance, since the charge transport through OSCs is very sensible to the molecular arrangement. In this context, several matters could only be clarified, since a comprehensive multi-technique approach was followed, which I assume to be mandatory for effective progress in this application directed research field. On the other hand, issues of fundamental physical relevance like the impact of intramolecular polar bonds on the thin film energetics were addressed, which can now be used well directed in technological applications.

Bibliography

[1] F. Garnier, G. Horowitz, X. Peng, and D. Fichou. An all-organic 'soft' thin film transistor with very high carrier mobility. *Adv. Mater.*, 2(12): 592–594, 1990.

[2] S. R. Forrest. The path to ubiquitous and low-cost organic electronic appliances on plastic. *Nature*, 428:911–918, 2004.

[3] G. Horowitz. Organic field-effect transistors. *Adv. Mater.*, 10(5):365–377, 1998.

[4] J. H. Burroughes, D. D. C. Bradley, A. R. Brown, R. N. Marks, K. Mackay, R. H. Friend, P. L. Burns, and A. B. Holmes. Light-emitting diodes based on conjugated polymers. *Nature*, 347(6293): 539–541, 1990.

[5] H. Sirringhaus, N. Tessler, and R. H. Friend. Integrated optoelectronic devices based on conjugated polymers. *Science*, 280:1741–1744, 1998.

[6] J. R. Sheats, H. Antoniadis, M. Hueschen, W. Leonard, J. Miller, R. Moon, D. Roitman, and A. Stocking. Organic electroluminescent devices. *Science*, 273:884–888, 1996.

[7] C. W. Tang and A. C. Albrecht. Photovoltaic effects of metal–chlorophyll-a–metal sandwich cells. *J. Chem. Phys.*, 62(6):2139–2149, 1975.

[8] C. W. Tang. Two-layer organic photovoltaic cell. *Appl. Phys. Lett.*, 48: 183–185, 1986.

[9] G. Yu, J. Gao, J. C. Hummelen, F. Wudl, and A. J. Heeger. Polymer photovoltaic cells: Enhanced efficiencies via a network of internal donor-acceptor heterojunctions. *Science*, 270(5243):1789–1791, 1995.

[10] P. Peumans, S. Uchida, and S. R. Forrest. Efficient bulk heterojunction photovoltaic cells using small-molecular-weight organic thin films. *Nature*, 425:158–162, 2003.

[11] C. W. Tang and S. A. VanSlyke. Organic electroluminescent diodes. *Appl. Phys. Lett.*, 51:913–915, 1987.

[12] N. Koch. Organic Electronic Devices and Their Functional Interfaces. *ChemPhysChem*, 8:1438–1455, 2007.

[13] M. Schwoerer and H. C. Wolf. *Organic Molecular Solids*. Wiley-VCH, 2006.

[14] C. D. Dimitrakopoulos and P. R. L. Malenfant. Organic Thin Film Transistors for Large Area Electronics. *Adv. Mater.*, 14:99–117, 2002.

[15] J. E. Anthony. Functionalized acenes and heteroacenes for organic electronics. *Chem. Rev.*, 106(12):5028–5048, 2006.

[16] C. D. Dimitrakopoulos and D. J. Mascaro. Organic thin-film transistors: A review of recent advances. *IBM J. Res. Dev.*, 45(1):11–27, 2001.

[17] F. J. Meyer zu Heringdorf, M. C. Reuter, and R. M. Tromp. Growth dynamics of pentacene thin films. *Nature*, 412(6846):517–520, 2001.

[18] A. K. Pandey and J.-M. Nunzi. Efficient flexible and thermally stable pentacene/C_{60} small molecule based organic solar cells. *Appl. Phys. Lett.*, 89(21):213506, 2006.

[19] J. Yang and T. Q. Nguyen. Effects of thin film processing on pentacene/C60 bilayer solar cell performance. *Org. Electron.*, 8(5):566–574, 2007.

[20] S. Yoo, B. Domercq, and B. Kippelen. Efficient thin-film organic solar cells based on pentacene/C_{60} heterojunctions. *Appl. Phys. Lett.*, 85: 5427–5429, 2004.

[21] S. Yoo, W. J. Potscavage Jr., B. Domercq, S. Han, T. Li, S.C. Jones, R. Szoszkiewicz, D. Levi, E. Riedo, S. R. Marder, and B. Kippelen. Analysis of improved photovoltaic properties of pentacene/C60 organic solar cells: Effects of exciton blocking layer thickness and thermal annealing. *Solid-State Electron.*, 51(10):1367–1375, 2007.

[22] D. M. Nanditha, M. Dissanayake, A. A. D. T. Adikaari, Richard J. Curry, Ross A. Hatton, and S. R. P. Silva. Nanoimprinted large area heterojunction pentacene-C_{60} photovoltaic device. *Appl. Phys. Lett.*, 90:253502, 2007.

[23] Y. Inoue, Y. Sakamoto, T. Suzuki, M. Kobayashi, Y. Gao, and S. Tokito. Organic thin-film transistors with high electron mobility based on perfluoropentacene. *Jpn. J. Appl. Phys.*, 44:3663–3668, 2005.

[24] Y. Sakamoto, T. Suzuki, M. Kobayashi, Y. Gao, Y. Fukai, Y. Inoue, F. Sato, and S. Tokito. Perfluoropentacene: High-Performance p-n Junctions and Complementary Circuits with Pentacene. *J. Am. Chem. Soc.*, 126(26):8138–8140, 2004.

[25] Y. Sakamoto, T. Suzuki, M. Kobayashi, Y. Gao, Y. Inoue, and S. Tokito. Perfluoropentacene and Perfluorotetracene: Syntheses, Crystal Structures, and FET Characteristics. *Mol. Cryst. Liq. Cryst.*, 444(1): 225–232, 2006.

[26] P. Walden. Von der Iatrochemie zur Organischen Chemie. *Zeitschrift für Angewandte Chemie*, 40(1):1–16, 1927.

[27] H. Haken and H. C. Wolf. *Molekülphysik und Quantenchemie: Einführung in die experimentellen und theoretischen Grundlagen*. Springer, Berlin, Heidelberg, 5th edition, 2006.

[28] A. Bondi. van der Waals Volumes and Radii. *J. Phys. Chem.*, 68: 441–451, 1964.

[29] S. S. Batsanov. Van der Waals Radii of Elements. *Inorg. Mater.*, 37: 1031–1046, 2001.

[30] A. Gavezzotti and G. R. Desiraju. A systematic analysis of packing energies and other packing parameters for fused-ring aromatic hydrocarbons. *Acta Cryst.*, B44:427–434, 1988.

[31] G. R. Desiraju and A. Gavezzotti. Crystal structures of polynuclear aromatic hydrocarbons. Classification, rationalization and prediction from molecular structure. *Acta Cryst.*, B45:473–482, 1989.

[32] C. A. Hunter and J. K. M. Sanders. The Nature of π-π Interactions. *J. Am. Chem. Soc.*, 112:5525–5534, 1999.

[33] E. Venuti, R. G. Della Valle, A. Brillante, M. Masino, and A. Girlando. Probing Pentacene Polymorphs by Lattice Dynamics Calculations. *J. Am. Chem. Soc.*, 124(10):2128–2129, 2002.

[34] R. G. Della Valle, E. Venuti, A. Brillante, and A. Girlando. Are Crystal Polymorphs Predictable? The Case of Sexithiophene. *J. Phys. Chem. A*, 112(29):6715–6722, 2008.

[35] G. Hlawacek, P. Puschnig, P. Frank, A. Winkler, C. Ambrosch-Draxl, and C. Teichert. Characterization of Step-Edge Barriers in Organic Thin-Film Growth. *Science*, 321(5885):108–111, 2008.

[36] S. Zorba, Y. Shapir, and Y. Gao. Fractal-mound growth of pentacene thin films. *Phys. Rev. B*, 74(24):245410, 2006.

[37] J. A. Venables, G. D. T. Spiller, and M. Hanbucken. Nucleation and growth of thin films. *Rep. Prog. Phys.*, 47:399–459, 1984.

[38] J. G. Amar and F. Family. Critical cluster size: Island morphology and size distribution in submonolayer epitaxial growth. *Phys. Rev. Lett.*, 74(11):2066–2069, 1995.

[39] R. Ruiz, B. Nickel, N. Koch, L. C. Feldman, R. F. Jr. Haglund, A. Kahn, F. Family, and G. Scoles. Dynamic scaling, island size distribution, and morphology in the aggregation regime of submonolayer pentacene films. *Phys. Rev. Lett.*, 91(13):136102, 2003.

[40] F. Schreiber. Organic molecular beam deposition: Growth studies beyond the first monolayer. *phys. stat. sol. (a)*, 201(6):1037–1054, 2004.

[41] S. Kowarik, A. Gerlach, and F. Schreiber. Organic molecular beam deposition: fundamentals, growth dynamics, and in situ studies. *J. Phys.: Condens. Matter*, 20(18):184005, 2008.

[42] T. A. Witten and L. M. Sander. Diffusion-limited aggregation, a kinetic critical phenomenon. *Phys. Rev. Lett.*, 47(19):1400–1403, 1981.

[43] T. Vicsek. Pattern formation in diffusion-limited aggregation. *Phys. Rev. Lett.*, 53(24):2281–2284, 1984.

[44] G. Ehrlich and F. G. Hudda. Atomic view of surface self-diffusion: Tungsten on tungsten. *J. Chem. Phys.*, 44(3):1039–1049, 1966.

[45] R. L. Schwoebel and E. J. Shipsey. Step motion on crystal surfaces. *J. Appl. Phys.*, 37(10):3682–3686, 1966.

[46] N. Karl. Organic semiconductors. *Festkörperprobleme*, 14:261–290, 1974.

[47] I. G. Hill, A. Kahn, Z. G. Soos, and R. A. Pascal, Jr. Charge-separation energy in films of π-conjugated organic molecules. *Chem. Phys. Lett.*, 327:181–188, 2000.

[48] Z. G. Soos, E. V. Tsiper, and A. Painelli. Polarization in organic molecular crystals and charge-transfer salts. *J. Lumin.*, 110(4):332–341, 2004.

[49] P. Peumans, A. Yakimov, and S. R. Forrest. Small molecular weight organic thin-film photodetectors and solar cells. *J. Appl. Phys.*, 93(7): 3693–3723, 2003.

[50] D. Cahen and A. Kahn. Electron Energetics at Surfaces and Interfaces: Concepts and Experiments. *Adv. Mater.*, 15:271–277, 2003.

[51] P. Cosseddu, A. Bonfiglio, I. Salzmann, J. P. Rabe, and N. Koch. Ambipolar transport in transparent and flexible all-organic heterojunction field effect transistors at ambient conditions. *Org. Electron.*, 9:191–197, 2008.

[52] P. W. Atkins. *Physical Chemistry*. W. H. Freeman & Company, 1982.

[53] N. Koch, S. Duhm, J. P. Rabe, A. Vollmer, and R. L. Johnson. Optimized hole injection with strong electron acceptors at organic-metal interfaces. *Phys. Rev. Lett.*, 95:237601, 2005.

[54] A. Kahn, N. Koch, and W. Y. Gao. Electronic structure and electrical properties of interfaces between metals and π-conjugated molecular films. *J. Poly. Sci. B*, 41:2529–2548, 2003.

[55] G. Witte, S. Lukas, P. S. Bagus, and C. Wöll. Vacuum level alignment at organic/metal junctions: "Cushion" effect and the interface dipole. *Appl. Phys. Lett.*, 87:263502, 2005.

[56] V. De Renzi, R. Rousseau, D. Marchetto, R. Biagi, S. Scandolo, and U. del Pennino. Metal work-function changes induced by organic adsorbates: A combined experimental and theoretical study. *Phys. Rev. Lett.*, 95:046804, 2005.

[57] H. Ishii, K. Sugiyama, E. Ito, and K. Seki. Energy level alignment and interfacial electronic structures at organic/metal and organic/organic interfaces. *Adv. Mater.*, 11:605–625, 1999.

[58] N. Koch, A. Kahn, J. Ghijsen, J.-J. Pireaux, J. Schwartz, R. L. Johnson, and A. Elschner. Conjugated organic molecules on metal versus polymer electrodes: Demonstration of a key energy level alignment mechanism. *Appl. Phys. Lett.*, 82(1):70–72, 2003.

[59] N. Koch, A. Elschner, J. P. Rabe, and R. L. Johnson. Work Function Independent Hole-Injection Barriers Between Pentacene and Conducting Polymers. *Adv. Mater.*, 17:330–335, 2005.

[60] C. Tengstedt, W. Osikowicz, W. R. Salaneck, I. D. Parker, C.-H. Hsu, and M. Fahlman. Fermi-level pinning at conjugated polymer interfaces. *Appl. Phys. Lett.*, 88:053502, 2006.

[61] N. Koch and A. Vollmer. Electrode-molecular semiconductor contacts: Work-function-dependent hole injection barriers versus fermi-level pinning. *Appl. Phys. Lett.*, 89:162107, 2006.

[62] X. Crispin, V. Geskin, A. Crispin, J. Cornil, R. Lazzaroni, W. R. Salaneck, and J.-L. Bredas. Characterization of the Interface Dipole at Organic/Metal Interfaces. *J. Am. Chem. Soc.*, 124:8131–8141, 2002.

[63] H. Fukagawa, S. Kera, T. Kataoka, S. Hosoumi, Y. Watanabe, K. Kudo, and N. Ueno. Role of ionization potential in vacuum-level alignment at organic semiconductors interfaces. *Adv. Mater.*, 19:665–668, 2007.

[64] S. Duhm, H. Glowatzki, J. P. Rabe, N. Koch, and R. L. Johnson. Spontaneous charge transfer at organic-organic homointerfaces to establish thermodynamic equilibrium. *Appl. Phys. Lett.*, 90:122113, 2007.

[65] H. Fukagawa, H. Yamane, T. Kataoka, S. Kera, M. Nakamura, K. Kudo, and N. Ueno. Origin of the highest occupied band position in pentacene films from ultraviolet photoelectron spectroscopy: Hole stabilization versus band dispersion. *Phys. Rev. B*, 73(24):245310, 2006.

[66] S. Duhm, H. Glowatzki, J. P. Rabe, N. Koch, and R. L. Johnson. Influence of alkyl chain substitution on sexithienyl-metal interface morphology and energetics. *Appl. Phys. Lett.*, 88(20):203109, 2006.

[67] E. A. Silinsh. *Organic Molecular Crystals*. Springer, Berlin, 1980.

[68] F. Gutmann and Lyons L. E. *Organic Semiconductors*. Wiley & Sons, New York, 1967.

[69] R. Friedlein, X. Crispin, M. Pickholz, M. Keil, S. Stafström, and W. R. Salaneck. High intercalation levels in lithium perylene stoichiometric compounds. *Chem. Phys. Lett.*, 354:389–394, 2002.

[70] S. Duhm, G. Heimel, I. Salzmann, H. Glowatzki, R. L. Johnson, A. Vollmer, J. P. Rabe, and N. Koch. Orientation-dependent ionization energies and interface dipoles in ordered molecular assemblies. *Nature Mater.*, 7(4):326–332, 2008.

[71] Y. Shen, A. R. Hosseini, M. H. Wong, and G. G. Malliaras. How to make ohmic contacts to organic semiconductors. *ChemPhysChem*, 5 (1):16–25, 2004.

[72] N. Karl. Charge carrier transport in organic semiconductors. *Synth. Met.*, 133-134:649–657, 2003.

[73] V. Coropceanu, J. Cornil, D. A. da Silva Filho, Y. Olivier, R. Silbey, and J. L. Bredas. Charge Transport in Organic Semiconductors. *Chem. Rev.*, 107(4):926–952, 2007.

[74] M. A. Baldo and S. R. Forrest. Interface-limited injection in amorphous organic semiconductors. *Phys. Rev. B*, 64:085201, 2001.

[75] S. M. Sze. *Physics of Semiconductor Devices*. John Wiley and Sons, 1981.

[76] R. W. I. de Boer, M. Jochemsen, T. M. Klapwijk, A. F. Morpurgo, J. Niemax, A. K. Tripathi, and J. Pflaum. Space charge limited transport and time of flight measurements in tetracene single crystals: A comparative study. *J. Appl. Phys.*, 95(3):1196–1202, 2004.

[77] O. D. Jurchescu, J. Baas, and T. T. M. Palstra. Effect of impurities on the mobility of single crystal pentacene. *Appl. Phys. Lett.*, 84(16): 3061–3063, 2004.

[78] O. Ostroverkhova, D. G. Cooke, S. Shcherbyna, R. F. Egerton, F. A. Hegmann, R. R. Tykwinski, and J. E. Anthony. Bandlike transport in pentacene and functionalized pentacene thin films revealed by subpicosecond transient photoconductivity measurements. *Phys. Rev. B*, 71 (3):035204, 2005.

[79] N. Ueno, K. Seki, N. Sato, H. Fujimoto, T. Kuramochi, K. Sugita, and H. Inokuchi. Energy-band dispersion in oriented thin films of pentatriacontan-18-one by angle-resolved photoemission with synchrotron radiation. *Phys. Rev. B*, 41(2):1176–1183, 1990.

[80] X. Crispin, J. Cornil, R. Friedlein, K. K. Okudaira, V. Lemaur, A. Crispin, G. Kestemont, M. Lehmann, M. Fahlman, R. Lazzaroni, Y. Geerts, G. Wendin, N. Ueno, J-L. Brédas, and W. R. Salaneck. Electronic delocalization in discotic liquid crystals: A joint experimental and theoretical study. *J. Am. Chem. Soc.*, 126:11889–11899, 2004.

[81] N. Koch, A. Vollmer, I. Salzmann, B. Nickel, H. Weiss, and J. P. Rabe. Evidence for temperature-dependent electron band dispersion in pentacene. *Phys. Rev. Lett.*, 96(15):156803, 2006.

[82] G. Koller, S. Berkebile, M. Oehzelt, P. Puschnig, C. Ambrosch-Draxl, F. P. Netzer, and M. G. Ramsey. Intra- and Intermolecular Band Dispersion in an Organic Crystal. *Science*, 317(5836):351–355, 2007.

[83] H. Bässler. Charge Transport in Disordered Organic Photoconductors a Monte Carlo Simulation Study. *phys. stat. sol. (b)*, 175(1):15–56, 1993.

[84] M. Volmer. The different photoelectrical occurrences on anthracene, their connections to each other, to fluorescence and dianthracene formation. *Ann. Phys.*, 40:775–796, 1913.

[85] H. Spanggaard and F. C. Krebs. A brief history of the development of organic and polymeric photovoltaics. *Sol. Energy Mater. Sol. Cells*, 83 (2-3):125–146, 2004.

[86] M. Hiramoto, H. Fujiwara, and M. Yokoyama. Three-layered organic solar cell with a photoactive interlayer of codeposited pigments. *Appl. Phys. Lett.*, 58(10):1062–1064, 1991.

[87] N. S. Sariciftci, L. Smilowitz, A. J. Heeger, and F. Wudl. Photoinduced Electron Transfer from a Conducting Polymer to Buckminsterfullerene. *Science*, 258(5087):1474–1476, 1992.

[88] C. J. Brabec, N. S. Sariciftci, and J. C. Hummelen. Plastic solar cells. *Adv. Funct. Mater.*, 11(1):15–26, 2001.

[89] H. Hoppe and N. S. Sariciftici. Organic solar cells: An overview. *J. Mater. Res*, 19:1924–1945, 2004.

[90] C. J. Brabec, A. Cravino, D. Meissner, N. S. Sariciftci, T. Fromherz, M. T. Rispens, L. Sanchez, and J. C. Hummelen. Origin of the open circuit voltage of plastic solar cells. *Adv. Funct. Mater.*, 11(5):374–380, 2001.

[91] R. Kersting, U. Lemmer, M. Deussen, H. J. Bakker, R. F. Mahrt, H. Kurz, V. I. Arkhipov, H. Bässler, and E. O. Göbel. Ultrafast field-induced dissociation of excitons in conjugated polymers. *Phys. Rev. Lett.*, 73(10):1440–1443, 1994.

[92] J. Xue, B. P. Rand, S. Uchida, and S. R. Forrest. Mixed donor-acceptor molecular heterojunctions for photovoltaic applications. II. Device performance. *J. Appl. Phys.*, 98(12):124903, 2005.

[93] U. Shmueli, editor. *International Tables for Crystallography*, volume B. Kluwer Academic Publishers, 2006.

[94] D. McKie and C. McKie. *Essentials of Crystallography.* Blackwell Scientific Publications, 1986.

[95] I. Salzmann. Structural order in epitaxially grown oligo-phenylene thin films on metallic surfaces: X-ray diffraction studies in combination with crystallographic simulations. Master's thesis, Graz University of Technology, 2003.

[96] M. Schmidbauer. *X-ray diffuse scattering from self-organized mesoscopic semiconductor structures*, volume 199 of *Springer Tr. Mod. Phys.* Springer-Verlag Berlin, Heidelberg, New York, 2003.

[97] J. J. Thompson. On the scattering of rapidly moving electrified particles. *Proc. Cambridge. Phil. Soc.*, 15:465, 1910.

[98] V. Holý, U. Pietsch, and T. Baumbach. *High-Resolution X-Ray Scattering from Thin Films and Multilayers*, volume 149 of *Springer Tr. Mod. Phys.* Springer-Verlag Berlin, Heidelberg, New York, 1999.

[99] I. K. Robinson and D. J. Tweet. Surface x-ray diffraction. *Rep. Prog. Phys.*, 55(5):599–651, 1992.

[100] D. M. Smilgies. Geometry-independent intensity correction factors for grazing-incidence diffraction. *Rev. Sci. Instrum.*, 73:1706, 2002.

[101] M. Laue. Röntgenstrahlinterferenzen. *Physikalische Zeitschrift*, 14: 1075–1079, 1913.

[102] A. C. Dürr, F. Schreiber, M. Munch, N. Karl, B. Krause, V. Kruppa, and H. Dosch. High structural order in thin films of the organic semiconductor diindenoperylene. *Appl. Phys. Lett.*, 81(12):2276–2278, 2002.

[103] R. Feidenhans'l. Surface structure determination by x-ray diffraction. *Surf. Sci. Rep.*, 10(3):105–188, 1989.

[104] I. K. Robinson. Crystal truncation rods and surface roughness. *Phys. Rev. B*, 33(6):3830–3836, 1986.

[105] S. K. Sinha, E. B. Sirota, S. Garoff, and H. B. Stanley. X-ray and neutron scattering from rough surfaces. *Phys. Rev. B*, 38(4):2297–2311, 1988.

[106] Y. Yoneda. Anomalous surface reflection of x-rays. *Phys. Rev.*, 131(5): 2010–2013, 1963.

[107] M. Tolan. *X-ray scattering from soft-matter thin films*, volume 148 of *Springer Tr. Mod. Phys.* Springer-Verlag Berlin, Heidelberg, New York, 1999.

[108] George H. Vineyard. Grazing-incidence diffraction and the distorted-wave approximation for the study of surfaces. *Phys. Rev. B*, 26(8): 4146–4159, 1982.

[109] M. Birkholz. *Thin Film Analysis by X-Ray Scattering.* Wiley-VCH Verlag GmbH, Weinheim, 2006.

[110] H. Kiessig. Interferenz von Röntgenstrahlen an dünnen Schichten. *Ann. Phys.-Berlin*, 402:769 – 788, 1931.

[111] H. Kiessig. Untersuchungen zur Totalreflexion von Röntgenstrahlen. *Ann. Phys.-Berlin*, 402(6):715–768, 1931.

[112] L. G. Parratt. Surface studies of solids by total reflection of x-rays. *Phys. Rev.*, 95(2):359–369, 1954.

[113] P. Scherrer. Determination of the Size and the Internal Structure of Colloid Particles by Means of X-rays. *Nachr. Ges. Wiss. Göttingen, Math.-Phys.*, 2:98–100, 1918.

[114] J. I. Langford and A. J. C. Wilson. Scherrer after sixty years: A survey and some new results in the determination of crystallite size. *J. Appl. Cryst.*, 11(2):102–113, 1978.

[115] J. I. Langford. A rapid method for analysing the breadths of diffraction and spectral lines using the Voigt function. *J. Appl. Cryst.*, 11(1):10–14, 1978.

[116] H. Savaloni, M. Gholipour-Shahraki, and M. A. Player. A comparison of different methods for x-ray diffraction line broadening analysis of Ti and Ag UHV deposited thin films: nanostructural dependence on substrate temperature and film thickness. *J. Phys. D: Appl. Phys.*, 39 (10):2231–2247, 2006.

[117] J. I. Langford. *Accuracy in Powder Diffraction II*, volume 846 of *National Institute of Standards and Technology Special Publication*, pages 110–126. NIST, 1992.

[118] R. L. Snyder, J. Fiala, and H. J. Bunge. *Defect and Microstructure Analysis by Diffraction*. Oxford University Press, 1999.

[119] P. Scardi, M. Leoni, and R. Delhez. Line broadening analysis using integral breadth methods: a critical review. *J. Appl. Cryst.*, 37(3): 381–390, 2004.

[120] O. M. Yefanov. Accessible reciprocal-space region for non-coplanar Bragg and Laue geometries. *J. Appl. Crystallogr.*, 41(1):110–114, 2008.

[121] J. Stangl. *High-resolution X-ray Diffraction Studies of Self-organized SiGe(C) Islands*. PhD thesis, Johannes Kepler University Linz, Austria, 2000.

[122] D. M. Smilgies and D. R. Blasini. Indexation scheme for oriented molecular thin films studied with grazing-incidence reciprocal-space mapping. *J. Appl. Cryst.*, 40(4):716–718, 2007.

[123] S. Schiefer. *Determination of the crystal structure of substrate induced pentacene polymorphs in fibre textured thin-films*. PhD thesis, Ludwig-Maximilians-Universität München, 2007.

[124] W. R. Busing and H. A. Levy. Angle calculations for 3- and 4-circle X-ray and neutron diffractometers. *Acta Cryst.*, 22:457–464, 1967.

[125] I. Salzmann and R. Resel. STEREOPOLE: software for the analysis of X-ray diffraction pole figures with IDL. *J. Appl. Cryst.*, 37(6):1029–1033, 2004.

[126] R. Magnee, Z. Mekhalif, C. Doneux, A.-S. Duwez, C. Gregoire, J. Riga, J. Delhalle, and J.-J. Pireaux. On the impact of electron spectroscopies (versus optical techniques) to study organized organic layers and their interfaces. *J. Electron Spectrosc. Relat. Phenom.*, 88-91:855–860, 1998.

[127] N. Koch. Energy levels at interfaces between metals and conjugated organic molecules. *J. Phys.: Condens. Matter*, 20(18):184008, 2008.

[128] S. Hüfner. *Photoelctron Spectroscopy*, volume 82 of *Solid-State Sciences*. Springer, 1995.

[129] M. Cardona and L. Ley, editors. *Photoemission in Solids I*, volume 26 of *Topics in Applied Physics*. Springer, Berlin, 1978.

[130] F. J. Himpsel. Angle-resolved measurements of the photoemission of electrons in the study of solids. *Adv. Phys.*, 32:1–51, 1983.

[131] H. Hertz. Ueber einen Einfluss des ultravioletten Lichtes auf die electrische Entladung. *Ann. Physik*, 267(8):983–1000, 1887.

[132] A. Einstein. Über einen die Erzeugung und Verwandlung des Lichtes betreffenden heuristischen Gesichtspunkt. *Ann. Physik*, 322(6):132–148, 1905.

[133] R. Smoluchowski. Anisotropy of the electronic work function of metals. *Phys. Rev.*, 60:661–674, 1941.

[134] T. Koopmans. Über die Zuordnung von Wellenfunktionen und Eigenwerten zu den einzelnen Elektronen eines Atoms. *Physica*, 1(1-6):104–113, 1934.

[135] N. Koch, G. Heimel, J. Wu, E. Zojer, R. L. Johnson, J.-L. Brédas, K. Müllen, and J. P. Rabe. Influence of molecular conformation on organic/metal interface energetics. *Chem. Phys. Lett.*, 413:390–395, 2005.

[136] J. L. Koenig. Fourier-Transform Infrared Spectroscopy of Polymers. *Adv. Polym. Sci.*, 54:87–154, 1984.

[137] J. R. Ferraro and K. Krishnan, editors. *Practical Fourier Transform Infrared Spectroscopy*. Academic Press, San Diego, Toronto, 1990.

[138] W. Demtröder. *Experimentalphysik 3*. Springer, Berlin, Heidelberg, New York, 3 edition, 2005.

[139] J. W. Cooley and J. W. Tukey. An Algorithm for the Machine Calculation of Complex Fourier Series. *Math. Comput.*, 19(90):297–301, 1965.

[140] D. R. T. Zahn, G. N. Gavrila, and G. Salvan. Electronic and Vibrational Spectroscopies Applied to Organic/Inorganic Interfaces. *Chem. Rev.*, 107:1161–1232, 2007.

[141] R. Silbey, J. Jortner, and S. A. Rice. On the Singlet-Exciton States of Crystalline Anthracene. *J. Chem. Phys.*, 42(5):1515–1534, 1965.

[142] A. V. Snigur and V. M. Rozenbaum. Davydov splitting of vibrational spectra of adsorbates. *Opt. Spectrosc.*, 95(5):685–689, 2003.

[143] G. Binnig, H. Rohrer, Ch. Gerber, and E. Weibel. Surface studies by scanning tunneling microscopy. *Phys. Rev. Lett.*, 49(1):57–61, 1982.

[144] G. Binnig, C. F. Quate, and Ch. Gerber. Atomic force microscope. *Phys. Rev. Lett.*, 56(9):930–933, 1986.

[145] E. Meyer, H. J. Hug, and R. Bennewitz. *Scanning Probe Microscopy. The Lab on a Tip.* Springer, Berlin, Heidelberg, New York, 2004.

[146] R. Wiesendanger. *Scanning Probe Microscopy and Spectroscopy.* Cambridge Univ. Press, Cambridge, 1994.

[147] Q. Zhong, D. Inniss, K. Kjoller, and V. B. Elings. Fractured polymer/silica fiber surface studied by tapping mode atomic force microscopy. *Surf. Sci.*, 290(1-2):L688–L692, 1993.

[148] R. García and R. Pérez. Dynamic atomic force microscopy methods. *Surf. Sci. Rep.*, 47(6-8):197–301, 2002.

[149] H. C. Hamaker. The London–van der Waals attraction between spherical particles. *Physica*, 4(10):1058–1072, 1937.

[150] F. J. Giessibl. Forces and frequency shifts in atomic-resolution dynamic-force microscopy. *Phys. Rev. B*, 56(24):16010–16015, 1997.

[151] F. J. Giessibl. Advances in atomic force microscopy. *Rev. Mod. Phys.*, 75(3):949–983, 2003.

[152] T. Stifter, O. Marti, and B. Bhushan. Theoretical investigation of the distance dependence of capillary and van der waals forces in scanning force microscopy. *Phys. Rev. B*, 62(20):13667–13673, 2000.

[153] S. N. Magonov, V. Elings, and M. H. Whangbo. Phase imaging and stiffness in tapping-mode atomic force microscopy. *Surf. Sci.*, 375(2-3): L385–L391, 1997.

[154] K. J. Stout, P. J. Sullivan, W. P. Dong, E. Mainsah, N. Luo, T. Mathia, and H. Zahouani. The development of methods for the characterization of roughness on three dimensions. Technical report, Publication no. EUR 15178 EN of the Commission of the European Communities (Luxembourg), 1994.

[155] C. D. Dimitrakopoulos, S. Purushothaman, J. Kymissis, A. Callegari, and J. M. Shaw. Low-voltage organic transistors on plastic comprising high-dielectric constant gate insulators. *Science*, 283(5403):822–824, 1999.

[156] M. Halik, H. Klauk, U. Zschieschang, T. Kriem, G. Schmid, W. Radlik, and K. Wussow. Fully patterned all-organic thin film transistors. *Appl. Phys. Lett.*, 81(2):289–291, 2002.

[157] Y. Y. Lin, D. J. Gundlach, S. F. Nelson, and T. N. Jackson. Stacked pentacene layer organic thin-film transistors with improved characteristics. *IEEE Electron Device Lett.*, 18(12):606–608, 1997.

[158] S. Lee, B. Koo, J. Shin, E. Lee, H. Park, and H. Kim. Effects of hydroxyl groups in polymeric dielectrics on organic transistor performance. *Appl. Phys. Lett.*, 88(16):162109, 2006.

[159] Y. Kato, S. Iba, R. Teramoto, T. Sekitani, T. Someya, H. Kawaguchi, and T. Sakurai. High mobility of pentacene field-effect transistors with polyimide gate dielectric layers. *Appl. Phys. Lett.*, 84(19):3789–3791, 2004.

[160] M. Shtein, J. Mapel, J. B. Benziger, and S. R. Forrest. Effects of film morphology and gate dielectric surface preparation on the electrical characteristics of organic-vapor-phase-deposited pentacene thin-film transistors. *Appl. Phys. Lett.*, 81(2):268–270, 2002.

[161] F. Garnier. Thin-film transistors based on organic conjugated semiconductors. *Chem. Phys.*, 227(1-2):253–262, 1998.

[162] T. Minari, T. Nemoto, and S. Isoda. Fabrication and characterization of single-grain organic field-effect transistor of pentacene. *J. Appl. Phys.*, 96(1):769–772, 2004.

[163] T. B. Singh, P. Senkarabacak, N. S. Sariciftci, A. Tanda, C. Lackner, R. Hagelauer, and G. Horowitz. Organic inverter circuits employing ambipolar pentacene field-effect transistors. *Appl. Phys. Lett.*, 89: 033512, 2006.

[164] H. W. Kroto, J. R. Heath, S. C. O'Brien, R. F. Curl, and R. E. Smalley. C60: Buckminsterfullerene. *Nature*, 318(6042):162–163, 1985.

[165] K. Itaka, M. Yamashiro, J. Yamaguchi, M. Haemori, S. Yaginuma, Y. Matsumoto, M. Kondo, and H. Koinuma. High-Mobility C_{60} Field-Effect Transistors Fabricated on Molecular- Wetting Controlled Substrates. *Adv. Mater.*, 18(13):1713–1716, 2006.

[166] S. D. Wang, K. Kanai, Y. Ouchi, and K. Seki. Bottom contact ambipolar organic thin film transistor and organic inverter based on C60/pentacene heterostructure. *Org. Electron.*, 7(6):457–464, 2006.

[167] C. R. Newman, C. D. Frisbie, D. A. da Silva Filho, J.-L. Bredas, P. C. Ewbank, and K. R. Mann. Introduction to Organic Thin Film Transistors and Design of n-Channel Organic Semiconductors. *Chem. Mater.*, 16(23):4436–4451, 2004.

[168] I. Salzmann, S. Duhm, G. Heimel, J. P. Rabe, N. Koch, M. Oehzelt, Y. Sakamoto, and T. Suzuki. Structural Order in Perfluoropentacene Thin Films and Heterostructures with Pentacene. *Langmuir*, 24(14): 7294–7298, 2008.

[169] N. Koch, A. Vollmer, S. Duhm, Y. Sakamoto, and T. Suzuki. The Effect of Fluorination on Pentacene/Gold Interface Energetics and Charge Reorganization Energy. *Adv. Mater.*, 19:112–116, 2007.

[170] A. Hinderhofer, U. Heinemeyer, A. Gerlach, S. Kowarik, R.M.J. Jacobs, Y. Sakamoto, T. Suzuki, and F. Schreiber. Optical properties of pentacene and perfluoropentacene thin films. *J. Chem. Phys.*, 127(19): 194705, 2007.

[171] S. Kowarik, A. Gerlach, A. Hinderhofer, S. Milita, F. Borgatti, F. Zontone, T. Suzuki, F. Biscarini, and F. Schreiber. Structure, morphology, and growth dynamics of perfluoro-pentacene thin films. *phys. stat. sol. (RRL)*, 2(3):120–122, 2008.

[172] N. Koch, A. Vollmer, and A. Elschner. Influence of water on the work function of conducting poly(3,4- ethylenedioxythiophene)/ poly(styrenesulfonate). *Appl. Phys. Lett.*, 90:043512, 2007.

[173] S. Kirchmeyer and K. Reuter. Scientific importance, properties and growing applications of poly(3,4-ethylenedioxythiophene). *J. Mater. Chem.*, 15:2077 – 2088, 2005.

[174] R. L. Johnson and J. Reichardt. FLIPPER II – a new photoemission system in HASYLAB. *Nucl. Instrum. Methods Phys. Res.*, 208:791–796, 1983.

[175] A. Vollmer, O. D. Jurchescu, I. Arfaoui, I. Salzmann, T. T. M. Palstra, P. Rudolf, J. Niemax, J. Pflaum, J. P. Rabe, and N. Koch. The effect of oxygen exposure on pentacene electronic structure. *Eur. Phys. J. E*, 17(3):339–343, 2005.

[176] N. Koch, D. Pop, R. L. Weber, N. Böwering, B. Winter, M. Wick, G. Leising, I. V. Hertel, and W. Braun. Radiation induced degradation and surface charging of organic thin films in ultraviolet photoemission spectroscopy. *Thin Solid Films*, 391(1):81–87, 2001.

[177] I. Salzmann, S. Duhm, R. Opitz, J. P. Rabe, R. L. Johnson, and N. Koch. Structural and electronic properties of pentacene-fullerene heterojunctions. *J. Appl. Phys.*, 104:114518, 2008.

[178] J. Nelson. Solar cells by self-assembly? *Science*, 293:1059–1060, 2001.

[179] P. Sullivan, S. Heutz, S. M. Schultes, and T. S. Jones. Influence of codeposition on the performance of CuPc–C60 heterojunction photovoltaic devices. *Appl. Phys. Lett.*, 84(7):1210–1212, 2004.

[180] B. Brousse, B. Ratier, and A. Moliton. Vapor deposited solar cells based on heterojunction or interpenetrating networks of zinc phthalocyanine and C60. *Thin Solid Films*, 451-452:81–85, 2004.

[181] J. Xue, S. Uchida, B. P. Rand, and S. R. Forrest. 4.2% efficient organic photovoltaic cells with low series resistances. *Appl. Phys. Lett.*, 84(16): 3013–3015, 2004.

[182] I. Salzmann, R. Opitz, S. Rogaschewski, J. P. Rabe, and N. Koch. Phase separation in vacuum co-deposited pentacene/6,13-pentacenequinone thin films. *Phys. Rev. B*, 75:174108, 2007.

[183] I. Salzmann, S. Duhm, R. Opitz, J. P. Rabe, and N. Koch. Impact of low 6,13-pentacenequinone concentration on pentacene thin film growth. *Appl. Phys. Lett.*, 91(5):051919, 2007.

[184] A. K. Pandey, K. N. N. Unni, and J. Nunzi. Pentacene/perylene co-deposited solar cells. *Thin Solid Films*, 511-512:529–532, July 2006.

[185] N. Koch, I. Salzmann, R. L. Johnson, J. Pflaum, R. Friedlein, and J. P. Rabe. Molecular orientation dependent energy levels at interfaces with pentacene and pentacenequinone. *Org. Electron.*, 7:537–545, 2006.

[186] H. Vázquez, W. Gao, F. Flores, and A. Kahn. Energy level alignment at organic heterojunctions: Role of the charge neutrality level. *Phys. Rev. B*, 71:041306, 2005.

[187] B. P. Rand, J. Xue, S. Uchida, and S. R. Forrest. Mixed donor-acceptor molecular heterojunctions for photovoltaic applications. I. Material properties. *J. Appl. Phys.*, 98(12):124902, 2005.

[188] A. H. Jayatissa, T. Gupta, and A. D. Pandya. Heating effect on C60 films during microfabrication: structure and electrical properties. *Carbon*, 42(5-6):1143–1146, 2004.

[189] M. Vogel, S. Doka, Ch. Breyer, M. Ch. Lux-Steiner, and K. Fostiropoulos. On the function of a bathocuproine buffer layer in organic photovoltaic cells. *Appl. Phys. Lett.*, 89(16):163501, 2006.

[190] S. Duhm, I. Salzmann, R. L. Johnson, and N. Koch. Organic/organic heterostructures: Exploring thermodynamic non-equilibrium conditions. *in preparation*, 2008.

[191] S. J. Kang, Y. Yi, C. Y. Kim, S. W. Cho, M. Noh, K. Jeong, and C. N. Whang. Energy level diagrams of C60/pentacene/Au and pentacene/C60/Au. *Synth. Met.*, 156(1):32–37, 2006.

[192] F. J. Zhang, A. Vollmer, J. Zhang, Z. Xu, J. P. Rabe, and N. Koch. Energy level alignment and morphology of interfaces between molecular and polymeric organic semiconductors. *Org. Electron.*, 8:606–614, 2007.

[193] G. Koller, F. P. Netzer, and M. G. Ramsey. Band alignment on a nanoscopically patterned inorganic–organic interface. *Appl. Phys. Lett.*, 83:563–565, 2003.

[194] R. Fischer, S. Schuppler, N. Fischer, Th. Fauster, and W. Steinmann. Image states and local work function for Ag/Pd(111). *Phys. Rev. Lett.*, 70:654–657, 1993.

[195] R. Mitsumoto, K. Seki, T. Araki, E. Ito, Y. Ouchi, Y. Achiba, K. Kikuchi, S. Yajima, S. Kawasaki, F. Okino, H. Touhara, H. Kobayashi, T. Sonoda, and H. Kurosaki. Soft X-ray absorption,

UV photoemission, and VUV absorption spectroscopic studies of fluorinated fullerenes. *J. Electron Spectrosc. Relat. Phenom.*, 78(1-3): 453–456, 1996.

[196] C. C. Mattheus, A. B. Dros, J. Baas, G. T. Oostergetel, A. Meetsma, J. L. de Boer, and T. T. M. Palstra. Identification of polymorphs of pentacene. *Synth. Met.*, 138(3):475–481, 2003.

[197] Jan L. de Boer, S. van Smaalen, V. Petricek, P. M. Dusek, M. A. Verheijen, and G. Meijer. Hexagonal close-packed C60. *Chem. Phys. Lett.*, 219(5-6):469–472, 1994.

[198] S. Schiefer, M. Huth, A. Dobrinevski, and B. Nickel. Determination of the crystal structure of substrate-induced pentacene polymorphs in fiber structured thin films. *J. Am. Chem. Soc.*, 129(34):10316–10317, 2007.

[199] D. Nabok, P. Puschnig, C. Ambrosch-Draxl, O. Werzer, R. Resel, and D. M. Smilgies. Crystal and electronic structures of pentacene thin films from grazing-incidence x-ray diffraction and first-principles calculations. *Phys. Rev. B*, 76(23):235322, 2007.

[200] U. Zhokhavets, T. Erb, H. Hoppe, G. Gobsch, and N. S. Sariciftci. Effect of annealing of poly(3-hexylthiophene)/fullerene bulk heterojunction composites on structural and optical properties. *Thin Solid Films*, 496(2):679–682, 2006.

[201] I. I. Potemkin and M. Moller. Microphase separation in ultrathin films of diblock copolymers with variable stickiness of one of the blocks to the surface. *Macromolecules*, 38(7):2999–3006, 2005.

[202] S. Walheim, M. Ramstein, and U. Steiner. Morphologies in ternary polymer blends after spin-coating. *Langmuir*, 15(14):4828–4836, 1999.

[203] P. Müller-Buschbaum, E. Bauer, O. Wunnicke, and M. Stamm. The control of thin film morphology by the interplay of dewetting, phase separation and microphase separation. *J. Phys.: Condens. Matter*, 17 (9):S363–S386, 2005.

[204] Y. Thomann, H.-J. Cantow, G. Bar, and M.-H. Whangbo. Investigation of morphologies and nanostructures of polymer blends by tapping mode phase imaging. *Appl. Phys. A*, 66(0):S1233–S1236, 1998.

[205] S. N. Magonov, V. Elings, and V. S. Papkov. AFM study of thermotropic structural transitions in poly(diethylsiloxane). *Polymer*, 38 (2):297–307, 1997.

[206] P. Busch, D. Posselt, D.-M. Smilgies, B. Rheinlander, F. Kremer, and C.M. Papdakis. Lamellar diblock copolymer thin films investigated by tapping mode atomic force microscopy: Molar-mass dependence of surface ordering. *Macromolecules*, 36(23):8717–8727, 2003.

[207] J. Szczepanski, C. Wehlburg, and M. Vala. Vibrational and electronic spectra of matrix-isolated pentacene cations and anions. *Chem. Phys. Lett.*, 232:221–228, 1995.

[208] D. M. Hudgins and S. A. Sandford. Infrared Spectroscopy of Matrix Isolated Polycyclic Aromatic Hydrocarbons. 2. PAHs Containing Five or More Rings. *J. Phys. Chem. A*, 102:344–352, 1998.

[209] S. E. Fritz, S. M. Martin, C. D. Frisbie, M. D. Ward, and M. F. Toney. Structural Characterization of a Pentacene Monolayer on an Amorphous SiO_2 Substrate with Grazing Incidence X-ray Diffraction. *J. Am. Chem. Soc.*, 126(13):4084–4085, 2004.

[210] L. F. Drummy and D. C. Martin. Thickness-driven orthorhombic to triclinic phase transformation in pentacene thin films. *Adv. Mater.*, 17 (7):903–907, 2005.

[211] A. C. Mayer, A. Kazimirov, and G. G. Malliaras. Dynamics of bimodal growth in pentacene thin films. *Phys. Rev. Lett.*, 97(10):105503, 2006.

[212] X. L. Chen, A. J. Lovinger, Z. Bao, and J. Sapjeta. Morphological and transistor studies of organic molecular semiconductors with anisotropic electrical characteristics. *Chem. Mater.*, 13(4):1341–1348, 2001.

[213] P. Sreearunothai, A. C. Morteani, I. Avilov, J. Cornil, D. Beljonne, R. H. Friend, R. T. Phillips, C. Silva, and L. M. Herz. Influence of copolymer interface orientation on the optical emission of polymeric semiconductor heterojunctions. *Phys. Rev. Lett.*, 96(11):117403, 2006.

[214] N. Koch, A. Elschner, J. Schwartz, and A. Kahn. Organic molecular films on gold versus conducting polymer: Influence of injection barrier height and morphology on current–voltage characteristics. *Appl. Phys. Lett.*, 82(14):2281–2283, 2003.

[215] H. Sirringhaus, P. J. Brown, R. H. Friend, M. M. Nielsen, K. Bechgaard, B. M. W. Langeveld-Voss, A. J. H. Spiering, R. A. J. Janssen, E. W. Meijer, P. Herwig, and D. M. de Leeuw. Two-dimensional charge transport in self-organized, high-mobility conjugated polymers. *Nature*, 401:685, 1999.

[216] H. Yoshida, K. Inaba, and N. Sato. X-ray diffraction reciprocal space mapping study of the thin film phase of pentacene. *Appl. Phys. Lett.*, 90(18):181930, 2007.

[217] M. Oehzelt, R. Resel, C. Suess, R. Friedlein, and W. R. Salaneck. Crystallographic and morphological characterization of thin pentacene films on polycrystalline copper surfaces. *J. Chem. Phys.*, 124(5):054711, 2006.

[218] I. P. M. Bouchoms, W. A. Schoonveld, J. Vrijmoeth, and T. M. Klapwijk. Morphology identification of the thin film phases of vacuum evaporated pentacene on SiO_2 substrates. *Synth. Met.*, 104(3):175–178, 1999.

[219] T. Minakata, H. Imai, M. Ozaki, and K. Saco. Structural studies on highly ordered and highly conductive thin films of pentacene. *J. Appl. Phys.*, 72(11):5220–5225, 1992.

[220] S. D. Wang, X. Dong, C. S. Lee, and S. T. Lee. Molecular orientation and film morphology of pentacene on native silicon oxide surface. *J. Phys. Chem. B*, 109:9892–9896, 2005.

[221] R. Ruiz, B. Nickel, N. Koch, L. C. Feldman, R. F. Haglund, A. Kahn, and G. Scoles. Pentacene ultrathin film formation on reduced and oxidized Si surfaces. *Phys. Rev. B*, 67(12):125406, 2003.

[222] G. Koller, S. Berkebile, J. R. Krenn, F. P. Netzer, M. Oehzelt, T. Haber, R. Resel, and M. G. Ramsey. Heteroepitaxy of Organic-Organic Nanostructures. *Nano Lett.*, 6(6):1207–1212, 2006.

[223] G. Heimel, D. Somitsch, P. Knoll, and E. Zojer. Ab initio study of vibrational anharmonic coupling effects in oligo(para-phenylenes). *J. Chem. Phys.*, 116(24):10921–10931, 2002.

[224] G. Heimel, Q. Cai, C. Martin, P. Puschnig, S. Guha, W. Graupner, C. Ambrosch-Draxl, M. Chandrasekhar, and G. Leising. On the structure of oligophenylenes. *Synth. Met.*, 119(1-3):371–372, 2001.

[225] G. Heimel, P. Puschnig, Q. Cai, C. Martin, E. Zojer, W. Graupner, M. Chandrasekhar, H. R. Chandrasekhar, C. Ambrosch-Draxl, and G. Leising. High pressure raman studies on the structural conformation of oligophenyls. *Synth. Met.*, 116(1-3):163–166, 2001.

[226] M. J. Frisch, G. W. Trucks, H. B. Schlegel, G. E. Scuseria, M. A. Robb, J. R. Cheeseman, J. A. Montgomery, Jr., T. Vreven, K. N. Kudin, J. C. Burant, J. M. Millam, S. S. Iyengar, J. Tomasi, V. Barone, B. Mennucci, M. Cossi, G. Scalmani, N. Rega, G. A. Petersson, H. Nakatsuji, M. Hada, M. Ehara, K. Toyota, R. Fukuda, J. Hasegawa, M. Ishida, T. Nakajima, Y. Honda, O. Kitao, H. Nakai, M. Klene, X. Li, J. E. Knox, H. P. Hratchian, J. B. Cross, V. Bakken, C. Adamo, J. Jaramillo, R. Gomperts, R. E. Stratmann, O. Yazyev, A. J. Austin, R. Cammi, C. Pomelli, J. W. Ochterski, P. Y. Ayala, K. Morokuma, G. A. Voth, P. Salvador, J. J. Dannenberg, V. G. Zakrzewski, S. Dapprich, A. D. Daniels, M. C. Strain, O. Farkas, D. K. Malick, A. D. Rabuck, K. Raghavachari, J. B. Foresman, J. V. Ortiz, Q. Cui, A. G. Baboul, S. Clifford, J. Cioslowski, B. B. Stefanov, G. Liu, A. Liashenko, P. Piskorz, I. Komaromi, R. L. Martin, D. J. Fox, T. Keith, M. A. Al-Laham, C. Y. Peng, A. Nanayakkara, M. Challacombe, P. M. W. Gill, B. Johnson, W. Chen, M. W. Wong, C. Gonzalez, and J. A. Pople. Gaussian 03, Revision C.02, 2004. Gaussian, Inc., Wallingford, CT.

[227] J.-O. Vogel, I. Salzmann, R. Opitz, S. Duhm, B. Nickel, J. P. Rabe, and N. Koch. Sub-nanometer control of the interlayer spacing in thin films of intercalated rodlike conjugated molecules. *J. Phys. Chem. B*, 111:14097–14101, 2007.

[228] A. Troisi and G. Orlandi. Band structure of the four pentacene polymorphs and effect on the hole mobility at low temperature. *J. Phys. Chem. B*, 109(5):1849–1856, 2005.

[229] I. Salzmann, S. Duhm, G. Heimel, M. Oehzelt, R. Kniprath, R. L. Johnson, J. P. Rabe, and N. Koch. Tuning the ionization energy of organic-semiconductor films: The role of polar intra-molecular bonds. *J. Am. Chem. Soc.*, 130:12870–12871, 2008.

[230] A. Natan, L. Kronik, H. Haick, and R. T. Tung. Electrostatic properties of ideal and non-ideal polar organic monolayers: Implications for electronic devices. *Adv. Mater.*, 19(23):4103–4117, 2007.

[231] G. Koller, B. Winter, M. Oehzelt, J. Ivanco, F.P. Netzer, and M.G.

Ramsey. The electronic band alignment on nanoscopically patterned substrates. *Org. Electron.*, 8(1):63–68, 2007.

[232] K. H. Probst and N. Karl. Energy-levels of electron and hole traps in band-gap of anthracene-crystals. *Phys. stat. sol.*, 27(2):499–508, 1975. ISSN 0031-8965.

[233] J. Pflaum, J. Niemax, and A. K. Tripathi. Chemical and structural effects on the electronic transport in organic single crystals. *Chem. Phys.*, 325(1):152–159, 2006.

[234] N. J. Watkins, L. Yan, and Y. Gao. Electronic structure symmetry of interfaces between pentacene and metals. *Appl. Phys. Lett.*, 80(23): 4384–4386, 2002.

[235] M. Eremtchenko, R. Temirov, D. Bauer, J. A. Schaefer, and F. S. Tautz. Formation of molecular order on a disordered interface layer: Pentacene/Ag(111). *Phys. Rev. B*, 72(11):115430, 2005.

[236] G. Witte and C. Wöll. Growth of aromatic molecules on solid substrates for applications in organic electronics. *J. Mater. Res.*, 19:1889–1916, 2004.

[237] N. Koch, J. Ghijsen, R. L. Johnson, J. Schwartz, J.-J. Pireaux, and A. Kahn. Physisorption-like interaction at the interfaces formed by pentacene and samarium. *J. Phys. Chem. B*, 106:4192–4196, 2002.

[238] D. K. Hwang, K. Kim, J. H. Kim, S. Im, D.-Y. Jung, and E. Kim. Structural and optical properties of 6,13-pentacenequinone thin films. *Appl. Phys. Lett.*, 85(23):5568–5570, 2004.

[239] Th. B. Singh, F. Meghdadi, S. Günes, N. Marjanovic, G. Horowitz, P. Lang, and N. S. Bauer, S. Sariciftci. High-performance ambipolar pentacene organic field-effect transistors on poly(vinyl alcohol) organic gate dielectric. *Adv. Mater.*, 17(19):2315–2320, 2005.

[240] M. Ahles, R. Schmechel, and H. v. Seggern. Complementary inverter based on interface doped pentacene. *Appl. Phys. Lett.*, 87(11):113505, 2005.

[241] T. Yasuda, T. Goto, K. Fujita, and T. Tsutsui. Ambipolar pentacene field-effect transistors with calcium source-drain electrodes. *Appl. Phys. Lett.*, 85(11):2098–2100, 2004.

[242] J. H. Kang, D. A. da Silva Filho, J. L. Bredas, and X. Y. Zhu. Shallow trap states in pentacene thin films from molecular sliding. *Appl. Phys. Lett.*, 86(15):152115, 2005.

[243] J. Nelson. Organic photovoltaic films. *Curr. Opin. Solid State Mater. Sci.*, 6(1):87–95, 2002.

[244] A. V. Dzyabchenko, V. E. Zavodnik, and V. K. Belsky. 6,13-pentacenequinone: molecular packing analysis. *Acta Cryst. B*, 35(9): 2250–2253, 1979.

[245] R. Ruiz, D. Choudhary, B. Nickel, T. Toccoli, K.-C. Chang, A.C. Mayer, P. Clancy, J.M. Blakely, R.L. Headrick, S. Iannotta, and G.G. Malliaras. Pentacene thin film growth. *Chem. Mater.*, 16(23):4497–4508, 2004.

[246] R. Ruiz, A. C. Mayer, G. G. Malliaras, B. Nickel, G. Scoles, A. Kazimirov, H. Kim, R. L. Headrick, and Z. Islam. Structure of pentacene thin films. *Appl. Phys. Lett.*, 85(21):4926–4928, 2004.

[247] A. C. Mayer, R. Ruiz, R. L. Headrick, A. Kazimirov, and G. G. Malliaras. Early stages of pentacene film growth on silicon oxide. *Org. Electron.*, 5(5):257–263, 2004.

[248] D. K. Hwang, K. Kim, J. H. Kim, D.-Y. Jung, E. Kim, and S. Im. Structural and optical properties of 6,13-pentacenequinone film. *Appl. Surf. Sci.*, 244(1-4):615–618, 2005.

[249] S. Pratontep, M. Brinkmann, F. Nuesch, and L. Zuppiroli. Correlated growth in ultrathin pentacene films on silicon oxide: Effect of deposition rate. *Phys. Rev. B*, 69(16):165201, 2004.

[250] H. Klauk and T. Jackson. Pentacene organic thin-film transistors and ics. *Solid State Technol.*, 43:63–77, 2000.

[251] C. F. Macrae, P. R. Edgington, P. McCabe, E. Pidcock, G. P. Shields, R. Taylor, M. Towler, and J. van de Streek. Mercury: visualization and analysis of crystal structures. *J. Appl. Cryst.*, 39:453–457, 2006.

[252] W. Kraus and G. Nolzeb. *POWDER CELL* – a program for the representation and manipulation of crystal structures and calculation of the resulting x-ray powder patterns. *J. Appl. Cryst.*, 29(3):301–303, 1996.

[253] Terence L. Threlfall. Analysis of organic polymorphs. a review. *The Analyst*, 120(10):2435 – 2460, 1995.

[254] J. H. Sharp and M. Abkowitz. Dimeric structure of a copper phthalocyanine polymorph. *J. Phys. Chem.*, 77(4):477–481, 1973.

[255] A. Napier and R. A. Collins. FTIR characteristics of haloginated phthalocyanines exhibiting polymorphism. *Thin Solid Films*, 248:166–177, 1994.

[256] M. M. El-Nahass, K. F. Abd-El-Rahman, and A. A. A. Darwish. Fourier-transform infrared and UV-vis spectroscopes of nickel phthalocyanine thin films. *Mat. Chem. Phys.*, 92:185–189, 2005.

[257] M. Avram and G. D. Mateescu. *Infrared spectroscopy.* Wiley, New York, 1972.

[258] D. Hadži and N. Sheppard. The "carbonyl" frequency in polycyclic quinones. *J. Am. Chem. Soc.*, 73:5460, 1951.

[259] S. R. Langhoff. Theoretical infrared spectra for polycyclic aromatic hydrocarbon neutrals, cations, and anions. *J. Phys. Chem.*, 100:2819–2841, 1996.

[260] Y. Hosoia, K. Okamuraa, Y. Kimuraa, H. Ishiia, and M. Niwanoa. Infrared spectroscopy of pentacene thin film on SiO_2 surface. *Appl. Surf. Sci.*, 244:607–610, 2005.

[261] I. Salzmann, S. Duhm, M. Oehzelt, D. Nabok, P. Puschnig, J. P. Rabe, and N. Koch. Crystal and electronic structures of the 6,13-pentacenequinone thin film phase: Combining grazing-incidence x-ray diffraction and force field calculations. *in preparation*, 2008.

[262] S. L. Mayo, B. D. Olafson, and W. A. Goddard. DREIDING: a generic force field for molecular simulations. *J. Phys. Chem.*, 94(26):8897–8909, 1990.

[263] C. D. Dimitrakopoulos, A. R. Brown, and A. Pomp. Molecular beam deposited thin films of pentacene for organic field effect transistor applications. *J. Appl. Phys.*, 80(4):2501–2508, 1996.

[264] A. Vollmer, H. Weiss, S. Rentenberger, I. Salzmann, J. P. Rabe, and N. Koch. The interaction of oxygen and ozone with pentacene. *Surf. Sci.*, 600(18):4004–4007, 2006.

[265] B. Stadlober, V. Satzinger, H. Maresch, D. Somitsch, A. Haase, H. Pichler, W. Rom, and G. Jakopic. Structural and electrical properties of polymorphic pentacene thin films. *Proc. SPIE*, 5217:112–123, 2003.

[266] N. Karl. *Charge Carrier Mobility in Organic Molecular Crystals*. Springer, Berlin, 2001.

[267] V. Y. Butko, X. Chi, D. V. Lang, and A. P. Ramirez. Field-effect transistor on pentacene single crystal. *Appl. Phys. Lett.*, 83(23):4773–4775, 2003.

[268] C. Goldmann, S. Haas, C. Krellner, K. P. Pernstich, D. J. Gundlach, and B. Batlogg. Hole mobility in organic single crystals measured by a "flip-crystal" field-effect technique. *J. Appl. Phys.*, 96(4):2080–2086, 2004.

[269] C. Pannemann, T. Diekmann, and U. Hilleringmann. Degradation of organic field-effect transistors made of pentacene. *J. Mater. Res.*, 19: 1999–2002, 2004.

[270] J. E. Northrup and M. L. Chabinyc. Gap states in organic semiconductors: Hydrogen- and oxygen-induced states in pentacene. *Phys. Rev. B*, 68(4):041202, 2003.

[271] O. D. Jurchescu, J. Baas, and T. T. M. Palstra. Electronic transport properties of pentacene single crystals upon exposure to air. *Appl. Phys. Lett.*, 87(5):052102, 2005.

[272] A. R. Brown, C. P. Jarrett, D. M. de Leeuw, and M. Matters. Field-effect transistors made from solution-processed organic semiconductors. *Synth. Met.*, 88(1):37–55, 1997.

[273] J. Jo, J. J. Heremans, F. Bradbury, H. Chen, and V. Soghomonian. Gate tunable electron injection in submicron pentacene transistors. *Nanotechnol.*, 15(8):1023–1026, 2004.

[274] N. J. Watkins and Y. Gao. Interface formation and energy level alignment of pentacene on SiO_2. *J. Appl. Phys.*, 94(9):5782–5786, 2003.

[275] W. Gao and A. Kahn. Controlled p-doping of zinc phthalocyanine by coevaporation with tetrafluorotetracyanoquinodimethane: A direct and inverse photoemission study. *Appl. Phys. Lett.*, 79:4040–4042, 2001.

[276] K. Seki and H. Ishii. Photoemission studies of functional organic materials and their interfaces. *J. Electron Spectrosc. Relat. Phenom.*, 88-91: 821–830, 1998.

[277] Y. Harada, H. Ozaki, and K. Ohno. Selective observation of outermost surface layer during epitaxial growth by penning-ionization electron spectroscopy: Pentacene on graphite. *Phys. Rev. Lett.*, 52(25):2269–2272, 1984.

[278] Y. Azuma, T. Hasebe, T. Miyamae, K. K. Okudaira, Y. Harada, K. Seki, E. Morikawa, V. Saile, and N. Ueno. Angle-resolved UV photoelectron spectra (UPS) of thin films of perylene-3,4,9,10-tetracarboxylic dianhydride on MoS_2. *J. Synchrotron Radiation*, 5(3):1044–1046, 1998.

Abbreviations

PQ	6,13-pentacenequinone
6T	α-sexithiophene
η_A	absorption efficiency
A	area factor
AFM	Atomic Force Microscope
$f(q)$	atomic form factor
Z	atomic number
N_A	Avogadro constant
U_{bias}	bias voltage
E_B	binding energy
Θ	Bragg angle
U_{bi}	built-in voltage
f_C	Cauchy (Lorentz) function
η_{cc}	charge collection efficiency
D_L	coherent film thickness perpendicular to the surface
r	complex reflection coefficient
t	complex transmission coefficient
COM	conjugated organic molecule
α_c	critical angle of total external reflection
JV-curves	current density vs. voltage curves
D	Davydov splitting
(ν, δ)	detector angles in the laboratory system
(φ, β)	detector angles in the sample system
DLA	diffusion-limited aggregation
DWBA	distorted-wave Born approximation
$\vec{E}$	electric field vector
EA	electron affinity
ϱ_e	electron density of the medium
Δ_e	electron injection barrier
$\Xi(x)$	electrostatic potential

EDC	energy distribution curve
E_{ex}^{bind}	exciton binding energy
η_{ed}	exciton diffusion efficiency
L_D	exciton diffusion length
η_{ct}	exciton dissociation efficiency
α_f	exit angle of the diffracted beam
η_{eqe}	external quantum efficiency
FFT	Fast Fourier Transform
E_F	Fermi energy
FF	fill factor
FT-IR	Fourier-transform infrared spectroscopy
$2w$	full width at half maximum
C60	fullerene
f_G	Gaussian function
GID	grazing incidence diffraction
H	Hamilton operator
HOMO	highest occupied molecular orbital
HOPG	highly oriented pyrolytic graphite
Δ_h	hole injection barrier
α_i	incident angle of the primary beam
ITO	indium tin oxide
$\beta_{2\Theta}$	integral breadth in 2Θ of a Bragg peak
Δq_z	integral peak breadth in terms of momentum transfer
ID	interface dipole
η_{iqe}	internal quantum efficiency
ICP	intrinsically conducting polymer
IPES	inverse photoelectron spectroscopy
IE	ionization energy
E_F^{kin}	kinetic energy of electrons emitted from the Fermi level
E_{homo}^{kin}	kinetic energy of the HOMO emission onset
E_{seco}^{kin}	kinetic energy of the SECO
D_K	layer thickness as determined from Kiessig fringes
$\mu(\lambda)$	linear attenuation coefficient
L	Lorentz factor
LEED	Low Energy Electron Diffraction
LUMO	lowest unoccupied molecular orbital
e	maximum (upper limit) strain
MPP	maximum power point
(hkl)	net planes of Miller indices h, k, l
θ_x	nominal coverage of compound "x"
J_N	N-slit interference function

f	number of degrees of freedom of a molecule
U_{oc}	open circuit voltage
P_{inc}	optical power density
OH	organic heterojunction
OPVC	organic photovoltaic cell
OSC	organic semiconductor
D_S	out-of-plane crystalline coherence length
Λ	penetration depth
PEN	pentacene
PFP	perfluoropentacene
PES	photoelectron spectroscopy
d_{hkl}	plane spacing of planes with Miller indices h, k, l
P	polarization factor
PEDOT:PSS	poly(3,4-ethylenedioxythiophene):poly(styrenesulfonate)
$q_{\parallel}$	projection of $\vec{q}$ on the scattering plane
$f_{pV}(2\Theta)$	pseudo-Voigt function
$\Delta q_z^{Kiessig}$	q_z-spacing of the Kiessig fringes
$\vec{H}_{hkl}$	reciprocal lattice vector
RSM	reciprocal space mapping
n	refractive index
R	rod intersection factor
rms	root-mean square
$\vec{q}$	scattering vector (momentum transfer)
SECO	secondary electron cutoff
Δ_{vac}	shift of the vacuum level
J_{sc}	short circuit current density
SiO_x	silicon oxide
$g(D)$	size distribution function
XRD	specular x-ray diffraction
$F(\vec{q})$	structure factor
TF-SCLC	trap-free space charge limited current
UHV	ultra-high vacuum
UPS	ultraviolet photoelectron spectroscopy
uc	unit cell
VL	vacuum level
VUV	vacuum-ultraviolet
VdW	Van der Waals
$q_{\perp}$	vertical component of the momentum transfer
$f_V(2\Theta)$	Voigt-function
$\langle D \rangle_V$	volume-weighted average crystallite size

$\vec{k}_f$	wave vectors of the diffracted beam
$\vec{k}_i$	wave vectors of the incoming beam
λ	wavelength
WHA	Williamson-Hall analysis
ϕ	work function
ϕ_{spec}	work function of the spectrometer
XPS	x-ray photoelectron spectroscopy
XRR	x-ray reflectivity
q_z	z-component of the momentum transfer